

Online: <http://dust.ess.uci.edu/facts>

Built: Tue 5th Feb, 2019, 08:09

Natural Aerosols in the Climate System

by Charlie Zender
University of California, Irvine

Department of Earth System Science
University of California
Irvine, CA 92697-3100

zender@uci.edu
Voice: (949) 891-2429
Fax: (949) 824-3256

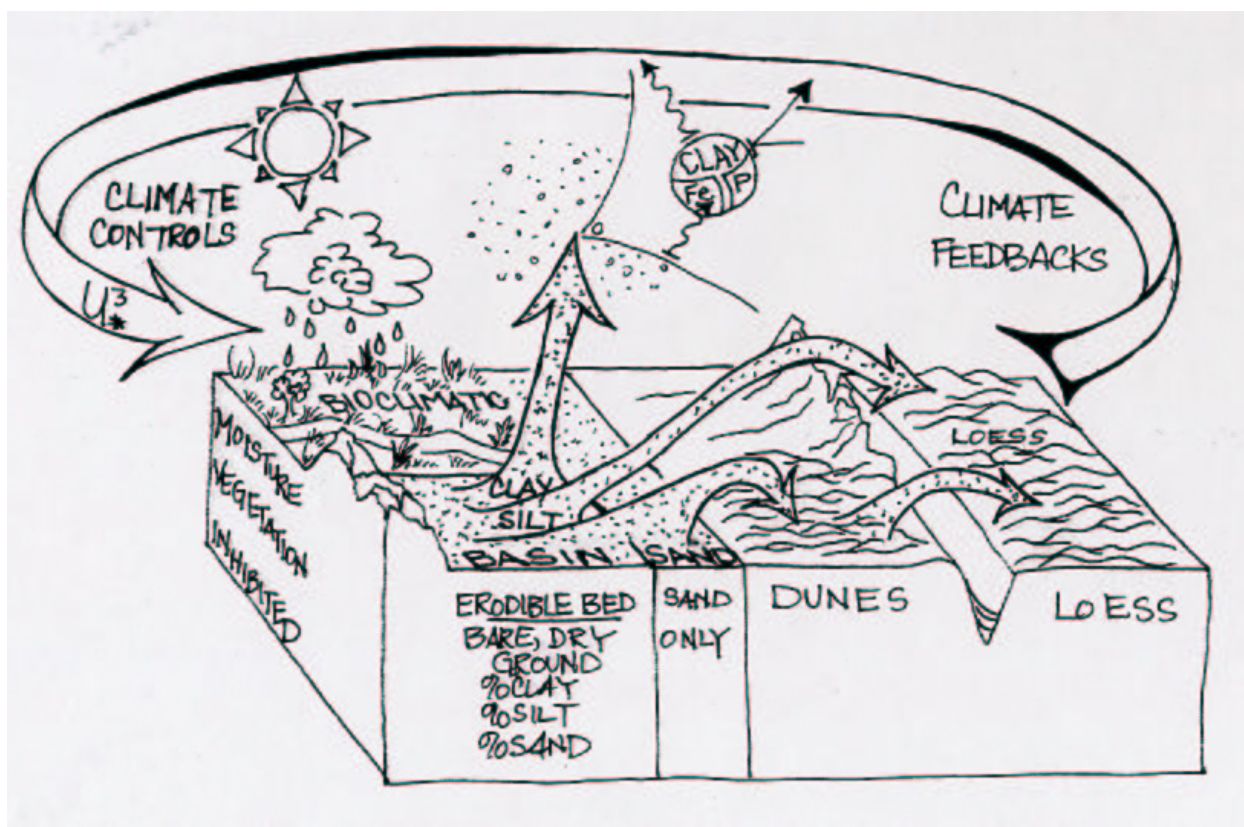


Figure 1: Mineral dust lifecycle. Illustration by Robynn Zender.

We gratefully acknowledge [The Annotated Grateful Dead Lyrics](#) site by David Dodd.
Lyric to “Box of Rain” (p. [87](#)), © Ice Nine Publishing Company. Used with permission.

Contents

Contents	iii
List of Figures	ix
List of Tables	xi
1 Introduction	1
1.1 Acknowledgements	1
1.2 Literature Review	1
1.2.1 Meteoric Dust	3
2 Boundary Layer Physics	5
2.1 Definitions	5
2.1.1 Wind Stress	5
2.1.2 Friction Velocity	6
2.1.3 Conversions	6
2.1.4 Neutral Stability	6
2.2 Surface Fluxes	7
2.2.1 Bulk Aerodynamic Approximation	8
2.2.2 Roughness Length	10
2.2.3 Stability Corrections	13
2.2.4 Flux-Gradient Relationships	14
2.2.5 Similarity Functions	15
2.2.6 Monin-Obukhov Length	15
2.3 Wind Speed	17
2.3.1 Reference Level Wind Speed	17
3 Dust Source Processes	19
3.1 Literature Review	19
3.2 Threshold Wind Friction Speed	20
3.2.1 Bagnold's Original Theory	20
3.2.2 Reynolds Number	22
3.2.3 Iversen's Theory	24
3.3 Horizontal Dust Flux	29
3.3.1 Original Theory	31

3.3.2	Owen's Theory	33
3.3.3	Kawamura/White Formulation	34
3.3.4	Australian School	37
3.3.5	My Theory	38
3.4	Vertical Dust Flux	39
3.4.1	Australian School	40
3.4.2	Marticorena's Theory	43
3.4.3	My Theory	51
3.5	Sub-Gridscale Properties	51
3.5.1	Weibull Distribution	52
3.5.2	Dust Devils	53
3.6	Drag Partitioning	53
3.7	Dependence On Soil Moisture	55
3.7.1	Soil Water Content	55
3.7.2	Characterization of Soil Water Energy	58
3.7.3	Capillary and Adsorptive Forces	61
3.7.4	Empirical Adjustments to Threshold Speed	61
3.7.5	McKenna-Neuman's Theory	63
3.7.6	Fécan's Theory	64
3.8	Geomorphology	65
3.9	Dust Source Regions	65
3.9.1	Bodélé Depression	66
3.9.2	Takla Makan Desert	66
3.9.3	Lake Eyre Basin	66
4	Sea Salt	69
4.1	Literature Review	69
4.2	Sea Salt Generation	69
5	Dry Deposition	75
5.1	Dry Deposition Literature	75
5.2	Deposition Velocity	76
5.3	Dry Deposition Theory	77
5.3.1	Sehmel's Experiments	78
5.4	Resistance Method	78
5.4.1	Gravitational Settling	79
5.4.2	Aerodynamics of Aspherical Particles	82
5.4.3	Volume-to-Surface Techniques	83
5.4.4	Large Dust Particles	85
5.5	Quasi-Laminar Layer Resistance	85
5.5.1	Stokes Number	85
5.5.2	Brownian Diffusion	85

6	Wet Deposition	87
6.1	Wet Deposition Literature	87
6.2	Collision Processes	88
6.2.1	Brownian Diffusion	89
6.2.2	Interception	89
6.2.3	Inertial Impaction	89
6.3	Collision Efficiency	91
6.4	Sticking Efficiency	91
6.5	Scavenging Efficiency	92
6.6	Precipitation-Aerosol Interactions	100
6.7	Hygroscopic Growth	100
7	Paleoclimate Aerosols	103
8	Thermodynamics of Gases	105
8.1	Temperature	105
8.2	Ideal Gas Law	105
8.2.1	Change in Saturation with Temperature	106
9	Radiative Properties	107
9.1	Radiation Literature Review	107
9.2	Refractive Indices	107
9.2.1	Reflectance-Based Refractive Indices	109
9.3	Effective Medium Approximations	110
9.3.1	General Considerations	111
9.3.2	Hollow Sphere Equivalent	111
9.3.3	Volume-Weighted	111
9.3.4	Maxwell Garnett Approximation	112
9.3.5	Bruggeman Approximation	113
9.3.6	Extended Effective Medium Approximation	115
9.4	Refractive Indices of Dust	115
9.5	Liquid or solid mantle coatings	116
9.6	Homogeneously Mixed Liquids	116
9.6.1	Partial Molar Refraction	116
9.7	Sulfate Aerosols	118
9.8	Radiative Heating of Particles	118
9.8.1	Latent Heating	119
9.8.2	Sensible Heating	121
9.8.3	Radiant Heating	122
9.8.4	Particle Temperature Evolution	122
9.8.5	Temperature Adjustment	124

10	Gas Phase Chemistry	125
10.1	Literature Review	125
10.2	Oxidation States	126
10.3	Stratospheric Chemistry	128
10.4	Sulfur Chemistry	129
10.4.1	Sulfur Emissions	129
10.4.2	Gas Phase Sulfur Chemistry	129
10.5	Nitrogen Chemistry	129
10.5.1	Nitrogen Emissions	129
10.5.2	Gas Phase Nitrogen Chemistry	129
11	Heterogeneous Chemistry	131
11.1	Mass Transfer Rates	131
11.1.1	Mean Free Path	132
11.1.2	Binary Gaseous Diffusion Coefficient	133
11.2	Surface Reaction Rates	134
11.3	Uptake coefficients	135
11.3.1	Laboratory Measurements of Mass Uptake	138
11.3.2	Gas Transport Limitation	143
11.3.3	Uptake on Solids	143
11.3.4	Field Measurements of Mass Uptake	144
11.4	Vapor Diffusion to Spherical Particles	144
11.4.1	Knudsen Number	145
11.4.2	Continuum Regime	145
11.4.3	Kinetic Regime	150
11.4.4	Transition Regime	151
11.4.5	Aerosol Motion	153
11.5	Diffusion Limited Rates	153
12	Aqueous Chemistry	155
12.1	Henry's Law	155
12.2	Aqueous Equilibria	156
12.2.1	Water	157
12.2.2	Carbon Dioxide	158
12.2.3	Sulfur Dioxide SO_2	161
12.2.4	Ammonia	163
12.2.5	Nitric Acid	164
12.2.6	Hydrogen Peroxide	166
12.3	Aqueous Sulfur Chemistry	167
12.4	Aqueous Iron Chemistry	167
12.5	Aqueous Nitrogen Chemistry	167
12.6	Mass Transport and Diffusion	168
13	Aerosol Physics	169

14	Chemistry and Mineral Dust	171
14.1	Role of Carbonate	172
14.2	Hygroscopic Growth	172
14.2.1	Zhang's Mechanism	177
14.2.2	Dentener's Mechanism	177
14.2.3	Bauer's Mechanism	180
14.2.4	My Mechanism	180
14.3	Global Sulfur Cycle	181
15	Photochemistry	185
15.1	Heterogeneous Photochemistry	186
16	Biogeochemistry	187
16.1	Biogeochemistry Literature	187
16.2	Limiting Nutrients: Iron	188
16.3	Limiting Nutrients: Nitrogen	188
16.4	Limiting Nutrients: Phosphorous	188
17	Implementation in NCAR models	189
17.1	Initialization	189
17.2	Main Loop	189
17.2.1	Mobilization	189
18	Appendix	191
18.1	Physical Constants	191
18.2	Common Chemical Conversions	192
18.3	Surface Tension of Water	192
18.4	Atmospheric Viscosity	193
18.5	Error Function	194
18.6	Gamma Function	194
18.7	Incomplete Gamma Functions	195
18.8	Marshall-Palmer Distribution	195
18.9	Rayleigh Distributions	196
18.10	Weibull Distribution	196
18.10.1	Truncated Weibull Distributions	199
18.10.2	Wind Speed Observations	200
18.11	Aspherical Shapes	200
18.11.1	Cylinders	201
18.11.2	Ellipsoids	201
18.11.3	Hexagonal Prisms	201
18.12	Vector Mathematics	204
18.12.1	Del Operator	204
18.12.2	Gradient	204
18.12.3	Divergence	204
18.12.4	Curl	205

18.12.5 Laplacian	205
18.13 Spherical Coordinates	205
18.13.1 Cartesian-Spherical Transformations	206
18.13.2 Gradient	207
18.13.3 Divergence	207
18.13.4 Curl	207
18.13.5 Laplacian	208
18.14 Fluid Mechanics	208
Bibliography	213
Index	242

List of Figures

1	Mineral Dust Lifecycle	1
5.1	Dry Deposition Velocity	79
6.1	Collision Efficiency	92
6.2	Scavenging coefficient	96
6.3	Scavenging coefficient for polydisperse raindrops	99

List of Tables

2.1	Boundary Layer Physics Conversion Table	7
2.2	Drag Coefficients	10
2.3	Momentum Roughness Length	12
3.1	Erodibility Properties of Nine Soils	45
3.2	Characteristic Arid Soil Populations	46
3.3	Mineral Composition of Windblown Dust	48
3.4	Elemental Composition of Earth's Crust and Surface Oceans	49
3.5	Western Sahara Soil Types	50
3.6	Soil Volume, Mass, Density and Moisture	57
3.7	Moisture Constraints	62
3.8	Erodibility Responses of Major Dust Source Regions	67
4.1	Tri-modal Sea Salt Parameters	74
10.1	Constituents of Important Chemical Families	127
10.2	Oxidation States Of Sulfur Species	127
10.3	Oxidation States of Nitrogen Species	128
11.1	Molecular Collision Diameters	134
11.2	Binary Gaseous Diffusion Coefficients	135
11.3	Measured Mass Accomodation Coefficients	136
11.4	Measured Uptake Coefficients	139
11.5	Deposition Velocity of O ₃	144
12.1	Henry's Law Coefficients	157
12.2	Aqueous Equilibrium Constants	158
14.1	Deliquescence Relative Humidity	172
14.2	Activity Coefficients	174
14.3	Saturation Vapor Pressure of Water	175
14.4	Hygroscopic Growth of Saharan Dust	177
14.5	Uptake Coefficients of Mineral Dust in UCI CTM	180
14.6	Uptake coefficients in Global Mineral Dust Model	181
14.7	Reactions in Global Mineral Dust Model	181
14.8	Reaction Rates in Global Sulfur Model	183

18.1 Physical Constants	191
18.2 Concentration Conversion Table	192

Chapter 1

Introduction

This monograph describes mathematical, physical, chemical, and computational considerations pertinent to understanding and simulating the distribution and effects of natural aerosols in Earth's atmosphere. Much of the content applies generically to any aerosol, but the majority of the aerosol-specific sections focus on mineral dust. There are also minor sections on sea salt mobilization and gaseous uptake on sulfate particles.

1.1 Acknowledgements

This monograph benefits from my discussions with many scientists. Their names appear in citations whenever possible. However, many of their ideas, presented at meetings or in private conversations, are recapitulated here without acknowledgement. These people include Drs. Stephane Alfaro (Université Paris), Richard Arimoto (New Mexico State University), Vicki Grassian (University of Iowa), Zev Levin (Tel Aviv University), Natalie Mahowald (National Center for Atmospheric Research), Bill Nickling (Guelph University), Greg Okin (University of Virginia), Kevin Perry (University of Utah), Yaping Shao (University of New South Wales), and Richard Washington (Oxford University).

1.2 Literature Review

[Heintzenberg \(1989\)](#) reviewed the state of knowledge of tropospheric aerosol composition gleaned mainly from boundary layer observations. [Gomes et al. \(1990\)](#) report the observed size distributions and elemental compositions of mineral aerosols measured by a cascade impactor in the Sahara. [Greeley et al. \(1996\)](#) report measurements of natural saltation (at Pismo Beach, California) that form a useful dataset for testing saltation theories. [Alfaro et al. \(1997\)](#) describe results of wind-tunnel experiments to deduce the dependence of the emitted dust size distribution on the saltation intensity and u_* . [Prigent et al. \(1999\)](#) and [Lacaze et al. \(1999\)](#) show how multi-angle and microwave satellite sensors can adequately retrieve land surface properties such as LAI and roughness length, key to determining dust mobilization. [Sokolik et al. \(1998\)](#) show the important role of infrared absorption by mineral dust. [Sokolik and Toon \(1999\)](#) analyze the effects of mineral composition on dust optical properties. [Chiapello et al. \(1999\)](#) compared the in situ observations of mineral dust with

TOMS satellite retrievals. [Lohmann et al. \(1999\)](#) counted mineral dust particles smaller than $2\mu\text{m}$ as cloud droplet condensation nuclei. [Reader et al. \(1999a\)](#) and [Reader et al. \(1999b\)](#) analyzed changes between mineral dust climatologies during the Last Glacial Maximum and the present. [Gillette \(1999\)](#) describes the factors contributing to the recurrence of dust emission “hot spots” as seen from TOMS. [Hamonou et al. \(1999\)](#) characterize the vertical structure of Saharan dust exported to the Mediterranean basin. [Claquin et al. \(1999\)](#) combined the FAO soil map of the world with surface mineralogy of specific samples to create predictive relationships linking soil type to surface mineralogy on a global scale. [Li et al. \(1999\)](#) showed it is possible to identify specific soil types from as few as six narrow-band infrared measurements. [Batt and Peabody II \(1999\)](#) measured threshold friction velocities for beds of pebbles 5–50 mm in diameter. [Ichoku et al. \(1999\)](#) describe an intensive field campaign in which radiative, microphysical, and chemical properties of various aerosols in the Negev desert were measured and inter-correlated. [King et al. \(1999\)](#) present an overview of the potential of current and future space-borne platforms to measure tropospheric aerosols including dust. [Rillig et al. \(1999\)](#) discovered that the proportion of soil aggregates larger than $250\mu\text{m}$ increases linearly with CO_2 concentration in certain grasslands due to biological effects. [Wang et al. \(2000\)](#) describe a Kosa (yellow dust) deflation model and evaluate its fidelity over East Asia. [Alfaro and Gomes \(2001\)](#) describe how to estimate the size distribution of the emitted dust by accounting for the size-dependent binding energy of the saltating particles. [Arimoto \(2001\)](#) present a broad overview of the climate factors influencing the abundance of atmospheric dust, as well as the radiative properties controlling the climate impact of dust. [Myhre and Stordal \(2001\)](#) performed sensitivity tests of the global radiative forcing of anthropogenic mineral dust. [Grini et al. \(2002b\)](#) discuss the stability, accuracy, and behavior of sandblasting fluxes determined by the [Alfaro and Gomes \(2001\)](#) model. [Lunt and Valdes \(2002\)](#) develop the Hadley Centre dust model and evaluate it against the standard suite of observations available on Earth. [Namikas \(2003\)](#) conclude from saltation measurements and modeling that the “launch speed” of saltators remains relatively constant during saltation, rather than increasing with friction speed. [Léon and Legrand \(2003\)](#) combined visible and infrared satellite measurements to identify dust sources and track dust plumes near the north Indian Ocean. [VanCuren \(2003\)](#) directly measure chemical composition of aerosol, including mineral dust, from Asia which dominates the mass concentration of remote, high altitude sites as far east as the western United States. [van Donk et al. \(2003\)](#) examine anthropogenic erosion on military bases in the Mojave Desert. [Kurosaki and Mikami \(2003\)](#) discovered that increased frequency of strong winds explains much of the observed increase in Dust Storm Frequency (DSF) in East Asia from 2000–2002 relative to the previous decade. [Cakmur et al. \(2004\)](#) show how sub-gridscale gustiness, driven largely by dry convection, explains dust emissions in regions where mean winds are otherwise too weak to generate observed emissions. [Kurosaki and Mikami \(2004\)](#) derive an empirical Snow Cover Factor (SCF) that accounts for the influence of snow on the threshold wind velocity for dust mobilization. [Grini and Zender \(2004\)](#) apply show that accounting for saltation, sandblasting, and wind-speed PDFs improves the simulated size distribution of long range transported dust in a global model. [Menut et al. \(2005\)](#) further discuss the problems with determining sandblasting fluxes highlighted by [Grini et al. \(2002b\)](#), and present a new numerically stable scheme for their evaluation. [Brooks et al. \(2005\)](#) describe the interaction between climate and society in the Sahara. [Arimoto et al.](#)

(2006) summarize dust measurements and modeling during ACE Asia. Many studies examine the possible role of dust as a vector for disease organisms affecting humans (Zender and Talamantes, 2006) and downwind ecosystems such as coral reefs (Shinn et al., 2000; Prospero et al., 2005). Yang et al. (2006) quantify the sensitivity of global dust mobilization, loading, and deposition to assumed size distribution. S. et al. (2006) characterize the effects of iron oxides on dust optical properties.

Many researchers have investigated the Martian dust cycle. In fact, until the 1990s, probably more dust research was performed by researchers more concerned with Mars than Earth. Recent global dust simulations on Mars are described in Pankine and Ingersoll (2002), Newman et al. (2002), and Basu et al. (2004).

1.2.1 Meteoric Dust

Deposition of Meteoric dust has occurred since Earth's formation. Annual deposits of extra-terrestrial dust are much less than terrestrial. However, meteoric dust has unique mineralogical characteristics that make even a small flux interesting. Peucker-Ehrenbrink et al. (1994) estimates a flux of $40 \pm 20 \text{ kt yr}^{-1}$ based on Osmium isotopes in seawater. Gabrielli et al. (2004) estimate a flux of $14 \pm 5 \text{ kt yr}^{-1}$ based on iridium and platinum measurements from a Greenland ice core. ? fxm.

Chapter 2

Boundary Layer Physics

2.1 Definitions

2.1.1 Wind Stress

Surfaces dissipate the momentum of the wind blowing over them. This dissipation is the result of tangential shear stress between the wind and the surface elements. The rate of change of atmospheric momentum $M_a \vec{v}$ defines a stress force $\vec{\tau}$ and the magnitude of this stress force $\tau = (\vec{\tau} \cdot \vec{\tau})^{1/2}$ expresses the total momentum the surface extracts from the wind per unit surface area per unit time. Hence the surface wind stress is also called the surface momentum flux. Some fraction of this wind stress τ does work on the surface in the form of moving the surface elements, e.g., moving leaves, or causing waves. Over bare or nearly bare ground much of the wind stress must go into aeolian abrasion (over stony surfaces) or soil movement since there is little else to absorb the force. The remainder of the wind stress may be converted to frictional heating of the surface, or small scale atmospheric turbulence.

We define the horizontal wind stress τ by appealing to basic principles of fluid dynamics. A fluid of density ρ moving at speed U exerts a pressure p (force per unit area) of $\frac{1}{2}\rho U^2$ on a stationary object transverse to the flow. The wind stress τ tangential to the surface takes a similar form,

$$\tau = C_m \rho U^2 \quad (2.1)$$

where C_m is the exchange coefficient for momentum. The dimensionless C_m may be thought of as twice the equivalent vertical obstruction created by a given horizontal surface. C_m , in turn, depends on the properties and distribution of surface elements. The quadratic dependence of τ on U results from the ... (fxm: look this up in Kundu, Bernoulli's equation).

The total stress to the surface $\vec{\tau}$ is the vector sum of individual components representing stress dissipated by the plant canopy, stress dissipated by airborne (saltating and suspended) particles, and, finally, wind stress dissipated by the solid surface itself. This stress partition or drag partition has important implications for dust studies.

$$\tau = \tau_a + \tau_p \quad (2.2)$$

Drag partitioning is discussed further in §3.6 and §3.3.

Using (2.5) to express the wind stress τ (2.1) solely in terms of u_* we obtain

$$\tau = \rho u_*^2 \quad (2.3)$$

2.1.2 Friction Velocity

We now consider the wind speed profile $U(z)$ between the free atmosphere and the surface. The planetary surface is the interface between the fluid atmosphere and the “solid” surface (soil, ocean, etc). A solid land surface requires a no slip boundary condition, i.e., the wind speed is zero exactly at the surface. To a good approximation, the ocean may also be treated with the no slip boundary condition since the atmospheric wind speed U_a is usually much larger than the surface current in the ocean u_o , i.e., $U_a \gg u_o$. Let us assume that we know the measured or predicted wind speed U_a at a height z above the surface.

Knowing the wind with speed U at height z exerts a stress τ on the surface,

$$u_* = \sqrt{\frac{\tau}{\rho}} \quad (2.4)$$

u_* is called the friction velocity, drag velocity, or, more appropriately, the friction speed.

Substituting (2.1) into (2.4) we see that

$$u_* = C_m^{1/2} U \quad (2.5)$$

The friction velocity u_* is the fundamental quantity determining the flux of dust into the atmosphere. Nevertheless, it is difficult to attach a simple physical interpretation to the friction velocity. However we now demonstrate two important physical properties of u_* . First, the mean horizontal wind speed at the top of the laminar layer is u_* . Thus immediately after uplift, a particle is embedded in a horizontal wind of speed u_* . In §3.3 we use this property of u_* to explain the observed cubic dependence of the horizontal mass flux of saltating particles on the wind speed.

Secondly, u_* is proportional to the mean velocity gradient $\frac{\partial u}{\partial z}$ near the surface.

2.1.3 Conversions

There are many other useful relations which can be established between U , u_* , r_m , C_m , and τ . These relations are simple, but tedious, to derive. Table 2.1 lists many of the relations between frequently occurring boundary layer parameters.

2.1.4 Neutral Stability

The thermodynamic properties of the boundary layer determine the vertical gradient of fluxes within the boundary layer. In neutral conditions the wind speed varies logarithmically with height according to

$$U^n(z) = \frac{u_*}{k} \ln \left(\frac{z}{z_{0,m}} \right) \quad (2.6)$$

Table 2.1: Conversion Factors Between Quantities In The Boundary Layer^a

	U m s^{-1}	u_* m s^{-1}	r_m s m^{-1}	C_m	τ N m^{-2}
U	—	$u_* C_m^{-1/2}$	$\frac{u_*}{k} \ln \left(\frac{z}{z_{0,m}} \right)$	$\sqrt{\frac{u_*^2}{C_m}}$	
u_*	$U C_m^{1/2}$	—			$\sqrt{\frac{\tau}{\rho}}$
r_m		$\frac{1}{k u_*} \ln \left(\frac{z}{z_{0,m}} \right)$	—	$(C_m U)^{-1}$	
C_m	$\frac{\tau}{\rho U^2}$	$\frac{u_*^2}{U^2}$	$(r_m U)^{-1}$	—	
τ	$-\frac{\rho U}{r_m}$	ρu_*^2		$-C_m \rho U^2$	—

^aNote that the numerators of the logarithmic profiles should actually be the difference between atmospheric height and zero plane displacement height $z - D$. For convenience we define $\tau \equiv |\vec{\tau}|$. Stability corrections are omitted for brevity.

where k is the Von Karman constant. The “n” superscript indicates neutral conditions. Strictly speaking, a logarithmic wind profile refers to a wind profile which obeys (2.6). Loosely used, the term refers to any wind profile in the lowest hundred meters or so of the atmosphere. The neutral exchange coefficient for momentum, also called the neutral drag coefficient, is then

$$C_m^n(z, z_{0,m} + D) = k^2 \left[\ln \left(\frac{z - D}{z_{0,m}} \right) \right]^{-2} \quad (2.7)$$

Finally, it is sometimes useful to invert (2.7) in order to obtain $z_{0,m}$ in terms of C_m^n

$$z_{0,m} = z \exp \left(-\frac{k}{\sqrt{C_m^n}} \right) \quad (2.8)$$

2.2 Surface Fluxes

The surface fluxes for momentum, heat, and vapor transfer are coupled by micrometeorological exchanges between the surface and the atmosphere in the surface (constant flux) layer. Determination of these fluxes from observation is possible via eddy flux correlation techniques. From a modeling perspective, the fluxes may determined by solving coupled non-linear differential equations in the surface layer. This technique is employed in Large Eddy Simulation (LES) models. LES solution resolve, as exactly as practical, the complex, turbulent eddies which determine the thermodynamic behavior of the boundary layer. However, large scale atmospheric models cannot afford to solve the continuous equations of motions throughout the boundary layer. Instead, a class of bi-level solutions for boundary layer fluxes has been developed based on Monin-Obukhov similarity theory.

Monin-Obukhov similarity theory is usually applied in terms of resistance r and conductance $C \equiv r^{-1}$ which describe the transfer of scalar quantities between two levels within the boundary layer. For simplicity, one of these levels is taken as z_{atm} the midpoint height of the lowest atmospheric layer in the large scale atmospheric model. A host model provides the potential temperature θ_{atm} , pressure p_{atm} , specific humidity q_{atm} , and meridional and zonal winds v_{atm} and u_{atm} . The subscript atm indicates the quantities are defined at the height z_{atm} . The momentum fluxes τ_x and τ_y [$\text{kg m}^{-1} \text{s}^{-2}$], sensible heat flux H [W m^{-2}], and moisture flux E [$\text{kg m}^{-2} \text{s}^{-1}$] are defined by the vertical gradient of the appropriate thermodynamic quantity between $z = z_{\text{atm}}$ and $z = z_s$, where z_s is the “surface height” (defined below). The fluxes are expressed as

$$\tau_x = -\rho \frac{(u_{\text{atm}} - u_s)}{r_m} \quad (2.9)$$

$$\tau_y = -\rho \frac{(v_{\text{atm}} - v_s)}{r_m} \quad (2.10)$$

$$H = -\rho c_p \frac{(\theta_{\text{atm}} - \theta_s)}{r_h} \quad (2.11)$$

$$E = -\rho \frac{(q_{\text{atm}} - q_s)}{r_v} \quad (2.12)$$

The similarity of these expressions to one another arises from the definitions of the resistances r_m , r_h , and r_v . These resistances depend implicitly on the fluxes τ , H , and E , through Monin-Obukhov similarity theory. Thus (2.9)–(2.12) must be solved iteratively.

Solutions to (2.9)–(2.12) must balance the surface energy budget. In other words, power absorbed by the surface must be dissipated by surface heating/cooling, and energy divergence to the atmosphere or soil in the form of latent, sensible, and radiative heating or cooling.

2.2.1 Bulk Aerodynamic Approximation

The turbulent surface fluxes, also called Reynolds fluxes, are the fluxes of heat, moisture, and momentum between the surface and the atmosphere. These fluxes arise as the atmosphere and the surface attempt to reach equilibrium states with the prevailing conditions. Because they are usually unresolved, the turbulent fluxes are usually determined by the application of Monin-Obukhov theory to the prevailing mean conditions. One simple and popular method, the bulk aerodynamic approximation, is of particular utility to large scale atmospheric models. We shall describe the essential physics for determining the turbulent surface fluxes, and related parameters, using the bulk aerodynamic approximation and more complex approximations.

There are three turbulent fluxes of interest: the momentum flux (also called the surface stress or wind stress) τ [$\text{kg m}^{-1} \text{s}^{-2}$], and the sensible and latent heat fluxes H and L , respectively, both measured in W m^{-2} . These fluxes are defined in terms of the eddy fluxes of the appropriate fields. Any scalar field $x(t)$ may be decomposed into time-mean and fluctuating components, \bar{x} and x' , respectively

$$x(t) = \bar{x} + x'(t) \quad (2.13)$$

By definition the time-mean component does not depend on time t and the time average of the fluctuating component vanishes.

$$\bar{\bar{x}} = \bar{x} \quad (2.14a)$$

$$\overline{x'(t)} = 0 \quad (2.14b)$$

Atmospheric models always predict the time-mean components of state variables like wind speed and temperature. The time-mean components satisfy the mass, energy, and momentum conservation equations (i.e., the primitive equations) which underpin fluid mechanics. Rarely do models predict the variance about the mean. Parameterizations of this variance usually invoke an extra degree of freedom to describe the PDF of the variance about the mean.

Eddy fluxes arise from the fluctuating components of state variables. Consider the vertical fluxes of the scalar quantity x (2.13). For concreteness, imagine that x represents horizontal wind speed U , temperature T , or specific humidity q . Using (2.13) we see that the instantaneous vertical flux of x is

$$\begin{aligned} w(t)x(t) &= [\bar{w} + w'(t)][\bar{x} + x'(t)] \\ &\equiv (\bar{w} + w')(\bar{x} + x') \\ &= \bar{w}\bar{x} + w'\bar{x} + x'\bar{w} + x'w' \end{aligned} \quad (2.15)$$

The time-mean surface flux of x is obtained by applying the time-average operator to (2.16)

$$\begin{aligned} \overline{w(t)x(t)} &= \overline{\bar{w}\bar{x} + w'\bar{x} + x'\bar{w} + w'x'} \\ &= \overline{\bar{w}\bar{x}} + \overline{w'\bar{x}} + \overline{x'\bar{w}} + \overline{w'x'} \\ &= \bar{w}\bar{x} + \overline{w'x'} \\ &= \overline{w'x'} \end{aligned} \quad (2.16)$$

where we have used the time-mean properties of \bar{x} and x' (2.14) and the further property that the vertical wind vanishes at the surface $\bar{w}(z=0) \equiv 0$.

The eddy fluxes are multiplied by a pre-factor to obtain the conventional units

$$\tau = -\rho \overline{w'U'} \quad (2.17a)$$

$$H = c_p \rho \overline{w'T'} \quad (2.17b)$$

$$L = l \rho \overline{w'q'} \quad (2.17c)$$

The bulk aerodynamic approximation for turbulent fluxes defines the eddy fluxes in terms of the time-mean state variables. The eddy correlations are assumed to be proportional to the product of the horizontal wind speed U and change of the appropriate state variable (U , θ , or q) between the surface and the height of interest.

$$-\overline{w'U'} = C_m U \Delta U = C_m U^2 \quad (2.18a)$$

$$\overline{w'T'} = C_h U \Delta \theta \quad (2.18b)$$

$$\overline{w'q'} = C_v U \Delta q \quad (2.18c)$$

Table 2.2: Drag Coefficients^{ab}

Name	Symbol	Defining Relationship
Drag coefficient	C_m	$\tau = C_m \rho U^2$
Drag coefficient at reference height	$C_{m,r}$	$C_{m,r} U_r^2 = \tau / \rho = -\overline{w'U'}$
Neutral drag coefficient at $z_r = 10$ m	C_m^n	$C_m^n = k^2 \left[\ln \left(\frac{z_r}{z_{0,m}} \right) \right]^{-2}$
Wind speed at $z = z_r$	U_r	$U - \frac{u_*}{k} \left[\ln \left(\frac{z - D}{z_r - D} \right) - \psi_m \left(\frac{z - D}{L} \right) + \psi_m \left(\frac{z_r - D}{L} \right) \right]$
Neutral wind speed at $z = z_r$	U_r^n	$U_r^n \sqrt{C_m^n} = U \sqrt{C_m} = u_*$

^aSources: [Large and Pond \(1981, 1982\)](#)

^bUsually the reference height is 10 m but we use z_r for generality.

where C_m , C_h , and C_v are dimensionless. These constants of proportionality are the called exchange coefficients for momentum, heat, and moisture, respectively. The atmosphere to surface changes in potential temperature and specific humidity may be written $\Delta\theta = \theta - \theta_s$ and $\Delta q = q - q_s$, respectively. We shall take (2.18) to be the definition of the exchange coefficients, although many other definitions are possible. Note that the vertical eddy correlation flux of temperature is parameterized in terms of the potential temperature.

Combining (2.17) with (2.18) we obtain

$$\begin{aligned}
 \tau &= -\rho \overline{w'U'} = \rho C_m U^2 \\
 H &= c_p \rho \overline{w'T'} = \rho c_p C_h U \Delta\theta \\
 L &= l \rho \overline{w'q'} = l \rho C_v U \Delta q
 \end{aligned} \tag{2.19}$$

Each of the variables in (2.19) is height dependent. However, it is very common to evaluate the exchange coefficients at a particular height known as the reference height z_r . The reference height is usually taken to be 10 m. Shifting the exchange coefficients between z_r an arbitrary height z is useful for putting measurements from a variety of heights into a common framework for analysis.

Table 2.2 describes the defining relations of many of the related quantities which prove useful in boundary layer meteorology. [Garratt \(1977\)](#) reviews drag coefficient terminology, relationships, measurements, and constraints.

2.2.2 Roughness Length

We assume aerosol has the same flux properties in the boundary layer as momentum. The roughness length for momentum transfer $z_{0,m}$ is a property of the surface characteristics only, i.e., $z_{0,m}$ is independent of wind speed when the following conditions are met:

1. All roughness elements are inelastic. Inelastic elements, such as rocks, do not deform under wind stress whereas elastic elements, such as some vegetation does. For flexible

vegetation, $z_{0,m}$ increases with wind speed U up to a critical speed U_c , and decreases thereafter. Ordinary lawn grass displays this behavior as it flutters in gentle breezes and bows before stiff winds.

2. Saltation is not occurring. Saltation roughens the boundary layer once it commences (Section 3.6).

Rougher surfaces tend to absorb more wind stress into non-erodible elements. Thus saltation decreases as $z_{0,m}$ increases, and visa versa. The frequency of saltation events follows the same pattern, since smooth surface initiate saltation more readily.

[Raupach \(1994\)](#) derived simple analytic relations for the roughness length $z_{0,m}$ and the zero-plane displacement D of vegetated surfaces as functions of vegetation height h and area index Λ . Microwave radar data may be inverted to obtain high resolution roughness length (and soil moisture) data of bare ground globally (e.g., [Prigent et al., 1999](#); [Lacaze et al., 1999](#); [Zribi and Dechambre, 2003](#)).

There are two roughness lengths pertinent to wind erosion over bare ground. The first is the aerodynamic roughness length of the bare ground including the non-erodible elements such as pebbles, rocks, and vegetation. This is what is traditionally known as the roughness length for momentum transfer, $z_{0,m}$. The second roughness length is the so-called “smooth” roughness length, $z_{0,m}^s$ ([Marticorena and Bergametti, 1995](#)). $z_{0,m}^s$ is the roughness length of a bed of potentially erodible particles without any non-erodible elements. The roughness length most easily measured in laboratory wind tunnel experiments is $z_{0,m}^s$. Wind tunnel experiments over uniform beds comprised of known particle sizes show that

$$z_{0,m}^s \approx D/30 \quad (2.20)$$

However, uniform beds of purely erodible particles are rare in Nature.

It is useful to distinguish between the susceptibility of soil to erosion, called erodibility, from the power of the wind (or some other force) to cause erosion, called erosivity. Erodibility depends on the microphysical, chemical, and mechanical properties of the the soil, vegetation, and topography ([D’Odorico et al., 2001](#)). Erosivity depends on the wind speed, intermittency, shear, and turbulence.

Discounting erodible particles which are sheltered by non-erodible elements, the roughness length felt by the atmosphere over erodible particles is $z_{0,m}^s$. Moreover, our theoretical understanding of threshold wind velocities is based on $z_{0,m}^s$, while most large scale atmospheric models are concerned with total momentum flux, and thus tend to compute $z_{0,m}$. Thus a theory is necessary to connect the $z_{0,m}^s$ to $z_{0,m}$. This is the theory of drag partition. The increase f_d in threshold friction velocity for saltation u_{*t} due to drag partition is ([Marticorena and Bergametti, 1995](#))

$$f_d = \left[1.0 - \left(\frac{\ln(z_{0,m}/z_{0,m}^s)}{\ln\{0.35[(0.1/z_{0,m}^s)^{0.8}]\}} \right) \right]^{-1} \quad (2.21)$$

The inverse of f_d is the fraction of momentum transferred that is available for inducing saltation, called the wind friction efficiency, $f_e = f_d^{-1}$. The roughness lengths $z_{0,m}$ and $z_{0,m}^s$ are properties of the surface characteristics only, i.e., they are independent of wind speed

Table 2.3: Momentum Roughness Lengths of Non-Vegetated Surface Types^a

Surface Type	$z_{0,m}$ m
Glacial ice	0.05
Lake ice	0.04
Warm lake	0.001
^b Sea ice	0.0005
Bare ground	0.05
Snow	0.04
^c Ocean	0.0001

^aSources: [Bonan \(1996\)](#), p. 59; [Bryan et al. \(1997\)](#), p. F-3

^bMore appropriate for newly formed, seasonal ice. For ridged, multi-year ice, $z_{0,m} \sim 0.05$ m.

^cMaritime $z_{0,m}$ depends strongly on surface conditions, see, e.g., [Large and Pond \(1981\)](#)

so long as the surface is not in motion. [Gillette et al. \(1998\)](#) present corrections to this assumption for saltating surfaces.

Strong saltation can modify $z_{0,m}$ because the saltators provide a sink for momentum distinct from the surface. Consider a saltator ejected from the surface with an initial speed proportional to u_* . It is common assumption that, after launching, a saltating particle experiences no vertical acceleration except gravity. Such trajectories are called ballistic. In a ballistic trajectory, the vertical velocity decreases linearly with time, and the initial upwards velocity equals the final downwards velocity. It is easy to show the height reached by a ballistic saltator is proportional to u_*^2/g . Strong saltation causes an effective thickening of the roughness length also in proportion to u_*^2/g . For strongly saltating surfaces with $u_* \gg u_{*t}$, [Chamberlain \(1983\)](#) suggests

$$z_{0,m} = c_0 u_*^2 / g \quad (2.22)$$

For moderate wind friction speeds $u_* \sim u_{*t}$, such effects may be neglected ([Leys and Raupach, 1991](#)).

Table 2.3 shows typical roughness lengths of non-vegetated surface types.

The roughness length of fluids depends on the surface wind shear. The shear stress deforms the fluid and generate ripples or waves at higher wind speeds. These waves, in turn, modify the surface roughness length. [Chamberlain \(1983\)](#) pointed out that, in certain circumstances, wind drag entrains very similar amounts of surface mass into the atmosphere over many different surface types. He assembled a variety of observational data which showed that saltation of sand and snow was analogous to entrainment of sea-spray over the ocean. This agreement could be explained by assuming $z_{0,m}$ was proportional to u_*^2/g over each of the surfaces. Over oceans, we adopt the dependence of $z_{0,m}$ on U proposed by [Large and](#)

Pond (1982)

$$z_r = 10.0 \text{ m} \quad (2.23)$$

$$U_r = U(z_r) = U_{10} \quad (2.24)$$

$$U_{10} = \max(1.0, U_{10}) \quad (2.25)$$

$$C_m^n = \frac{0.0027}{U_{10}} + 0.000142 + 0.0000764 U_{10} \quad (2.26)$$

$$z_{0,m} = 10.0 \exp(-k/\sqrt{C_m^n}) \quad (2.27)$$

$$D = 0.0 \quad (2.28)$$

The reference height z_r is the height at which the neutral exchange coefficient C_m^n is determined. In theory this could be any height but in practice C_m^n is measured and parameterized as a function of the wind speed at 10 m (e.g., Large and Pond, 1981; NCAR Oceanography Section, 1997; Bryan et al., 1997). Thus we use U_{10} instead of U_r . The constraint that $U_{10} > 1 \text{ m s}^{-1}$ prevents surface exchanges from vanishing at small wind speeds.

Note that C_m^n (2.28) is the neutral drag coefficient, not the drag coefficient. Stability-based corrections must be applied to C_m^n in order to obtain C_m . Large and Pond (1981) summarize the procedure used to convert C_m^n to a (non-neutral) drag coefficient, shifted to any height z :

$$C_m(z) = C_m^n \left\{ 1 + \frac{\sqrt{C_m^n}}{k} \left[\ln \left(\frac{z}{z_r} \right) - \psi_m \left(\frac{z}{L} \right) \right] \right\}^{-2} \quad (2.29)$$

When $z = z_r$, then C_m is the drag coefficient at the reference height.

Exchange coefficients such as the drag coefficient C_m (2.29) are positive-definite by definition, e.g., (2.1). Some care must be taken to ensure numerical procedures do not erroneously predict negative-valued exchange coefficients. For example, (2.29) predicts $C_m(z) < 0$ when ...fxm

2.2.3 Stability Corrections

As mentioned above, the vertical profile of momentum in the boundary layer is, to a first approximation, logarithmic with height (2.6). However, the stability properties of the atmosphere introduce a correction

$$U(z_2) - U(z_1) = \frac{u_*}{k} \left[\ln \left(\frac{z_2 - D}{z_1 - D} \right) - \psi_m \left(\frac{z_2 - D}{L} \right) + \psi_m \left(\frac{z_1 - D}{L} \right) \right] \quad (2.30)$$

where ψ_m is the stability correction factor for momentum.

The stability parameter ζ is the ratio of the height z to the Monin-Obukhov length L [m] (defined below).

$$\zeta = z/L \quad (2.31)$$

The stability parameter is the non-dimensionalized height in the surface turbulence equations.

In the surface layer, the stability parameter equals the flux Richardson number, $\zeta = \text{Rf}$. The flux Richardson number is the ratio of the production (or loss) of turbulent kinetic energy (TKE) by buoyancy to the production of turbulent kinetic energy by shear stresses. When $\text{Rf} = 1$, turbulence is consumed by buoyancy as fast as it is produced by shear stress. This is why the similarity functions defined below have discontinuous first derivatives at $\zeta = 1$. This behavior is well-documented in nature.

It is convenient to define separate stability parameters for the processes of momentum, vapor, and heat transfer in the boundary layer:

$$\begin{aligned}\zeta_{\text{m}} &= z_{0,\text{m}}/L \\ \zeta_{\text{v}} &= z_{0,\text{v}}/L \\ \zeta_{\text{h}} &= z_{0,\text{h}}/L\end{aligned}\tag{2.32}$$

The correction factor ψ_{m} is defined in terms of the similarity function ϕ via

$$\psi_{\text{m}}(\zeta) = \int_{z_{0,\text{m}}}^{\zeta} \frac{[1 - \phi_{\text{m}}(x)]}{x} dx\tag{2.33}$$

Correction factors ψ_{v} and ψ_{h} for vapor and heat transfer are defined analogously to (2.33).

2.2.4 Flux-Gradient Relationships

Monin-Obukhov similarity theory is a more physically accurate description of surface turbulent fluxes than the bulk aerodynamic formulation (2.19). We may re-write in terms of the mean gradients of the scalar properties and their respective transfer resistances.

$$\tau = \rho(U_{\text{r}} - U_{\text{s}})/r_{\text{m}}\tag{2.34a}$$

$$H = -c_{\text{p}}\rho(T_{\text{r}} - T_{\text{s}})/r_{\text{h}}\tag{2.34b}$$

$$L = -l\rho(q_{\text{r}} - q_{\text{s}})/r_{\text{v}}\tag{2.34c}$$

The Monin-Obukhov similarity theory relates surface turbulent flux to the mean gradients of the scalar quantities in the surface (constant flux) layer.

$$\tau = \rho \left[\frac{ku_*(z - D)}{\phi_{\text{m}}(\zeta)} \right] \frac{\partial U}{\partial z}\tag{2.35a}$$

$$H = -c_{\text{p}}\rho \left[\frac{ku_*(z - D)}{\phi_{\text{h}}(\zeta)} \right] \frac{\partial T}{\partial z}\tag{2.35b}$$

$$L = -l\rho \left[\frac{ku_*(z - D)}{\phi_{\text{h}}(\zeta)} \right] \frac{\partial q}{\partial z}\tag{2.35c}$$

The relationship between surface fluxes and vertical gradients is expressed in terms of similarity functions which express the theoretical forms of the transfer resistances in (2.34).

2.2.5 Similarity Functions

Many studies have constructed empirical similarity functions from boundary layer experiments. We adopt forms for the similarity functions summarized by (Brutsaert, 1982, p. 71) and Zeng et al. (1998):

$$\phi_m(\zeta) = \phi_h(\zeta) = \phi_v(\zeta) = 1 + 5\zeta \quad \zeta \geq 0 \quad (2.36a)$$

$$\phi_m(\zeta) = (1 - 16\zeta)^{-1/4} \quad \zeta < 0 \quad (2.36b)$$

$$\phi_h(\zeta) = \phi_v(\zeta) = (1 - 16\zeta)^{-1/2} \quad \zeta < 0 \quad (2.36c)$$

Hence the similarity function for momentum, heat, and vapor are equal in stable conditions, and differ slightly in unstable conditions. For lack of evidence to the contrary, the forms for heat and vapor are identical and only the forms for heat will be explicitly presented in the following. The numerical constants appearing in (2.36) are subject to slight alteration depending on the exact value of the Von Karman constant (we assume $k = 0.4$) and the dataset employed. (Arya, 1988, pp. 162–165) shows that (2.36) fits data from Kansas with astonishing fidelity.

Zeng et al. (1998) find that the similarity functions for very stable ($\zeta > 1$) and very unstable ($\zeta_m < -1.574$, $\zeta_h < -0.465$) conditions approach different limits than (2.36). For completeness, we present the Zeng et al. (1998) recommendations for the entire range of ζ for momentum

$$\phi_m(\zeta) = \begin{cases} 0.7k^{2/3}(-\zeta)^{-1/3} & : \quad \zeta < -1.574 \\ (1 - 16\zeta)^{-1/2} & : \quad -1.574 \leq \zeta < 0 \\ 1 + 5\zeta & : \quad 0 \leq \zeta < 1 \\ 5 + \zeta & : \quad 1 \leq \zeta \end{cases} \quad (2.37)$$

and for heat (and vapor)

$$\phi_h(\zeta) = \begin{cases} 0.9k^{4/3}(-\zeta)^{-1/3} & : \quad \zeta < -0.465 \\ (1 - 16\zeta)^{-1/2} & : \quad -0.465 \leq \zeta < 0 \\ 1 + 5\zeta & : \quad 0 \leq \zeta < 1 \\ 5 + \zeta & : \quad 1 \leq \zeta \end{cases} \quad (2.38)$$

The locations of the functional interfaces in (2.37) and (2.38) were, to some degree, chosen to ensure the stability functions evenly match eachother.

2.2.6 Monin-Obukhov Length

The Monin-Obukhov length L [m] characterizes the stability of a fluid. There are many equivalent definitions of L , such as

$$L = \frac{\theta_v u_*^2}{k g_s \theta_{v*}} \quad (2.39)$$

where θ_v [K] is the virtual potential temperature and θ_{v*} [K] is the scaling parameter for temperature. The Monin-Obukhov length is the height above the ground at which the production

of turbulence by mechanical (shear) and thermal (buoyancy) forces are equal. L increases with friction velocity (shear turbulence), and decreases with buoyancy flux (convective turbulence). Positive and negative L indicate stable and unstable atmospheres, respectively. When the magnitude of L is very large, e.g., $|L| > 10^5$, the atmosphere is neutrally stable.

The procedure for estimating the surface turbulent fluxes often begins with an initial estimate of the Monin-Obukhov length L . The following method is based on [Zeng et al. \(1998\)](#) and is used in CLM ([Dai et al., 2003](#)). We assume use five quantities to estimate L : First, the wind speed at reference height U_r . Second and third, the virtual potential temperatures at reference height θ_{vr} and at surface θ_{vs} [K] (or, equivalently, their difference $\Delta\theta_v \equiv \theta_{vr} - \theta_{vs}$). Fourth, the reference height z_r [m]. Fifth and finally, the roughness length for momentum $z_{0,m}$ [m]. These five quantities may be measured or, in a model, their values from the previous timestep may be used.

Given these quantities, we first estimate a flux wind speed U_f [m s⁻¹] which depends on stability. We define the term “flux wind speed” operationally as the wind speed used to compute surface fluxes. In stable conditions, the flux wind speed is simply the vector magnitude of the mean zonal and meridional components, u and v .

$$U_f(\Delta\theta_v) = \begin{cases} \max(\sqrt{u^2 + v^2}, 0.1) & : \Delta\theta_v \geq 0 \quad (\text{Neutral or Stable}) \\ \sqrt{u^2 + v^2 + (\beta w_*)^2} & : \Delta\theta_v < 0 \quad (\text{Unstable}) \end{cases} \quad (2.40)$$

The minimal value of 0.1 m s⁻¹ avoids singularities and represents the small eddies present even in a becalmed, stable atmosphere. In unstable conditions, U_f includes the convective velocity scale w_* as well. The inclusion of w_* (2.40) helps U_f account for the contributions of large eddies in the convective boundary to the surface fluxes ([Zeng et al., 1998](#)).

After the flux wind speed is estimated (2.40), we obtain the bulk gradient Richardson number Ri

$$Ri = \frac{g_s \Delta z \Delta\theta_v}{\theta_v U_f^2} \quad (2.41)$$

where $\Delta z \equiv z_r - D$ is the difference between the reference height z_r and the zero plane displacement height D . The gradient Richardson number characterizes the turbulence intensity. Formally, Ri is the ratio of convectively available potential energy (CAPE) to the magnitude of low-level shear. Hence (2.41) is simply a first estimate for Ri .

We use Ri to form an initial guess for ζ_m (2.32)

$$\zeta_m(Ri) = \begin{cases} Ri \ln(\Delta z / z_{0,m}) / [1.0 - 5.0 \min(Ri, 0.19)] & : Ri \geq 0 \quad (\text{Neutral or Stable}) \\ Ri \ln(\Delta z / z_{0,m}) & : Ri < 0 \quad (\text{Unstable}) \end{cases}$$

However, these guesses allow ζ_m outside the range of measured values. Hence we constrain the results of (2.42) as follows:

$$\zeta_m(Ri) = \begin{cases} \min[2.0, \max(\zeta_m, 0.01)] & : Ri \geq 0 \quad (\text{Neutral or Stable}) \\ \max[-100.0, \min(Ri, -0.01)] & : Ri < 0 \quad (\text{Unstable}) \end{cases}$$

Finally, we estimate L from ζ_m (2.42) and $z_{0,m}$ using (2.32)

$$L = (z_r - D) / \zeta_m \quad (2.42)$$

This initial estimate for L (2.42) is refined in subsequent iterations.

2.3 Wind Speed

2.3.1 Reference Level Wind Speed

The single most important parameter determining surface erosion is the wind speed. In practice we predict or measure the wind speed U at a certain height above the ground and wish to relate U to an observed or predicted dust flux. It is convenient to define a reference height z_r so that U and Q may be intercompared at disparate locations. By convention z_r is set to 10 m, which is a standard height both for field observations and for numerical model output. As discussed below, it is actually the wind friction speed which is directly linked to dust mobilization.

Chapter 3

Dust Source Processes

A lot of real estate changin'
hands today.

Saying in West Texas
Anonymous

This section describes the wind driven processes which determine the flux of long-lived mineral dust into the atmosphere. The atmospheric dust burden is the end result of a chain of processes which begins with saltation. Saltation is the wind-initiated movement of large soil particles in the downstream direction. Particles large enough to be entrained into motion directly by wind are called sand. Sand ranges in texture (size) from very fine to coarse, $1/16 < D < 2 \text{ mm}$ ($62 < D < 2000 \mu\text{m}$) respectively. Smaller particles of crustal material, those susceptible to long term suspension and transport in the atmosphere, are collectively referred to as dust. When the drag on the particles is large enough to overcome the inertial and cohesive forces attaching the particle to the soil bed, the particle suddenly lifts from the bed in a nearly vertical trajectory. Blown from behind and unable to resist gravitational settling for very long, the particle arcs back to the surface along a shallower trajectory. The energy dissipated by the impact of the saltating particles on the surface, may, in turn, break adhesive bonds and liberate much smaller dust particles known as dust from the surface. Although the distinction is somewhat arbitrary, dust particles are smaller than the population of saltators which liberate them.

The size of dust particles is generally taken to be $D < 50 \mu\text{m}$. Since the time a particle requires to settle out of the atmosphere under the influence of gravitation alone is proportional to the square of the particle diameter (see §5 below), dust particles have significantly longer atmospheric residence times than sand.

3.1 Literature Review

Two books are devoted to physical mechanisms of wind erosion, [Bagnold \(1941\)](#) and [Shao \(2000\)](#). [Raupach and Lu \(2004\)](#) provide an excellent review of all aspects of dust mobilization and dry deposition.

3.2 Threshold Wind Friction Speed

The conditions necessary to initiate or maintain the movement of particles depend on many properties, including wind speed, particle size, surface roughness, stability, sheltering effects, surface moisture, and interparticle forces. Laboratory experiments have been performed over a wide range of ambient pressures and particle densities to isolate and define these dependencies (Iversen and White, 1982; Shao et al., 1996). We now characterize the aerodynamic forces on particles which initiate and maintain particle motion which in turn causes saltation, dust mobilization and wind erosion.

3.2.1 Bagnold's Original Theory

Bagnold (1941) first derived the size dependence of the threshold wind velocity by considering the balance of forces on a particle. His lucid derivation, though lacking in completeness, nevertheless provides the starting point for more complete theory of mobilization. Consider a particle of density ρ_p resting atop a bed of similar particles in a fluid of density ρ traveling above and around the particles with speed u_* . Define the packing angle α as the angle from the vertical subtended by the downstream point of contact P of the particle with the bed it lies atop. If the particles are all spherical and regularly packed, then α is the angle from the center of the upper sphere to the center of one of the lower spheres.

The forces considered by Bagnold (1941) are drag and gravity. Bagnold assumes particle movement initiates when the aerodynamic drag exerted by the wind on the particle overcomes the component of the particle's weight directed opposite to the wind stream. A more complete physical statement of the balance of forces leading to saltating is that particle motion commences when the sum of the forces acting on the particle result in a net moment of zero at the downstream point of contact P . We shall use this more general principle to include the cohesive and lift forces later; for now, we retrace Bagnold's original derivation.

The mass of the particle is $\pi D^3 \rho_p / 6$ and its net weight relative to the surrounding fluid is $\pi g D^3 (\rho_p - \rho) / 6$. The contact point P is the pivot, or axis of support, about which gravity attempts to pull the particle downwards and backwards. The gravitational torque acts through the center of mass of the particle to create a moment of force. The gravitational moment M_W is the product of the gravitational force and the distance between the axis through which gravity acts (i.e., the center of mass) and the point P . This distance is $(D \sin \alpha) / 2$, and thus

$$\begin{aligned} M_W &= \frac{\pi g D^3 (\rho_p - \rho)}{6} \times \frac{D}{2} \sin \alpha \\ &= \frac{\pi g D^4 (\rho_p - \rho) \sin \alpha}{12} \end{aligned} \tag{3.1}$$

The horizontal drag force M_D exerted on the particle by the fluid is proportional to the exposed cross sectional area of the particle normal to the fluid flow, $M_D \propto D^2$. The drag per unit particle surface area is proportional to ρu_*^2 . Assuming the net drag force is directed through the center of mass of the particle, then the distance from the axis of drag force to

P is $(D \cos \alpha)/2$, and thus the drag moment is

$$\begin{aligned} M_D &= C_1 \times \rho u_*^2 \times D^2 \times \frac{D}{2} \cos \alpha \\ &= C_2 \rho u_*^2 D^3 \cos \alpha \end{aligned} \quad (3.2)$$

where $C_2 = C_1/2$ is a constant of proportionality which depends upon the exact grain geometry, micrometeorology, and grain packing.

At the threshold velocity u_{*t} , the gravitational moment equals the drag moment on the particle so that any small perturbation in wind speed may initiate particle motion, i.e., saltation. Equating M_W (3.1) and M_D (3.2)

$$\begin{aligned} \frac{\pi g D^4 (\rho_p - \rho) \sin \alpha}{12} &= C_2 \rho u_{*t}^2 D^3 \cos \alpha \\ u_{*t}^2 &= \left(\frac{\pi}{12 C_2} \right) \tan \alpha \frac{g D (\rho_p - \rho)}{\rho} \\ u_{*t} &= A \sqrt{\frac{g D (\rho_p - \rho)}{\rho}} \end{aligned} \quad (3.3)$$

where $A^2 \equiv (\frac{\pi}{12 C_2}) \tan \alpha$. For particles in air, $\rho_p \gg \rho$ and so (3.3) becomes

$$u_{*t}(D) \approx A \sqrt{\frac{\rho_p g D}{\rho}} \quad (3.4)$$

The preceding discussion applies to the initiation of particle motion in a bed of grains initially at rest. Thus u_{*t} defined by (3.3) is called the fluid threshold friction velocity or aerodynamic threshold friction velocity. Once particle motion begins, the threshold velocity actually decreases since some of the momentum needed to initiate further particle motion is supplied by particles already in motion. The friction velocity in an environment of particles already in motion is known as the impact threshold friction velocity u_{*ti} . For large sand grains, Bagnold (1941) found that $u_{*ti} \sim 0.8 u_{*t}$. The effect of particle motion on the surface wind speed and its feedbacks to further particle motion will be discussed further in §3.3 below.

Subsequent developers of this theory have continued to use the parameter A as it appears in (3.3) and in (3.4), i.e., as the proportionality factor between u_{*t} and the factor containing the square root of the particle diameter.

$$A \approx u_{*t} \sqrt{\frac{\rho}{g \rho_p D}} \quad (3.5)$$

A is called the dimensionless threshold friction speed, or simply the threshold parameter (Iversen and White, 1982). Theoretical approximations and empirical parameterizations of A will be discussed in §3.2.3 below.

Bagnold (1941) developed (3.3) for particles large enough to appear as isolated elements to the fluid flow. In particular, experiments confirm the predictions of (3.3) only for particle

sizes larger than about $200\text{ }\mu\text{m}$. $A \sim 0.1$ for large particles in air and $A \sim 0.2$ for particles in water (Bagnold, 1941, p. 88). In this size range u_{*t} increases linearly with $D^{1/2}$. For smaller particles, however, it is found that cohesive and lift forces may not be neglected, and that these forces combine to produce an optimum size for particle saltation, i.e., a minimum in $u_{*t}(D)$ not suggested by (3.3).

3.2.2 Reynolds Number

In order to develop a more complete theory of saltation and dust emissions, let us first examine the physics of airflow around a single particle. The balance of these forces determine when particle motion is initiated by airflow. Consider an isolated particle of size D at rest in a Newtonian fluid of density ρ moving with velocity \vec{v} . For simplicity, we consider the component of motion in the x direction. As shown in §18.14, the equation of continuity (conservation of mass) for an incompressible fluid (18.83) requires

$$\frac{\partial v_x}{\partial x} + \frac{\partial v_y}{\partial y} + \frac{\partial v_z}{\partial z} = 0 \quad (3.6)$$

and momentum conservation in the x direction (18.93) requires (18.95)

$$\frac{\partial v_x}{\partial t} + \left(v_x \frac{\partial v_x}{\partial x} + v_y \frac{\partial v_x}{\partial y} + v_z \frac{\partial v_x}{\partial z} \right) = -\frac{1}{\rho} \frac{\partial p}{\partial x} + \frac{\mu}{\rho} \left(\frac{\partial^2 v_x}{\partial x^2} + \frac{\partial^2 v_x}{\partial y^2} + \frac{\partial^2 v_x}{\partial z^2} \right) \quad (3.7)$$

We can gain insight into the relevant physical processes by non-dimensionalizing the equations. We do this by changing to a non-dimensional coordinate space which is scaled by the relevant physical dimensions of the fluid flow. For fluid flow around an isolated particle at rest, the relevant velocity is the upstream velocity v_∞ far from the particle. The relevant length scale is D .

$$\tilde{x} = \frac{x}{D}, \quad \tilde{y} = \frac{y}{D}, \quad \tilde{z} = \frac{z}{D}, \quad \tilde{v}_x = \frac{v_x}{v_\infty}, \quad \tilde{v}_y = \frac{v_y}{v_\infty}, \quad \tilde{v}_z = \frac{v_z}{v_\infty} \quad (3.8)$$

The dimensionless time and pressure variables are

$$\tilde{t} = \frac{tv_\infty}{D} \quad \text{and} \quad \tilde{p} = \frac{p}{\rho v_\infty^2} \quad (3.9)$$

Thus, by definition, none of the transformed coordinates has any physical dimensions. Substituting the non-dimensional coordinate definitions into (3.6) we obtain

$$\begin{aligned} \left(v_\infty \times \frac{1}{D} \right) \left(\frac{\partial \tilde{v}_x}{\partial \tilde{x}} + \frac{\partial \tilde{v}_y}{\partial \tilde{y}} + \frac{\partial \tilde{v}_z}{\partial \tilde{z}} \right) &= 0 \\ \frac{\partial \tilde{v}_x}{\partial \tilde{x}} + \frac{\partial \tilde{v}_y}{\partial \tilde{y}} + \frac{\partial \tilde{v}_z}{\partial \tilde{z}} &= 0 \end{aligned} \quad (3.10)$$

where the constant factor v_∞/D results from the coordinate transformation. Thus the incompressible continuity equation does not change in the transformed coordinate system.

Substituting the non-dimensional coordinate definitions into (3.7), and using $\nu \equiv \mu/\rho$ (18.6),

$$\begin{aligned} \left(v_\infty \times \frac{v_\infty}{D}\right) \frac{\partial \tilde{v}_x}{\partial \tilde{t}} + \left(v_\infty \times v_\infty \times \frac{1}{D}\right) \left(\tilde{v}_x \frac{\partial \tilde{v}_x}{\partial \tilde{x}} + \tilde{v}_y \frac{\partial \tilde{v}_x}{\partial \tilde{y}} + \tilde{v}_z \frac{\partial \tilde{v}_x}{\partial \tilde{z}}\right) = \\ -\frac{1}{\rho} \left(\rho v_\infty^2 \times \frac{1}{D}\right) \frac{\partial \tilde{p}}{\partial \tilde{x}} + \nu \left(v_\infty \times \frac{1}{D^2}\right) \left(\frac{\partial^2 \tilde{v}_x}{\partial \tilde{x}^2} + \frac{\partial^2 \tilde{v}_x}{\partial \tilde{y}^2} + \frac{\partial^2 \tilde{v}_x}{\partial \tilde{z}^2}\right) \end{aligned} \quad (3.11)$$

Factoring the physical scales from each side we obtain

$$\frac{v_\infty^2}{D} \left[\frac{\partial \tilde{v}_x}{\partial \tilde{t}} + \left(\tilde{v}_x \frac{\partial \tilde{v}_x}{\partial \tilde{x}} + \tilde{v}_y \frac{\partial \tilde{v}_x}{\partial \tilde{y}} + \tilde{v}_z \frac{\partial \tilde{v}_x}{\partial \tilde{z}}\right) \right] = -\frac{v_\infty^2}{D} \frac{\partial \tilde{p}}{\partial \tilde{x}} + \frac{v_\infty \nu}{D^2} \left(\frac{\partial^2 \tilde{v}_x}{\partial \tilde{x}^2} + \frac{\partial^2 \tilde{v}_x}{\partial \tilde{y}^2} + \frac{\partial^2 \tilde{v}_x}{\partial \tilde{z}^2}\right)$$

Multiplying each side by D/v_∞^2 we find

$$\frac{\partial \tilde{v}_x}{\partial \tilde{t}} + \tilde{v}_x \frac{\partial \tilde{v}_x}{\partial \tilde{x}} + \tilde{v}_y \frac{\partial \tilde{v}_x}{\partial \tilde{y}} + \tilde{v}_z \frac{\partial \tilde{v}_x}{\partial \tilde{z}} = -\frac{\partial \tilde{p}}{\partial \tilde{x}} + \frac{\nu}{v_\infty D} \left(\frac{\partial^2 \tilde{v}_x}{\partial \tilde{x}^2} + \frac{\partial^2 \tilde{v}_x}{\partial \tilde{y}^2} + \frac{\partial^2 \tilde{v}_x}{\partial \tilde{z}^2}\right) \quad (3.12)$$

Note that all physical scales in the problem appear in a group which multiplies the diffusion term. This single dimensionless factor must determine the behavior of the entire system. The Reynolds number Re is defined as the inverse of this factor

$$\text{Re} = v_\infty D / \nu \quad (3.13)$$

The Reynolds number expresses the ratio of inertial to viscous forces. The nature of the solutions to (3.12) is strongly sensitive to whether $\text{Re} < 1$ or $\text{Re} > 1$. When $\text{Re} \ll 1$, viscous forces dominate and the LHS of (3.12) is small relative to the RHS (because $\text{Re}^{-1} \gg 1$) and may be neglected. The steady state behavior of (3.12) then approaches

$$\frac{\partial \tilde{p}}{\partial \tilde{x}} = \frac{1}{\text{Re}} \left(\frac{\partial^2 \tilde{v}_x}{\partial \tilde{x}^2} + \frac{\partial^2 \tilde{v}_x}{\partial \tilde{y}^2} + \frac{\partial^2 \tilde{v}_x}{\partial \tilde{z}^2}\right) \quad (3.14)$$

The solution to (3.14) for a sphere at rest in a fluid is one of the central results of fluid mechanics.

The Reynolds number of an arbitrary flow is defined as

$$\text{Re} = UD / \nu \quad (3.15)$$

so that Re varies with position. The gravitational settling speed v_g of particles smaller than $10 \mu\text{m}$ is less than 10^{-2} m s^{-1} . This implies $\text{Re} < 10^{-2}$ for $D < 10 \mu\text{m}$ (3.15). Thus inertial effects may be neglected for most aerosols falling at terminal velocity. However, v_g increases as the square of the particle diameter so that $\text{Re} > 1$ for $D > 50 \mu\text{m}$. When $\text{Re} \gg 1$, then inertia plays a large role in the motion. In this case, the flows described by (3.12) become highly turbulent.

The relative velocity between strong winds and an undisturbed sand grain at the surface, however, easily exceeds v_g . The relevant wind speed for entraining particles from the surface is not the atmospheric wind speed, but the friction velocity u_* . Section 2 defines and describes the friction velocity as the characteristic wind velocity dissipated by shear stress and small

scale turbulent interactions between the surface and the atmosphere. In complete analogy with (3.15) we define the friction Reynolds number as

$$\text{Re}_* = u_* D / \nu \quad (3.16)$$

Windy conditions in the free atmosphere, e.g., wind speeds of $5\text{--}10\text{ m s}^{-1}$, typically correspond to u_* between $10\text{--}50\text{ cm s}^{-1}$ over barren surfaces. In such conditions, $\text{Re} > 1$ for particles larger than about $20\text{ }\mu\text{m}$, and inertial forces should not be neglected.

The friction Reynolds number at the threshold friction velocity is called the threshold friction Reynolds number

$$\text{Re}_{*t} = u_{*t} D / \nu \quad (3.17)$$

The literature of particle mobilization quite often uses B instead of Re_{*t} . The symbols are equivalent, and the following sections shall use both notations.

3.2.3 Iversen's Theory

Our presentation follows the detailed summary of [Greeley and Iversen \(1985\)](#), which remains the state-of-the-art in theoretical modeling of particle mobilization in planetary atmospheres. Most of the empirical elements were presented in a unified theory in [Iversen and White \(1982\)](#). We begin by reconsidering a loose particle at rest atop a bed of similar particles. We shall account for the effects of five moments acting on this particle. The forces creating these moments are drag F_D , gravity F_W , lift F_L , interparticle cohesion F_C , and rotational inertia. Drag and gravity were explicitly considered by [Bagnold \(1941\)](#) and were discussed in §3.2.1.

The lift force is due to the extremely large velocity gradient above the particle. For Re smaller than about 5, the particle resides in a thin ($1\text{--}10\text{ mm}$) quasi-laminar sublayer where the velocity profile is

$$U(z) = \frac{u_*^2 z}{\nu} \quad (3.18)$$

Thus the velocity shear is constant in the quasi-laminar sublayer

$$\frac{\partial U}{\partial z} = \frac{u_*^2}{\nu} \quad (3.19)$$

In typical dust-prone conditions on Earth, $u_* = 0.25\text{ m s}^{-1}$ and $\nu = 1.3 \times 10^{-5}\text{ m}^2\text{ s}^{-1}$, so that the velocity shear (3.19) is nearly $5 \times 10^3\text{ m s}^{-1}\text{ m}^{-1}$. The strong velocity shear is an indication that the pressure distribution along the top of the particle generates a lift force akin to an airfoil. The lift force acts through the center of mass of the particle in the vertical direction, i.e., opposite to the gravitational force.

Once the particle is lifted out of the quasi-laminar sublayer the lift force is expected to decrease significantly. Some particles receive their initial vertical momentum from the impact of being struck by other saltating particles. However, the vertical momentum of particles not released due to ballistic impact is thought to be due to the lift force. Experiments ([Chepil, 1958](#); [Einstein and El-Samni, 1949](#), [MFC](#)) show that lift and drag forces on hemispheres are of the same order of magnitude. Experiments show qualitatively similar behavior in the lift force occurs in fully turbulent boundary layers ($\text{Re}_* > 5$).

Originally, it was thought that the observed optimal size for initiation of particle saltation was due to aerodynamic effects. The observations suggested the existence of forces which act in opposition to the drag on small particles (3.2). [Iversen and White \(1982\)](#) demonstrated that interparticle cohesive forces are important for small particles. Interparticle cohesive forces include a number of processes including moisture, suction, electric charge, and chemical reactions. Many of these forces may be conceived as acting along the line connecting the centers of adjacent particles. The sum of all interparticle cohesive forces is denoted F_C .

The angle of repose of a soil is the maximum inclination at which the soil does not undergo spontaneous slippage. Thus the angle of repose is a qualitative estimate of the importance of interparticle cohesion. The greater the tilt, the more important interparticle cohesion is in preventing slippage. The angle between the leeward face of a sand dune and the horizontal is an excellent proxy for the angle of repose. For ordinary dune sand, the angle is 34° but, for very small particles, the angle can approach the vertical ([Iversen and White, 1982](#)). [Bagnold \(1941\)](#) conjectured that the packing angle α (§3.2.1) is, on average, close to the angle of repose.

The forces described above act on the particle along axes at varying distances from the downstream point of contact P . The distance between the axis of force and P is called the moment arm. From the figure we see that the moment arm for drag is a , for gravity and lift is b , and for interparticle cohesion is c . Thus the moments associated with each force are

$$\begin{aligned} M_D &= aF_D \\ M_W &= bF_W \\ M_L &= bF_L \\ M_C &= cF_C \end{aligned} \tag{3.20}$$

At the threshold velocity, these moments are assumed to sum to zero so that any small perturbation in wind speed may initiate particle motion, i.e., saltation. The balance at threshold is

$$\begin{aligned} M_D + M_L + I &= M_W + M_C \\ aF_D + bF_L + I &= bF_W + cF_C \end{aligned} \tag{3.21}$$

where the RHS contains the moments which tend to dislodge the particles and the LHS contains the moments which stabilize the particles. Note the moment of rotational inertia I has been introduced on the LHS. The rotational inertia is not a force per se, rather, it measures of resistance of an object to angular acceleration about a specified axis. The rotational inertia I of an object is defined as $\int r^2 dM$, where r is the distance of the element of mass dM from the origin of coordinates. A solid sphere has a rotational inertia $I = 2Mr^2/5 = MD^2/10$ about its center. Assuming the particle is spherical, we apply the parallel axis theorem to obtain the rotational inertia of the particle about P

$$\begin{aligned} I &= MD^2/10 + M \left(\frac{D}{2} \right)^2 \\ &= 7MD^2/20 \\ &= 7\pi\rho_p D^5/120 \end{aligned} \tag{3.22}$$

where we have expressed the particle mass in terms of its diameter in the last step.

It is possible to measure the relative strength of lift, drag, and rotational inertia by non-dimensionalizing the forces in (3.20) and (3.22). Following [Greeley and Iversen \(1985\)](#), the small particle shear flow force coefficients K_D , K_L , K_I , for drag, lift, and rotational inertia, respectively, are defined as

$$\begin{aligned} F_D &= K_D \rho u_*^2 D^2 \\ F_L &= K_L \rho u_*^2 D^2 \\ M_C &= K_I \rho u_*^2 D^3 \end{aligned} \quad (3.23)$$

[Greeley and Iversen \(1985\)](#) summarize the agreement between the measured and theoretical values of K_D , K_L , and K_I . Relatively good agreement is found for measured and theoretical values of the drag parameter, with all values falling in the range $4.65 < K_D < 9.82$ for $\text{Re} = 0.95$. Wind tunnel inferences of K_L are much larger (factor of 40) than theoretical values (Saffman, 1965, 1968, MFC).

All three moment arms in (3.20) are proportional to D , and so may be defined as $a = \tilde{a}D$, $b = \tilde{b}D$, and $c = \tilde{c}D$. The non-dimensional moment arms \tilde{a} , \tilde{b} , and \tilde{c} may be obtained for a specified packing geometry. Coleman (1967, MFC) showed that, for closely packed spheres of identical size,

$$\begin{aligned} \tilde{a} &= \frac{1}{\sqrt{6}} \\ \tilde{b} &= \frac{1}{4\sqrt{3}} \\ \tilde{c} &= ??? \end{aligned} \quad (3.24)$$

Empirical constraints on K_D , K_L , and K_I were inferred by [Iversen and White \(1982\)](#) using data from the Mars Surface Wind Tunnel, MARSWIT. Wind tunnels allow direct measurement of T , p , D , ρ_p , $U(z)$, and, most importantly, $U_t(z)$. From these, one uses theory to infer $z_{0,m}$, ρ , ν , u_* , u_{*t} , and Re_{*t} . $f(\text{Re}_{*t})$. [Iversen and White \(1982\)](#) performed wind tunnel observations with MARSWIT over wide ranges of ρ , U , and D . The data were expressed in terms of A , the non-dimensional threshold friction speed from (3.3).

Substituting (3.20), (3.23) and (3.24) into (3.21) we obtain

$$\tilde{a}D \times K_D \rho u_*^2 D^2 + \tilde{b}D \times K_L \rho u_*^2 D^2 + K_I \rho u_*^2 D^3 = \tilde{b}D \times \frac{\pi \rho_p g D^3}{6} + \tilde{c}D \times F_C \quad (3.25)$$

$$\rho u_*^2 D^3 (\tilde{a}K_D + \tilde{b}K_L + K_I) = \rho_p g D \left(\frac{\pi \tilde{b} D^3}{6} + \frac{\tilde{c} F_C}{\rho_p g} \right) \quad (3.26)$$

With the atmospheric approximation $\rho_p \gg \rho$, $A^2 \approx u_{*t}^2 \rho / (g \rho_p D)$ (3.4). Thus we manipulate (3.26) to solve for A^2

$$\begin{aligned} \frac{\rho u_*^2}{\rho_p g D} &= \frac{1}{D^3} \left(\frac{\pi \tilde{b} D^3}{6} + \frac{\tilde{c} F_C}{\rho_p g} \right) (\tilde{a}K_D + \tilde{b}K_L + K_I)^{-1} \\ A^2 &= \frac{\pi \tilde{b}}{6} \left(1 + \frac{6 \tilde{c} F_C}{\pi \tilde{b} \rho_p g D^3} \right) (\tilde{a}K_D + \tilde{b}K_L + K_I)^{-1} \end{aligned} \quad (3.27)$$

Substituting (3.24) into (3.27) we obtain

$$A^2 = \frac{\pi}{24\sqrt{3}} \left(\frac{K_D}{\sqrt{6}} + \frac{K_L}{4\sqrt{3}} + K_I \right)^{-1} \left(1 + \frac{6\tilde{c}F_C}{\pi\tilde{b}\rho_p g D^3} \right) \quad (3.28)$$

The final term on the RHS represents the effects of cohesion. The D^{-3} dependence of the cohesion term suggest that A^2 may approach an asymptotic value for large D as long as K_L is not strongly dependent on D .

Iversen and White (1982) defined the cohesionless threshold coefficient A_1 by setting the cohesion force $F_C = 0$ in (3.28)

$$A_1^2 = \frac{\pi}{24} \left(\frac{K_D}{\sqrt{2}} + \frac{K_L}{4} + \sqrt{3}K_I \right)^{-1} \quad (3.29)$$

Note that A_1 does not depend on D , and thus, in principle, may be inferred from measurements of A^2 when the influence of cohesion on (3.28) is known.

Greeley et al. (1980, MFC) and Iversen and White (1982) used experiments with MAR-SWIT to infer K_D , K_L , and K_I (3.23). They removed the effects of cohesion from the data and performed a least squares fit to find

$$\begin{aligned} K_D + \sqrt{6}K_I &= 4.65 \\ K_L &= 32.8\text{Re}_{*t} \end{aligned} \quad (3.30)$$

for $0.03 < \text{Re}_{*t} < 0.3$. Note that the lift parameter K_L was found to explicitly depend on Re_{*t} . This dependence on Re_{*t} suggests that the form of K_L chosen to non-dimensionalize F_L in (3.23) could be improved.

If the measured values in (3.30) are used in (3.29), we find

$$A_1^2 = 0.43 + 1.07\text{Re}_{*t} \quad (3.31)$$

Equation (3.31) predicts $A_1 > 0.66$. As previously mentioned, many observations suggest $A \approx 0.2$ for large particles (e.g., Bagnold, 1941, p. 88) where cohesive force are presumably small. Thus the assumptions leading to (3.31) have rendered the theory a qualitative, rather than an exact, description of saltation initiation.

In order to reconcile theory with observations, Iversen, Greeley, and colleagues set forth to isolate each functional dependence in (3.28) which could be independently measured. They assumed A could be expressed as the product of three factors: the cohesionless threshold A_1 (3.29), a function $f(\text{Re}_{*t})$ (3.17), and a function $g(D)$ which accounts for all interparticle cohesive forces (Iversen et al., 1976a,b, MFC)

$$A = A_1 f(\text{Re}_{*t}) g(D) \quad (3.32)$$

The absence of interparticle cohesion corresponds to $g = 1$.

Based on the theoretical influence of F_C on A (3.28), g is assumed to have a square-root relationship with A and to be a function of particle size to an unknown power n

$$g(D) = \left(1 + \frac{I}{\rho_p g D^n} \right)^{1/2} \quad (3.33)$$

where n and I are to be determined empirically. Clearly $g(D)$ is a generalized version of the final term in (3.28): the factor $6\tilde{c}F_C/(\pi\tilde{b})$ is combined into I , and n allows cohesion to depend on a non-integer power of D . The latter assumption is intuitively appealing because cohesive forces depend on surface properties (e.g., van der Waal's forces, capillarity) as well as volume properties (e.g., electrostatic charge).

In order to determine I and n , Iversen and White (1982) grouped together many observations of $A^2(D)$ for a fixed value of Re_{*t} . Each such curve showed A was strongly dependent on particle size for $D < 80\mu\text{m}$, but confirmed that A approaches an asymptotic value of about 0.02 for $D > 150\mu\text{m}$. Iversen and White (1982) found that these data were best fit by $I = 6 \times 10^{-7} \text{ kg m}^{1/2} \text{ sec}^{-2}$ and $n = 2.5$

$$g(D) = \left(1 + \frac{6 \times 10^{-7}}{\rho_p g D^{2.5}}\right)^{1/2} \quad (3.34)$$

where all quantities are expressed in MKS units. Taken together with (3.28), the observed of best fit value $n = 2.5$ implies the $F_C \propto \sqrt{D}$. The quality of the fit in (3.34) adds confidence to the form of parameterization chosen for A (3.32).

Once $g(D)$ was known from (3.34), Iversen and White (1982) were able to infer the product $A_1 f(\text{Re}_{*t})$ from A (3.32). The data were found to obey different functional relations depending on the value of Re_{*t} ,

$$A_1 f(B) = \begin{cases} 0.1291(-1 + 1.928B^{0.0922})^{-1/2} & : 0.03 \leq B \leq 10 \\ 0.120(1 - 0.0858e^{-0.0617(B-10)}) & : B > 10 \end{cases} \quad (3.35)$$

where, following many of the source references, we have used B instead of Re_{*t} . Note that A approaches a limiting value near 0.120 for $B > 10$.

Using (3.32), (3.34), and (3.35) to compute $u_{*t}(D, B)$ (3.4),

$$u_{*t} = \begin{cases} \left(1 + \frac{6 \times 10^{-7}}{\rho_p g D^{2.5}}\right)^{1/2} 0.1291(-1 + 1.928B^{0.0922})^{-1/2} \sqrt{\frac{\rho_p g D}{\rho}} & : 0.03 \leq B \leq 10 \\ \left(1 + \frac{6 \times 10^{-7}}{\rho_p g D^{2.5}}\right)^{1/2} 0.120(1 - 0.0858e^{-0.0617(B-10)}) \sqrt{\frac{\rho_p g D}{\rho}} & : B > 10 \end{cases} \quad (3.36)$$

Since Re_{*t} is defined in terms of u_{*t} (3.17), (3.36) is an implicit definition of u_{*t} which must be solved numerically. Note that the semi-empirical u_{*t} defined by (3.36) is a fluid threshold friction velocity, as opposed to an impact threshold friction velocity (cf. §3.3). A computationally efficient form of (3.36) is given in (17.1).

Rather than solving (3.36) iteratively, Marticorena and Bergametti (1995) parameterized $\text{Re}_{*t}(D)$ using ρ and ν typical of dust source regions

$$\text{Re}_{*t}(D) = 0.38 + 1331(100D)^{1.56} \quad (3.37)$$

The RHS of (3.37) is usually known. Thus $\text{Re}_{*t}(D)$ may be evaluated without iteration, a considerable advantage. However, we are unable to reproduce the accuracy of (3.37) demonstrated in their Figure 1.

The numerical solution of (3.36) shows that $u_{*t}(D)$ has a fairly shallow minima at u_{*t0} which defines the optimal particle diameter for saltation, D_0 . For a steady friction velocity

$u_* > u_{*t0}$ over dry, bare ground, we expect saltation to initiate with particles of size D_0 . For typical arid regions of Earth, $D_0 \sim 75 \mu\text{m}$ (Iversen and White, 1982; Pye, 1987; Shao et al., 1996; Marticorena et al., 1997). The minima is not symmetric in D or u_* , however, due to the rapid increase of cohesive forces with decreasing size. Broadly speaking, particles in the range $40 < D < 200 \mu\text{m}$ are susceptible to saltation.

Predictions of (3.36) agree remarkably well with wind tunnel observations. Iversen and White (1982) tested (3.36) over a wide range of Re_{*t} for particles as small as $D = 12 \mu\text{m}$. Agreement was within 5% for particles larger than $D = 40 \mu\text{m}$. Uncertainties in both the model and the measurements become significant for $D < 40 \mu\text{m}$, which is outside the saltation range. Thus, these uncertainties need not be worrisome. As previously mentioned (3.36) agrees with Bagnold's formulation for particles larger than $200 \mu\text{m}$.

For particles smaller than D_0 , u_{*t} increases very quickly. In fact, for particles $D < \mu\text{m}$, (3.36) predicts $u_{*t} > 1 \text{ m s}^{-1}$, i.e., the threshold speed exceeds values plausible for terrestrial conditions.

Shao and Lu (2000) derive an alternative theory for u_{*t} that fits the wind tunnel data of Iversen and White (1982) but which also has the virtue of resulting in simpler expressions than (3.36).

To summarize, Bagnold's formulation (3.4) predicts that u_{*t} decreases with D so that very small particles should be most efficiently mobilized. Noting, however, that all observations show that $u_{*t}(D)$ decreases with D until a critical particle size $D = D_0$, Iversen and colleagues developed a semi-empirical formulation for u_{*t} (3.36) which accounts for lift and cohesive forces. Their formulation agrees well with wind tunnel measurements for $12 < D < 1000 \mu\text{m}$.

3.3 Horizontal Dust Flux

Until now we have concentrated on the determination of the threshold friction velocity u_{*t} required to initiate motion of particles of diameter D initially at rest. A useful theory of dust mobilization also requires specification of the horizontal mass flux of all particle sizes and at all heights, since this quantity can be measured in a wind tunnel.

$$q(z) = \int_{D=0}^{D=\infty} n(D, z) M(D) v(D, z) dD \quad (3.38)$$

where n is the number distribution of particles, M their mass, and v their horizontal velocity. The units of q are $\text{kg m}^{-2} \text{s}^{-1}$. In addition to $u_{*t}(D)$, a useful theory of dust mobilization requires specification of the vertically integrated horizontal mass flux due to saltation

$$Q = \int_{z=0}^{z=z_s} \int_{D=0}^{D=\infty} n(D, z) M(D) v(D, z) dD dz \quad (3.39)$$

where z_s is the height of the saltation layer,

The units of Q are $\text{kg m}^{-1} \text{s}^{-1}$ rather than $\text{kg m}^{-2} \text{s}^{-1}$ since a vertical integration of the streamwise mass flux has been performed. The integration over D ensures Q includes all sizes of saltating particles, while the integration over z ensures Q includes particles (including suspended dust) at all levels. Thus Q is the mass crossing orthogonally through an infinitely

tall column per unit width of the column. Q is often called the streamwise mass flux since it measures the movement of crustal material in the direction of the prevailing winds.

The total streamwise movement of surface material Q is the result of three intertwined processes, saltation, suspension, and surface creep. Saltation includes the movement of all airborne particles which are too large to become suspended. Suspension, on the other hand, includes the movement of all particles. The prevailing aerodynamic conditions play a role in determining what particles are susceptible to long term suspension and transport, so there is no single size below which particles are always suspended and above which never suspended. However, as a rule of thumb we call particles larger than $60\mu\text{m}$ in diameter sand, other particles are collectively referred to as dust.

Surface creep accounts for the movement of particles which are pushed along the surface. The creep may be caused by the wind directly or by nudges from saltator impacts. The important distinction is that saltating particles remove momentum from the near surface wind which decreases the friction velocity felt by the surface. Creeping particles, on the other hand, do not directly remove any momentum from the near surface wind, and thus do not lessen the surface friction velocity.

With the above discussion in mind, we may also write Q (3.39) as the sum of the individual streamwise fluxes due to saltation Q_s , surface creep Q_c , and suspended dust Q_d thusly

$$Q = Q_s + Q_c + Q_d \quad (3.40)$$

According to [Bagnold \(1941\)](#), $Q_c \sim \frac{1}{4}Q_s$ in typical conditions. Observations by [Shao et al. \(1993\)](#) indicate that $Q_d \lesssim Q_s$. As described in §3.3.4, Q_d/Q_s is called the bombardment efficiency.

A primary goal of mineral dust studies is the prediction of the lifecycle of dust particles which begins with Q_d . As shown above, wind tunnel studies (e.g., [Iversen and White, 1982](#)) show that the threshold velocity u_{*t} (3.36) increases rapidly (due to cohesive forces) for particles smaller than about $60\mu\text{m}$, and exceeds terrestrial conditions for $D < 10\mu\text{m}$. Thus most long-lived dust particles are thought to be initially lofted by impacts from more massive saltators rather than directly lofted by the wind. Hence particles in suspension are said to be secondary particles. For this reason Q_d depends intimately on Q_s . Thus we concentrate on Q_s before turning our attention to the link between Q_s and Q_d in §3.4.

Many expressions have been proposed which express Q in terms of u_* and u_{*t} . [Greeley and Iversen \(1985\)](#) summarize these expressions in their Table 3.5. These expressions are based on theories or observations of particle saltation. The theories must predict the concentration and motion of particles set into motion by u_* , as well as particles released by the impact of saltating particles. Complicating these theories is the interaction between particles of different sizes.

Theoretical and empirical evidence strongly suggests the horizontal flux of saltating particles Q varies with the cube of the wind friction velocity during saltation $u_{*,s}$ [Owen \(1964\)](#); [Shao et al. \(1993\)](#)

$$Q = \begin{cases} 0 & : u_{*,s} < u_{*t} \\ Cu_{*,s}^3 \left(1 - \frac{u_{*t}^2}{u_{*,s}^2}\right) & : u_{*,s} > u_{*t} \end{cases} \quad (3.41)$$

For now C is a dimensional constant which is a function of aerodynamic, surface, and soil properties to be defined below. Note that (3.41) is equivalent to (41) of Owen (1964).

Since the wind speed is related to the wind friction speed by $U = C_m^{1/2} u_*$, we may rewrite (3.41) as

$$Q = \begin{cases} 0 & : U < U_t \\ CU^3 \left(1 - \frac{U_t^2}{U^2}\right) & : U > U_t \end{cases} \quad (3.42)$$

Leys and Raupach (1991) used a portable wind erosion tunnel to measure $u_{*t}(D)$ and total streamwise mass flux Q in field conditions in Australia. The observed Q was well described by (3.39). They also predicted u_{*t} with four competing methods, including Equation (3.36). Unfortunately, no method, including (3.36), adequately predicted the observed u_{*t} .

We now show the development of many theories for Q , including those of Bagnold, Kawamura, Owen, and the Australian school. Unfortunately, authors in this field have often inadvertently incorporated typographical errors into their papers (and models) (Namikas and Sherman, 1997). Baas (2005) covers this subject with more up-to-date examples, and inter-compares some of these theories. Papers with known typographical errors include Blumberg (1993, equation 3.2), Lancaster (1995, equation 2.12), White (1979) (equation 22), Greeley et al. (1996, table 2, equation 4), Pye and Tsoar (1990, equation 4.48), Pankine and Ingersoll (2002) (equation 19), and Zender et al. (2003a) (equation 10). Equation 27 in the influential paper Marticorena and Bergametti (1995) (and subsequently in Lunt and Valdes (2002) (equation 6), Tegen et al. (2002b) (equation 3) and Shannon and Lunt (2011) (equation 11)), is correct even though it may appear at first glance to be algebraically distinct. Researchers are urged to verify the correctness of their saltation formulations by comparison to the original formulations.

3.3.1 Original Theory

Bagnold (1941) developed the original theory relating Q to wind speed based on the energetics of an idealized, steady state, linear, saltation zone. A few qualitative observations motivate the strategy of Bagnold's theory of saltation. The first, alluded to in §3.2.1, is that once saltation has initiated by winds exceeding the fluid threshold ($u_* > u_{*t}$), the downstream surface wind speed drops because some fraction of the drag is now exerted on suspended particles rather than directly on the surface. Downstream saltation continues as long as the surface wind speed exceeds the impact threshold, i.e., $u_* > u_{*ti}$.

Once saltation initiates, moreover, the ambient wind speed U may reach any strength but the surface wind speed is relatively constant. In other words the velocity gradient near the surface can grow without bound, but the surface wind speed at about 3 mm height is insensitive to this gradient. These qualitative observations strongly suggest that drag in excess of that necessary to maintain saltation is dissipated in the atmosphere by the saltating grains. Note that this observation is the basis of the second hypothesis of Owen (1964) (cf. §3.3.2).

These observations underpin Bagnold's simple energetic explanation of the cubic dependence of Q on u_* . Consider the following idealized scenario: A bed of particles of identical size D and mass M_s saltates in a steady state wind with friction velocity u_* . The wind

(rather than impacts by other particles) is responsible for lifting each particle into the atmosphere with an initial horizontal velocity u_0 . The wind transports each particle a mean horizontal distance L before the particle fall to the surface. During this transport, the wind accelerates the particle to a final horizontal velocity u_1 which is completely dissipated in the impact.

We now impose energy conservation constraints on this system. The initial and final momenta of the particle are $M_s u_0$ and $M_s u_1$, respectively. The difference between these momenta, $M_s(u_1 - u_0)$, is extracted from the atmosphere over the distance L . Therefore the rate of loss of atmospheric momentum per unit area due to a total horizontal mass flux of saltating particles Q_s must be

$$\frac{dp}{dt} = \frac{Q_s(u_1 - u_0)}{L} \quad (3.43)$$

Newton's second law (18.84) tells us that the rate of change of momentum is equivalent to the applied force. In this case, the applied force is the surface wind stress due to particle the drag of the particles on the wind τ_p .

$$\frac{Q_s(u_1 - u_0)}{L} = \tau_p \quad (3.44)$$

We note that $\tau_p < \tau$ since some of the total wind stress τ (2.1) goes directly into the surface rather than into increasing the momentum of airborne particles. Subsequent theories of Q_s , presented below, explicitly account for the distinction between τ and τ_p . Inserting (2.3) into (3.44)

$$\frac{Q_s(u_1 - u_0)}{L} = \rho u_*^2 \quad (3.45)$$

To progress further, Bagnold (1941) made use of two qualitative observations. First, the initial trajectory of a particle uplifted by wind is nearly vertical, but the trajectory at impact is nearly horizontal which implies $u_1 \gg u_0$ so that

$$\frac{Q_s u_1}{L} = \rho u_*^2 \quad (3.46)$$

Second, Bagnold observed that $u_1/L \approx g/w_0$, where w_0 is the mean initial vertical velocity of a saltating particle. This observation is consistent with the approximation that sand particles undergo ballistic trajectories. The atmospheric residence time Δt of a sand particle ejected into the atmosphere at speed w_0 is $\Delta t = 2w_0/g$. If the mean horizontal velocity of the particle is \bar{u} then the total streamwise distance traversed is

$$L = \frac{2\bar{u}w_0}{g} \quad (3.47)$$

Inserting (3.47) in (3.46) and assuming $\bar{u} \sim u_1$ leads to

$$\begin{aligned} \frac{Q_s g}{w_0} &= \rho u_*^2 \\ Q_s &= \frac{\rho w_0 u_*^2}{g} \end{aligned} \quad (3.48)$$

where we have dropped the factor of 2 in (3.47) for consistency with Bagnold's original formulation.

To proceed further than (3.48), is necessary to discover or formulate a relationship between w_0 and u_* . Bagnold argued that, on average, $w_0 = C_1 u_*$ where C_1 is called the impact coefficient. In a perfectly elastic reflection, or ricochet, $C_1 = 1$. An elastic collision may also eject multiple saltators as products, in which case $C_1 < 1$ for each product. However, it is quite possible to have $C_1 > 1$ when large particles eject smaller particles. Bagnold reasoned that particles are ejected with a velocity proportional to the incident velocity of the impacting particle which, he argued, ought to be u_* on average. This reasoning is somewhat difficult to defend, but the assumption turns out to be correct. A better justification for this assumption is that fxm. This leads to our first derivation of the well known phenomena that the horizontal mass flux due to saltation is proportional to the cube of the friction velocity

$$Q_s = \frac{C_1 \rho u_*^3}{g} \quad (3.49)$$

Bagnold's observations fit (3.49) best with $C_1 \sim 0.8$.

Based on careful analysis, Bagnold empirically modified (3.49) to include a factor of $(D)^{1/2}$. With this correction, and subsuming C_1 into a new empirical constant c_s

$$Q = c_s \left(\frac{\rho}{g} \right) \left(\frac{D}{250 \times 10^{-6}} \right)^{1/2} u_{*,s}^3 \quad (3.50)$$

where all parameters are specified in MKS.

Expressing (3.50) in terms of U rather than u_* , Bagnold found

$$Q = c_s \left(\frac{\rho}{g} \right) \left(\frac{D}{250 \times 10^{-6}} \right)^{1/2} u_{*,s}^3 \quad (3.51)$$

$$\sim 1.5 \times 10^{-9} (U - U_t)^3 \quad (3.52)$$

where (3.51) yields (3.52) for typical conditions in natural dunes.

3.3.2 Owen's Theory

Owen (1964) developed a physical theory describing the saltation of uniform particles in air. His theory continues to serve as the best mathematical definition and description of saltation, as well as being a valuable exposition of mathematical physics in its own right.

Owen's two hypotheses are:

- I. The saltation layer behaves, so far as the flow outside it is concerned, as an aerodynamic roughness whose height is proportional to the thickness of the layer.
- II. The concentration of particles within the saltation layer is governed by the condition that the shearing stress borne by the fluid falls, as the surface is approached, to a value just sufficient to ensure that the surface grains are in a mobile state.

3.3.3 Kawamura/White Formulation

Kawamura's work on sand transport in the late 1940s and early 1950s is not widely known. During this time Kawamura developed a rather complete theory for the streamwise saltation flux (1951) which appeared in translated form in 1964. White based his formulation for the streamwise saltation flux (White et al., 1976; White, 1979) squarely on Kawamura's work. Thus, White appears to be the first to recognize the efficacy of Kawamura's work for modern dust models. Unfortunately (but understandably), many references inadvertently attribute Kawamura's formulation of streamwise mass transport to White (1979). In recognition of White's association, we sometimes refer to this as the Kawamura/White formulation.

Rather uniquely, White and colleagues performed numerical simulations of the saltation jumps of individual particles based on first principles, i.e., the equations of motion. These simulations, in aggregate, later serve to validate simplifying assumptions he makes in his bulk theory. The equations of motion for a particle saltation take the form

$$M_s \ddot{x} = -F_D \frac{\dot{x} - u}{u_r} + F_L \frac{\dot{y}}{u_r} \quad (3.53)$$

$$M_s \ddot{y} = -F_L \frac{\dot{x} - u}{u_r} - F_D \frac{\dot{y}}{u_r} - M_s g \quad (3.54)$$

where (\dot{x}, \dot{y}) and (\ddot{x}, \ddot{y}) are the x and y components of the particle's velocity and acceleration, respectively, F_L and F_D are the lift and drag forces on the particle, u is the streamwise wind speed, and u_r is the relative speed of the particle to the wind. By definition the mean vertical wind speed is zero in the saltation layer so that

$$u_r = \sqrt{(\dot{x} - u)^2 + \dot{y}^2} \quad (3.55)$$

The lift and drag forces on the particle are expressed in terms of the lift and drag coefficients C_L and C_D as

$$F_L = \frac{1}{8} \pi \rho C_L u_r^2 D^2 \quad (3.56)$$

$$F_D = \frac{1}{8} \pi \rho C_D u_r^2 D^2 \quad (3.57)$$

The drag force on a particle is usually expressed in terms of the density of the medium, the projected area of the particle, and the square of the particle's velocity.

$$F_D = \frac{1}{2} \rho C_D A v_\infty^2 \quad (3.58)$$

where A is the cross-sectional area of the particle. This form of relationship between C_D and F_D has been chosen for several reasons. First, the solution to the problem of flow over a sphere tells that $F_D \propto v_\infty$ when $\text{Re} \ll 1$. However, we also know that the pressure, or force per unit area, should vary as ρv_∞^2 (from Bernoulli's theorem?) as $\text{Re} \rightarrow 1$, F_D . For spherical particles, (3.58) implies

$$F_D = \frac{1}{8} \pi \rho C_D v_\infty^2 D^2 \quad (3.59)$$

As presented in §2.1.1, the total stress to the surface τ is the sum of a particle drag and an aerodynamic drag. The particle drag on the surface, τ_p , is caused by the horizontal deceleration of the impactors by the surface. The aerodynamic drag on the surface, τ_a , is the drag directly due to gas flow over the surface (2.2). We know τ (2.3) and can obtain τ_a using Owen's second hypothesis (§3.3.2)

$$\begin{aligned}\tau &= \rho u_*^2 \\ \tau_a &= \rho u_{*t}^2\end{aligned}\tag{3.60}$$

Together with (2.2), this implies

$$\begin{aligned}\tau_p &= \tau - \tau_a \\ &= \rho(u_*^2 - u_{*t}^2) \\ &= \rho(u_* + u_{*t})(u_* - u_{*t})\end{aligned}\tag{3.61}$$

Thus τ_p appears as the difference between two fluid stresses, ρu_*^2 and ρu_{*t}^2 . The former is the total stress available to do turbulent work, and the latter is the threshold required to initiate saltation. Note that these fluid stresses are dimensionally equivalent to volumetric energy densities.

Equation (3.61) defines τ_p as a residual between the total surface stress and the aerodynamic stress. We may also define τ_p directly from kinematic considerations as the rate of deposition of streamwise momentum to the surface by the saltating particles. If F_s is the downward mass flux of saltating particles per unit area per unit time, then the total streamwise momentum deposited to the bed by the particles is

$$\tau_p = F_s(u_1 - u_0)\tag{3.62}$$

where u_0 and u_1 are the mean initial and final streamwise velocities during a saltator jump. Conceptually, we may view $u_1 - u_0$ as the velocity change of the same saltator as it repeatedly skips of the surface, depositing some momentum with each impact. Then the particulate mass flux F_s times the mean change in particle velocity is the momentum flux. Note that the initial saltator velocity u_0 contributes to particle momentum rather than surface stress, so it is subtracted from τ_p .

Let us denote the mean initial vertical velocity of saltating particles as w_0 . Then the mean initial vertical momentum of saltating particles is $w_0 F_s$. Clearly the initial vertical momentum of saltating particles varies with the intensity of saltation. One possibility is that $w_0 F_s$ obeys a functional relationship with the surface saltation stress τ_p . For example, one might hypothesize that τ_p is converted into vertical momentum with some non-unity efficiency. More specifically, we shall assume that $w_0 F_s$ is linearly proportional to τ_p . Then (3.61) and (3.62) imply

$$\begin{aligned}w_0 F_s &\propto \tau_p \\ &\propto \rho(u_*^2 - u_{*t}^2) \\ &\propto F_s(u_1 - u_0)\end{aligned}\tag{3.63}$$

Note that (3.63) assumes If the initial vertical momentum of a saltating particle is proportional to the kinetic energy released by surface bombardment then (or is this assuming the

vertical momentum flux of ejected particles must vary as the horizontal momentum flux deposited by bombarding particles)

The relationship in (3.63) assumes that the kinetic energy of bombardment converts to vertical momentum of the product saltators with an imperfect, but constant, efficiency. In other words the bombardment process is inelastic. The disposition of the unaccounted-for energy is not specified. The theory of [Shao et al. \(1993\)](#), presented below, extends this treatment of energy conversion in developing a theory for the vertical flux of small dust particles.

The crucial advance of Kawamura’s theory is made possible by the assumption of a relation between F_s and the friction speeds. MARSWIT data and the saltation model of [White \(1979\)](#) (described above) both support the following empirical relationship

$$F_s \propto \rho(u_* - u_{*t}) \quad (3.64)$$

Combining (3.64) with (3.63) we obtain

$$w_0 \propto u_* + u_{*t} \quad (3.65)$$

$$L \propto (u_* + u_{*t})^2/g \quad (3.66)$$

[White \(1979\)](#) noted that the values of w_0 and L predicted by (3.65)–(3.66) agreed with direct numerical integration of the equations of motions for saltating particles.

The total streamwise saltation flux is simply the product of F_s and L . Using (3.64) and (3.66),

$$\begin{aligned} Q_s &= F_s \times L \\ &= c_s \times \rho(u_* - u_{*t}) \times (u_* + u_{*t})^2/g \\ &= \frac{c_s \rho}{g} (u_* - u_{*t})(u_* + u_{*t})^2 \\ &= \frac{c_s \rho u_*^3}{g} \left(1 - \frac{u_{*t}}{u_*}\right) \left(1 + \frac{u_{*t}}{u_*}\right)^2 \end{aligned} \quad (3.67)$$

where, as before, c_s is the dimensionless constant of proportionality between saltation mass flux and the factors proportional to the cube of the friction speed. Factoring out the u_*^3 factor in the final step brings the form of (3.67) into closer agreement with Bagnold (3.50) and Owens. Note that (3.67) was derived and tested for monodisperse soil distributions.

[Namikas and Sherman \(1997\)](#) and [Baas \(2005\)](#) document that Equation (19) in [White \(1979\)](#), which corresponds to our Equation (3.67), has a typographical error which propagated into some dust emission models apparently including [Pankine and Ingersoll \(2002\)](#). If adopted, this error would cause models to overpredict dust emissions. In practice, however, the erroneous equation performs no worse than other (correct) mobilization implementations. By coincidence, [Zender et al. \(2003a\)](#) also contains a typo in its version of Equation (3.67)¹.

[White \(1979\)](#) used MARSWIT to replicate a variety of Earth and Martian saltation conditions in order to determine c_s . With small glass beads ($D = 0.208$ mm) as saltators,

¹ This typo was not present in the submitted manuscript. The error was introduced by the JGR copy editor. The mistake was never present in DEAD, and so it never affected any simulations.

they found $c_s = 2.61$ under a wide range of conditions. This differed by only 6% from Kawamura's original estimate of $c_s = 2.78$ (Namikas and Sherman, 1997; Baas, 2005). From this we may infer that (3.67) contains all the relevant physics of saltation for both the Earth and Mars simulations. Of course, such complicating factors as moisture, heterogeneous soil sizes, and vegetation were not considered in the tests. Nevertheless, the consistency of the experiments of White (1979) with (3.67) are very encouraging as a point from which to begin to include the effects of more complicating factors.

3.3.4 Australian School

Researchers in Australia published theories for saltation and sandblasting beginning in the 1990s. This research involved many groups, though Michael Raupach and Yaping Shao appear to be most consistently behind it. I refer to their approach as the Australian School, since it is nicely synthesized and originally evaluated with Australian models. Shao et al. (1993) present a theory for the streamwise saltation flux which differs slightly from the Kawamura/White formulation (§3.3.3). Lu and Shao (1999) and Shao (2001) summarize the full development of this theory. Raupach and Lu (2004) includes these theories in the context of more general treatments of mobilization and dry deposition.

The Australians' approach considers uniform particles of mass M_s in steady state saltation. In steady state, the mean rates of saltator bombardment and ejection per unit surface area are equal, and denoted by N_s^\uparrow which has units of $\text{m}^{-2}\text{s}^{-1}$. With these assumptions the vertically integrated streamwise saltation flux defined in (3.39) may be rewritten as

$$Q_s = M_s N_s^\uparrow L \quad (3.68)$$

where, as before, L is the downstream projection of the mean particle jump.

As in the Kawamura/White formulation (§3.3.3), we assume τ and τ_a are given by (3.60). Combining Bagnold's expression for τ_p (3.44) with (3.68) we obtain

$$\begin{aligned} \tau_p &= \frac{Q_s(u_1 - u_0)}{L} \\ &= \frac{M_s N_s^\uparrow L(u_1 - u_0)}{L} \\ &= M_s N_s^\uparrow (u_1 - u_0) \end{aligned} \quad (3.69)$$

Finally we obtain a relation for N_s^\uparrow by substituting values from (3.60) and (3.69) into each term in (2.2)

$$\begin{aligned} \rho u_*^2 &= \rho u_{*t}^2 + M_s N_s^\uparrow (u_1 - u_0) \\ \rho u_*^2 \left(1 - \frac{u_{*t}^2}{u_*^2}\right) &= M_s N_s^\uparrow (u_1 - u_0) \\ N_s^\uparrow &= \rho u_*^2 \left(1 - \frac{u_{*t}^2}{u_*^2}\right) [M_s (u_1 - u_0)]^{-1} \end{aligned} \quad (3.70)$$

Following Bagnold, Shao et al. (1993) note that $L = \bar{u}\Delta t$ where \bar{u} is the mean streamwise velocity during the jump. For ballistic trajectories, $\Delta t = 2w_0/g$ so $L = 2w_0\bar{u}/g$. Thus, using

the ballistic assumption for L and (3.70) for N_s^\uparrow in (3.68)

$$\begin{aligned} Q_s &= M_s \times \rho u_*^2 \left(1 - \frac{u_{*t}^2}{u_*^2}\right) \frac{\bar{u}}{(u_1 - u_0)} \times \frac{2w_0}{g} \\ &= \frac{\rho u_*^3}{g} \left(1 - \frac{u_{*t}^2}{u_*^2}\right) \times \frac{\bar{u}}{(u_1 - u_0)} \times \frac{2w_0}{u_*} \end{aligned} \quad (3.71)$$

$$= \frac{c_s \rho u_*^3}{g} \left(1 - \frac{u_{*t}^2}{u_*^2}\right) \quad (3.72)$$

where c_s is a dimensionless coefficient which incorporates the last two factors on the RHS of (3.71). Following reasoning similar to that presented in the development of (3.47) and (3.49), Shao et al. (1993) assert $\bar{u} \sim u_1$ and $w_0 \sim u_*^2$. If both factors comprising c_s are of order unity, then c_s is $\mathcal{O}(1)$ as well.

The parameter c_s (3.72) appears in most theories of Q_s (e.g., Greeley and Iversen, 1985, p. 100). As presented in §3.3.1, Bagnold (1941) estimated $c_s \sim 0.8$. Equation (47) of Owen (1964) estimates c_s empirically to be

$$c_s = 0.25 + \frac{v_g(D)}{3u_*} \quad (3.73)$$

where v_g (5.25) is the terminal fall speed of the particle. For $D \sim 150 \mu\text{m}$ and $u_* \sim 0.8 \text{ m s}^{-1}$, (3.73) predicts $c_s \sim 0.8$, which agrees with Bagnold's estimate.

Note that N_s^\uparrow (3.70) can be expressed in terms of Q_s using (3.68) and the ballistic approximation for L

$$\begin{aligned} N_s^\uparrow &= \frac{Q_s}{LM_s} \\ &= \frac{gQ_s}{2w_0\bar{u}M_s} \end{aligned} \quad (3.74)$$

3.3.5 My Theory

If a saltating particle undergoes constant streamwise acceleration while airborne then its mean horizontal velocity is $\bar{u} = (u_0 + u_1)/2$. Constant acceleration is a plausible assumption for some particles (fxm: which???). The total streamwise distance traversed is then

$$\begin{aligned} L &= \frac{u_0 + u_1}{2} \times \frac{2w_0}{g} \\ &= \frac{w_0(u_0 + u_1)}{g} \end{aligned} \quad (3.75)$$

² This is equivalent to assuming Bagnold's impact coefficient $C_1 \sim 1$ in (3.49).

Employing (3.75) for L and (3.70) for N_s^\uparrow in (3.68) we find

$$\begin{aligned} Q_s &= M_s \times \rho u_*^2 \left(1 - \frac{u_{*t}^2}{u_*^2}\right) [M_s(u_1 - u_0)]^{-1} \times \frac{w_0(u_0 + u_1)}{g} \\ &= \frac{\rho u_*^2}{g} \left(1 - \frac{u_{*t}^2}{u_*^2}\right) \frac{w_0(u_0 + u_1)}{(u_1 - u_0)} \\ &= \frac{\rho u_*^3}{g} \left(1 - \frac{u_{*t}^2}{u_*^2}\right) \frac{w_0(u_0 + u_1)}{u_*(u_1 - u_0)} \end{aligned} \quad (3.76)$$

As far as I can tell, no one, not even [Owen \(1964\)](#), has derived a relationship between w_0 and u_* from first principles. All theories seem to base the assumption that $w_0 \sim u_*$ on dimensional analysis and observations.

3.4 Vertical Dust Flux

Until now we have concentrated on predicting the wind-initiated motion of saltating particles but we have put aside consideration of the mass flux of the smaller, suspended particles known as dust. Bombardment by saltating particles, or sandblasting, is thought to be the ultimate source of most fine dust emissions. The theory of sandblasting has been extensively developed by Alfaro, Gomes and coworkers ([Gomes et al., 1990](#); [Alfaro and Gomes, 1995](#); [Alfaro et al., 1997, 1998](#); [Alfaro and Gomes, 2001](#)). Applications of these theories in regional scale models is infrequent ([Shao et al., 1996](#); [Shao and Leslie, 1997](#); [Gong et al., 2003](#)). Saltation-sandblasting is beginning to appear in global scale models ([Grini and Zender, 2004](#); [Grini et al., 2005](#)). The small size and long atmospheric residence time of dust particles causes them to exert significant influences over climate.

Saltation is summarized by the streamwise saltation flux Q_s . Likewise, the streamwise mass flux of dust is denoted Q_d . The vertical mass flux of dust particles through a horizontal plane is

$$F(z) = \int_{D=0}^{D=\infty} n(D, z) M(D) w(D, z) dD \quad (3.77)$$

When $z > z_s$, then (3.77) includes only dust mass so that $F = F_d$. The units of F are $\text{kg m}^{-2} \text{s}^{-1}$. To distinguish dust particles from saltating particles, we shall use M_d and M_s , respectively. Dust, by definition, is suspended in the atmosphere and does not immediately settle back to the surface. Thus F is somewhat insensitive to z once $z > z_s$. Many large scale atmospheric models assume turbulence uniformly mixes all dust emissions into the lowest atmospheric layer, so that the net dust source term is taken to be $F(z = z_s)$. Note that the mean streamwise distance from ejection to impact L , which proved useful in defining Q_s (3.68), does not appear in (3.77).

Prediction of F_d is the crux of mineral dust aerosol models. To date, all theories are based on establishing a relation between Q (3.41) and F_d (3.77). There is good observational evidence to support this link ([Shao et al., 1993](#); [Gillette et al., 1997](#), e.g.), but the lack of theoretical support is somewhat discomfiting.

The most successful theories are based on the energetics of the impact-ejection mechanism. Each ballistic impact a saltating particle with the surface results in a transfer and

conversion of momentum and kinetic energy from the saltating particle to the surface. We have seen that some horizontal momentum is transferred into soil creep. The vertical momentum may be reflected into the next bounce of the saltator, or it may initiate the ejection of another saltator. When the product of an impact is the ejection of dust, however, it is likely that some energy has been used to break the cohesive bonds binding the dust particle to the surface. Thus some fraction of the energy from particle bombardment is responsible for the injection of dust into the atmosphere. The theory of [Shao et al. \(1993\)](#) explains many, but not all, of the observed features of the F_d - Q_s relationship.

3.4.1 Australian School

[Shao et al. \(1993\)](#) developed a theoretical framework for the rupture of the interparticle bonds between dust particles and the surface. They allow for a mean interparticle binding energy of ψ . ψ is the depth of the energy potential well which must be surmounted in order to free the dust grain from the surface. Thus ψ accounts for the forces of cohesion F_C and gravity F_W discussed in §3.2.3. ψ is also related to the modulus of surface rupture discussed by [Gillette and Passi \(1988\)](#).

They consider a scenario where a saltator impacts the surface and ruptures the bonds of, on average, Π dust grains which are then ejected from the surface along with zero or more saltators. We call this the impact-rupture-ejection scenario. Let the kinetic energy of the impacting saltator be E_1 and the total kinetic energy of the product saltators (which include the original when reflection occurs) be E_2 . Thus the energy available for freeing dust bonds is $\Delta E = E_1 - E_2$. Let us define c_ϵ as the mean fraction of ΔE which is channeled to rupturing dust bonds. Energy conservation requires $c_\epsilon < 1$ since, in addition to other sinks, some of E_1 is converted into the kinetic energy of the ejected dust particles. Then the energy balance of each saltator impact is

$$\Pi\psi = c_\epsilon\Delta E \quad (3.78)$$

By definition, dust is suspended once it is emitted, so there is no downward flux of dust particles in the saltation layer. Therefore the net vertical dust flux is simply the dust emission flux, which is the product of the areal rate of saltator impacts N_s^\uparrow and the dust production efficiency per impact Π . With these assumptions the areal rate of emission of dust mass from the surface defined in (3.77) may be rewritten as

$$F_d = M_d N_d^\uparrow \quad (3.79)$$

$$= M_d N_s^\uparrow \Pi \quad (3.80)$$

Substituting Π from (3.78) into (3.80) we obtain

$$F_d = M_d N_s^\uparrow c_\epsilon \Delta E / \psi \quad (3.81)$$

We use (3.70) for N_s^\uparrow to rewrite the RHS of (3.81) in terms of Q_s

$$\begin{aligned} F_d &= \frac{M_d c_\epsilon \Delta E}{\psi} \times \rho u_*^2 \left(1 - \frac{u_{*t}^2}{u_*^2}\right) \times [M_s(u_1 - u_0)]^{-1} \\ &= \frac{M_d c_\epsilon \Delta E}{\psi} \times \frac{g Q_s}{c_s u_*} \times [M_s(u_1 - u_0)]^{-1} \end{aligned} \quad (3.82)$$

Let us now examine the ΔE term. If u_1 and w_1 are the mean streamwise and vertical components of a saltator's velocity at impact, then its kinetic energy is $E_1 = \frac{1}{2}M_s(u_1^2 + w_1^2)$. [Shao et al. \(1993\)](#) assume that $u_1 \gg w_1$ so that $E_1 \sim \frac{1}{2}M_s u_1^2$. Then, they assume each bombardment ejects only one saltator. We call this conservative bombardment since, on average, it is equivalent to an inelastic saltator reflection at each impact-rupture-ejection event. In conservative bombardment every sand grain is the sole product of one bombardment, i.e., $E_2 = E_0$. Clearly this assumption is only plausible for steady state saltation. In these conditions

$$\begin{aligned}\Delta E &= E_1 - E_2 \\ &= \frac{M_s(u_1^2 - u_0^2)}{2}\end{aligned}\tag{3.83}$$

If the conditions for conservative bombardment are met, then we may substitute (3.83) for ΔE so that

$$\begin{aligned}F_d &= \frac{M_d c_\epsilon}{\psi} \times \frac{M_s(u_1 + u_0)(u_1 - u_0)}{2} \times \frac{g Q_s}{c_s u_*} \times [M_s(u_1 - u_0)]^{-1} \\ &= \frac{M_d c_\epsilon}{\psi} \times \frac{(u_1 + u_0)}{2} \times \frac{g Q_s}{c_s u_*} \\ &= \frac{M_d g Q_s}{\psi} \times \frac{c_\epsilon}{c_s} \times \frac{u_1 + u_0}{2 u_*}\end{aligned}\tag{3.84}$$

$$\equiv \alpha Q_s\tag{3.85}$$

where α , which has dimensions of m^{-1} , is the ratio of the dust vertical mass flux F_d to the streamwise saltation flux Q_s . α is called the flux ratio³. As described below, it is possible to infer α from measurements of Q_d and Q_s ([Shao et al., 1993](#)). Thus we shall compare the α defined by (3.85) to the α predicted using alternate theories.

Inserting (3.72) back into (3.84), [Shao et al. \(1993\)](#) defined a new parameter α_1

$$\begin{aligned}F_d &= \frac{c_s \rho u_*^3}{g} \left(1 - \frac{u_{*t}^2}{u_*^2}\right) \times \frac{M_d g}{\psi} \times \frac{c_\epsilon}{c_s} \times \frac{u_1 + u_0}{2 u_*} \\ &= u_*^3 \left(1 - \frac{u_{*t}^2}{u_*^2}\right) \times \frac{M_d \rho c_\epsilon}{\psi} \times \frac{u_1 + u_0}{2 u_*} \\ &\equiv \alpha_1 u_*^3 \left(1 - \frac{u_{*t}^2}{u_*^2}\right)\end{aligned}\tag{3.86}$$

where α_1 , whose units are $\text{kg s}^2 \text{m}^{-5}$, subsumes the final two factors on the RHS of the preceding equation. Note that the RHS of (3.84) and (3.86) is a function of the size of the saltating particles D_s . Since surface soils comprise a continuous size distribution of saltators, (3.84)–(3.86) should be discretized into bins which each represent the dust emissions produced by a given D_s . An example of this discretization in a global mineral dust model is described in §17.

The factors defining α (3.85) and α_1 (3.86) are similar and bear further examination. Consider first the dimensionless speed factor $\gamma = (u_1 + u_0)/(2u_*)$. Equations (19) and

³This definition of α is identical to α in Equation (40) of [Marticorena and Bergametti \(1995\)](#).

(20) of Owen (1964) are formulae for u_0 and u_1 in terms of u_* and D . Shao et al. (1996) evaluated these expressions numerically and found that $\gamma \approx 2.5$ for most conditions. Hence the proportionality parameters from (3.85) and (3.86) are, respectively,

$$\alpha = \gamma M_d g c_\epsilon / (\psi c_s) \quad (3.87)$$

$$\alpha_1 = \gamma M_d \rho c_\epsilon / \psi \quad (3.88)$$

where $\gamma \approx 2.5$. Knowing all the terms in (3.88) would allow us to predict vertical dust emissions at all scales. The two terms which remain ill-defined are the mean kinetic energy transfer efficiency, c_ϵ , and the mean energy binding dust particles to the surface, ψ (3.78). Estimating c_ϵ and ψ from first principles is currently one of the most pressing challenges in theoretical studies of aeolian erosion.

Shao et al. (1996) introduced a semi-empirical method for obtaining c_ϵ and ψ . First, they assumed that ψ is the product of a length scale determined by the dust particle size and the mean drag force due to the friction wind

$$\begin{aligned} \psi &= c_\psi D \times \frac{\pi D^2}{4} \rho [u_{*t}(D_d)]^2 \\ &= \frac{\pi c_\psi \rho [u_{*t}(D_d)]^2 D_d^3}{4} \end{aligned} \quad (3.89)$$

where c_ψ is the dimensionless length scale and is $\mathcal{O}(1)$. Substituting (3.89) into (3.88)

$$\begin{aligned} F_d &= \frac{\gamma M_d g c_\epsilon}{c_s} \times \frac{4}{\pi c_\psi \rho [u_{*t}(D_d)]^2 D_d^3} \times Q_s \\ &= \frac{\gamma M_d g c_\epsilon}{c_s} \times \frac{4}{c_\psi \rho [u_{*t}(D_d)]^2} \times \frac{\rho_p}{6 M_d} \times Q_s \\ &= \frac{2}{3} \times \frac{\rho_p}{\rho} \times \frac{\gamma g c_\epsilon}{c_s c_\psi [u_{*t}(D_d)]^2} \times Q_s \\ &\equiv \frac{2}{3} \times \frac{\rho_p}{\rho} \times \frac{\beta \gamma g}{[u_{*t}(D_d)]^2} \times Q_s \end{aligned} \quad (3.90)$$

where we have defined the bombardment parameter $\beta \equiv c_\epsilon / (c_s c_\psi)$ in the last step. The bombardment parameter contains most of the uncertainties in the problem.

We may invert (3.90) to solve for β

$$\beta \equiv \frac{3}{2} \times \frac{\rho}{\rho_p} \times \frac{[u_{*t}(D_d)]^2}{\gamma g} \times \frac{F_d}{Q_s} \quad (3.91)$$

In a wind tunnel experiment, all quantities on the RHS of (3.91) are inputs known a priori (ρ, ρ_p, g, D_d, U), are determined by theory and/or measurements (u_{*t}, γ), or are directly measured after the experiment (Q_s, F_d). The best empirical fit to the wind tunnel dataset gathered by Shao et al. (1993) is

$$\beta = [0.125 \times 10^{-4} \ln(D_s) + 0.328 \times 10^{-4}] \exp(-140.7 D_d + 0.37) \quad (3.92)$$

where D_d, D_s are in mm and $\beta > 0$.

Shao and Li (1999) further developed these theories and applied them in a Large Eddy Simulation.

3.4.2 Marticorena's Theory

Marticorena and Bergametti (1995) have synthesized many theories and observations into a comprehensive global mineral dust emission model. Many components of their model are described in the sections above. We focus now on the components which are native to their model.

Marticorena and Bergametti (1995) begin by adapting the streamwise saltation results of White (1979) for Q_s (3.67) to account for more realistic soil conditions. First, they accounted for the fraction of surface that actually consists of erodible soils. This fraction, E , includes only bare ground or sparsely vegetated surfaces susceptible to saltation. For example, E excludes bare stone surfaces, swamps, and lakes. However, E does not exclude surfaces which require only large friction speeds to initiate saltation, e.g., wetted soils. Clearly Q_s is linearly proportional to E . Defining R as the ratio of threshold friction speed to friction speed, (3.67) may be rewritten as

$$\begin{aligned} R &= u_{*t}/u_* \\ Q_s(D) &= \frac{c_s E \rho u_*^3}{g} (1 - R)(1 + R)^2 \end{aligned} \quad (3.93)$$

where the functional dependence of Q_s on D indicates that (3.93) applies only to a monodisperse distribution of particles of size D .

In order to apply (3.93) to a continuous size distribution $n(D)$ in the source soil, some simplifying assumptions are required. First, Marticorena and Bergametti (1995) assume that the value $c_s = 2.61$, empirically derived from monodisperse saltation experiments in MAR-SWIT (White, 1979), is size-independent and applies equally to heterogeneous, polydisperse size distributions. Second, they assume that the mass flux $Q_s(D)$ arises only from motions of particle sizes between D and $D + \Delta D$. In other words they assume that interactions between particles of different sizes do not contribute significant errors to (3.93), which is based on monodisperse assumptions. This approximation breaks down in the limit of dust production by ballistic impacts, since the impact of one large particle is assumed to eject many small dust particles. Shao et al. (1996) contains a more thorough discussion of the validity of these approximations. Nevertheless, with these two assumptions,

$$Q_s = \int_0^\infty Q_s(D) p(D) dD \quad (3.94)$$

where $p(D)$ is the PDF which defines the normalized, fractional contribution of each size D to the total mass flux. These assumptions imply that $c_s = 2.61$ defines Q_s through (3.93), regardless of the underlying size distribution of the parent soil. The only remaining difficulty is in determining $p(D)$.

Marticorena and Bergametti (1995) assume that $p(D)$ is best represented by the fractional cross-sectional area distribution of the soil. This appears to be a reasonable assumption because, in the absence of information to the contrary, the fractional surface area covered by grains of a given size should vary linearly with the cross-sectional area of the grains. Moreover, the exposure of saltation grains to wind also is proportional to the cross-sectional area of the grains. Another plausible assumption is made by Shao et al. (1996), who, as described below, set $p(D)$ to the fractional mass distribution of the soil.

The discretization of (3.94) proceeds as follows. Continuous soil size distributions are most often approximated as multi-modal log-normal distributions, i.e., The three parameters required to define each mode. The parameters usually available from soil sieving techniques are the mass median diameter \tilde{D}_v , the geometric standard deviation σ_g , and the mass fraction M . Thus it will be convenient to express $p(D)$ in terms of $M(D)$. To do so, we first put down the geometric relations between the cross-sectional area, mass, and volume of spherical particles

$$\begin{aligned} A &= \frac{\pi D^2}{4} = \frac{3}{2\rho_p D} M \\ M &= \frac{\pi D^3 \rho_p}{6} = \frac{2\rho_p D}{3} A \end{aligned} \quad (3.95)$$

We now take the limit of (3.95) to define the differential changes of area and mass in terms of each other

$$\begin{aligned} dA &= \frac{\pi D}{2} dD = \frac{3}{2\rho_p D} dM - \frac{3M}{2\rho_p D^2} dD \\ dM &= \frac{\pi D^2 \rho_p}{2} dD = \frac{2\rho_p D}{3} dA + \frac{2\rho_p A}{3} dD \end{aligned} \quad (3.96)$$

We may normalize the increments of area and of mass by dividing (3.96) by A and M , respectively

$$\begin{aligned} d\underline{A} &= \frac{dA}{A} = \frac{4}{\pi D^2} \times \frac{\pi D}{2} dD = \frac{2}{D} dD \\ d\underline{M} &= \frac{dM}{M} = \frac{6}{\pi \rho_p D^3} \times \frac{\pi D^2 \rho_p}{2} dD = \frac{3}{D} dD \end{aligned} \quad (3.97)$$

By definition, $\int d\underline{A} = 1$ and $\int d\underline{M} = 1$. Thus \underline{A} and \underline{M} are properly normalized PDFs and either may take the place of $p(D)$ in (3.94).

Using (3.97), we may discretize (3.94)

$$\begin{aligned} \sum_{i=0}^{i=N} \Delta \underline{A}_i &= 1 \\ Q_s &= \sum_{i=0}^{i=N} Q_s \Delta \underline{A}_i \end{aligned} \quad (3.98)$$

To convert this to a vertical dust flux F_d , Marticorena and Bergametti (1995) assume the relation

$$F_d = \alpha Q_s \quad (3.99)$$

Subject to the approximations discussed in § 3.4.1, (3.99) was proved by Shao et al. (1993) (3.85). Instead of attempting to evaluate α from first principles, they take an empirical approach.

Gillette (1979, 1981) describes a dataset comprised of measurements of F_d and Q_s at numerous (anywhere from two to ten) friction velocities for each of nine distinct soils. These data are reproduced in Table 3.1.

Table 3.1: Erodibility Properties of Nine Soils^a

Soil	Soil moisture θ %	Cloddiness %	Vegetative residue g m ⁻²	Ridge roughness cm	Erosion fetch km	Texture		
						Sand $M_{\text{sand}}^{\%}$ %	Silt $M_{\text{silt}}^{\%}$ %	Clay $M_{\text{clay}}^{\%}$ %
1	0.52 ± 0.61	95.0 ± 2.78	26.67	2.5	1.6	96.0	0.5	3.5
2	0.99	98.9	8.25	2.5	0.8	95.5	1.0	3.5
3	1.29 ± 0.20	89.1 ± 5.0	3.67	2.5	1.6	81.5	8.5	10.0
4	0.41 ± 0.10	95.9 ± 1.6	91.6	3.7	1.6	96.8	1.4	1.8
5	0.52 ± 0.13	98.8 ± 0.6	19.1	2.5	0.2	93.1	1.0	5.9
6	0.75	36.7	3.5	5.0	0.5	77.7	3.3	19.0
7	0.6	60.0	161.0	5.0	0.5	88.0	3.2	8.8
8	0.6	53.0	39.0	22.5	0.5	88.0	3.2	8.8
9	6.6	9.3	2.9	2.5	0.1	28.0	20.0	52.0

^aSource: Gillette (1979, 1981), Tables 4.3 and 3, respectively.

Table 3.2: Characteristic Arid Soil Populations^a

Type	Code	Minerological Features	Size \tilde{D}_n μm	GSD σ_g	Clay M_{clay} %	Efficiency α cm^{-1}
Aluminosilicated silt	ASS	Clay minerals dominant	125	1.6	9.7	1.0×10^{-5}
Fine sand	FS	Quartz dominant	210	1.8	3.6	1.0×10^{-6}
Coarse sand	CS	Quartz only	690	1.6	0	1.0×10^{-7}
Salts	Sa	Salt and clay minerals	520	1.6	3.2	3.3×10^{-6}

^aSource: [Chatenet et al. \(1996\)](#) Table 8, [Marticorena et al. \(1997\)](#) Tables 1 and 3. In this table Clay refers to particles with $D < 5.8\mu\text{m}$.

All soils except soil 9 (a clay) are very dry, with volumetric water contents $\theta < 0.013$ (θ is defined in § 3.7.1). These data show that more finely textured soils (i.e., with higher clay content) produce more dust per unit Q_s than coarser soils (i.e., with higher sand content).

[Marticorena and Bergametti \(1995\)](#) showed that, in this dataset, the percentage of clay particles ($D < 2\mu\text{m}$) in the source soil explains more than 90% of the covariation of F_d with Q_s . Their best linear fit is

$$\begin{aligned} \log_{10}(F_d/Q_s) &= \log_{10} \alpha \\ &= 0.134M_{\text{clay}}^{\%} - 6.0 \quad : \quad M_{\text{clay}}^{\%} < 20, \text{ CGS} \end{aligned} \quad (3.100)$$

where $M_{\text{clay}}^{\%}$ is the mass fraction (in percent) of clay particles in the parent soil. Thus α is extremely sensitive to M_{clay} , increasing by nearly three orders of magnitude as M_{clay} the soil texture changes from $M_{\text{clay}} = 0.0$ (sand) to 0.20 (sandy loam). In SI units, (3.100) becomes

$$\alpha \equiv F_d/Q_s = 100 \exp[(13.4M_{\text{clay}} - 6.0) \ln 10] \quad : \quad M_{\text{clay}} < 0.20, \text{ MKS} \quad (3.101)$$

Thus, α is observed to increase exponentially with M_{clay} for $M_{\text{clay}} < 0.20$. For clayier soils the few available observations suggest α eventually begins to decrease with M_{clay} . This reduced deflation efficiency for soils very rich in clay is consistent with interparticle cohesive forces increasing the mobilization inhibition as clay particles begin to dominate the soil ([Gillette, 1979, 1981](#); [Marticorena and Bergametti, 1995](#)). The physical arguments for mobilization inhibition due to interparticle cohesive forces is discussed more quantitatively in § 3.7 below. Unfortunately the soils in Gillette's dataset with $M_{\text{clay}} > 0.20$ had significantly higher soil water content than did the soils with $M_{\text{clay}} < 0.20$. Thus it is difficult to use these data to form conclusions regarding the behavior of α for dry soils when $M_{\text{clay}} > 0.20$.

In their regional dust model, [Marticorena et al. \(1997\)](#) used a blended average approach rather than using (3.100) directly. First they defined four distinct characteristic populations of coarse particles found in arid and semiarid regions based on [Chatenet et al. \(1996\)](#). The mineralogical and geometric features of these populations are described in Table 3.2. The value of α assigned to each population was arrived at by blending the observed α from the dataset of [Gillette \(1979, 1981\)](#). The first soil type, Aluminosilicated Silt, refers to many compounds such as Al_2O_3 , SiO_2 , ...The second soil type, Fine sand, includes ...The third soil type, Coarse sand, includes ...The fourth soil type, Salts, includes ...fxm

Alfaro and co-workers find that soil texture and composition affect soil crusting and aggregation in wind-tunnel experiments on soils of widely varying composition and texture. In particular, CaCO_3 affects aggregation. Interestingly, they found no detectable influence of texture and composition on sandblasting efficiency per se. Thus, composition and texture may influence the threshold velocity of saltation, but have no direct affect on sandblasting. This surprising result de-couples composition from sandblasting and helps to simplify models.

Shao represents the size distribution of saltators in air, $n_m^s(D)$ as a weighted combination of the size distribution of the source soil in a “natural” (undisturbed) state, $n_m^n(D)$, and in a “fully disturbed” state, $n_m^f(D)$.

$$n_m^s(D) = an_m^n(D) + (1 - a)n_m^f(D) \quad (3.102)$$

where a is fractional area of the fully disturbed soil. The relationship between n_m^n and n_m^f must be determined empirically.

Aeolian soils are those formed with significant contributions from upwind dust sources. These soils are often called loess, although the specific definition of loess is context-sensitive (fxm: add note loess commission in INQUA). Soils accumulate and form downwind of dust sources when bioclimatic constraints such as vegetation and incisions trap near-surface clay and silt particles. [Muhs \(1983\)](#) shows that regional winds called Santa Anas deposit silty loam soils on the Channel Islands in California. [Sweeney et al. \(2005\)](#) and [Stroeve et al. \(2005\)](#) describe the evidence for loess-production in the the Eureka Flat region of the Palouse in the northwest U.S.A.

The composition of many of the most common minerals comprising dust is given in Table 3.3. Quartz (SiO_2) is most commonly associated with sand. Opal ($\text{SiO}_2(\text{H}_2\text{O})_n$) content is often measured in oceanographic cores (e.g., Adkins). Goethite ($\alpha - \text{Fe}^{3+}\text{O}(\text{OH})$) may be the optically dominant constituent of mineral dust (Irina Sokolik, private communication, 2006). Unfortunately, its optical properties have not yet been measured.

For lack of other information, many studies assume mineral dust comprises the same elemental distribution as is found, on average, in Earth’s mantle. Table 3.3 list the elemental composition of Earth’s crust according according to [Lide and Frederikse \(1995\)](#).

[Marticorena et al. \(1997\)](#) found that the Western Sahara desert could be adequately described by eight different soil types. Each of the eight possible soil types is a predefined blend of the four soil populations described in Table 3.2. Table 3.5 defines the populations composing each of the eight soil types.

Table 3.3: Mineral Composition of Windblown Dust

Name	Formula	Density ^a ρ_p g cm^{-3}	Size ^b	Properties ^c	Ref. ^d
^e Calcite	CaCO_3	2.95	All	Weak IR bands, Limits acid uptake	2, 3
^f Feldspar	$\text{MAl}(\text{Al}, \text{Si})_3\text{O}_3$	Various	Silt	Weak IR	2
^g Goethite	$\alpha - \text{Fe}^{3+}\text{O}(\text{OH})$	3.8		Optically dominant?	5
^h Gypsum	$\text{CaSO}_4 \cdot 2\text{H}_2\text{O}$	2.3		Limits acid uptake?	5
ⁱ Hematite	Fe_2O_3	5.26	Silt	Strong Visible & IR	5
^j Illite	$\text{K}_y(\text{Al}, \text{Mg}, \text{Fe})_2(\text{Al}_y, \text{Si}_{4-y}\text{O}_{10}(\text{OH})_2)$	2.75	Clay	T , RH tracer	2, 5
^k Kaolinite	$\text{Al}_2\text{Si}_2\text{O}_5(\text{OH})_4$	2.6	Clay	T , RH tracer	5
^l Mica	$(\text{K}, \text{Na}, \text{Ca})(\text{Mg}, \text{Fe}, \text{Li}, \text{Al})_{2,3}(\text{Al}, \text{Si})_4\text{O}_{10}(\text{OH}, \text{F})_2$		Silt	Weak IR	2
^m Opal	$\text{SiO}_2(\text{H}_2\text{O})_n$	2.1	All	Hygroscopic?	4
ⁿ Quartz	SiO_2	2.62	All	Hydrophobic	2, 5
^o Smectite	$(\text{Na}, \text{Ca}_{0.5})_{0.33}(\text{Al}, \text{Mg})_2\text{Si}_4\text{O}_{10}(\text{OH})_2 \cdot n\text{H}_2\text{O}$	2.7	Clay	Hygroscopic, T , RH tracer	1, 2, 5

^aSource: <http://www.ssc.on.ca/mandm>

^bClay defined as $D < 2 \mu\text{m}$, Silt as $2 < D < 50 \mu\text{m}$. From Claquin et al. (1999).

^cAluminosilicates have similar radiative properties both in the visible and the infrared.

^dReferences: 1, Pruppacher and Klett (1978); 2, Pye (1987); 3, Dentener et al. (1996); 4, Adkins et al. (1999); 5, Claquin et al. (1999);

^e Calcite. A very common mineral, principle constituent of limestone. Neutralizes particle acidity, limits formation of SO_4^{2-} , NO_3^- .

^fFeldspars form about 60% of Earth's crust. Aluminosilicate. M can be K, Na, Ca, Ba, Rb, Sr, Fe.

^gGoethite, aka hydrated iron oxide, may be the dominate optically active form of iron in mineral dust.

^hGypsum is a possible acid buffer?

ⁱHematite is a principle source of free (soluble) iron. Strong visible and IR absorption bands. Mass fraction correlated to soil "redness" index

^jIllite are clay minerals, dominant in many windblown dust samples, abundant in sedimentary rocks, hydrophobic. Aluminosilicate.

^kKaolinite is an Aluminosilicate.

^lMicas are phyllosilicates, dominant in many windblown dust samples

^mOpal is extractable from deep sea sediments.

ⁿQuartz is nearly always a dominant constituent of windblown dust.

^oSmectite is a group, particular values are for Montmorillonite. Smectites are characterized by swelling in water. Aluminosilicate.

Table 3.4: Elemental Composition of Earth's Crust and Surface Oceans

Name	Mass fraction	mg l ⁻¹
Al	0.0823	2e-3
Ca	0.0415	4.12e2
Fe	0.0563	2e-3
K	0.0209	3.99e2
Mg	0.0233	1.29e3
Na	0.0236	1.08e4
O	0.461	8.57e5
Si	0.282	2.2

Table 3.5: Western Sahara Soil Types^a

Soil Type	Code	Population 1			Population 2			Population 3			Flux Ratio α cm^{-1}
		\tilde{D}_n μm	σ_g	M %	\tilde{D}_n μm	σ_g	M %	\tilde{D}_n μm	σ_g	M %	
Silty fine sand	SFS	210	1.8	62.5	125	1.6	37.5	—	—	—	4.5×10^{-6}
Medium sand	MS	690	1.6	80	210	1.8	20	—	—	—	5.5×10^{-7}
Coarse sand	CS	690	1.6	100	—	—	—	—	—	—	1.0×10^{-7}
Coarse medium sand	CMS	690	1.6	90	210	1.8	10	—	—	—	3.3×10^{-7}
Fine sand	FS	210	1.8	100	—	—	—	—	—	—	1.0×10^{-6}
Silty medium sand	SMS	125	1.6	37.5	210	1.8	31.25	690	1.6	31.25	4.2×10^{-6}
Moderately salty sand	SEM	125	1.6	50	520	1.5	50	—	—	—	4.1×10^{-6}
Highly salty sand	SEF	520	1.5	75	125	1.6	25	—	—	—	3.1×10^{-6}

^aSource: [Marticorena et al. \(1997\)](#), Table 2. Soil types comprising the erodible surfaces of the Western Saharan region. The populations are arranged in decreasing order of mass fraction. Each population corresponds to a characteristic soil described in Table 3.2.

The characteristics of the complete soil size distribution of a given soil type are a weighted average of the characteristics of each of the soil sub-populations. Thus the mean flux ratio for a given soil type with N distinct soil subpopulations, shown in the last column of Table 3.5, is computed as

$$\alpha = \sum_{i=1}^{i=N} \alpha_i M_i \quad (3.103)$$

where M_i , given in Table 3.5, is the relative mass fraction of the i th subpopulation. Each soil type is comprised of up to three log-normal size distributions in the saltation range $125 \leq \tilde{D}_n \leq 690 \mu\text{m}$.

The dynamical model of Marticorena et al. (1997) has $1^\circ \times 1^\circ$ horizontal resolution. Using a GIS database of surface features, they subdivided each of these dynamical gridpoints in the Western Sahara into at most five subgrid soil types. The total dust emission flux into each dynamical gridpoint was then composed of the areal weighted fraction of its constituent soil types.

3.4.3 My Theory

One of the aspects of wind tunnel observations which has not been explained by (3.84) is the apparent increase in bombardment efficiency, as measured by Q_d/Q_s (c.f. Shao et al., 1993, Figure 5).

Relaxing the conservative bombardment assumption so that more than one saltator ejection per impact is allowed results in

$$E_2 = \sum_{i=0}^{i=\Pi} \frac{M_s u_i^2}{2} \quad (3.104)$$

where u_i is the initial streamwise velocity of the i th product saltator.

$$F_d = \frac{M_d c_\epsilon \Delta E}{\psi} \times \rho u_*^2 \left(1 - \frac{u_{*t}^2}{u_*^2} \right) [M_s (u_1 - u_0)]^{-1} \quad (3.105)$$

$$= M_d \frac{c_\epsilon \Delta E}{\psi} \times \frac{g Q_s}{2 w_0 \bar{u} M_s} \quad (3.106)$$

$$= M_d \frac{c_\epsilon \Delta E}{\psi} \times Q_s [M_s (u_1 - u_0)]^{-1} \quad (3.107)$$

3.5 Sub-Gridscale Properties

Equation (3.39) is valid only in an instantaneous or equilibrium sense. Prediction of wind erosion in large scale atmospheric models is complicated by the non-linearity of (3.39). To obtain the total horizontal flux in a given period of time we must include the effects of spatial and temporal wind speed variation.

Consider a time-series of wind speeds $U(t)$ with time mean wind speed \bar{U} . In practice \bar{U} is known either from observations or model predictions, and represents the mean of the “actual” wind speed $U(x, y, t)$ over given region and period of time. In a typical large scale atmospheric model \bar{U} may be a 10–30 minute average wind speed over an area of 10^4 km^2 . The non-linear, cubic relation between Q and U causes $Q(\bar{U})$ to differ significantly from $\overline{Q(U)}$ on such scales. To more accurately estimate of \bar{Q} we must make assumptions about the temporal and spatial distributions of the wind whose mean value is \bar{U} .

The importance of the sub-gridscale wind PDF cannot be overstated. Both Aeolian and fluvial shear stress experiments show that the tail-end of the fluid velocity distribution causes much, if not most, of the entrainment. Since wind variability is related to the mean wind speed (Justus et al., 1978) and saltation is driven by high wind speeds, it follows that dust events are characterized by highly variable winds. In turbulence studies, these are called burst and sweep cycles. A “burst” is a high-intensity shear event which creates a micro-low pressure zone. The “sweep” occurs as the fluid fills in this low, often excavating (eroding) the surface at the same time. These events may remove the quasi-laminar layer (Section 5.5) (Sehmel and Hodgson, 1978a).

We assume that an analytic probability distribution function (PDF) governs the spatial and temporal distribution of surface wind speeds. The PDF differential $p(U) dU$ is the probability that the wind speed at a given time or location is between U and $U + dU$. This is equivalent to the relative fraction of time or space⁴ occupied by wind speeds between U and $U + dU$. Since the probability of having a finite wind speed is exactly one, the PDF must be normalized such that $\int_0^\infty p(U) dU = 1$. A suitable PDF thus acts as a weighting function to the instantaneous horizontal flux. The temporal and spatial average horizontal flux is found by convolving $p(U)$ with (3.42)

$$Q = C \int_{U_t}^{+\infty} p(U) U^3 \left(1 - \frac{U_t^2}{U^2}\right) dU \quad (3.108)$$

3.5.1 Weibull Distribution

Justus et al. (1978) showed that an analytic form well suited for describing the probability density function of the surface wind field is the Weibull distribution. More recent studies have justified the use of the Weibull distribution for dust emissions in particular (e.g., Gillette and Passi, 1988; Shao et al., 1996; Cakmur et al., 2004). We define and derive the analytic properties of the Weibull distribution of wind speeds $p_W(U)$ (18.20) in §18.10 below. In a Weibull distribution the frequency of occurrence of winds exceeding U_t decreases exponentially with U_t , i.e., $p_W(U > U_t) = \exp(-U_t/c)^k$ where c and k are, respectively, the scale parameter and shape parameter of the Weibull distribution (18.29). Employing $p_W(U)$

⁴ In fact the spatial and temporal variability of wind are not interchangeable. The dust emission flux depends differently on the spatial and temporal coherence of the wind. The spatial coherence determines the fetch, or distance over which the saltation flux develops to an equilibrium value. Likewise, the temporal coherence determines whether the saltation has enough time to reach an equilibrium value. Shao et al. (1996) discuss a method of separating these two processes. However, we shall neglect this distinction in the present study.

in (3.108) we obtain

$$Q = C \int_{U_t}^{+\infty} \frac{k}{c} \left(\frac{U}{c}\right)^{k-1} \exp \left[- \left(\frac{U}{c}\right)^k \right] U^3 \left(1 - \frac{U_t^2}{U^2}\right) dU \quad (3.109)$$

As shown in §18.10, integrals of the form $U^n p_W(U)$ may be expressed analytically in terms of the incomplete gamma function. Applying (18.26) to (3.109) we obtain

$$Q = \quad (3.110)$$

3.5.2 Dust Devils

Gillette and Sinclair (1990) estimated that the injection of mineral dust into the atmosphere over the United States by dust devils is comparable to that injected by large scale dust mobilization. Renno (fxm: find this reference) also suspect dust devils are important.

Golitsyn et al. (2003) investigated weak dust emission processes, i.e., processes important in weak wind conditions when saltation is minimal and dust fluxes are small. They found emissions in the Aral Sea region are consistent with a dust devils and, possibly, with electrophoresis. Yablokov and Andronova (2004) explain the conditions under which electrostatic effects may be import for dust liftoff. Koch and Renno (2005) develop a theory for dust entrainment by dry convective plumes and vortices, and estimate such dust devils are responsible for about one-third of total dust mobilization on Earth.

3.6 Drag Partitioning

In a series of papers M. Raupach and colleagues have developed a theory of the drag partition between erodible and non-erodible surfaces (Raupach, 1991, 1992; Raupach et al., 1993; Raupach, 1994). Part of this theory recognizes that saltation alters the roughness characteristics of the boundary layer. In neutral conditions the relation between wind speed U and wind friction speed u_* is a logarithmic profile (2.6). The relationship depends on height z above the surface and the roughness length. In a non-saltating environment, (2.6) may be re-expressed as

$$U^n(z) = \frac{u_*}{k} \ln \left(\frac{z}{z_{0,0}} \right) \quad (3.111)$$

In (3.111), the symbol $z_{0,0}$ is the non-saltating roughness length. The Owen effect is the name given to the positive feedback of saltation on wind erosion via roughness length increases. Owen (1964) showed that the saltation layer which develops during wind erosion events acts as an additional sink of atmospheric momentum, causing an increase in momentum deposition to the surface and thus an increase in roughness length. Saltating particles mediate this effect by removing momentum from the atmosphere and transferring it to the surface during each (non-ballistic) impact.

Raupach (1991) showed that the Owen effect entails an implicit relationship between the saltating roughness length $z_{0,s}$ in terms of the non-saltating roughness length $z_{0,0}$

$$z_{0,s} = \left(A \frac{u_*^2}{2g} \right)^{1-R} z_{0,0}^R \quad (3.112)$$

where A is a constant of order unity, g is the acceleration of gravity, and R is the ratio of u_{*t} to u_* (3.93). Equation (3.112) must be solved iteratively because the friction speed u_* itself depends upon $z_{0,s}$ (cf. §2.2.2). Studies have verified that roughening of the surface due to the Owen effect could be quite dramatic (Gillette et al., 1998), although difficult to predict using (3.112).

Gillette et al. (1998) tested Raupach's theory (Raupach, 1991) of the Owen effect (Owen, 1964) against data from Owens Lake, California. Using measurements of saltation events taken at three stations over the course of a year, Gillette et al. not only verified (3.112), but parameterized it into a form easier to evaluate. First, they defined the saltating friction velocity $u_{*,s}$ as the friction velocity measured during fully developed saltation, when the roughness length $z_{0,m} \equiv z_{0,s}$, the saltating roughness length. Under neutral conditions, and with reference to (3.111), the relation between U^n , $u_{*,s}$, and $z_{0,s}$ is

$$U^n(z) = \frac{u_{*,s}}{k} \ln \left(\frac{z}{z_{0,s}} \right) \quad (3.113)$$

Gillette et al. (1998) reasoned that the saltating friction speed $u_{*,s}$ is composed of two parts, the non-saltating friction speed u_* and the contribution due to the Owen effect. Defining the difference between the saltating and non-saltating friction speeds as

$$\Delta u_* = u_{*,s} - u_* \quad (3.114)$$

they used the Owen's Lake data to parameterize Δu_* in terms of the 10 m wind speed U_{10} and the 10 m threshold wind speed $U_{10,t}$.

$$\Delta u_* = 0.003(U_{10} - U_{10,t})^2 \quad (3.115)$$

According to (3.116), the saltating friction speed $u_{*,s}$ increases quadratically with windspeed in excess of the the friction speed⁵ Since $u_{*,s}$ determines the saltation mass flux [e.g., (3.41), (3.50), (3.51), (3.67)] neglecting the Owen effect (3.115) would cause significant underprediction of saltation⁶. Rearranging (3.114) and using (3.115), the saltating friction speed is

$$u_{*,s} = u_* + 0.003(U_{10} - U_{10,t})^2 \quad (3.116)$$

The proliferation of terminology regarding friction speeds can lead to confusion. With saltating and non-saltating friction speeds, smooth and non-erodible roughness lengths, drag

⁵The relationship in Gillette et al. (1998) equation (12) contains a units conversion error and the coefficient is 0.003, not 0.3 (Gillette, 1999).

⁶The Owen effect has not been conclusively measured at locations other than Owen's Lake (the names are coincidentally the same). Zobeck could not discern the effect in data from Texas.

partition and wind friction efficiency, it may be difficult to understand how to predict wind erosion given output of a large scale atmospheric model. It is important to remember that the wind friction speed u_* predicted in such models is generally not the relevant friction speed to employ in dust emissions schemes. First, large scale models use a roughness length $z_{0,m}$ typifying momentum exchange on a scale of order 100 km to predict u_* .

$$u_*, z_{0,m} = \begin{cases} u_{*,0}, z_{0,0} & : u_* < u_{*t} \\ u_{*,s}, z_{0,s} & : u_* \geq u_{*t} \end{cases} \quad (3.117)$$

The wind friction speed u_* and roughness length $z_{0,m}$ measured in wind tunnels changes qualitatively once saltation develops.

The ideas behind drag partitioning are quite general. [Sullivan \(2002\)](#) applied the drag partitioning theory of [Raupach \(1992\)](#) and [Raupach et al. \(1993\)](#) to Mars. [Sullivan](#) estimates that Martian threshold friction velocity and surface wind speed (at 1.6 m height) must be near $u_{*t} \approx 4.5 \text{ m s}^{-1}$ and $U \approx 45 \text{ m s}^{-1}$ near the Pathfinder landing site. [MacKinnon et al. \(2004\)](#) generalize Raupach's drag partition theory to apply to an arbitrary number of roughness surfaces. They applied this generalization to measured and modeled surfaces in the Mojave Desert. [Okin \(2008\)](#) develop a shear-stress partitioning model arguably superior to Raupach's model.

As the preceding section shows, the susceptibility of soils to wind erosion is highly sensitive to particle size. In nature, soils are composed not of a discrete, monodisperse size of particles, but of a continuous distribution of particles and compositions which define the soil texture.

3.7 Dependence On Soil Moisture

As is clear from many experiments, interparticle cohesive forces rapidly begins to dominate the moment balance on dust particles as the size of the particles falls beneath about $40 \mu\text{m}$ [White \(1979\)](#); [Iversen and White \(1982\)](#); [Greeley and Iversen \(1985\)](#). Most of the aforementioned experiments, however, were performed upon dry soil beds. Thus these experiments suit completely dry environments such as Mars, but idealize field conditions in partially wet environments such as the semi-arid regions of Earth. The notion that a wet soil bed will not detrain any dust particles agrees with experience, and the quantification of this phenomena for the entire soil spectrum from dry to saturated is the topic of this section. These effects are especially important when considering the persistence of soil moisture perturbations or soil moisture memory (e.g., [Koster and Suarez, 2001](#)).

See the discussion in [Pye \(1987\)](#), p. 31.

3.7.1 Soil Water Content

In this section we summarize the traditional measures of soil-water interaction. The following sections will build upon these definitions to present parameterization of the influence of soil moisture on u_{*t} .

The fundamental determinant of soil-water interactions is the amount of water contained in the soil. The most easily (and frequently) measured descriptor of soil water content is the

gravimetric water content w on a dry-mass basis

$$w = M_{\text{H}_2\text{O}}/M_{\text{s,d}} \quad (3.118)$$

where $M_{\text{H}_2\text{O}}$ is the mass of liquid water and $M_{\text{s,d}}$ is the mass of dry soil. The driest condition attained by a soil in nature is called air dry. The driest condition to which a soil can be brought in the laboratory is called oven dry. By convention, $M_{\text{s,d}}$ is defined as the mass of soil in equilibrium with an oven at a temperature of 105°C (Hillel, 1982). Even at this temperature, clay soils may retain appreciable moisture, i.e., up to a few percent.

The wettest possible condition of soil, in which all pores are filled with water, is called saturated soil. We shall affix the subscript s to quantities to indicate the saturation condition, e.g., w_s is the gravimetric water content at saturation. The value of w_s , depends on the soil type, but typically $0.25 < w_s < 0.60$. Soils rich in organic matter, e.g., peat, may have $w_s > 1$. Occasionally in the literature the gravimetric water content is expressed on a wet-mass basis, which is simply defined by replacing $M_{\text{s,d}}$ with $M_{\text{s,m}}$, the mass of moist soil, in (3.118). In this text we shall only use w defined on a dry-mass basis, as in (3.118).

The other frequently used measure of soil moisture is the volumetric water content θ

$$\begin{aligned} \theta &= \frac{V_{\text{H}_2\text{O}}}{V_{\text{H}_2\text{O}} + V_p + V_a} \\ &= V_{\text{H}_2\text{O}}/V_b \end{aligned} \quad (3.119)$$

$V_{\text{H}_2\text{O}}$, V_p , and V_a are the volumes of water, (moist) soil particles, and interparticle gases (i.e., air) in the sample. The total volume or bulk volume V_b of the soil sample is defined as

$$V_b = V_{\text{H}_2\text{O}} + V_p + V_a \quad (3.120)$$

V_p measures only the volume of the soil particles themselves, whereas V_b includes volume occupied by porous interparticle spaces and by water. Thus θ is the fractional volume of liquid water relative to the bulk volume (water plus soil plus air) of the soil. Typically it is assumed that $V_{\text{H}_2\text{O}} \ll V_p$ and $V_a \ll V_p$ so that (3.120) may be approximated as

$$V_b \approx V_p \quad (3.121)$$

This approximation, which appears to be standard in the literature, may be inappropriate for loose, wet soils. As discussed above, θ_s will denote the volumetric water content at saturation.

A further distinction may be made between the volume of ambient soil particles V_p and the volume of the dry soil particles $V_{p,d}$. The two quantities are related by the swelling of the soil under moist conditions which depend on the amount of swelling. We define the dimensionless soil swelling function S to depend on gravimetric water content and on soil mineralogy χ as follows

$$V_p = V_{p,d}S(w, \chi) \quad (3.122)$$

For minerals which do not absorb water, e.g., quartz, $S(w, \chi) = 1$, while $S(w, \chi) > 1$ for minerals which swell with water, e.g., smectites (Table 3.3). Note that θ (3.120) is defined

Table 3.6: Soil Volume, Mass, Density and Moisture^a

Symbol	Name	Meaning
V_p	Soil Volume	Ambient soil particle volume (moist, non-porous)
V_b	Bulk Soil Volume	Ambient soil volume (moist, porous)
$V_{b,d}$	Bulk Dry Soil Volume	Dry soil volume (porous)
$V_{p,d}$	Dry Soil Volume	Dry soil particle volume (non-porous)
V_w	Water Volume	Interparticle water volume
V_a	Air Volume	Porous interparticle space

^aSources:

relative to the bulk soil volume V_b while w (3.118) is defined relative to the dry soil mass $M_{s,d}$. This can lead to confusion since ambient soil volume V_p depends on water content for some soils (3.122). Although measurement of w is more straightforward than θ , the literature appears to favor use of θ hydrologic theory.

Converting between θ and w simply requires knowledge of the densities of water ρ_{H_2O} and of dry soil particles $\rho_{p,d}$. If we assume $V_b = V_{b,d}$

$$\begin{aligned}
 w &\equiv \frac{M_{H_2O}}{M_{s,d}} = \frac{V_{H_2O}}{V_{b,d}} \times \frac{\rho_{H_2O}}{\rho_{b,d}} \\
 &= \frac{V_{H_2O}}{V_b} \times \frac{\rho_{H_2O}}{\rho_{b,d}} \\
 &= \theta \rho_{H_2O} / \rho_{b,d}
 \end{aligned} \tag{3.123}$$

The so-called dry density of the soil, $\rho_{b,d}$, is defined by the dry mass of the soil $M_{s,d}$ and the bulk volume V_b (3.120) of the soil

$$\begin{aligned}
 \rho_{b,d} &\equiv \frac{M_{s,d} + M_a}{V_{H_2O} + V_p + V_a} \\
 &\approx \frac{M_{s,d}}{V_b}
 \end{aligned} \tag{3.124}$$

where we have made the approximation that $M_a \ll M_{s,d}$ in the second equation. The operational determination of $\rho_{b,d}$ (3.124) must be made in two stages. First the ambient (moist) bulk soil sample volume V_b must be determined. Next, the sample is dried so that the soil dry mass $M_{s,d}$ may be determined. Therefore natural soil “in the field” never has $\rho = \rho_{b,d}$. Soil models employ a variety of strategies to determine $\rho_{b,d}$ (3.124). One such strategy is to assume knowledge of the soil particle density ρ_p ...

If we do not assume $V_b = V_{b,d}$, then

$$\begin{aligned}
 w &\equiv \frac{M_{H_2O}}{M_{s,d}} = \frac{V_{H_2O}}{V_{p,d}} \times \frac{\rho_{H_2O}}{\rho_{p,d}} \times \frac{V_b}{V_b} \\
 &= \frac{V_{H_2O}}{V_b} \times \frac{\rho_{H_2O}}{\rho_{p,d}} \times \frac{V_b}{V_{p,d}} = \theta \times \frac{\rho_{H_2O}}{\rho_{p,d}} \times \frac{V_b}{V_{p,d}} \\
 &\approx \theta \rho_{H_2O} / \rho_{p,d}
 \end{aligned} \tag{3.125}$$

where the approximation (3.121) has been made in the final step. Alternatively, we can define θ in terms of w as

$$\begin{aligned}
 \theta &\equiv \frac{V_{\text{H}_2\text{O}}}{V_b} = \frac{M_{\text{H}_2\text{O}}}{\rho_{\text{H}_2\text{O}}} \times \frac{\rho_b}{M_b} = \frac{M_{\text{H}_2\text{O}}}{M_{\text{H}_2\text{O}} + M_{s,d} + M_a} \times \frac{\rho_b}{\rho_{\text{H}_2\text{O}}} \\
 &\approx \frac{M_{\text{H}_2\text{O}}}{M_{\text{H}_2\text{O}} + M_{s,d}} \times \frac{M_{s,d}}{M_{s,d}} \times \frac{\rho_b}{\rho_{\text{H}_2\text{O}}} \\
 &= \frac{M_{\text{H}_2\text{O}}}{M_{s,d}} \times \frac{M_{s,d}}{M_{\text{H}_2\text{O}} + M_{s,d}} \times \frac{\rho_b}{\rho_{\text{H}_2\text{O}}} \\
 &= w \times \frac{\rho_b}{\rho_{\text{H}_2\text{O}}} \times \frac{M_{s,d}}{M_{\text{H}_2\text{O}} + M_{s,d}} \\
 &\approx w \rho_b / \rho_{\text{H}_2\text{O}}
 \end{aligned} \tag{3.126}$$

where the last step has used an approximation, analogous to (3.121) that

$$M_b = M_{\text{H}_2\text{O}} + M_{s,d} + M_a \approx M_{s,d} \tag{3.127}$$

Like (3.121), approximation (3.127) is only valid if $M_{\text{H}_2\text{O}} \ll M_{s,d}$ and so breaks down for very wet soils. Conversely, approximations (3.121) and (3.127) are both well-suited for use determining moisture inhibition of dust deflation in arid soils. As described in §3.7.4–3.7.6, moisture inhibition of deflation is virtually assured for $w \gtrsim 0.2 \text{ kg kg}^{-1}$.

By convention, both w and θ are reported as percentages (i.e., multiplied by 100) rather than as fractions. When a soil moisture or mass value is to be expressed in percent, we superscript it with the % symbol, i.e., $\theta\% \equiv 100\theta$ and $w\% \equiv 100w$. Otherwise the value is assumed to be a fraction.

3.7.2 Characterization of Soil Water Energy

The energy of a water parcel in soil determines its hydraulic behavior. The total potential energy of a parcel of soil water, Φ , is the sum of the forces acting on the water which cause it to differ from a surface of pure, bulk water. These forces include gravitation, pressure, and osmotic properties, respectively:

$$\Phi = \Phi_g + \Phi_p + \Phi_o \tag{3.128}$$

Both the gravitational potential Φ_g and the pressure potential Φ_p may be converted to mechanical (kinetic) energy of flow in open soils. Φ_g and Φ_p are discussed in more detail below. The osmotic potential Φ_o is due to the presence of salts in the water, and will not be discussed further. Darcy's law states that the mass flux of water flowing through a surface is proportional to the gradient of Φ across the surface. Of course water tends to flow downgradient, i.e., from high to low Φ .

The gravitational potential of a parcel of soil water is defined in exact analogy to the potential energy of an air parcel. Thus the gravitational potential Φ_g of a mass M at a height z is

$$\Phi_g = \int_{z_r}^z M g(z) dz \tag{3.129}$$

where z_r is the height of the reference level. In soil energy studies it is common to define the reference level as the level of the soil surface, i.e., $z_r = 0$. For the remainder of this work we take $z_r = 0$ and assume that $g(z)$ equals the mean acceleration of gravity at the Earth's surface, g . Then (3.129) reduces to

$$\Phi_g = Mgz \quad (3.130)$$

$$= \rho_l Vgz \quad (3.131)$$

where ρ_l is the density of liquid water and V is its volume. Thus $\Phi_g < 0$ for water beneath the soil surface.

The pressure potential of a water parcel is due to the displacement of the parcel relative to a free surface of water. In other words, a water parcel at the surface of a free body of water feels no pressure potential. A parcel residing at a depth d beneath the free surface of water feels a total pressure p_t which is the sum of the atmospheric pressure p and the hydrostatic pressure p_l due to the column of liquid water above it

$$\begin{aligned} p_t &= p + p_l \\ &= p + \rho_l g d \end{aligned} \quad (3.132)$$

If the volume of the parcel is V , then the pressure potential energy of the parcel is

$$\Phi_p = p_l V \quad (3.133)$$

Thus the pressure potential per unit volume is $\tilde{\Phi}_p/V = p_l$.

In soil energy studies it is very common to normalize the total potential energy of the water by the amount of water. When applied to (3.131), this results in the gravitational potential energy of the water per unit mass, Φ_g , and per unit volume, $\tilde{\Phi}_g$. Dividing (3.131) by M and by V , respectively, we obtain

$$\Phi_g = gz \quad (3.134)$$

$$\tilde{\Phi}_g = \rho_l gz \quad (3.135)$$

At STP, $\rho_l \approx 1000 \text{ kg m}^{-3}$, so that $\tilde{\Phi}_g \approx 1000\Phi_g$.

Work by Clapp and Hornberger (1978) and Cosby et al. (1984) provided widely used approximate empirical relationships between the soil matric potential, water content, and soil texture. First, the saturated volumetric water content θ_s depends weakly on the mass fraction of sand in the soil

$$\theta_s \approx 0.489 - 0.126M_{\text{sand}} \quad (3.136)$$

Knowledge of θ_s is important since, under a simplifying assumption, be used to obtained the bulk density of the soil. If the process of soil saturation is assumed is due to filling of pores (rather than soil swelling), then θ_s equals the volume concentration of air pores which have been displaced. Assuming soils reach saturation once all air pores have been displaced then

$$\theta_s = V_a \Big|_{\theta=0} \quad (3.137)$$

where LHS and RHS are evaluated at complete saturation and at oven-dry conditions, respectively. For values of M_{sand} in $[0.0, 1.0]$ (3.136) predicts $V_a(\theta = 0) \in [0.489, 0.363]$.

For soils with a swelling function S equal to unity (3.122), the volumetric water content at saturation and the (poreless) volume V_p occupied by soil particles are simply related

$$\begin{aligned}\theta_s + V_p &= 1 \\ V_p &= 1 - \theta_s\end{aligned}\tag{3.138}$$

The dry bulk density or dry density of the soil $\rho_{p,d}$ is this poreless soil volume V_p times the mean mass density ρ_p of individual soil particles

$$\begin{aligned}\rho_{p,d} &= \rho_p V_p \\ &= \rho_p(1 - \theta_s)\end{aligned}\tag{3.139}$$

The contribution of air has been neglected in (3.139) since $\rho \ll \rho_p$. It follows from (3.136) that (3.139) is also an approximation which is best suited to sandy soils. In particular, (3.136) and (3.139) together imply that soil bulk density have no dependence on clay or silt content.

Since ρ_p measures the mass density of the particle solids only, it does not depend on the structure or texture of the soil. Therefore ρ_p does not depend on water content (except for swelling soils), but is sensitive to particle coatings and aggregates, such as organics. Soil Organic Matter (SOM) is less dense than most minerals, so soils high in organic matter (such as those near the surface), are less dense than mineral-dominated soils of the same texture. Values of ρ_p for important mineral types are presented in Table 3.3. A standard value of $\rho_p = 2.65 \text{ g cm}^{-3}$ (valid for pure quartz) is often employed when the specific soil mineralogy is unknown. This value is especially appropriate in mineral dust source regions, which are typically very low in SOM and high in quartz, feldspars, and colloidal silicates. Dust from volcanic and meteoric ash is less dense, closer to $\rho_p = 2.65 \text{ g cm}^{-3}$.

The relative saturation of the soil s is somewhat analogous to relative humidity:

$$s = \theta/\theta_s\tag{3.140}$$

Thus s expresses the degree of saturation on a normalized scale $0 \leq s \leq 1$.

The soil matric potential at saturation, ψ_s , is, to a first approximation, a function only of the mass fraction of the soil that is sand, M_{sand}

$$\psi_s = -10.0 \times 10^{1.88 - 0.000131 M_{\text{sand}}}\tag{3.141}$$

where ψ_s is in mm H₂O.

Finally, Clapp and Hornberger (1978) and Cosby et al. (1984) showed that the measured soil matric potential fits a power law dependence on the relative saturation

$$\psi = \psi_s s^{-b} \quad \text{where}\tag{3.142}$$

$$b = 2.91 + 0.159 \times M_{\text{clay}}\tag{3.143}$$

where the dimensions of ψ are mm H₂O. Thus b depends upon both the sand mass fraction through s (3.140) and the clay mass fraction through b . Clearly the omission of any dependence on the silt mass fraction in (3.142) is an approximation.

3.7.3 Capillary and Adsorptive Forces

The influence of moisture on the threshold friction velocity arises from two forces caused by the presence of liquid water between grains of soil. The first force is the capillary force, which arises from the surface tension of water and the size and geometry of grains and pores. As described in §18.3, capillary forces cause a pressure differential to develop between the curved meniscus of a liquid phase water wedge and the air with which it is in equilibrium. The second force is the adsorptive force, which arises from the attraction of polarized water molecules to charged surfaces of soil grains. Adsorptive forces cause liquid water (and water vapor) to coat the surfaces of soil grains.

The combined forces of capillarity and adsorption are called the matric suction or matric potential. The soil matric potential ψ is usually expressed as the potential energy per unit volume of soil in J kg^{-1} . However, the dimensions and definition of ψ are somewhat confusing. For example, (3.142) below is an expression for ψ in $\text{mm H}_2\text{O}$. Thus we describe how to convert between various descriptions and units of the energy levels of soil water.

3.7.4 Empirical Adjustments to u_{*t}

Based on the above discussion, it is clear that the friction threshold of a soil is sensitive to the water content of the soil, i.e., $u_{*t} = u_{*t}(w)$. Generally, the influence of moisture on u_{*t} is described by the threshold inhibition function f_w , defined as the ratio between the wet and dry friction thresholds, u_{*tw} and u_{*td} , respectively

$$f_w(\theta) = \frac{u_{*t}(\theta)}{u_{*t}(\theta = 0)} = \frac{u_{*tw}}{u_{*td}} \quad (3.144)$$

Thus $f_w > 1$. In practice, the functional dependence on θ may be replaced by any other measure of water content, e.g., w . In addition to water content, f_w can depend on soil texture (i.e., size), salt content, and time since precipitation. For the time being we neglect these dependencies and refer the interested reader to the discussions in Pye (1987) and Gillette (1988).

A number of investigators have created simple parameterizations which account for the increase of u_{*t} with θ (Belly, 1964; Pye, 1987; Gillette, 1988; Selah and Fryrear, 1995; Shao et al., 1996; Fécan et al., 1999). Belly (1964) measured u_{*t} for various soil moisture contents. His results fit the logarithmic parameterization

$$H_w(\theta) = 1.8 + 0.6 \log_{10} \theta\% \quad (3.145)$$

where $\theta\%$ is the percent volumetric water content. Unlike most authors, Belly (1964) measured the threshold friction velocity required to develop a sustained saltation, rather than the fluid threshold friction velocity. As a result, (3.145) tends to predict higher values of u_{*t} than other parameterizations (Shao et al., 1996; Fécan et al., 1999).

The wind tunnel experiments of Shao et al. (1996) fitted the exponential relationship

$$f_w(\theta) = e^{22.7\theta} \quad (3.146)$$

In practice (3.146) predicts that f_w becomes so large for $\theta > 0.04 \text{ m}^3 \text{ m}^{-3}$ that dust mobilization effectively ceases.

Table 3.7: Regimes of Soil Moisture Inhibition of Dust Emissions

Regime	Constraint
$0 < w < w_t < w_T < w_s < 1$	Emissions occur without constraint, moisture is adsorptive
$0 < w_t < w < w_T < w_s < 1$	Emissions occur with constraint, some moisture is capillary
$0 < w_t < w_T < w < w_s < 1$	No emissions occur, moisture inhibition too high
$0 < w_t < w_T < w_s < w < 1$	No emissions occur, soil is waterlogged

The differences between (3.145) and (3.146) are significant. The logarithmic form of (3.145) curves concave downwards starting from $f_w(0.01) = 1.2$. The exponential form of (3.146) curves concave upwards starting from $f_w(0) = 1$.

Gillette (1988) studied the dependence of u_{*t} on soil type and condition. He characterized the modulus of rupture of the soil.

Selah and Fryrear (1995) studied the behavior of erosive thresholds on soil moisture in carefully controlled wind tunnel experiments. Two soil moisture reading were made for each of five different soil textures considered. The first is the water holding content, w_s , which is simply the gravimetric water content at saturation. Selah and Fryrear (1995) found that w_s is tightly correlated with soil clay fraction M_{clay}

$$w_s = 0.433M_{\text{clay}} \quad (3.147)$$

This relationship (3.147) is in contrast to previous studies which found θ_s depends most on sand fraction M_{sand} (3.136) (Clapp and Hornberger, 1978; Cosby et al., 1984; Bonan, 1996). Second is the maximum gravimetric water content which permits erosion w_T , i.e., wind erosion ceases for $w > w_T$.⁷ The experimental design allowed separate retrieval of w_T in both abrading and non-abrading environments where the difference was the presence or absence, respectively, of upstream saltation (which assists triggering local saltation). Regressions of their measurement results showed high-correlation when defined in terms the non-dimensional equivalent threshold moisture \tilde{w}_t

$$\tilde{w}_t \equiv w_T/w_s \quad (3.148)$$

Clearly $\tilde{w}_t < 1$ for standard soils.

It may be helpful to recap the various moisture thresholds related to wind erosion. The soil water content w falls into four possible ranges described in Table 3.7.

The following relations between u_{*t} , and \tilde{w}_t were obtained:

$$u_{*t}(\tilde{w}_t) = \begin{cases} 0.305 + 0.022\tilde{w}_t + 0.506\tilde{w}_t^2 & : u_* < u_{*t} \quad (\text{non-saltating}) \\ 0.205 + 0.182\tilde{w}_t + 0.375\tilde{w}_t^2 & : u_* \geq u_{*t} \quad (\text{saltating}) \end{cases} \quad (3.149)$$

The first of the two domains of (3.149) applies to the non-saltating (non-abraded) conditions which exist prior to the development of a mature saltation layer, or upwind of the layer. The

⁷The terminology threshold gravimetric water content is somewhat ambiguous. The quantity w_T defined by Selah and Fryrear (1995) is not to be confused with the related w_t defined by Fécan et al. (1999). The maximum gravimetric water content w which permits erosion is w_T , i.e., erosion ceases for $w > w_T$. The maximum w which does not impede erosion. is w_t , i.e., soil water reduces erosion for $w > w_t$.

second domain applies to the saltating friction velocity which is the parameter of merit in saltating conditions. The threshold friction velocity is seen to increase approximately 20% per 10% increase in \tilde{w}_t in both cases.

3.7.5 McKenna-Neuman's Theory

McKenna-Neuman and Nickling (1989) developed a theoretical expression for the increase of u_{*t} due to soil moisture valid for sandy soils. Adsorptive forces are thought to be insignificant in soils containing only coarse sand particles ($D > 100\mu\text{m}$) (Hillel, 1982). This is because the molecular forces which lead to adsorption are largely caused by clay sized particles.

McKenna-Neuman and Nickling (1989) assume that the only remaining force able to cause significant interparticle cohesion in sandy texture soils is the capillary force F_c . Assuming a disymmetrical conical geometry represented the grain-pore relationship, they found that F_c could be expressed solely in terms of the surface tension of liquid water σ , a factor G determined by the grain-pore geometry, and the pressure deficit P as

$$F_c = \frac{\pi\sigma^2 G}{P} \quad (3.150)$$

The pressure deficit P is the only factor in (3.150) which directly depends on the moisture content. Note that as $P \rightarrow 0$, F_c becomes ill-defined. Thus (3.150) is not valid for planar water surfaces where the capillary forces become very weak.

The work of McKenna-Neuman and Nickling (1989) showed that, for coarse sandy soils, f_w depended on the square root of the capillary force. Two geometrically distinct arrangements of particles and pores were analyzed. The first, corresponding to a particle resting angle of $\beta = 30^\circ$, is called an open packed system. The second, corresponding to a particle resting angle of $\beta = 45^\circ$, is called an close packed system. For each of these systems, they found $f_w \propto \sqrt{F_c}$. As indicated in (3.150), F_c depends on the grain geometry through both G and P . The resulting expressions for f_w are

$$f_w = \begin{cases} \left(1 + \frac{6F_c \sin(2\beta) \cos(2\beta)}{\pi D^3(\rho_p - \rho)g \sin(\beta)}\right)^{1/2} & : \text{ Open packed system} \\ \left(1 + \frac{6F_c \sin(2\beta)(1 + 2 \cos \beta)}{\pi D^3(\rho_p - \rho)g \sin(\beta)}\right)^{1/2} & : \text{ Close packed system} \end{cases} \quad (3.151)$$

Wind tunnel data for three sizes of sand ($D = 190, 270$, and $510\mu\text{m}$) fit (3.151) reasonably well over the experimental range of moisture contents tested, $0 < \theta < 0.02$. The predictive skill of this theory in the absence of any treatment of adsorptive forces substantiates the hypothesis that adsorptive forces are insignificant at increasing u_{*t} for large particles.

The dominance of capillary over adhesive forces in coarse sand soil supports a hypothesis about the partitioning of water between capillary pores and surface coatings. If the interparticle forces due to adsorption are negligible for coarse sandy soil, then it is reasonable to assume that the fraction of liquid water which is adsorbed to surfaces is negligible compared to the fraction bound into capillary wedges. Thus McKenna-Neuman and Nickling (1989) assume that virtually all of the soil water in coarse soils is found in capillary wedges and pores, and very little is found in surface coatings. Since the interparticle cohesive forces for

coarse sandy soils are dominated by F_c (3.150), the soil matric potential, which is the sum of the gravitational and pressure potentials (3.128), and must be closely related to F_c as well. In fact, McKenna-Neuman and Nickling (1989) assumed that the soil matric potential is equivalent to the capillary potential, i.e.,

$$\psi \approx F_c \quad (3.152)$$

For clayey soils a significant fraction of the water is bound into adsorptive coatings, so that a simple relationship between ψ and F_c (3.152) is not justified. However, a similar relationship may be posited and its results tested against experiments, as is done by Fécan et al. (1999).

3.7.6 Fécan's Theory

Fécan et al. (1999) developed a semi-empirical parameterization for $f_w(w)$ suitable for use in large scale atmospheric models. Their parameterization extends the theory of McKenna-Neuman and Nickling (1989) for coarse sandy soils to realistic soils containing arbitrary amounts of clay and silt. The major limitation of McKenna-Neuman and Nickling (1989) is its neglect of these smaller particles. As already discussed, the stronger electrostatic surface forces of clays, together with their higher surface area to volume ratio, causes adsorptive forces to become significant in the presence of clays. As noted by Hillel (1982), the adsorptive and capillary forces are difficult to disentangle when small particles are present because the distinction between the coatings and wedges at the contact points is ill-defined. In fact, the adsorptive coatings and capillary wedges are essentially distinct thermodynamic phases of water whose equilibrium is very difficult to predict for an arbitrary geometry.

Thus, in the absence of a theoretical description of the simultaneous effects of both capillary and adsorptive forces, Fécan et al. (1999) chose to fit an assumed functional form to experimental data. First they noted that the combined cohesive forces due to water (capillary and adsorptive) are what determines the soil matric potential of soil with arbitrary clay and silt content

$$\psi \approx F_c + F_a \quad (3.153)$$

Unlike (3.152), (3.153) applies to any soil type, include clayey soils. According to the work of Clapp and Hornberger (1978) and Cosby et al. (1984) presented earlier (3.136)–(3.143), ψ may be empirically expressed in terms of coefficients which explicitly depend only on the soil sand and clay contents.

The total water content of an arbitrary soil may be considered as the sum of two components, water at contact points which contributes to capillary forces, θ_c , and water in surface coatings which contributes to adhesive forces, θ_a ,

$$\theta = \theta_c + \theta_a \quad (3.154)$$

As noted earlier, f_w is proportional to the square root of the capillary force (3.151) for coarse sand-textured soils.

Fécan et al. (1999) parameterized f_w in terms of gravimetric water content w rather than volumetric water content θ because most of the field measurements were reported in terms

of w . Fécan et al. (1999) posit that $f_w(w)$ is unity for water contents less than the threshold gravimetric water content w_t . For $w < w_t$, the water is mostly distributed in adsorptive coatings which do not affect u_{*t} . When $w = w_t$, the adsorptive capacity of the soil has been reached and additional water increases the capillary forces in the soil, which do increase u_{*t} . Thus, for soils wetter than w_t , inhibition of particle deflation through increasing u_{*t} is to be expected. Fécan et al. (1999) show that most variation in w_t is an explicit function of the soil clay content. Using multiple datasets (Belly, 1964; McKenna-Neuman and Nickling, 1989, , and others) spanning the domain $0.0 < M_{\text{clay}} < 0.5$, they found

$$\begin{aligned} w_t^{\%} &= 0.17M_{\text{clay}}^{\%} + 0.0014 \times (M_{\text{clay}}^{\%})^2 \\ w_t &= 0.17M_{\text{clay}} + 0.14 \times M_{\text{clay}}^2 \end{aligned} \quad (3.155)$$

Note that all gravimetric water contents and soil textures in Fécan et al. (1999) are assumed to be in percent. According to (3.155), as M_{clay} increases from 0.0 to 1.0, w_t increases quadratically from 0.0 to 0.31 kg kg⁻¹. Typical Saharan desert clay contents of $0.1 < M_{\text{clay}} < 0.2$ lead to $0.018 < w_t < 0.04$ kg kg⁻¹.

Fécan et al. (1999) parameterized the observed relationship between f_w , w , and w_t from multiple datasets.

$$f_w = \begin{cases} 1 & : w \leq w_t \\ \sqrt{1 + 1.21(w^{\%} - w_t^{\%})^{0.68}} & : w > w_t \\ \sqrt{1 + 1.21[100(w - w_t)]^{0.68}} & : w > w_t \end{cases} \quad (3.156)$$

By construction, moisture does not affect u_{*t} until $w > w_t$, after which increased w quickly quenches dust production by increasing u_{*t} . Note that (3.156) maintains the quadratic dependence of f_w on θ explained by McKenna-Neuman and Nickling (1989) (3.151), but also allows for the influence of clay on soil. These results may be expressed in terms of θ by employing (3.125).

3.8 Geomorphology

Schaaf et al. (2002) Tsvetsinskaya et al. (2002) Ballantine et al. (2005) use spectral unmixing techniques to produce landform distributions for North Africa. Tegen et al. (2002a) Zender et al. (2003b) Gillette et al. (2001) describe three phases of saltation activity related to crusting on the saline playa of Owens Lake. Gill (1996) reviews evidence for anthropogenic and dessication-induced dust emission from playas and dry lakes worldwide. Evans et al. (2004) describe the provenance of dust from the Bodélé Depression. Koven and Fung (2008) investigate the sensitivity of dust erodibility to geomorphological parameters in a CTM evaluated with MISR optical depths.

3.9 Dust Source Regions

Prospero et al. (2002) characterize dust source regions on the basis of satellite retrieved indices from the Total Ozone Mapping Spectrometer (TOMS). Washington et al. (2003)

use TOMS and in situ observations to characterize source regions. [Sun et al. \(2001\)](#) use in situ dust storm reports to analyze the climatology and distribution of dust sources in the Gobi Desert, Takla Makan Desert, and other regions of China. Table 3.8 characterizes the most important dust source regions. [Koren and Kaufman \(2004\)](#) use satellite measurements to show funneling effects of topography appear to significantly enhance wind speed in the Bodélé Depression relative to surrounding regions. [Zender and Kwon \(2005\)](#) analyze TOMS aerosol and satellite-derived climate timeseries to infer the dominant erodibility mechanisms in source regions. [in Semiarid Soils Using Airborne Hyperspectral Technology \(2004\)](#) and [Goldshleger et al. \(2004\)](#) characterize soil crusting and rainfall infiltration in terms of near infrared soil spectral reflectance. While dust emissions often peak in playas and dried lakebeds, they are strongly-structured, not uniformly distributed, throughout these sources. Emissions seem to peak at the windward edge of playas.

3.9.1 Bodélé Depression

The Bodélé Depression is presently Earth's strongest dust source. Half of its emissions cross 15°W and enter the Subtropical Atlantic Region, where they contribute to the trans-Atlantic dust plume seen clearly in satellite measurements ([Husar et al., 1997](#); [Herman et al., 1997](#); [Prospero et al., 2002](#)). Conversely, much of the Bodélé dust remains over North Africa, where it contributes to the background dust reservoir. Indirect evidence for this reservoir is seen in the insensitivity of trans-Atlantic dust events to the timing of wind events in African source regions ([Colarco et al., 2003](#)).

One research group which visited the region found that white diatomite from Paleolake Megachad covers a large fraction of the region ([Giles, 2005](#)). Diatomite is the ultimate source of much of the Bodélé's dust. The dust appears to form by splintering and erosion of large diatomite particles saltating in sand dunes, rather than by lofting of fine diatomite powders seen in other regions of the Sahara.

[Washington et al. \(2006\)](#) summarize the physical, meteorological, geomorphological, and anthropogenic reasons why the Bodélé Depression emits dust so efficiently. The depression is situated between two mountain ranges, the Tibesti and the Ennedi. These topographic features funnel a low-level easterly jet over the depression.

3.9.2 Takla Makan Desert

The Takla Makan Desert in the Tarim Basin is the most active dust source in Asia ([Husar et al., 1997](#); [Herman et al., 1997](#); [Prospero et al., 2002](#)).

3.9.3 Lake Eyre Basin

The Lake Eyre Basin is the most important dust source in Australia. It is an inland-drainage basin and vestigial wetland.

Table 3.8: Erodibility Responses of Major Dust Source Regions^{ab}

Region	P, τ	P, N	N, τ	P, U	U, τ	Cat. ^c
Eastern Sahel 10°N–15°N, 10°W–20°E	−0.27(9)	+0.33(1)	−0.31(0)			I
Bodélé Depression 15°N–20°N, 10°E–20°E	−0.28(9)	+0.26(9)	−0.31(0)			I
Western US 25°N–35°N, 110°W–100°W	−0.22(0)	+0.47(1)	−0.35(0)			I
Lake Eyre Basin 30°S–25°S, 136°E–145°E	−0.36(1)	+0.61(1)	−0.29(1)			I
Botswana 25°S–20°S, 20°E–30°E	−0.39(1), −0.23(0)	+0.56(2), +0.31(0)	−0.28(9)			I
Gobi Desert 42.5°N–45°N, 105°E–110°E			−0.28(2)			I
China Loess Plateau 32.5°N–37.5°N, 105°E–110°E	−0.27(0)					II
Great Salt Lake 40°N–42.5°N, 115°W–112.5°W	−0.37(0)	−0.27(0)		+0.26(0)		II
Zone of Chotts 32.5°N–35°N, 5°E–10°E	+0.21(44)	+0.42(26)		+0.26(0)		III
Tigris/Euphrates 27.5°N–32.5°N, 45°E–57.5°E	+0.21(14)	−0.26(8)				III
Saudi Arabia 20°N–25°N, 47.5°E–52.5°E	+0.36(0)	−0.27(0)				IV
Oman 17.5°N–20°N, 52.5–57.5°E	+0.40(0)					IV
Tarim Basin 35°N–40°N, 75°E–90°E			+0.28(21)		+0.23(0), −0.24(2)	IV
Thar Desert 25°N–30°N, 70–75°E	+0.25(0), −0.24(1), −0.21(2)	+0.57(1)	−0.3(0), −0.33(10)	−0.35(0)	+0.3(1)	I, IV

^aHighly significant ($p < 0.01$) cross-correlations r between autoregression-corrected erodibility indicators (dust AOD τ) and climate constraints (precipitation P , NDVI N , and wind speed U) from 1979–1994. Lag in months of indicated cross-correlation is shown in parentheses.

^bSources: Dust source regions identified by Prospero et al. (2002) and subsequent analyses of Torres et al. (2002) data.

^cErodibility Category Assigned

Chapter 4

Sea Salt

The natural aerosols with the greatest mass burden and optical depth are mineral dust and sea salt. As we have seen, the entrainment of mineral dust into the atmosphere is a very complicated process. Sea salt aerosol is also produced by Aeolian erosion but the source material, the ocean, is much more homogeneous than land. While a complete understanding of the generation of all sizes of sea salt has not been achieved, the fundamental relationships between wind speed and mass fluxes are known empirically and are less controversial than dust fluxes.

Sea salt and desert dust mix more often than their names imply. [Levin, Zev]Zev Levin finds that about 60% of all coarse particles 500 m over the Mediterranean are internal mixtures of dust and sea salt.

4.1 Literature Review

Monahan (1971) has a very concise title. Monahan et al. (1982) used closed tanks experiments to empirically determine the spectral mass flux of sea salt generated by bubble-bursting. Monahan et al. (1986) presented the first model with distinct parameterizations for the direct and indirect formation mechanisms. Testing of this model showed it overpredicted direct droplet production at high wind speeds, a deficiency which has been addressed by more recent studies. Smith et al. (1993) developed a generation function based on two-lognormal modes. Gong et al. (1997a) and Gong et al. (1997b) present a global model of the generation and distribution of sea salt aerosol. Andreas et al. (1995) reviewed and summarized extent production mechanisms. Andreas (1998) contrasted various spume productions parameterizations with theory and modified the best of these into an improved parameterization. Vignati et al. (2001) present a tri-modal lognormal generation function based on open ocean, ship-borne observations.

4.2 Sea Salt Generation

Sea salt aerosol is generated by two fundamentally distinct mechanisms (e.g., Monahan et al., 1986). Wind drag in rough seas detaches droplets directly from the surface. Surface tension prevents wind from directly separating droplets smaller than $D_p \sim 40 \mu\text{m}$ from waves. These

relatively large droplets are called spume and the generation of spume by wind drag is known as the direct mechanism of sea salt generation. Spume generation occurs most readily at the crests of breaking waves where internal forces binding liquid together are overcome by the wind drag acting on the cross-sectional area of the crest water. Thus the direct mechanism is a source exactly at the ocean-atmosphere interface that occurs only during strong wind events, say $U \gtrsim 10 \text{ m s}^{-1}$.

The indirect mechanism of sea salt generation is mediated by air bubbles. Whitecaps form when ocean surface waves break and generate small scale turbulent motions in the surface ocean. The white appearance is caused by air trapped in small bubbles on the surface called foam or by bubbles entirely within the near surface water. When bubbles buoyantly reach the ocean surface and burst their liquid shells explode into film drops. Film drops are typically $0.1 < D < 5 \mu\text{m}$ with a modal size of about $1\text{--}2 \mu\text{m}$. During the subsequent collapse of the bubble, a plume of about $1\text{--}10$ tiny drops known as jet drops may be released into the atmosphere. The surface tension of the bubble contributes to the generation of the jet. Jet drops range in size from $3 < D_p < 100 \mu\text{m}$ with a modal size of about $10 \mu\text{m}$.

A sea salt generation function which represents the indirect mechanism must estimate the fraction of ocean surface which is foam-covered under specified conditions. Whitecap coverage depends on wind speed, stability, temperature, salinity, wind duration, fetch, and surfactant amount.

Monahan et al. (1982) performed tank experiments to deduce the spectral mass flux of sea salt by the indirect mechanism (bubble-bursting). Based on these experiments, Monahan et al. (1986) reported the expression for N_{ss}^{\uparrow} the vertical number flux of sea salt particles entering the atmosphere as a function of 10 m wind speed U_r

$$\frac{\partial N_{\text{ss}}^{\uparrow}}{\partial R_p} \quad [\# \text{ m}^{-2} \text{ s}^{-1} \mu\text{m}^{-1}] = 1.373 U_r^{3.41} R_p^{-3} (1 + 0.057 R_p^{1.05}) 10^{1.19 e^{-B^2}} \quad (4.1a)$$

$$\frac{\partial N_{\text{ss}}^{\uparrow}}{\partial R_p} \quad [\# \text{ m}^{-2} \text{ s}^{-1} \text{ m}^{-1}] = 1.373 U_r^{3.41} \dots \quad (4.1b)$$

where $B = (0.380 - \log R_p)/0.650$. Note that the particle radius R_p in (4.1a) is expressed in microns not meters. The identical expression is re-written in terms of particle diameter D_p in meters in (4.1b).

Monahan et al. (1986) also parameterized the size-dependent vertical number flux of sea salt aerosol due to the direct mechanism F_{ss}

$$\frac{\partial N_{\text{ss}}^{\uparrow}}{\partial R_p} \quad [\# \text{ m}^{-2} \text{ s}^{-1} \mu\text{m}^{-1}] = 8.60 \times 10^{-6} e^{2.08 U_r} R_p^{-2} \quad (4.2a)$$

$$\frac{\partial N_{\text{ss}}^{\uparrow}}{\partial R_p} \quad [\# \text{ m}^{-2} \text{ s}^{-1} \mu\text{m}^{-1}] = 6.45 \times 10^{-4} e^{2.08 U_r} R_p^{-3} e^{-D^2} \quad (4.2b)$$

where $D = 2.18(1.88 - \ln R_p)$. The version of Monahan et al. (1986) shown in Smith et al. (1993) is shown in (4.2b). The version of Monahan et al. (1986) shown in Grini et al. (2002a) is shown in (4.2a). As mentioned above, (4.2) overestimates spume production (Andreas, 1998) and should not be used.

Smith et al. (1993) developed a more accurate (and complicated) parameterization of sea salt formation based on measurements taken on the coast of South Uist Island in the

Outer Hebrides, about 100 km in the North Sea northwest of the Scottish mainland. The measurements comprehensively sampled aerosols in wind speeds of $U \in [0.0, 34.0] \text{ m s}^{-1}$ at a It was found that the number fluxes at a height of about 14 m over the surface were comprised of two log-normal distributions whose mean and geometric standard deviation were insensitive to wind speed. The measurements were made in a range of environmental conditions and the parameterization (4.3) was normalized to predict fluxes of particles whose radii are in equilibrium with a relative humidity of 80%, r_{80} .

$$\frac{\partial N_{\text{ss}}^{\uparrow}}{\partial r_{80}} \quad [\# \text{ m}^{-2} \text{ s}^{-1} \mu\text{m}^{-1}] = \sum_{i=1}^2 A_i \exp \left[-f_i \left(\ln \frac{r_{80}}{r_i} \right)^2 \right] \quad (4.3)$$

where the empirically determined parameters f_1 , f_2 , r_1 , and r_2 are 3.1, 3.3, 2.1 μm , and 9.2 μm , respectively. The f_i and r_i parameters do not depend on wind speed. These field measurements could not distinguish between differing production mechanisms, so (4.3) implicitly accounts for film, jet, and spume mechanisms.

The relative contribution of the two modes, represented by the A_i parameters, strongly depends on wind speed.

$$A_1 = \exp(0.0676U_{14} + 2.43) \quad (4.4a)$$

$$A_2 = \exp(0.959\sqrt{U_{14}} - 1.476) \quad (4.4b)$$

These expressions for A_i were developed for use with wind speeds evaluated at 14 m, U_{14} . They may be re-expressed in terms of the more standard 10 m wind speed U_{10} by using boundary layer theory. Neglecting stability corrections yields (e.g., [Andreas, 1998](#))

$$\begin{aligned} U_{14} &= U_{10} + \frac{u_*}{k} \ln \left(\frac{14}{10} \right) \\ &= U_{10} \left[1 + \frac{\sqrt{C_m^n}}{k} \ln \left(\frac{14}{10} \right) \right] \end{aligned} \quad (4.5)$$

where C_m^n is the neutral exchange coefficient for momentum at 10 m (2.7).

[Andreas \(1998\)](#) presents a thorough comparison of existing spume production parameterizations ([Monahan et al., 1986](#); [Smith et al., 1993](#)) and contrasts these to theoretical models. He identifies important characteristics which accurate parameterizations should contain, and then modifies the spume generation parameterization of [Smith et al. \(1993\)](#) (4.3) to reflect this.

[Andreas \(1998\)](#) argues convincingly that (4.3) underestimates the number of both film drops and spume drops for two reasons. The measurements resulting in (4.3) were probably biased by a number of factors ([Andreas, 1998](#)). First, the measurements were taken from a 10 m tower located on the high-water mark of a gently sloping beach. During high tide the water reached the foot of the tower, but during low tide the water was approximately 300 m away. While the distance from the instruments to the water isolated the measurements from the immediate surf zone, it also meant that particles were subject to several seconds of atmospheric transport before reaching the tower. During this transport, evaporation and gravitational sedimentation remove particles from the marine air and this, argues [Andreas](#),

causes (4.3) to underestimate number fluxes by a factor of about 3.5, an argument not disputed by [Smith et al.](#)

Therefore [Andreas \(1998\)](#) recommend using (4.3) for $r_{80} \in [1, 10] \mu\text{m}$ ($r_0 \in [2, 21] \mu\text{m}$), but multiplying it by 3.5. Presented in terms of radius at point of droplet formation r_0 , the spectral vertical number flux of the modified [Smith et al.](#) generation function is

$$\frac{\partial N_{\text{ss}}^{\uparrow}}{\partial r_0} \quad [\# \text{ m}^{-2} \text{ s}^{-1} \mu\text{m}^{-1}] = 3.5 \frac{\partial N_{\text{ss}}^{\uparrow}}{\partial r_{80}} \frac{dr_{80}}{dr_0} \quad (4.6)$$

The first term on the RHS is evaluated using [Smith et al. \(1993\)](#) (4.3) for $r_{80} \in [1, 10]$, and using simple power laws described below (4.9) for large spume. The relation between sea spray droplet size at formation, r_0 , and the droplet size at relative humidity of 80%, r_{80} , is determined by the hygroscopic growth properties of sea salt. [Smith et al. \(1993\)](#) adopted an equilibrium relative humidity $\text{RH} = 98.3\%$ for the near surface ocean. This is close to the $\text{RH} = 98\%$ used in [Large and Pond \(1981\)](#). Assuming r_0 is in equilibrium with $\text{RH} = 98.3\%$, [Andreas \(1998\)](#) suggest

$$r_{80} = 0.518 r_0^{0.976} \quad (4.7a)$$

$$r_0 = 1.963 r_{80}^{1.0246} \quad (4.7b)$$

Taking the derivative of (4.7) we obtain

$$\frac{dr_{80}}{dr_0} = 0.506 r_0^{-0.024} \quad (4.8a)$$

$$\frac{dr_0}{dr_{80}} = 2.011 r_{80}^{0.0246} \quad (4.8b)$$

which may be used in (4.6).

For larger spume droplets, [Andreas \(1998\)](#) parameterizes droplet concentration data measured within 20 cm of the ocean surface. The parameterization simply scales the number flux with a power of the droplet radius, and there are three different regimes

$$\frac{\partial N_{\text{ss}}^{\uparrow}}{\partial r_{80}} = \begin{cases} C_1 U_{10} r_{80}^{-1} & : r_{80} \in [10, 37.5] \mu\text{m} \\ C_2 U_{10} r_{80}^{-2.8} & : r_{80} \in [37.5, 100] \mu\text{m} \\ C_3 U_{10} r_{80}^{-8.0} & : r_{80} \in [100.0, 250] \mu\text{m} \end{cases} \quad (4.9)$$

The parameters C_1 – C_3 depend only on wind speed. They are evaluated by requiring the modified [Smith et al.](#) distribution (4.6) be continuous with (4.9) at $r_{80} = 10 \mu\text{m}$.

It may be more convenient to forecast $N_{\text{ss}}^{\uparrow}(r_0)$ directly rather than $N_{\text{ss}}^{\uparrow}(r_{80})$. Substituting

(4.7) and (4.8) into (4.9) we obtain N_{ss}^\uparrow in terms of r_0 , and remove the $\text{RH} = 80\%$ assumption

$$\begin{aligned}
\frac{\partial N_{ss}^\uparrow}{\partial r_0} &= 3.5 \frac{\partial N_{ss}^\uparrow}{\partial r_{80}} \frac{dr_{80}}{dr_0} \\
&= \begin{cases} 3.5C_1U_{10}(1.931r_0^{-0.976})(0.506r_0^{-0.024}) & : r_0 \in [20.8, 80.5] \mu\text{m} \\ 3.5C_2U_{10}(6.308r_0^{-2.7328})(0.506r_0^{-0.024}) & : r_0 \in [80.5, 219.8] \mu\text{m} \\ 3.5C_3U_{10}(192.9r_0^{-7.808})(0.506r_0^{-0.024}) & : r_0 \in [219.8, 562.1] \mu\text{m} \end{cases} \\
&= \begin{cases} 3.5C_1U_{10}(0.977r_0^{-1}) & : r_0 \in [20.8, 80.5] \mu\text{m} \\ 3.5C_2U_{10}(3.192r_0^{-2.757}) & : r_0 \in [80.5, 219.8] \mu\text{m} \\ 3.5C_3U_{10}(97.61r_0^{-7.832}) & : r_0 \in [219.8, 562.1] \mu\text{m} \end{cases} \\
&= \begin{cases} 3.4195C_1U_{10}r_0^{-1} & : r_0 \in [20.8, 80.5] \mu\text{m} \\ 11.172C_2U_{10}r_0^{-2.757} & : r_0 \in [80.5, 219.8] \mu\text{m} \\ 341.64C_3U_{10}r_0^{-7.832} & : r_0 \in [219.8, 562.1] \mu\text{m} \end{cases} \quad (4.10)
\end{aligned}$$

For studies which work in terms of particle diameter D_0 rather than radius, we may simplify (4.3) and (4.10). Using $dr_0 = \frac{1}{2}dD_0$, and rewriting r_0^x as $2^{-x}D_0^x$ we obtain

$$\begin{aligned}
\frac{\partial N_{ss}^\uparrow}{\partial D_0} &= \frac{\partial N_{ss}^\uparrow}{\partial r_0} \frac{dr_0}{dD_0} = \frac{1}{2} \frac{\partial N_{ss}^\uparrow}{\partial r_0} \\
&= \begin{cases} & : D_0 \in [20.8, 41.6] \mu\text{m} \\ 3.4195C_1U_{10}D_0^{-1} & : D_0 \in [41.6, 161.0] \mu\text{m} \\ 11.172C_2U_{10}D_0^{-2.757} & : D_0 \in [161.0, 439.6] \mu\text{m} \\ 341.64C_3U_{10}D_0^{-7.832} & : D_0 \in [439.6, 1124.2] \mu\text{m} \end{cases} \quad (4.11)
\end{aligned}$$

According to Grini et al. (2002a), the experiments of (4.1) were also conducted at 80% relative humidity. The particle size in these parameterizations is, therefore, the ambient size of deliquescent sea salt aerosol in equilibrium with $\text{RH} = 80\%$ environment. Consequently the mass flux associated with (4.1) should represent particles whose density is the correct average of the salts and the water.

Vignati et al. (2001) present a tri-modal lognormal generation function based on open ocean, ship-borne observations. These observations show that a fine particle mode ($\tilde{D}_n = 0.4 \mu\text{m}$) is present in the surf zone. Table 4.1 shows the parameters of the tri-modal log-normal number distribution generation function which gives the best fit to the observations. For the three modes the median radii $\tilde{r}_n^i \mu\text{m}$ at 80% relative humidity are $[0.2, 2.0, 12.0]$ and the geometric standard deviations $\sigma_{g,i}$ are $[1.9, 2.0, 3.0]$. The total number flux $N_{ss}^\uparrow \# \text{m}^{-2} \text{s}^{-1} \mu\text{m}^{-1}$ of the tri-modal distribution is

$$\frac{dN_{ss}^\uparrow}{dr_{80}} = \sum_{i=1}^3 \frac{N_0^i}{\sqrt{2\pi} r_{80} \ln \sigma_{g,i}} \exp \left[-\frac{1}{2} \left(\frac{\ln(r_{80}/\tilde{r}_n^i)}{\ln \sigma_{g,i}} \right)^2 \right] \quad (4.12)$$

Table 4.1: Tri-modal Sea Salt Parameters^{ab}

i	N_0^i # cm ⁻³	\tilde{r}_n^i ^c μm	$\sigma_{g,i}$
1	$10^{0.095U_{10}+0.283}$	0.2	1.9
2	$10^{0.0422U_{10}+0.288}$	2.0	2.0
3	$10^{0.069U_{10}-3.5}$	12.0	3.0

^aSource: [Vignati et al. \(2001\)](#), p. 20228.

^bAll parameters are for 80% relative humidity.

^cModal radius \tilde{r}_n^i for RH = 80% and 10 m wind speed U_{10} .

Chapter 5

Dry Deposition

The processes by which aerosols are removed from the atmosphere in the absence of precipitation are collectively termed dry deposition. The dry deposition processes which remove aerosols from the atmosphere to the surface (or canopy) include gravitational sedimentation, inertial impaction, and Brownian diffusion. Dry deposition processes determine the atmospheric residence time of large aerosols. Dry deposition processes are analogous to electrical resistances in that each process is like a path to ground, and the efficiency of each path may be construed as a resistance and included in parallel or series with all other possible routes by which an aerosol may reach the surface.

5.1 Dry Deposition Literature

[Slinn et al. \(1978\)](#) is a review paper on all aspects of air-sea transfer, including wet and dry deposition. [Sehmel \(1980, 1984\)](#) form a comprehensive review of particle and gaseous dry deposition. [Wesely \(1989\)](#) presents a regional scale dry deposition parameterization for gases. [Slinn and Slinn \(1980\)](#) introduced a widely-used two layer model of particulate deposition to water surfaces. [Williams \(1982\)](#) presents a deposition model for water surfaces that explicitly accounts for atmospheric stability and for hygroscopic particle growth in the deposition (quasi-laminar) layer. [Rojas and Grieken \(1993\)](#) perform an inter-model comparison of [Slinn and Slinn \(1980\)](#), [Williams \(1982\)](#), and their own model, a generalization of [Slinn and Slinn \(1980\)](#) that accounts for arbitrary reference heights and stability. [Peters and Eiden \(1992\)](#) derive from first principles a complex model of particle deposition to vegetated surfaces. [Zhang et al. \(2001\)](#) present a size-segregated particle dry deposition scheme with partially addresses underestimates of sub-micron aerosol deposition velocities prevalent in models. [Landing et al. \(1995\)](#) examined dust deposition and mineralogy in Florida from 1992–1994. [Raupach et al. \(2001b\)](#) and [Raupach et al. \(2001a\)](#) derive and present a detailed dry deposition model for particles and apply it to pesticide spray. The articles are notable for their clear statement of physical and mathematical assumptions.

5.2 Deposition Velocity

We make the steady state assumption that the net flux F_d of a species from a reference height z_r to a given surface is related to the concentration of the species $N(z_r)$ by a parameter having units of velocity,

$$F_d = -v_d N \quad (5.1)$$

where v_d (m s^{-1}) is known as the deposition velocity of the species.

The physics of dry deposition are entirely contained in v_d , the rate of removal of the species due to all dry deposition processes. Note that v_d is positive when the net flux is F_d is from the atmosphere to the surface. In the following we assume that there is no upward flux of particles due to dry deposition. This is equivalent to stating that the sticking efficiency (6.13) is zero so that particles which strike the surface remain there. Since the upward or resuspension flux is zero, F_d^m is both the net particle flux and the downward particle flux. For gas phase species, N may be expressed as either a number concentration in $\# \text{ m}^{-3}$ or a mass concentration in kg m^{-3} . The deposition flux F_d is then either a number flux or a mass flux of molecules in $\# \text{ m}^{-2} \text{ s}^{-1}$ or $\text{kg m}^{-2} \text{ s}^{-1}$, respectively.

For aerosol, the deposition velocity is a function of particle diameter so that $v_d = v_d(D)$. The fundamental assumption which defines deposition velocities for aerosols is that turbulent and diffusive processes maintain a constant proportion between the flux of particles of a given size to the surface and the concentration of these particles at a reference height above the surface. The fluxes of interest are the spectral deposition number flux $F_d^n(D)$ ($\# \text{ m}^{-2} \text{ s}^{-1} \text{ m}^{-1}$) and the spectral deposition mass flux $F_d^m(D)$ ($\text{kg m}^{-2} \text{ s}^{-1} \text{ m}^{-1}$).

$$F_d^n(D) = -v_d(D)n_n(D) \quad (5.2)$$

$$\begin{aligned} F_d^m(D) &= -\frac{\pi\rho_p}{6}D_p^3 v_d(D)n_n(D) \\ &= -v_d(D)n_m(D) \end{aligned} \quad (5.3)$$

The deposition velocity is the same for both types of spectral fluxes. Note the similarity between these definitions and the definition of precipitation fluxes in (6.16)–(6.18). Integrating (5.2) over particle size we obtain expression which defines the number mean deposition velocity $\bar{v}_{d,N}$

$$\begin{aligned} \int_0^\infty F_d^n(D) dD &= -\int_0^\infty v_d(D)n_n(D) dD \\ F_d^n &= -\frac{N_0}{N_0} \int_0^\infty v_d(D)n_n(D) dD \\ &= -\bar{v}_{d,N}N_0 \end{aligned} \quad (5.4)$$

The same integration procedure applied to (5.3) leads to

$$F_d^m = -\bar{v}_{d,M}M_0 \quad (5.5)$$

The explicit definitions for the number mean and mass mean deposition velocities in (5.4)

and (5.5) are

$$\bar{v}_{d,N} = \frac{1}{N_0} \int_0^\infty v_d(D) n_n(D) dD \quad (5.6)$$

$$\bar{v}_{d,M} = \frac{1}{M_0} \int_0^\infty v_d(D) n_m(D) dD \quad (5.7)$$

Two experimental methods to determine $v_d(D)$ are wind tunnel and field experiments. Wind tunnel experiments can select particle sizes and thus control $n_n(D)\Delta D$ (or $n_m(D)\Delta D$). Usually $F_d^n(D)\Delta D$ (or $F_d^m(D)\Delta D$) are measured in steady state conditions and $v_d(D)$ is then inferred from a discretized version of (5.7). In field experiments it is often impossible to control particle size so independent measurements of the integrated quantities F_d^n or $F_d^m(D)$ and N_0 or M_0 are made instead. From such measurements only $\bar{v}_{d,N}$ or $\bar{v}_{d,M}$ may be inferred. Additional assumptions or separate measurements of $n_n(D)$ or $n_m(D)$ are required to obtain information about the size dependence $v_d(D)$ from (5.7).

5.3 Dry Deposition Theory

It is reasonable to assume the particle number flux $F_d^n(D)$ is the result of diffusive and gravitational processes acting in parallel. The diffusive transport may be further decomposed into the sum of downgradient turbulent transport and Brownian diffusion. Let the turbulent transport be characterized by an eddy diffusion coefficient ϵ . According to Fick's first law (11.35), the Brownian diffusion is characterized by \mathcal{D}_B (5.39). The spectral number flux (defined to be positive downwards) may then be written as the sum of the diffusive and gravitational components as

$$F_d^n(D) = -(\epsilon + \mathcal{D}_B) \frac{dn_n(D)}{dz} - v_g(D) n_n(D) \quad (5.8)$$

$$F_d^n(D) + v_g(D) n_n(D) = -(\epsilon + \mathcal{D}_B) \frac{dn_n(D)}{dz} \quad (5.9)$$

One may define the non-dimensional length \tilde{z}

$$\begin{aligned} \tilde{z} &= u_* z / \nu \\ z &= \nu \tilde{z} / u_* \end{aligned} \quad (5.10)$$

Since the units of ν are $\text{m}^2 \text{s}^{-1}$ and the dimensions of u_* are m s^{-1} , \tilde{z} is dimensionless. Non-dimensionalizing (5.8) by (5.10) we obtain

$$-\frac{u_*}{F_d^n(D) + v_g(D) n_n(D)} = \frac{\nu}{\epsilon + \mathcal{D}_B} \quad (5.11)$$

Integrating over the particle concentration from the reference height z down to the height of zero particle concentration

$$\begin{aligned} - \int_{N(z)}^{N(\tilde{D})} \frac{u_*}{F_d^n(D) + v_g(D) n_n(D)} dN &= \int_{\tilde{z}}^{\tilde{D}} \frac{\nu}{\epsilon + \mathcal{D}_B} d\tilde{z} \\ &\equiv \text{Int}_1 + \text{Int}_2 + \text{Int}_3 \end{aligned} \quad (5.12)$$

The RHS is a negative-valued resistance integral which quantifies the diffusional resistance between the integration limits.

5.3.1 Sehmel's Experiments

Sehmel and Hodgson (1978a,b) performed wind tunnel experiments over a range of particle sizes $0.03 < D < 29 \mu\text{m}$, surface types (grass, gravel, and water) friction velocities $11\text{--}144 \text{ cm s}^{-1}$, and roughness lengths $0.001 < z_{0,m} < 0.6 \text{ cm}$. The results were used to parameterize the quasi-laminar layer resistance to particle deposition

$$\begin{aligned} \text{Int}_3 = \text{Int}_{1977W} = & -\exp \{ -378.051 + 16.498 \ln \text{Sc} \\ & + \ln \tilde{\tau}_r \left[-11.818 - 0.2863 \ln \tilde{\tau}_r + 0.3226 \ln \left(\frac{D}{z_{0,m}} \right) - 0.3385 \ln \left(\frac{\mathcal{D}_B}{z_{0,m} u_*} \right) \right] \\ & - 12.804 \ln D \} \end{aligned} \quad (5.13)$$

where $\tilde{\tau}_r$ is the dimensionless relaxation timescale

$$\tilde{\tau}_r = \frac{\rho_p D^2 u_*^2}{18 \mu \nu} \quad (5.14)$$

For particles $D \lesssim 0.01 \mu\text{m}$, (5.13) results in surface resistances that are too large, and Sehmel and Hodgson (1978a) recommend using pure Brownian diffusion in the quasi-laminar layer.

5.4 Resistance Method

The three most significant barriers to aerosol dry deposition are aerosol mass, boundary layer stability, and quasi-laminar layer resistance.

$$v_t = \frac{1}{r_a + r_b + r_a r_b v_g} \quad (5.15)$$

There is debate whether the transfer coefficient for aerosol deposition through the turbulent layer follows the aerodynamic resistance to heat transfer or to momentum transfer. Williams (1982) use $r_a = r_h$. Sehmel and Hodgson (1978a), Slinn and Slinn (1980) and derivatives use $r_a = r_m$.

Settling by aerosol due to gravity occurs independently of turbulent mechanisms of dry deposition. Thus v_g is added in parallel to deposition velocity due to turbulent mix-out.

$$\begin{aligned} v_d &= v_t + v_g \\ &= \frac{1}{r_a + r_b + r_a r_b v_g} + v_g \end{aligned} \quad (5.16)$$

$$\equiv r_d^{-1} \quad (5.17)$$

Figure 5.1 shows the simulated dry deposition velocity as a function of aerosol size and surface roughness length. Sehmel and Hodgson (1978a) and Sehmel (1980) predict a stronger

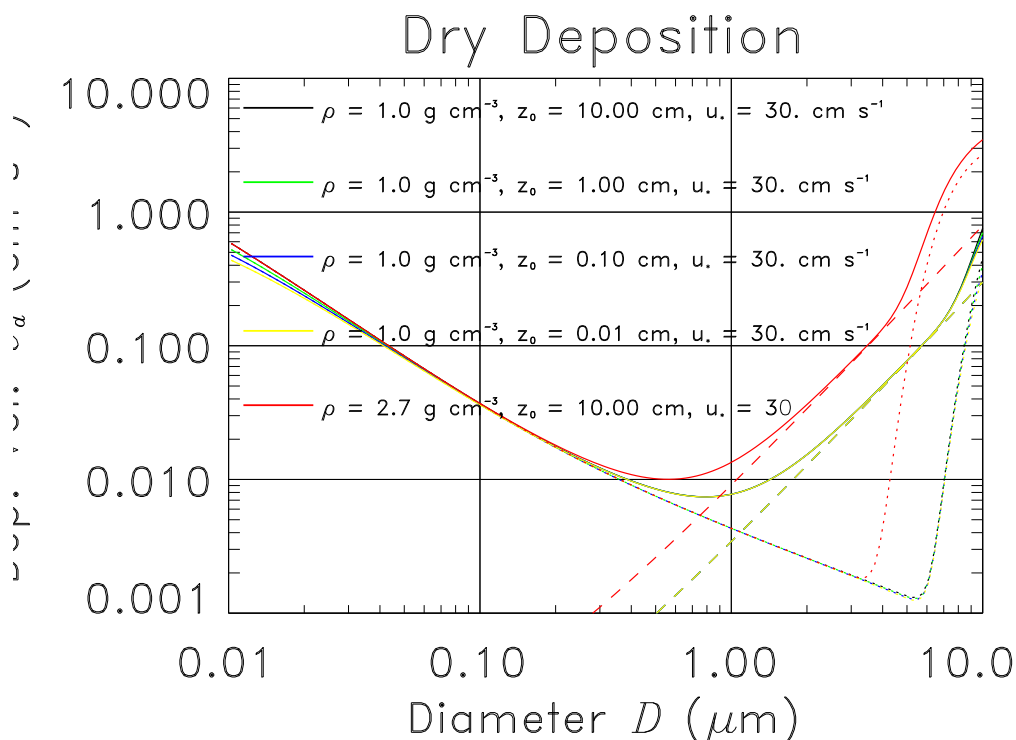


Figure 5.1: Dry deposition velocity v_d (cm s^{-1}) as a function of aerosol size D_p (μm), and surface roughness length $z_{0,m}$ (cm). Shown are the total dry deposition velocity v_d (solid), the gravitational settling velocity v_g (dashed), and the turbulent velocity v_t (dotted).

dependence of v_d on $z_{0,m}$ than is shown in Figure 5.1. The reason for the discrepancy is not yet understood.

Dry deposition of gaseous species requires consideration of an additional term accounting for the so-called canopy resistance r_c . The canopy resistance accounts for the process of gases becoming irreversibly absorbed by plant stomata.

5.4.1 Gravitational Settling

Gravity provides a direct force for moving particles through the turbulent boundary layer, through small scale eddies near the surface, and through the quasi-laminar layer immediately adjacent to the surface. However, gravity is an inefficient removal mechanism for particles smaller than $1 \mu\text{m}$. Our treatment of gravitational settling follows the method of Seinfeld and Pandis (1997).

First, we assume particles are always falling at their steady state gravitational settling velocity v_g . This is the speed at which aerodynamic drag balances gravitational acceleration so that net acceleration is zero. For this reason v_g is called the terminal velocity.

The Stokes' settling velocity u_{St} is the terminal fall speed of particles satisfying two aerodynamic criteria first identified by Stokes. First, the Reynolds number associated with the particle must be less than 0.1. Second, the particle must be large enough so that its slip

correction factor (defined below) is near unity. Under these conditions

$$u_{\text{St}} = \frac{D^2 \rho_p g C_c}{18\mu} \quad (5.18)$$

As a rule of thumb, $u_{\text{St}} = v_g$ for particles in the size range $0.01 < D < 1 \mu\text{m}$.

Very small particles undergo fewer collisions than large particles, and are susceptible to non-continuum or kinetic effects of fluids. These properties combine to define the slip correction factor

$$C_c = 1.0 + \frac{2.0\lambda}{D} \left[1.257 + 0.4 \exp\left(\frac{-1.1D}{2\lambda}\right) \right] \quad (5.19)$$

where λ is the mean free path of air, defined in §11.1.1. Corrections to (5.18) due to C_c exceed 10% for mineral particles smaller than about $1.5 \mu\text{m}$.

The drag coefficient C_D of particles is usually expressed in terms of the Reynolds number Re of the particle motion relative to the medium. Analytic solutions for drag coefficients exist for spherical particles for low Re . For high Re , and for most aspherical shapes, C_D are determined from computer simulations of the unsteady flow fields past the particle (Wang, 2002). For example, Wang (2002) define C_D for cylinders of diameter D as

$$C_D = \frac{D}{\rho_a \bar{v}^2 \alpha} \quad (5.20)$$

where α is one-half of the cross-sectional area of the particle normal to the flow direction, and \bar{v} is the velocity field.

Exact relationships exist for the Stokes regime where $\text{Re} < 0.1$. For $\text{Re} > 0.1$, theory and experiment provide parameterizations which match the available data, but do not always agree with one another. To begin with, Seinfeld and Pandis (1997), p. 463, suggest

$$C_D = \begin{cases} \frac{24}{\text{Re}} & : \quad \text{Re} < 0.1 \\ \frac{24}{\text{Re}} \left[1 + \frac{3\text{Re}}{16} + \frac{9}{160} \text{Re}^2 \ln(2\text{Re}) \right] & : \quad 0.1 \leq \text{Re} < 2 \\ \frac{24}{\text{Re}} (1 + 0.15\text{Re}^{0.687}) & : \quad 2 \leq \text{Re} < 500 \\ 0.44 & : \quad 500 \leq \text{Re} < 2 \times 10^5 \end{cases} \quad (5.21)$$

It can be seen that there are three regimes of Re beyond Stokes flow. In the transition regime, $0.1 < \text{Re} \lesssim 5$, the method of asymptotic expansions provides experimentally confirmed values. In the Turbulent regime, $5 \lesssim \text{Re} \lesssim 500$, a pure parameterization is used. In the Limiting regime, $\text{Re} \gtrsim 500$, C_D approaches a limiting value of 0.44.

In reality, objects encounter a turbulence transition in the limiting regime that causes C_D to decrease with increasing Re . Based on <http://aerodyn.org/Drag/speed-drag.html>, we changed the limiting regime cutoff from $\text{Re} = 2 \times 10^5$ (5.21) to 1×10^5 . Moreover, we

splice a new turbulence transition regime onto (5.21) where C_D decreases linearly with the logarithmic increase in Re according to

$$C_D = \begin{cases} \frac{24}{Re} & : Re < 0.1 \\ \frac{24}{Re} \left[1 + \frac{3Re}{16} + \frac{9}{160} Re^2 \ln(2Re) \right] & : 0.1 \leq Re < 2 \\ \frac{24}{Re} (1 + 0.15Re^{0.687}) & : 2 \leq Re < 500 \\ 0.44 & : 500 \leq Re < 1 \times 10^5 \\ 0.44 - 0.34[\log_{10}(Re) - 5] & : 1 \times 10^5 \leq Re < 1 \times 10^6 \end{cases} \quad (5.22)$$

There are two problems with (5.21). First, the expressions are not smoothly matched at the boundaries. This causes finite C_D jumps between continuously varying particle sizes. For example, when $\rho_p \sim 2.65 \text{ g cm}^{-3}$ (mineral dust), a jump occurs near $D = 80 \mu\text{m}$ because the motion Re suddenly changes from $Re < 2$ to $Re > 2$. This jump nearly doubles sedimentation speed and is very unrealistic. We attempt to solve this problem by blending solutions over limited ranges of Re . The second problem is the accuracy of the expressions in the transition regime. Asymptotic expansions in this regime (Proudman and Pearson, 1957; Chester and Breach, 1969; Pruppacher and Klett, 1978, 1998) show that

$$C_D = \frac{24}{Re} \left[1 + \frac{3Re}{16} + \frac{9}{160} Re^2 \ln(Re/2) + \frac{9}{160} Re^2 \left(\gamma + \frac{5}{3} \ln 2 - \frac{323}{360} \right) + \frac{27}{640} Re^3 \ln(Re/2) \right] \quad (5.23)$$

where $\gamma = 0.577215664$ is Euler's constant. The final term in the Seinfeld and Pandis (1997) expression in the transition regime (5.21) is $\ln(2Re)$ rather than $\ln(Re/2)$ as in (5.23). This appears to be a misprint in Seinfeld and Pandis and the (5.23) form is preferred, regardless of whether the final two terms in (5.23) are employed. Despite its apparent complexity, the fourth term in (5.23) has been verified independently (Pruppacher and Klett, 1998).

The complete solution of the equation of motion for a falling particle does not neglect the non-linear dependence of the drag coefficient on Re . The vertical equation of motion applicable to particles of any size falling in still air is

$$M \frac{dv_z}{dt} = Mg - \frac{\pi C_D \rho D^2 v_z^2}{8 C_c} \quad (5.24)$$

The particle reaches its terminal velocity when the LHS of (5.24) is zero, i.e., when the acceleration vanishes. Solving for v_g in this case yields

$$v_g = \left(\frac{4gDC_c\rho_p}{3C_D\rho} \right)^{1/2} \quad (5.25)$$

We use (5.25) to characterize the size range of particles which are susceptible to long term atmospheric suspension and transport, and the size range of saltators which fall too fast to become suspended.

Note that C_D (5.25) is a function of v_g through (3.15) and (5.21). Thus (5.25) is an implicit equation for v_g . An iterative solution to (5.25) is straightforward but too time consuming for large scale atmospheric models. A reasonable approximation is to define the Stokes correction factor C_{St} as

$$C_{St} = v_g/u_{St} \quad (5.26)$$

The C_{St} correction to (5.18) exceeds 10% for mineral particles larger than about 45 μm .

In the case where the particles are very large, such as falling raindrops, (5.25) simplifies considerably. For $D > 1 \text{ mm}$ we have $\text{Re} > 500$ and thus $C_D = 0.44$ (5.21) and $C_c \approx 1$. Inserting these values in (5.25) we obtain

$$v_g \quad (\text{m s}^{-1}) = 5.45 \left(\frac{D\rho_p}{\rho} \right)^{1/2} \quad (5.27)$$

for very large particles and raindrops. Finally, we may re-express the Reynolds number (3.13), (3.15) of flow around a falling particle explicitly in terms of its terminal velocity as

$$\text{Re} = v_g D / \nu \quad (5.28)$$

5.4.2 Aerodynamics of Aspherical Particles

Most mineral particles are not perfect spheres (Ginoux, 2003). Aspherical particles require modifications to the preceding formulation of kinematic properties, such as the settling speed. First, asphericity alters the drag coefficient which must be known over same range of Re as for spherical particles (5.21) in order to determine fall speeds. Theoretical treatments of the drag coefficient for aspherical particles are few (Abraham, 1970; Boothroyd, 1971; Mitchell, 1996; Ginoux, 2003). The microphysical treatise by Wang (2002) describes the types of analyses brought to bear on these problems with ice crystals. Many of these analyses hold for mineral dust particles as well. Ivanova et al. (2001) present a method for removing number and mass of aspherical ice crystals of various shapes that should be applicable to dust as well. VanCuren and Cahill (2002) describe the trajectory of Asian dust events which reach North America.

Wang (2002) performed ab initio simulations of flow past finite cylinders with aspect ratios satisfying the relations of Auer and Veal (1970). His results show that differences between the infinite and finite cylinder approximations are small for $\text{Re} > 100$. The following parameterization fits his data within a few percent

$$\begin{aligned} \log_{10} C_D &= 2.44389 - 4.21639A - 0.20098A^2 + 2.32216A^3 & : \quad 0.2 < \text{Re} < 1000 \\ \text{where } A &= \frac{\log_{10} \text{Re} + 1.0}{3.60206} \end{aligned} \quad (5.30)$$

Unfortunately, (5.30) was constructed from simulations of cylinders with prescribed aspect ratios typical of ice crystals (Wang, 2002, p. 53). It is desirable to find an analogue to (5.30) which is a function of aspect ratio.

Pitter et al. (1973) computed the drag coefficient of flow past very thin oblate spheroids for low and intermediate Reynolds numbers. Wang (2002) computed the drag coefficient

of flow past hexagonal plates and broad-branched crystals and fit his results to the same functional form as [Pitter et al.](#). For hexagonal plates, the results are

$$C_D = \left(\frac{64}{\pi \text{Re}} \right) (1 + 0.078 \text{Re}^{0.945}) \quad : \quad 0.2 < \text{Re} < 150 \quad (5.31)$$

For broad branch crystals, the results are

$$C_D = \left(\frac{64}{\pi \text{Re}} \right) (1 + 0.142 \text{Re}^{0.887}) \quad : \quad 0.2 < \text{Re} < 150 \quad (5.32)$$

Radiative Effects of Asphericity

[Kalashnikova and Sokolik \(2004\)](#) present a comprehensive analysis of the radiative properties of aspherical mineral dust using a Composition-Shape-Size (CSS) approach based on the Discrete Dipole Approximation (DDA). [Kalashnikova et al. \(2005a\)](#) apply these modeling techniques to dust aerosol retrievals from MISR. [Kalashnikova et al. \(2005c\)](#) document MISR dust retrievals in optically thick dust plumes. [Kalashnikova et al. \(2005b\)](#) show their CSS approach allows MISR retrievals to distinguish natural dust particle shapes and composition.

A number of recent papers are devoted to the effects of mineral dusts (and other aerosols) in determining surface reflectance in deserts and snowpack. [Painter et al. \(2001\)](#) demonstrate the retrieval of snow algal concentrations (based on properties *Chlamydomonas nivalis*) from AVIRIS instrument data. They conclude the visible albedo change due to *C. nivalis* is not significant. [Motoyoshi et al. \(2005\)](#) demonstrate the presence of soot in fresh snow by minimizing model fits to measured reflectances. [Kokhanovsky et al. \(2005\)](#) compare aspherical snow grain models to measured reflectances at high spectral resolution, and demonstrate the feasibility of retrieving snow grain size from such measurements. [Aoki et al. \(2005b\)](#) report high resolution spectral surface albedos over multiple desert surface types in western China including dunes and crusted soils. [Aoki et al. \(2005a\)](#) simulated the aerosol radiative forcing of multi-component dust aerosol over many surface types, and explored the sensitivity of the results to a number of assumptions such as underlying surface albedo, presence of other aerosols, and snowpack. [Krinner et al. \(2006\)](#) predicted that dust-induced snow melt would free Northern Asia of snow during the LGM.

Exact radiative treatments of particle asphericity are often hampered by the large number of computations required (e.g., DDA) the incomplete range of size parameters χ applicable (e.g., Geometric Optics for large χ , and Finite-Difference-Time-Domain (FDTD) for small χ), or the absence of crucial information such as the phase function (ADT).

5.4.3 Volume-to-Surface Techniques

Equal volume-to-surface area (V/S) (sometimes called volume-to-area or V/A) techniques simulate aspherical optical properties using a collection of spheres which preserve desired properties of the aspherical particles ([Grenfell and Warren, 1999](#); [Neshyba et al., 2003](#)). [Grenfell and Warren \(1999\)](#) note that

The use of “equivalent” spheres to represent the scattering and absorption properties of nonspherical particles has been unsatisfactory in the past because the

sphere of equal volume has too little surface area and thus too little scattering, whereas the sphere of equal area has too much volume giving too much absorption.

They suggest representing aspherical particles by distributions of spheres with the same volume-to-surface-area (V/S) ratio as the aspherical particle. They suggest the V/S technique works best for highly complex shapes, such as natural dust particles and ice crystals. The V/S technique requires as many, but no more, computations than the standard Mie theory.

The V/S ratio of a sphere is

$$\begin{aligned}\frac{V_s}{S_s} &= \frac{\frac{4}{3}\pi r^3}{4\pi r^2} \\ &= r/3\end{aligned}\tag{5.33}$$

Based on (5.33), the sphere with the same volume-to-surface ratio as an arbitrarily shaped aspherical particle with volume and surface area S [m²] and V [m³], respectively, must have radius $r_{V/S}$ [m] where

$$r_{V/S} = 3\frac{V}{S}\tag{5.34}$$

The final ingredient necessary to implement the V/S technique is the number $N_{V/S}$ [# m⁻³] of V/S-spheres with the same volume (or area) as the aspherical particles. We establish $N_{V/S}$ by imposing the condition that $N_{V/S}$ spheres with equal V/S ratios as the aspherical particles have the same total volume as N aspherical particles.

$$N_{V/S}V_{V/S} = NV\tag{5.35}$$

$$\begin{aligned}N_{V/S}\frac{4\pi r_{V/S}^3}{3} &= NV \\ \frac{N_{V/S}}{N} &= \frac{3V}{4\pi r_{V/S}^3}\end{aligned}\tag{5.36}$$

We could have imposed the condition of conserving the aspherical surface area instead of volume in (5.34). By construction V/S-spheres will have the correct area because V/S-spheres have, by definition, the correct V/S ratio. Once $N_{V/S}/N$ is known (5.36), we can construct a model population of spheres with the same total volume and surface area as the aspherical particles. What differs between the model population of spheres and the actual population of aspherical particles is the number concentration.

The special cases of $r_{V/S}$ and $N_{V/S}$ for hexagonal prisms are given in Section 18.11.3 in Equations (18.50) and (18.51), respectively.

Neshyba et al. (2003) evaluate the V/S approximation for hexagonal prisms over the range of densities from thin cirrus clouds to thick snowpack. One difficulty in applying the V/S approximation in both clouds and snowpacks is determining the correct V/S ratio. Knowledge of particle shape (e.g., hexagonal crystals) and aspect ratio for all particle sizes is necessary to apply the V/S approximation. While this is helpful in theory, in practice this shape and aspect ratio information is unavailable and difficult to measure.

One alternative is to estimate the bulk V/S ratio (e.g., of the entire cloud or snowpack) rather than the size-specific ratios and work backwards from there. For example, bulk snow mass concentration M_0 [kg m^{-3}] (i.e., density) may be available from model or observations. This may be combined with theoretical or empirical estimates of specific snow surface area $\hat{S} \equiv S_0/M_0$ [$\text{m}^2 \text{kg}^{-1}$] to yield the snow surface area concentration $S_0 = \hat{S}M_0$ [$\text{m}^2 \text{m}^{-3}$]. [Legagneux et al. \(2004\)](#) describe a theory for the time evolution of \hat{S} , and [Cabanès et al. \(2003\)](#) give examples of this function for particular snowpacks.

5.4.4 Large Dust Particles

[Betzer et al. \(1988\)](#) present evidence for particles as large as $75 \mu\text{m}$ reaching Hawaii from Asia. [Ginoux \(2003\)](#) studied the processes contributing to large particle transport.

5.5 Quasi-Laminar Layer Resistance

5.5.1 Stokes Number

Large particles less able to change direction with a boundary layer flow that must veer sharply to avoid obstructions such as roughness elements (plants, trees) and the surface. Instead, the particle's inertia carries it through the quasi-laminar layer, allowing the particle to be deposited on the surface. This dry depositional process is called inertial impaction. The Stokes number St determines the particle susceptibility to inertial impaction. The Stokes number relevant to boundary layer flow depends on the particle size D , particle density ρ , slip correction factor C_c , fluid velocity v_∞ , viscosity μ , and characteristic length scale L .

$$St = \frac{D^2 \rho_p C_c v_\infty}{18 \mu L} \quad (5.37)$$

St is the ratio of the particle stopping distance to the characteristic length of the flow.

It is difficult to apply (5.37) directly in the boundary layer since L and v_∞ have not been characterized yet. Instead, we make the assumptions that ...Then St may be computed as

$$St = \frac{v_g u_*^2}{g \nu} \quad (5.38)$$

Note that (5.38) employs v_g (5.25) rather than u_{St} (5.18).

5.5.2 Brownian Diffusion

Transport through the quasi-laminar layer also depends on the Brownian diffusivity \mathcal{D}_B of the particles. Brownian diffusivity measures the efficiency of particle displacements due to random motion between collisions. This thermally driven motion is isotropic and depends on the temperature of the fluid and the mass of the particle.

$$\mathcal{D}_B = \frac{kTC_c}{3\pi\mu D} \quad (5.39)$$

Without the slip correction factor (5.39) is known as the Stokes-Einstein relation. The displacement of a particle due to Brownian motion may carry the particle across the quasi-laminar layer and deposit it to the surface. It is instructive to compare the diffusivity of aerosols (5.39) to the diffusivity of gases (11.16).

The Schmidt number Sc is the ratio of the kinematic viscosity of the fluid to the Brownian diffusivity of the particle

$$Sc = \nu / \mathcal{D}_B \quad (5.40)$$

Thus Sc is the ratio of two diffusions: the diffusivity of momentum and vorticity ν to the Brownian diffusivity of the particle \mathcal{D}_B (Slinn, 1982).

The two most important processes (besides gravity) for aerosol transport through the quasi-laminar layer are inertial impaction (5.38) and Brownian diffusion (5.40). The total resistance of the quasi-laminar layer to aerosol dry deposition may be approximated as the resistance to these processes acting in parallel

$$r_b = \begin{cases} \frac{1}{u_* (Sc^{-2/3} + 10^{-3/St})} & : \text{ Solid surfaces} \\ \frac{1}{u_* (Sc^{-1/2} + 10^{-3/St})} & : \text{ Liquid surfaces} \end{cases} \quad (5.41)$$

The Schmidt number term in the denominator accounts for Brownian diffusion and is dominant for $D \lesssim 0.7 \mu\text{m}$. The Stokes number term accounts for inertial impaction and becomes important for $D \gtrsim 5 \mu\text{m}$. There is some confusion concerning the dependence of r_b on Sc . The resistance to particle or gaseous diffusion across the quasi-laminar layer to a solid surface is proportional to $Sc^{-2/3}$ (Slinn et al., 1978). This result can be derived by considering viscous flow at high Reynolds number over a fixed, smooth surface. A free surface such as liquid water, however, will tend to slip in the direction of the mean wind so that the characteristic air velocity in the diffusion layer is somewhat larger. According to Slinn and Slinn (1980), the resulting transfer coefficient for particles across the quasi-laminar layer to a free surface (e.g., ocean) is proportional to $Sc^{-1/2}$.

Equation (5.41) neglects the following processes which may contribute to aerosol transport across the quasi-laminar layer: thermophoresis, electrophoresis, and diffusiophoresis¹ (“phoresis” means “force”) (e.g., Slinn et al., 1978; Seinfeld and Pandis, 1997).

¹diffusiophoresis is also known as Stefan flow

Chapter 6

Wet Deposition

Just a box of rain—
Wind and water—
Believe it if you need it,
if you don't just pass it on

Box of Rain
Robert Hunter

This section describes the sink processes which occur in the presence of clouds and precipitation. Due to the problem of unresolved scales and uncertain collision and collection coefficients, representation of wet deposition in large scale atmospheric models is as much art as science. Wet depositional processes have accumulated much redundant terminology. For our purposes, wet deposition refers to (the sum of) all depositional processes by which aerosol are removed from the atmosphere due to physical uptake (collection, precipitation) by cloud or precipitation particles.

The efficacy of various aerosol wet deposition schemes has been tested for the case of ^{210}Pb deposition. ^{222}Rn is continuously emitted from the Earth's continental surfaces at a rate which is fairly well known on large scales, $0.72\text{--}1.2\text{ atom cm}^{-2}\text{ s}^{-1}$ (Guelle et al., 1998). ^{222}Rn has a half-life of 3.8 days and decays to ^{210}Pb with a half-life of 22 years. The ^{210}Pb gas attaches rapidly to ambient aerosol in the accumulation mode.

6.1 Wet Deposition Literature

Removal of accumulation mode ^{210}Pb by dry deposition is inefficient so that removal of atmospheric ^{210}Pb is due to wet deposition to first approximation. Giorgi and Chameides (1986) introduced a first-order loss rate method. Balkanski et al. (1993) apply the method of Giorgi and Chameides (1986) to ^{210}Pb . Guelle et al. (1998) generalize Balkanski et al. (1993) to include size-dependence and evaluate the scheme with ^{210}Pb . Lawrence and Crutzen (1998) show that the gravitational settling of smaller non-precipitating cloud particles may cause a significant downward redistribution of soluble trace gases. Collision or coalescence scavenging mechanisms are thought to be responsible for the incorporation of the dust particles into

raindrops. [Levin et al. \(1990\)](#) reported pH as high as 8.2 in raindrops containing mineral dust.

[Slinn \(1982, 1984\)](#) reviews the measurements and theory of wet and dry deposition and presents a summary of the various dimensionless fluid mechanical quantities which define particle flow. The Peclet number Pe is the ratio of the transport velocity of particles (i.e., v_g for gravitational sedimentation) to their diffusion velocity (\mathcal{D}_B/r).

$$Pe = \nu r / \mathcal{D}_B \quad (6.1)$$

Inserting (5.40) into (6.1) we obtain

$$Pe = ReSc \quad (6.2)$$

Although we shall not, many authors use Pe in place of the product of the $ReSc$ in aerosol kinematics such as (6.4) below.

[Dana and Hales \(1976\)](#) synthesized then available parameterizations of diffusion, impaction, and interception into a numerically tractable definition of the scavenging coefficient. [Nieto et al. \(1994\)](#) performed a sensitivity study of the scavenging coefficient to the formulation of the particle and droplet size distribution and showed that a lognormal distribution of raindrop sizes produce negligible bias compared to other size distributions.

? use SO_2 concentration as a proxy for chemical aging and hygroscopicity of mineral aerosol. Such aging exacerbates nucleation scavenging of dust downwind of polluted regions, and may help explain model underprediction of dust deposition in the northwest Pacific relative to the tropical North Atlantic.

6.2 Collision Processes

The collision efficiency between collector particles (i.e., raindrops) of size D_P and collected particles (i.e., aerosols) of size D_p ¹ is denoted $E(D_P, D_p)$. If aerodynamic interactions between the particles did not occur then $E(D_P, D_p)$ would be unity. Thus $E(D_P, D_p)$ corrects geometric collection volumes for the effects of streamline deformation due to particle-fluid interactions. In practice the processes accounted for by $E(D_P, D_p)$ include Brownian diffusion, interception, and inertial impaction and so we assume

$$E(D_P, D_p) = E_{BD} + E_{NTC} + E_{MPC} \quad (6.3)$$

where E_{BD} , E_{MPC} , and E_{NTC} are the individual collision efficiencies for the processes of Brownian diffusion, interception, and inertial impaction. Processes not typically accounted for include thermophoresis and electrophoresis. We next consider the physical forms of the individual processes.

¹In order to reduce confusion, this chapter uses lowercase D_p to denote the smaller, collected (i.e., aerosol) particle size and uppercase D_P to denote the larger, collector (i.e., raindrop) size. In the rest of this monograph, aerosol particle size is usually indicated simply by D .

6.2.1 Brownian Diffusion

The collision efficiency due to Brownian Diffusion, E_{BD} , accounts for particles “random walking” across streamlines due to thermal motion. Brownian diffusion is primarily important for very small particles, thus E_{BD} dominates $E(D_{\text{P}}, D_{\text{p}})$ for $D_{\text{p}} < 0.2 \mu\text{m}$ (cf. Figure 6.1, below). According to [Slinn \(1984\)](#),

$$E_{\text{BD}} = \frac{4}{\text{ReSc}} [1 + 0.4\text{Re}^{1/2}\text{Sc}^{1/3} + 0.16\text{Re}^{1/2}\text{Sc}^{1/2}] \quad (6.4)$$

The first two terms inside the brackets constitute the particle Sherwood number. The 0.4 coefficient was determined experimentally. Note that Re and Sc in (6.4) refer to different particles: Re is the Reynolds number of the raindrop, but Sc is the Schmidt number of the aerosol.

6.2.2 Interception

The collision efficiency due to interception, E_{NTC} , accounts for particles which follow the streamlines of fluid flow around an approaching raindrop, but whose radius is greater than the distance of the streamline to the raindrop. Thus interception is strictly due to particle size, not mass, and is primarily important for large particles. According to [Slinn \(1984\)](#),

$$E_{\text{NTC}} = 4\tilde{D}[\omega + \tilde{D}(1 + 2\sqrt{\text{Re}})] \quad (6.5)$$

where $\tilde{D} \equiv D_{\text{p}}/D_{\text{P}}$ is the ratio of the collectee to collector sizes. As in (6.4), the Re refers to the raindrop, not to the aerosol. The viscosity ratio, $\omega \equiv \mu_{\text{a}}/\mu_{\text{H}_2\text{O}}$, is the ratio of the dynamic viscosity of the atmosphere to the dynamic viscosity of the fluid in the collector (i.e., liquid water in the case of raindrops). [Slinn \(1982\)](#) uses f , the ratio of the maximum internal circulation speed within the raindrop to the raindrop fall speed, in place of ω in (6.5). Section 10.3.1 of [Pruppacher and Klett \(1998\)](#) contains an extensive discussion of both of these quantities. They suggest an appropriate viscosity ratio for falling raindrops of $\omega \approx 1/55$, and an appropriate velocity ratio $f \approx 1/25$. Interception E_{NTC} dominates $E(D_{\text{P}}, D_{\text{p}})$ for $1 < D_{\text{p}} < 3 \mu\text{m}$ ([Nieto et al., 1994](#)) (cf. Figure 6.1, below).

6.2.3 Inertial Impaction

The collision efficiency due to impaction, E_{MPC} , accounts for particles whose inertia prevents them from following the streamlines of fluid flow around an approaching raindrop. Due to their large size (and Stokes number) and the sharpness of the streamlines, inertia prevents these particles from being pushed out of the trajectory falling raindrops so collisions occur. A more apt description of this process is inertial impaction. Impaction is primarily important for very large particles.

The derivation of E_{MPC} depends on the fluid mechanical concept of potential flow. The relative flow between a raindrop and an aerosol is characterized by the difference in fall velocities, $V_g - v_g$. The Stokes number of the aerosol in this relative flow is

$$\text{St} = \frac{2\tau_{\text{r}}(V_g - v_g)}{D_{\text{P}}} \quad (6.6)$$

where τ_r is the characteristic relaxation timescale of the aerosol

$$\begin{aligned}
 \tau_r &= \frac{MC_c}{3\pi\mu_a D_p} \\
 \tilde{\tau}_r &= \frac{\rho_p D^2 u_*^2}{18\mu_a \nu} \\
 &= \frac{\rho_p D^2 u_*^2}{18\mu_a (\mu_a / \rho_p)} \\
 &= \frac{\rho_p^2 D^2 u_*^2}{18\mu_a^2} \\
 &= \frac{\pi \rho_p D^3}{6} \frac{\rho_p}{\pi D} \frac{u_*^2}{3\mu_a^2} \\
 &= \frac{M \rho_p u_*^2}{3\pi D \mu_a^2} \\
 &= \frac{M}{3\pi\mu_a D_p} \frac{\rho_p u_*^2}{\mu_a} \\
 &= \tau_r \frac{\rho_p u_*^2}{\mu_a} \\
 &= \text{s kg m}^{-3} \text{m}^2 \text{s}^{-2} (\text{kg m}^{-1} \text{s}^{-1})^{-1}
 \end{aligned} \tag{6.7}$$

Since $\rho_p u_*^2 / \mu_a$ has units of s^{-1} , $\tilde{\tau}_r$ is indeed dimensionless. The relaxation timescale is the e -folding time for a particle to approach its terminal velocity starting from a motionless state. τ_r is purely a function of the aerosol particle and the environment. The raindrop properties enter the definition of St by determining the speed of the relative flow, and by determining the characteristic length of the flow. This characteristic length, D_p , which appears in the denominator of (6.6), is the distance the aerosol must be displaced in order to avoid impaction.

A critical Stokes number St^* for this relative flow may be derived for particles directly in the path of the upstream stagnation point of the approaching sphere (raindrop). St^* is the maximum Stokes number of the relative flow a particle can have and not be impacted when it is directly in the path of the approaching sphere. Particles with $St < St^*$ are even less likely to impact in slower, more viscous flows (Slinn, 1982). A combination of numerical simulation and analytic expansion yields

$$St^* = \frac{\frac{12}{10} + \frac{1}{12} \ln(1 + Re)}{1 + \ln Re} \tag{6.9}$$

As before, Re (3.13) refers to the raindrop, not the aerosol.

The critical Stokes numbers for flow near the stagnation point past a sphere, circular cylinder, and disk have been derived analytically as $1/12$, $1/8$, and $\pi/16$, respectively (Slinn, 1982). Thus (6.9) asymptotes to the correct St^* for large Re past a sphere.

According to Slinn (1982), E_{MPC} may be expressed solely in terms of St and St^* as

$$E_{MPC} = \begin{cases} 0 & : St < St^* \\ \left(\frac{\rho_p}{\rho_p}\right)^{1/2} \left(\frac{St - St^*}{St - St^* + \frac{2}{3}}\right)^{3/2} & : St \geq St^* \end{cases} \tag{6.10}$$

The threshold in (6.10) results in a discontinuous transition from a regime of no impaction for $D_p \lesssim 3\mu\text{m}$ to impaction-dominated for $D_p \gtrsim 3\mu\text{m}$. E_{MPC} dominates $E(D_P, D_p)$ for $D_p \gtrsim 3\mu\text{m}$ (cf. Figure 6.1, below). Particle density ρ_p plays a role in the impaction efficiency as $E_{\text{MPC}} \propto \rho_p^{-1/2}$ (6.10). Raindrop density ρ_P plays two roles in the impaction efficiency. First, $E_{\text{MPC}} \propto \sqrt{\rho_P}$. Second, the Reynolds number determines St^* (6.9) and $\text{Re} \propto V_g \propto \sqrt{\rho_P}$ (5.25).

6.3 Collision Efficiency

Summing contributions from these three processes, Brownian diffusion, interception, and impaction, (6.3) becomes

$$\begin{aligned} E(D_P, D_p) = & \frac{4}{\text{ReSc}} [1 + 0.4\text{Re}^{1/2}\text{Sc}^{1/3} + 0.16\text{Re}^{1/2}\text{Sc}^{1/2}] \\ & + 4\tilde{D}[\omega + \tilde{D}(1 + 2\sqrt{\text{Re}})] \\ & + H(\text{St} - \text{St}^*) \left(\frac{\rho_P}{\rho_p} \right)^{1/2} \left(\frac{\text{St} - \text{St}^*}{\text{St} - \text{St}^* + \frac{2}{3}} \right)^{3/2} \end{aligned} \quad (6.11)$$

where $H(x)$ is the Heaviside step function, ρ_P is the density of the precipitation, and ρ_p is the aerosol density. [Slinn \(1982\)](#) cautions that although the processes discussed so far in (6.11) may be reasonably well known (i.e., within a factor of two), other processes (particle growth, thermophoresis and electrophoresis) may cause the actual $E(D_P, D_p)$ to differ from (6.11) by orders of magnitude.

Figure 6.1 shows the simulated collision efficiency $E(D_P, D_p)$ between monodisperse raindrops and an aerosol population. The transition between diffusion and interception regimes occurs near $D_p = 0.6\mu\text{m}$, and the transition between interception and impaction regimes occurs near $D_p = 5.0\mu\text{m}$. [Dana and Hales \(1976\)](#) present simpler, analytically integrable forms of $E(D_P, D_p)$.

The collision efficiency (6.11) embodies an impressive amount of theoretical and empirical physical studies. We shall note some interesting features of the solution. Particle density ρ_p appears directly only in the impaction term. Diffusion and interception are functions of aerosol size (not mass), and of environmental and raindrop properties. Thus aerosols of different compositions are expected to have similar collision efficiencies except in the inertial impaction regime where $E(D_P, D_p) \propto (\rho_P/\rho_p)^{1/2}$.

6.4 Sticking Efficiency

The preceding discussion covers only the geometric and fluid dynamical aspects of particle motion that contribute to particle collision. To compute the actual mass removal rate we must know how often collisions result in collection or retention of the aerosol. Thus we are interested in the sticking efficiency or retention efficiency of interparticle collisions. Sticking efficiency is defined as the fraction of collisions that result in immediate accretion of the collected particle, as opposed to collisions where the particle simply “bounces off” the

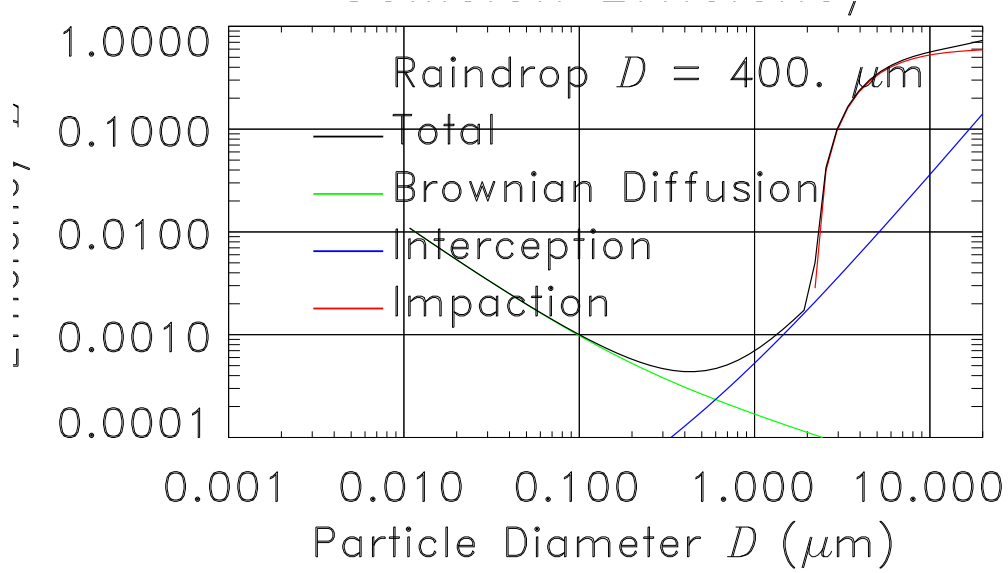


Figure 6.1: Collision efficiency E as a function of aerosol size D_p for monodisperse raindrops.

collector. The collection efficiency $\tilde{E}(D_P, D_p)$ is defined as the sticking efficiency times the collision efficiency

$$\xi = E/\tilde{E} \quad (6.12)$$

$$\tilde{E} = \xi E \quad (6.13)$$

Of course \tilde{E} may depend on many factors besides size, such as composition, charge, and relative humidity.

Submicron particles have surface areas very large relative to their volume (mass). In these conditions molecular forces such as dipole-dipole interactions and van der Waals forces are strong enough that $\xi = 1$ is well-justified particles are always retained after collisions (Slinn, 1982). There are no data suggesting the sticking (retention) efficiency ξ is other than unity for $D \lesssim 20 \mu\text{m}$. Larger particles are less susceptible to Van der Waals forces, and there is evidence that $\xi < 1$ (Slinn, 1982, p. 330), although ξ is still highly species-dependent. Lacking any comprehensive data we shall assume $\xi = 1$ unless otherwise noted.

6.5 Scavenging Efficiency

Having discussed the aerodynamic properties of particle-particle interactions we are now ready to formulate the problem of scavenging of aerosols by raindrops in a form suitable for numerical models. The problem is to determine the rate of removal of aerosols of a given size distribution by a precipitation rate of a given intensity and size distribution. We shall adopt the convention that uppercase symbols refer to the collector species (called “raindrops”) and lowercase symbols refer to the collected species (called “aerosols”).

It will prove useful to derive expressions for the precipitation fluxes in terms of the raindrop size distribution. The rainfall rate P may be expressed in terms of the microphysical distribution of raindrops of size D_P and their fallspeeds, V_g . The spectral precipitation intensity $P_z(D_P)$ ($\text{m}^3 \text{m}^{-2} \text{s}^{-1} \text{m}^{-1}$ or $\text{m s}^{-1} \text{m}^{-1}$) is the convolution of the raindrop volume distribution with the terminal velocity of the raindrops

$$P_z(D_P) = \frac{\pi}{6} V_g D_P^3 N_n(D_P) \quad (6.14)$$

The physical dimensions precipitation intensity can be confusing and require clarification. The spectral volume flux $P_z(D_P)$ ($\text{m}^3 \text{m}^{-2} \text{s}^{-1} \text{m}^{-1}$) is the volume of rain (m^3) falling per unit horizontal area (m^{-2}) per unit time (s^{-1}) per unit raindrop size (m^{-1}). Cancelling spatial dimensions in numerator and denominator leaves the dimensions s^{-1} , which lack any physically intuitive meaning. Canceling like dimensions less assiduously results in $\text{m s}^{-1} \text{m}^{-1}$, which is more easily interpreted as the rate of change of depth of water per unit surface area per unit raindrop size.

Usually P is measured or quoted as a precipitation intensity or precipitation volume flux P_z (m s^{-1}) which is the total rate of increase of liquid water depth in a unit area due to precipitation of all sizes. The total precipitation intensity P_z ($\text{m}^3 \text{m}^{-2} \text{s}^{-1}$ or m s^{-1}) is obtained by $P_z(D_P)$ integrating over all raindrop sizes

$$P_z = \frac{\pi}{6} \int_0^\infty V_g D_P^3 N_n(D_P) dD_P \quad (6.15)$$

To obtain P_z in the more commonly used units of mm hr^{-1} , multiply P_z by $1000 \times 3600 = 3,600,000$. For comparison, typical values of precipitation intensity P_z during drizzle and heavy rain are 0.5 and 25 mm hr^{-1} , respectively.

Precipitation intensity may also be expressed as a mass flux. The spectral precipitation mass flux $P_M(D_P)$ ($\text{kg m}^{-2} \text{s}^{-1} \text{m}^{-1}$) and precipitation mass flux P_M are defined analogously to (6.14) and (6.15), respectively, but with raindrop volume replaced by raindrop mass

$$P_M(D_P) = \frac{\pi \rho_l}{6} V_g D_P^3 N_n(D_P) \quad (6.16)$$

$$P_M = \frac{\pi \rho_l}{6} \int_0^\infty V_g D_P^3 N_n(D_P) dD_P \quad (6.17)$$

$$= P_z \rho_l \quad (6.18)$$

Here we have assumed that the precipitation is liquid water so that the density of the collectors $\rho_P = \rho_l$. In environments where precipitation composed of ice, snow, or other chemical constituents, ρ_l should be replaced by the appropriate density in the definition of $P_M(D_P)$. For the simple case of rain, however, $P_M \approx 1000 P_z$. Thus to convert P_M to P_z in mm hr^{-1} , multiply P_M by 3600 . Although P is relatively easy to measure at the surface, its vertical distribution is not.

Precipitation scavenging of aerosol takes place in the atmosphere below clouds when falling raindrops collide with and collect aerosols. Consider the physics of precipitation scavenging from the point of view of a single rain droplet of diameter D_P falling with speed V_g . During its descent this raindrop sweeps out a volume of $\pi D_P^2 V_g / 4$ per unit time. Any

aerosol partially located in this volume will also be collected, so the geometric collection volume of the raindrop is actually $\pi(D_P + D_p)^2 V_g / 4$ per unit time. Finally, the motion of the aerosol reduces the collection volume V_c ($\text{m}^3 \text{s}^{-1}$) of a raindrop to a cylinder expanding at the speed of the relative motion,

$$V_c = \pi(D_P + D_p)^2 (V_g - v_g) / 4 \quad (6.19)$$

The number of aerosols of size between D_p and $D_p + dD_p$ in a given volume of space is, by definition, $n_n(D_p) dD_p$. The number of aerosol particles a raindrop of size D_P encounters per unit time in its geometric path, \dot{N}_g , is

$$\dot{N}_g(D_P, D_p) = \frac{\pi}{4} (D_P + D_p)^2 (V_g - v_g) n_n(D_p) dD_p \quad (6.20)$$

Assuming a perfect sticking efficiency $\xi = 1$, \dot{N}_g is the rate of aerosol collection ($\# \text{m}^{-3} \text{s}^{-1}$) in the geometric limit. The rate of mass collection ($\text{kg m}^{-3} \text{s}^{-1}$) in the geometric limit would be obtained by simply replacing n_n with n_m in (6.20).

The great complication to the geometric formulation of aerosol number and mass scavenging is due to the aerodynamic interaction of the raindrop and aerosol described above. These interactions were combined into an aerodynamic correction factor called the collision efficiency, $E(D_P, D_p)$. We may now understand $E(D_P, D_p)$ to be the fraction of particles of size D_p contained within the geometric collision volume of raindrops of size D_P (6.20) that are actually encountered. With this aerodynamic correction, the definition of the actual rate of collection of aerosol by a raindrop, \dot{N} , is completed

$$\dot{N}(D_P, D_p) = \frac{\pi}{4} (D_P + D_p)^2 (V_g - v_g) E(D_P, D_p) n_n(D_p) dD_p \quad (6.21)$$

Note that in the following we use $E(D_P, D_p)$ rather than $\tilde{E}(D_P, D_p)$ in conformance with convention. However, if the sticking efficiency $\xi \neq 1$ then E must be replaced with \tilde{E} (6.13).

$\dot{N}(D_P, D_p)$ applies to a single raindrop and aerosol size. The total rate of collection of aerosol particles of size D_p is obtained by integrating (6.21) over the number distribution of the raindrops $N_n(D_P)$,

$$\dot{N}(D_p) = n_n(D_p) dD_p \int_0^\infty \frac{\pi}{4} (D_P + D_p)^2 (V_g - v_g) E(D_P, D_p) N_n(D_P) dD_P \quad (6.22)$$

Fortunately the complexity of (6.22) can be reduced for typical atmospheric conditions. The fall speed of rain ($D_P > 100 \mu\text{m}$) greatly exceeds the fall speed of any long-lived aerosol ($D_p < 20 \mu\text{m}$), so $V_g \gg v_g$ (5.25) and $(D_P + D_p)^2 \approx D_P^2$. These approximations are not necessarily valid for drizzle.

Using these approximations, in conditions of steady precipitation the rates of number and mass removal of aerosol particles of size D_p due to below cloud precipitation scavenging are

$$\begin{aligned} \dot{N}(D_p) &\approx n_n(D_p) dD_p \int_0^\infty \frac{\pi}{4} D_P^2 V_g E(D_P, D_p) N_n(D_P) dD_P \\ \dot{M}(D_p) &\approx n_m(D_p) dD_p \int_0^\infty \frac{\pi}{4} D_P^2 V_g E(D_P, D_p) N_n(D_P) dD_P \end{aligned} \quad (6.23)$$

With the great uncertainties presented above firmly in mind, we are ready to define the scavenging coefficient, Λ as the first order removal rate of aerosol mass and number concentration. Noting that $\dot{N} = dn_n/dt$ and $\dot{M} = dn_m/dt$, (6.23) may be rewritten as first order loss equations in $n_n(D_p)$ and $n_m(D_p)$, respectively

$$\frac{dn_n(D_p)}{dt} = -\Lambda(D_p)n_n(D_p) dD_p \quad (6.24)$$

$$\frac{dn_m(D_p)}{dt} = -\Lambda(D_p)n_m(D_p) dD_p \quad (6.25)$$

where the negative sign indicates removal of aerosol number and mass from the environment and the positive definite scavenging coefficient $\Lambda(D_p)$ (s^{-1}) is

$$\Lambda(D_p) = \int_0^\infty \frac{\pi}{4} (D_P + D_p)^2 (V_g - v_g) E(D_P, D_p) N_n(D_P) dD_P \quad (6.26)$$

$$\approx \int_0^\infty \frac{\pi}{4} D_P^2 V_g E(D_P, D_p) N_n(D_P) dD_P \quad (6.27)$$

Interestingly, $\Lambda(D_p)$ applies to both number and mass concentrations for any aerosol size. One difficulty in parameterizing (6.27) for large scale atmospheric models is that $\Lambda(D_p)$ is very sensitive to the raindrop distribution $N_n(D_P)$.

All the information about the raindrop size and rainfall intensity in $\Lambda(D_p)$ is contained in V_g and $N_n(D_P)$ (6.17). It is useful to recast $\Lambda(D_p)$ explicitly in terms of P , which is often measured (or predicted).

$$\Lambda(D_p) \approx \int_0^\infty \frac{\pi}{4} D_P^2 V_g E(D_P, D_p) N_n(D_P) dD_P \quad (6.28)$$

Suitable approximations for may considerably simplify the problem of parameterizing $\Lambda(D_p)$ in large scale models. Using the approximation for raindrop fall speed V_g (5.27), yields

$$\begin{aligned} \Lambda(D_p) &\approx \int_0^\infty \frac{\pi}{4} 5.45 \left(\frac{D \rho_l}{\rho} \right)^{1/2} D_P^2 E(D_P, D_p) N_n(D_P) dD_P \\ &\approx 4.28 \left(\frac{\rho_l}{\rho} \right)^{1/2} \int_0^\infty D_P^{5/2} E(D_P, D_p) N_n(D_P) dD_P \end{aligned} \quad (6.29)$$

Assuming analytically integrable distributions (e.g., lognormal) for $N_n(D_P)$, the principal difficulty in applying (6.29) is the complicated form of $E(D_P, D_p)$ (6.11).

Solving (6.24)–(6.25) for the time dependent number or mass concentration yields

$$n_n(D_p, t + \Delta t) = n_n(D_p, t) e^{-\Lambda(D_p) \Delta t} \quad (6.30)$$

$$n_m(D_p, t + \Delta t) = n_m(D_p, t) e^{-\Lambda(D_p) \Delta t} \quad (6.31)$$

The e -folding timescale for wet scavenging of particle number and mass is $[\Lambda(D_p)]^{-1}$. Figure 6.2 shows the simulated $\Lambda(D_p)$ for monodisperse raindrops ($D_P = 400 \mu m$) collecting aerosol during a mild precipitation event with intensity $P_z = 1.0 \text{ mm hr}^{-1}$. The disconti-

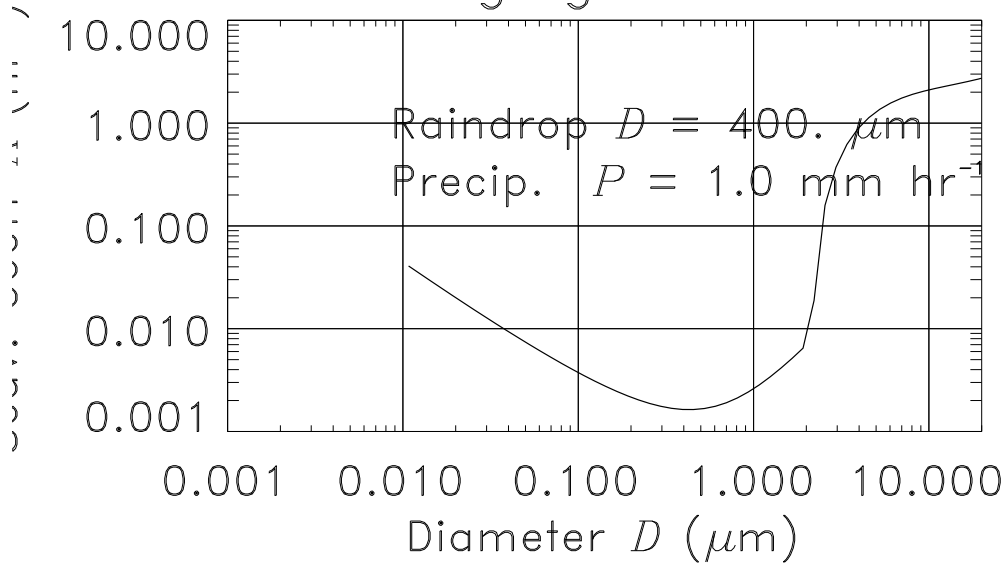


Figure 6.2: Scavenging coefficient $\Lambda \text{ s}^{-1}$ as a function of aerosol size $D_p \mu\text{m}$ for a monodisperse raindrop size.

nuity between the interception and impaction regimes is located at about $D_p = 2 \mu\text{m}$. On either side of this discontinuity removal timescales change from about 1 hr to a few days.

To determine the total removal of aerosol number and size by raindrops, we must integrate the scavenging rate of each aerosol size (6.24)–(6.25) over the aerosol size distribution $n_n(D_p)$

$$\begin{aligned} \frac{dN_p}{dt} &= \frac{d}{dt} \int_0^\infty n_n(D_p) dD_p = - \int_0^\infty \Lambda(D_p) n_n(D_p) dD_p \\ \frac{dM_p}{dt} &= \frac{d}{dt} \int_0^\infty n_m(D_p) dD_p = - \int_0^\infty \Lambda(D_p) n_m(D_p) dD_p \end{aligned} \quad (6.32)$$

Inserting $n_m(D_p) = \frac{\pi}{6} D_p^3 \rho_p n_n(D_p)$ into (6.32) we obtain

$$\begin{aligned} \frac{dM_p}{dt} &= - \int_0^\infty \Lambda(D_p) \frac{\pi}{6} D_p^3 \rho_p n_n(D_p) dD_p \\ &= - \frac{\pi \rho_p}{6} \int_0^\infty \Lambda(D_p) D_p^3 n_n(D_p) dD_p \\ &= - \Lambda_M \frac{\pi \rho_p}{6} \int_0^\infty D_p^3 n_n(D_p) dD_p \\ &= - \Lambda_M M_p \end{aligned} \quad (6.33)$$

where in the third step we removed the explicit dependence on $\Lambda(D_p)$ in the integrand by defining a new, integrated quantity, Λ_M , the mass mean scavenging coefficient:

$$\begin{aligned} \Lambda_M &= \frac{\frac{\pi \rho_p}{6} \int_0^\infty \Lambda(D_p) D_p^3 n_n(D_p) dD_p}{\frac{\pi \rho_p}{6} \int_0^\infty D_p^3 n_n(D_p) dD_p} \\ &= \frac{\int_0^\infty \Lambda(D_p) D_p^3 n_n(D_p) dD_p}{\int_0^\infty D_p^3 n_n(D_p) dD_p} \end{aligned} \quad (6.34)$$

The term mass-weighted scavenging coefficient is a better technical description of Λ_M , but is not widely used. Λ_M , which does not explicitly depend on particle size, is the first order rate coefficient for aerosol mass removal by precipitation. The solution of (6.33) for time dependent aerosol mass concentration is

$$M_p(t) = M_p(t=0)e^{-\Lambda_M t} \quad (6.35)$$

The timescale for mass depletion of the entire aerosol distribution by wet scavenging is thus Λ_M^{-1} .

The number mean scavenging coefficient Λ_N (s^{-1}) is defined by an analogous procedure. Beginning with (6.32) we have

$$\begin{aligned} \frac{dN_p}{dt} &= - \int_0^\infty \Lambda(D_p) n_n(D_p) dD_p \\ &= -\Lambda_N N_p \end{aligned} \quad (6.36)$$

where

$$\begin{aligned} \Lambda_N &= \frac{\int_0^\infty \Lambda(D_p) n_n(D_p) dD_p}{\int_0^\infty n_n(D_p) dD_p} \quad (6.37) \\ &= \frac{\int_0^\infty [\int_0^\infty \frac{\pi}{4} D_P^2 V_g N_n(D_P) E(D_P, D_p) dD_P] n_n(D_p) dD_p}{\int_0^\infty n_n(D_p) dD_p} \\ &= \frac{\frac{2D_P}{3} \frac{\pi}{4} \int_0^\infty [\int_0^\infty D_P^2 V_g N_n(D_P) E(D_P, D_p) dD_P] n_n(D_p) dD_p}{\frac{2D_P}{3} \int_0^\infty n_n(D_p) dD_p} \\ &= \frac{\frac{\pi}{6} \int_0^\infty D_P^3 V_g N_n(D_P) dD_P \int_0^\infty E(D_P, D_p) n_n(D_p) dD_p}{\frac{2D_P}{3} \int_0^\infty n_n(D_p) dD_p} \\ &= \frac{3P_z \int_0^\infty E(D_P, D_p) n_n(D_p) dD_p}{2D_P \int_0^\infty n_n(D_p) dD_p} \quad (6.38) \end{aligned}$$

where we have followed Seinfeld and Pandis (1997) in changing the order of integration to introduce P_z (6.15) into the final expression. This order change is only legal when raindrops are monodisperse because D_P is present in $E(D_P, D_p)$, see, e.g., (6.5). The solution of (6.36) for time dependent aerosol mass concentration is

$$N_p(t) = N_p(t=0)e^{-\Lambda_N t} \quad (6.39)$$

The timescale for number depletion of the entire aerosol distribution by wet scavenging is thus Λ_N^{-1} .

The scavenging efficiency $\eta(D_p)$ (dimensionless) is the fractional change in aerosol number or mass concentration during a time increment Δt . Applying this definition to either time-

dependent concentration (6.30) or (6.31) yields the same result,

$$\begin{aligned}
 \eta(D_p) &= \frac{n_m(D_p, t + \Delta t) - n_m(D_p, t)}{n_m(D_p, t)} \\
 &= \frac{n_m(D_p, t)e^{-\Lambda(D_p)\Delta t} - n_m(D_p, t)}{n_m(D_p, t)} \\
 &= \frac{n_m(D_p, t)(e^{-\Lambda(D_p)\Delta t} - 1)}{n_m(D_p, t)} \\
 &= e^{-\Lambda(D_p)\Delta t} - 1
 \end{aligned} \tag{6.40}$$

Thus $\eta(D_p)$ depends explicitly only on particle size. The sign convention used in (6.40) ensures that $\eta(D_p)$ is negative definite.

The mass mean scavenging efficiency η_M applies to the entire mass distribution. The derivation of η_M is analogous to (6.40), but begins with the time-dependent solution to total aerosol mass concentration (6.35),

$$\begin{aligned}
 \eta_M &= \frac{M_p(t) - M_p(t + \Delta t)}{M_p(t)} \\
 &= \frac{M_p(t) - M_p(t)e^{-\Lambda_M\Delta t}}{M_p(t)} \\
 &= \frac{M_p(t)(1 - e^{-\Lambda_M\Delta t})}{M_p(t)} \\
 &= 1 - e^{-\Lambda_M\Delta t}
 \end{aligned} \tag{6.41}$$

The derivation of the number mean scavenging efficiency η_N proceeds analogously from (6.39) and yields

$$\eta_N = 1 - e^{-\Lambda_N\Delta t} \tag{6.42}$$

Assuming precipitation falls at a uniform rate P during a time period Δt , we may redefine the scavenging efficiency in terms of rainfall depth rather than elapsed time. Let ΔP_z (m) be the depth of precipitation accumulated in time Δt , i.e.,

$$\Delta P_z = P_z \Delta t \tag{6.43}$$

To complement ΔP_z we define precipitation-volume-normalized scavenging coefficients whose dimensions are m^{-1} :

$$\bar{\Lambda}(D_p) = \Lambda(D_p)/P_z \tag{6.44}$$

$$\bar{\Lambda}_M = \Lambda_M/P_z \tag{6.45}$$

$$\bar{\Lambda}_N = \Lambda_N/P_z \tag{6.46}$$

and precipitation-mass-normalized scavenging coefficients whose dimensions are $\text{m}^2 \text{kg}^{-1}$:

$$\bar{\Lambda}(D_p) = \Lambda(D_p)/P_M \tag{6.47}$$

$$\bar{\Lambda}_M = \Lambda_M/P_M \tag{6.48}$$

$$\bar{\Lambda}_N = \Lambda_N/P_M \tag{6.49}$$

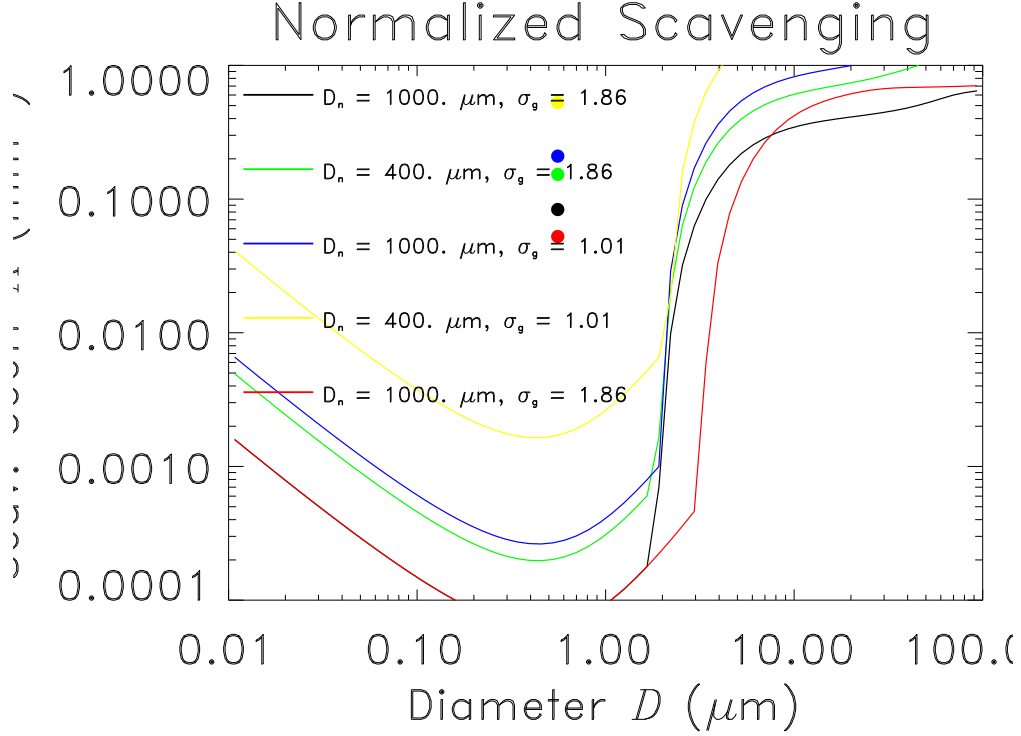


Figure 6.3: Precipitation-normalized scavenging coefficient $\bar{\Lambda} \text{ mm}^{-1}$ (same as $\text{m}^2 \text{ kg}^{-1}$) as a function of aerosol size D_p (μm) for polydisperse lognormal raindrop size distributions. Filled points are mass mean, precipitation-normalized scavenging coefficients computed for a lognormal size distribution typical of far-traveled mineral dust aerosol.

Note that $\bar{\Lambda}$ expressed in mm^{-1} (6.46) is numerically equal to $\bar{\Lambda}$ expressed in $\text{m}^2 \text{ kg}^{-1}$ (6.49) as long as the hydrometeor density is taken to be 1000 kg m^{-3} , which is accurate for rainwater.

Figure 6.3 shows the simulated $\bar{\Lambda}(D_p)$ for various lognormal size distributions of raindrops. The number median raindrop size and geometric standard deviation of lognormal raindrop distributions used to simulate convective and stratiform rain events are $\tilde{D}_{P,n} = 1000 \mu\text{m}$, $\sigma_{g,P} = 1.86$ and $\tilde{D}_{P,n} = 400 \mu\text{m}$, $\sigma_{g,P} = 1.86$, respectively (Nieto et al., 1994). These normalized scavenging coefficients can be scaled to any precipitation flux simply by multiplying by P_M (6.49). Polydisperse raindrops do not greatly reduce the scavenging discontinuity between interception and impaction regimes seen in monodisperse simulations (cf. Figure 6.1). As discussed in §6.3, aerosol density does not play a role in the scavenging efficiency except in the impaction process. Thus Figure 6.3 is virtually identical for all aerosol compositions (i.e., sulfate, dust, carbon, and sea salt) for sizes $D_p \lesssim 2 \mu\text{m}$.

Figure 6.3 also shows that great care must be taken in discretizing the continuous equations of aerosol evolution. If any part of a size bin contains Particles susceptible to inertial impaction ($D_p \gtrsim 2 \mu\text{m}$) should not be placed in the same bin as smaller particles. For instance, if a binning approach is taken and a bin contains any Given the uncertainties involved in predicting or measuring the raindrop size distribution $N_n(D_P)$, Slinn (1984) recommends using the mass-weighted mean raindrop size $D_{P,v}$ to determine the scavenging rates. Mason

(1971) found that the fourth power of $D_{P,v}$ varied linearly with the precipitation intensity:

$$\begin{aligned}
 D_{P,v} \text{ mm} &= 0.70 \text{ mm} \left(\frac{P_z}{1 \text{ mm hr}^{-1}} \right)^{1/4} \\
 D_{P,v} &= 700 \times 10^{-6} (3.6 \times 10^6 P_z)^{1/4} \\
 &= 0.0305 (P_z)^{1/4} \\
 D_{P,v} &= 700 \times 10^{-6} (3.6 \times 10^3 P_M)^{1/4} \\
 &= 5.42 \times 10^{-3} (P_M)^{1/4}
 \end{aligned} \tag{6.50}$$

where all equations except for the first are in SI units. According to (6.50), $D_{P,v} = 700 \mu\text{m}$ when $P_z = 1 \text{ mm hr}^{-1}$.

6.6 Precipitation-Aerosol Interactions

The microphysics of precipitation are simultaneously one of the most important and least understood aspects of the climate system. Precipitation prediction (and, eventually, modification) is the “holy grail” of weather forecasting. Aerosols interact with precipitation formation by serving as additional nucleation sites, and thus adjusting the overall competition for water vapor in the cloud. Hygroscopic dust may serve as CCN, and even hydrophobic dust with appropriate crystal structure may serve as IN. Relatively coarse-sized dust ($D \gtrsim 5 \mu\text{m}$) which nucleate immediately create large cloud droplets. These nuclei are called giant cloud condensation nuclei, or GCCN. [Levin, Zev]Zev Levin finds that about 30 GCCN cm^{-3} are enough to double integrated precipitation in warm clouds. This holds unless IN are present. [Möhler, O.]O. Möhler found that deposition freezing on Saharan dust commences at $1.1 \lesssim \text{RH}_i \lesssim 1.2$. This is far lower than the RH_i required for deposition freezing on carbonaceous or liquid aerosol. DeMott et al. (2003) found in that dust aerosols act as Ice Nuclei more efficiently than any other particles above homogeneous freezing temperatures. They found IN concentrations exceeded 1 cm^{-3} in aerosol layers containing sub-micron dust particles. Sassen et al. (2003) show that dust particles glaciated a supercooled ($-8.8 < T < -5.2^\circ\text{C}$) altocumulus cloud during CRYSTAL-FACE. This causes an indirect effect on climate through cloud structure. Yamagata et al. (2004) found mineral dust aerosol was included in more than 50% of droplets artificially formed in a mineshaft. Dunion and Velden (2004) show that the Saharan Air Layer (SAL), and the dust it often carries, sometimes plays an important role in suppression tropical cyclone activity in the North Atlantic.

6.7 Hygroscopic Growth

Hygroscopic growth of aerosol must be considered in the formulation of precipitation scavenging. Swelling and coating of aerosol can increase the number median diameter \tilde{D}_n of an aerosol distribution by a factor of two or more. This increase in size will change the mean scavenging properties of the aerosol distribution Λ_M . If the aerosol mass is largely contained within the accumulation mode then hygroscopic growth will increase Λ_M . If the aerosol mass

is largely contained in sizes smaller than the accumulation mode then hygroscopic growth could decrease Λ_M .

Chapter 7

Paleoclimate Aerosols

[Adams and Faure \(1995\)](#) and [Crowley \(1995\)](#) present vegetation reconstructions of the LGM climate. [Peltier and Marshall \(1995\)](#) present an energy-balance/ice-sheet model which accounts for dust triggered ice-albedo feedbacks that may play a role in deglaciations. [Overpeck et al. \(1996\)](#) use a modeled dust distribution to show that the longwave radiative effects of dust may have induced significant regional warming during the LGM. [Crowley and Baum \(1997\)](#) study the effects of vegetation on LGM climate (without aerosols). [Ram et al. \(1997\)](#) describe the eleven year cycle of dust found in the Greenland GISP2 ice core. [Andersen et al. \(1998\)](#) describe the behavior of atmospheric dust based on glacial and interglacial records. [Harrison et al. \(2001\)](#) review the role of dust in present day and LGM climate changes. Using extensive records ([Kohfeld and Harrison, 2001](#)) together with models, they predict the impact of dust on future climate. [Robertson et al. \(2001\)](#) assembled hypothesized aerosol and solar forcing time series, including mineral dust, from 1500–present. [Archer et al. \(2000\)](#) [Bopp et al. \(2003\)](#) use a global coupled climate ocean biogeochemistry model constrained by DIRTMAP data to estimate the glacial-interglacial effect of dust-supplied Fe on atmospheric p_{CO_2} is less than 30 ppm. [Claquin et al. \(2003\)](#) model the radiative forcing of dust during the last glacial conditions. [An et al. \(2005\)](#) summarize oceanic and terrestrial sediment records which demonstrate Global Iron Connections (GICs) on multiple timescales over the last 130 kya. The evidence they summarize is consistent with the Iron Hypotheses in all ocean basins except the South Pacific. Using a simple technique they estimate Asian dust is responsible for $\Delta p_{\text{CO}_2} \sim 4\text{--}9$ ppm, or one-tenth to one-third of the total dust effect estimated by [Bopp et al. \(2003\)](#). [Wolff et al. \(2006\)](#) show 750,000m,yr timeseries of natural aerosols from the EPICA ice core of Dome C in Antarctica. [Bigler et al. \(2006\)](#) apportion aerosol in Dome C into continental and sea-salt contributions. [McConnell et al. \(2006\)](#) show that dust deposition to Antarctica from Patagonia over the past few hundred years is highly correlated with Patagonian climate, which includes the signal of global warming.

Chapter 8

Thermodynamics of Gases

8.1 Temperature

The kinetic theory of temperature links relates the macroscopic temperature to statistical properties of the molecular ensemble comprising the parcel. Statistical mechanics (e.g., [Tsonis, 2002](#), p. 8) tells us that the mean kinetic energy of molecules with three spatial degrees of freedom is

$$\left\langle \frac{\bar{M}v^2}{2} \right\rangle = \frac{3}{2}kT \quad (8.1)$$

where k is Boltzmann's constant. Inverting this definition for temperature yields

$$T = \frac{2}{3kT} \left\langle \frac{\bar{M}v^2}{2} \right\rangle \quad (8.2)$$

$$= \frac{1}{3kT} \langle \bar{M}v^2 \rangle \quad (8.3)$$

8.2 Ideal Gas Law

$\tilde{e}_\infty(T)$ is given in Table [14.3](#). The Ideal Gas Law (IGL) has many forms. For purposes of illustration, we take the fundamental IGL form to be in terms of pressure p [Pa], volume V [m³], mole number n [mol], temperature T [K], and universal gas constant R^* [J mol⁻¹ K⁻¹]:

$$pV = nR^*T \quad (8.4)$$

The specific gas constant R [J kg⁻¹ K⁻¹] is the ratio of the universal gas constant to the mean molecular weight \mathcal{M} [kg mol⁻¹] of the gas

$$R \equiv R^*/\mathcal{M} \quad (8.5)$$

We may re-cast the IGL ([8.4](#)) in terms of gas-specific properties using ([8.5](#))

$$\begin{aligned} pV &= n\mathcal{M}RT \\ &= MRT \end{aligned} \quad (8.6)$$

where we have introduced the mass M [kg] of gas

$$M \equiv \mathcal{M}n \quad (8.7)$$

Introducing the specific volume v [m³ kg⁻¹] of gas

$$v \equiv V/M \quad (8.8)$$

leads to

$$pv = RT \quad (8.9)$$

Since the density ρ [kg m⁻³] is v^{-1}

$$p = \rho RT \quad (8.10)$$

The explicit presence of density in the equation of hydrostatic equilibrium (??) makes Equation (8.10) a particularly useful form of the IGL.

8.2.1 Change in Saturation with Temperature

Applying (8.4) to water vapor leads to

$$e = \rho_v R_v T \quad (8.11)$$

$$\rho_v = e/(R_v T) \quad (8.12)$$

$$\rho_{v,s}(T) = \tilde{e}(T)/(R_v T) \quad (8.13)$$

Thus $\rho_{v,s}$, like \tilde{e} , is a function of T only. The rate of change of saturated properties (vapor pressure, density, mixing ratio) with respect to temperature often appears in cloud and aerosol microphysics. Measurements of $d\tilde{e}/dT$ are available in a similar form to \tilde{e} (Table 14.3). These independent measurements result in a parameterization that is slightly different from a direct algebraic derivative of Table 14.3. Most commonly gradients of other saturated properties are expressed in terms of \tilde{e} and $d\tilde{e}/dT$. Differentiating the Ideal Gas Law for vapor (8.12) shows that

$$\begin{aligned} \frac{d\rho_{v,s}}{dT} &= \frac{d}{dT} \frac{\tilde{e}}{R_v T} \\ &= -R_v \tilde{e} + \frac{1}{R_v T} \frac{d\tilde{e}}{dT} \end{aligned} \quad (8.14)$$

Chapter 9

Radiative Properties

The interaction of particles and radiation determines the photochemical and radiative forcing of the particles.

9.1 Radiation Literature Review

[George \(2001\)](#) modeled radiative forcing by dust in the Arabian Sea region and evaluated the predictions against pre-INDOEX measurements. [Myhre et al. \(2003\)](#), [Highwood et al. \(2003\)](#), and [Haywood et al. \(2003\)](#) modeled radiative forcing by North African mineral dust during the Saharan Dust Experiment (SHADE) campaign ([Tanré et al., 2003](#)). [Christopher et al. \(2003\)](#) PRIDE fxm. [Miller et al. \(2004\)](#) examine the surface radiative forcing by dust and its influence on the hydrologic cycle. [Clarke et al. \(2004\)](#) measured the size distribution and analyzed the optical properties of soot-dust mixtures in Asian outflow. [Roush \(2005\)](#) presents the optical constants of montmorillonite, an important constituent of mineral dust. [Roush et al. \(1991\)](#) measure optical constants of kaolinite and montmorillonite. [Querry et al. \(1978\)](#) measure optical constants of limestone, aka amorphous calcite from 0.2–32.8 μm . [Egan and Hilgeman \(1979\)](#) report optical constants of many minerals including montmorillonite, illite, kaolinite, mica, and feldspar. [Long et al. \(1993\)](#) measure optical constants of crystalline and powdered calcite and gypsum from 2.5–300 μm .

9.2 Refractive Indices

The interaction of radiation with matter is characterized by the index of refraction of the material at a give wavelength, $n(\lambda)$. For non-absorbing media, such as air, the index of refraction is real-valued and represents the ratio of the speed of light through a vacuum to the speed of light through the material. For instance, the index of refraction of water is approximately 1.33, thus light propogates through a vacuum about one-third more quickly than through the ocean. In cloud and aerosol physics, however, absorption may not be neglected and the refractive index is best represented by a complex number, where the real part represents scattering and the imaginary part absorption. The nomenclature of refractive indices is quite intricate, since many related properties are also represented by complex numbers and this is not always made clear. Our discussion of refractive indices

adopts the notation of [Bohren and Huffman \(1983\)](#), whose notation is concise yet is not ambiguous.

Refractive indices describe the absorbing and scattering properties of the medium. As such, the refractive index is connected to the dielectric properties of the medium. Plane electromagnetic waves of the form

$$\begin{aligned}\mathbf{E}_c &= \mathbf{E}_0 \exp(i\mathbf{k} \cdot \mathbf{x} - i\omega t) \\ \mathbf{H}_c &= \mathbf{H}_0 \exp(i\mathbf{k} \cdot \mathbf{x} - i\omega t)\end{aligned}\tag{9.1}$$

satisfy Maxwell's equations under certain conditions. Here \mathbf{E}_c and \mathbf{H}_c are complex representations of the electric and magnetic fields, respectively. The actual electric and magnetic fields are the real components of the complex representations, i.e., $\mathbf{E} = \text{Re}(\mathbf{E}_c)$ and $\mathbf{H} = \text{Re}(\mathbf{H}_c)$, respectively. The wavenumber vector \mathbf{k} (m^{-1}) and the angular frequency ω (s^{-1}) define the spatial and temporal scales of the waves. The constant vectors \mathbf{E}_0 and \mathbf{H}_0 determine the amplitude and direction of the field.

When the medium is absorbing, the wavenumber vector is complex

$$\mathbf{k} = \mathbf{k}' + i\mathbf{k}''\tag{9.2}$$

where \mathbf{k}' and \mathbf{k}'' are positive, real vectors. The wave vector of a homogeneous wave may be simplified as

$$\mathbf{k} = (k' + ik'')\hat{\mathbf{e}}\tag{9.3}$$

When (9.2) is substituted into the constitutive relations (e.g., [Bohren and Huffman, 1983](#)), we obtain

$$\begin{aligned}k &= k' + ik'' = \frac{\omega n}{c} \\ n &= \frac{ck}{\omega} \\ &= \frac{c(k' + ik'')}{\omega} \\ &= c\sqrt{\mu\varepsilon} \\ &= \sqrt{\frac{\mu\varepsilon}{\mu_0\varepsilon_0}} \\ &= n_r + in_i\end{aligned}\tag{9.4}$$

where n is the index of refraction. The real and imaginary components of n , n_r and n_i , are positive definite due to the sign conventions chosen in (9.1) and (9.4).

For example, the irradiance of a plane wave passing through an electromagnetic medium is attenuated with the distance z within the medium that the wave has traversed. For a wave of initial irradiance F_0

$$F(z) = F_0 e^{-\alpha z}\tag{9.5}$$

where α is the absorption coefficient and is related to the index of refraction

$$\alpha = \frac{4\pi n_i}{\lambda}\tag{9.6}$$

Complex refractive indices (9.4) are not the only quantities which concisely describe the optical properties of a material. The permittivity ε is usually expressed in terms of the relative permittivity ϵ and the vacuum permittivity ε_0 , also called the permittivity of free space.

$$\varepsilon \equiv \epsilon \varepsilon_0 \quad (9.7)$$

$$\varepsilon_0 \equiv \frac{1}{c^2 \mu_0} \approx 8.8541878176 \times 10^{-12} \quad [\text{F m}^{-1}] \quad (9.8)$$

The vacuum permittivity ε_0 is a fundamental constant with SI units $[\text{F m}^{-1}]$. The relative permittivity ϵ is also called the dielectric function and dielectric constant and is dimensionless.

$$\begin{aligned} \epsilon &= \epsilon' + i\epsilon'' & (9.9) \\ &= n^2 \\ &= (n_r + in_i)^2 \\ &= n_r^2 - n_i^2 + 2n_r n_i i \\ \epsilon' &= \frac{\varepsilon'}{\varepsilon_0} = n_r^2 - n_i^2 \\ \epsilon'' &= \frac{\varepsilon''}{\varepsilon_0} = 2n_r n_i \\ n &= \sqrt{\epsilon} \\ &= \sqrt{\epsilon' + i\epsilon''} \\ n_r &= \sqrt{\frac{\sqrt{\epsilon'^2 + \epsilon''^2} + \epsilon'}{2}} \\ n_i &= \sqrt{\frac{\sqrt{\epsilon'^2 + \epsilon''^2} - \epsilon'}{2}} \end{aligned}$$

The square root in (9.9) with positive n_i conforms with the sign convention made in (9.1) and (9.4).

9.2.1 Reflectance-Based Refractive Indices

Refractive indices may be measured by many techniques, including Kramers-Kronig¹ analysis and dispersive analysis. The dispersive analysis measures the zenith (normal) spectral reflectance of the material, and fits this to a series of independent damped oscillator resonances known as Lorentz lines (Querry et al., 1978; Long et al., 1993)

$$\epsilon = \epsilon_\infty + \sum_{i=1}^{i=N} \frac{S_i}{\tilde{\nu}_{0,i}^2 - \tilde{\nu}^2 - i\gamma_i \tilde{\nu}} \quad (9.10)$$

where the three parameters for each Lorentz line are the line strength S_i , the resonance position $\tilde{\nu}_{0,i}$, and the damping constant γ_i $[\text{cm}^{-1}]$. We write (9.10) in terms of wavenumber

¹Named in honor of Hendrik Kramers and Ralph Kronig.

rather than frequency for consistency with [Querry et al. \(1978\)](#) and [Long et al. \(1993\)](#) who report line parameters in cm^{-1} units.

[Long et al. \(1993\)](#) tabulate a modified line strength A defined by

$$S_i = A_i \tilde{\nu}_{0,i}^2 \quad (9.11)$$

The modified line strengths A are smaller than S and this increases the convergence speed of data-fitting to (9.10).

[Querry et al. \(1978\)](#) report resonance parameters from a dispersive analysis which constructs the dielectric constant as

$$\epsilon = \epsilon_\infty + \sum_{i=1}^{i=N} \frac{4\pi A'_i \tilde{\nu}_{0,i}^2 [\tilde{\nu}_{0,i}^2 - \tilde{\nu}^2 + i\gamma'_i \tilde{\nu}]}{(\tilde{\nu}_{0,i}^2 - \tilde{\nu}^2)^2 + (\gamma'_i \tilde{\nu}_{0,i} \tilde{\nu})^2} \quad (9.12)$$

where A'_i is a line strength and γ'_i is a (dimensionless) damping constant. It is straightforward to verify that (9.12) is equivalent to (9.10) when the following equivalence between the line strength and damping parameter definitions of [Querry et al. \(1978\)](#) and [Long et al. \(1993\)](#)

$$S = A \tilde{\nu}_0^2 = 4\pi A' \tilde{\nu}_0^2 \quad (9.13a)$$

$$A' = S/(4\pi \tilde{\nu}_0^2) = A/(4\pi) \quad (9.13b)$$

$$\gamma = \tilde{\nu}_0 \gamma' \quad (9.13c)$$

$$\gamma' = \gamma/\tilde{\nu}_0 \quad (9.13d)$$

Fresnel's equation determines the normal spectral reflectance R in terms of the refractive index n

$$R = \left| \frac{1 - n}{1 + n} \right|^2 \quad (9.14)$$

$$= \frac{(n_r - 1)^2 + n_i^2}{(n_r + 1)^2 + n_i^2} \quad (9.15)$$

9.3 Effective Medium Approximations

Heterogeneous aerosols are very common in nature. Analytic solutions exist for certain geometries of mixtures, such as concentric spheres ([Bohren and Huffman, 1983](#)). One way to treat the optics of these complex particles is to determine an effective refractive index which implicitly accounts for the fraction and optical properties of each individual component. The search for the best effective refractive index has fostered a variety of approximations known as effective medium approximations (EMAs). The web site [Effective Medium Theories](#) is devoted to EMAs, and is remarkably useful. EMAs include volume-weighting, the Maxwell Garnett approximation ([Garnett, 1904](#)), the Bruggeman approximation ([Bruggeman, 1935](#)), the Hollow Sphere Equivalent ([Bohren and Huffman, 1983](#)), and the extended effective medium approximation ([Videen and Chýlek, 1998](#)). Effective medium approximations all have the virtue of not requiring exact knowledge of the geometries of the multi-component aerosols.

The use of inclusion mass fraction M and inclusion volume fraction V in effective medium approximations varies. If the density of the medium and the inclusion are equal, then M and V may be interchanged in (9.23) and (9.23). In general, V is more appropriate because it is a spatial measure and effective medium approximations are based on approximations to the spatial distribution of radiation. Most authors use V (e.g., [Videen and Chýlek, 1998](#)). However, some authors (e.g., [Bohren and Huffman, 1983](#)) use M . We consistently use V in favor of M .

9.3.1 General Considerations

A two component aerosol is the simplest example of a multi-component aerosol (MCA). An idealized geometry would be a spherical matrix containing a spherical inclusion. The mass M_m , and volume V_m of the matrix component do not depend on the inclusion, though the matrix radius r_m does. The inclusion radius r_n , mass M_n , and volume V_n are completely independent of the matrix. Relations among the radius fraction $r_{n/m}$, mass fraction $M_{n/m}$, and volume fraction $V_{n/m}$ of the inclusion relative to the matrix are

$$V_{n/m} \equiv \frac{V_n}{V_m} = M_{n/m} \frac{\rho_m}{\rho_n} \quad (9.16)$$

$$M_{n/m} \equiv \frac{M_n}{M_m} = V_{n/m} \frac{\rho_n}{\rho_m} \quad (9.17)$$

$$V_{n/m} \equiv \frac{V_n}{V_m} = \frac{r_{n/m}^3}{1 - r_{n/m}^3} \quad (9.18)$$

$$r_{n/m} \equiv \frac{r_n}{r_m} = \left(\frac{V_{n/m}}{V_{n/m} + 1} \right)^{1/3} \quad (9.19)$$

Note that (9.19) applies to the ratios of inclusion to matrix properties (analogous to dry mixing ratios), not inclusions to total properties (analogous to moist mixing ratios).

9.3.2 Hollow Sphere Equivalent

The Hollow Sphere Equivalent approximation ([Bohren and Huffman, 1983](#), p. 149) defines...

9.3.3 Volume-Weighted

The simplest estimate for the multi-component index of refraction is to weight the optical properties of each component by the volume occupied by that component.

$$\bar{n} = \sum_{i=1}^N V_i n_i \quad (9.20)$$

$$\bar{\epsilon} = \sum_{i=1}^N V_i \epsilon_i \quad (9.21)$$

Volume-weighting the refractive indices n (9.20) rather than the electric permittivity ε (9.21) leads to different answers since $\bar{\varepsilon} = \bar{n}^2$ (9.4). Whether (9.20) or (9.21) makes more physical sense or performs better should be investigated.

The volume-weighted approximation is often made for liquid mixtures. However, Section 9.6.1 describes a more accurate treatment, the theory of partial molar refraction.

9.3.4 Maxwell Garnett Approximation

The Maxwell Garnett approximation² (Garnett, 1904) defines an effective dielectric function $\bar{\varepsilon}$ for a medium formed of a background matrix containing random sizes, shapes, orientations, and positions of inclusions of different compositions. The approximation takes a relatively simple form for homogeneous spherical inclusions of any size and position and with the same composition embedded in a matrix of a distinct composition. Let the (complex) dielectric constants of the inclusions and the matrix be ε and ε_m , respectively, and let the total volume fraction of the inclusions be V . Then the Maxwell Garnett approximation for the effective dielectric constant of the two component mixture is

$$\begin{aligned}
 \bar{\varepsilon} &= \varepsilon_m \left[1 + \frac{3V \left(\frac{\varepsilon - \varepsilon_m}{\varepsilon + 2\varepsilon_m} \right)}{1 - V \left(\frac{\varepsilon - \varepsilon_m}{\varepsilon + 2\varepsilon_m} \right)} \right] \\
 &= \varepsilon_m \left[1 + \frac{3V(\varepsilon - \varepsilon_m)}{\varepsilon + 2\varepsilon_m - V(\varepsilon - \varepsilon_m)} \right] \\
 &= \varepsilon_m \left[\frac{\varepsilon + 2\varepsilon_m - V(\varepsilon - \varepsilon_m) + 3V(\varepsilon - \varepsilon_m)}{\varepsilon + 2\varepsilon_m - V(\varepsilon - \varepsilon_m)} \right] \\
 &= \varepsilon_m \left[\frac{\varepsilon + 2\varepsilon_m - V\varepsilon + V\varepsilon_m + 3V\varepsilon - 3V\varepsilon_m}{\varepsilon - V\varepsilon + 2\varepsilon_m + V\varepsilon_m} \right] \\
 &= \varepsilon_m \left[\frac{\varepsilon(1 + 2V) + 2\varepsilon_m(1 - V)}{\varepsilon(1 - V) + \varepsilon_m(2 + V)} \right]
 \end{aligned} \tag{9.22}$$

The original definition, Equation (9.23), although cumbersome, contains the fewest complex arithmetic operations, and is thus most efficiently evaluated.

We use (9.9) to rewrite the Maxwell Garnett approximation (9.23) in terms of refractive indices

$$\bar{n}^2 = n_m^2 \left[\frac{n^2(1 + 2V) + 2n_m^2(1 - V)}{n^2(1 - V) + n_m^2(2 + V)} \right] \tag{9.23}$$

where V is the volume fraction of the inclusion, and n_m and n are the matrix (medium) and inclusion (particle) refractive indices, respectively (Videen and Chýlek, 1998). Equation (9.23) is suitable for evaluation when refractive indices, rather than electrical permittivity, is the independent variable of choice. Equivalently,

$$\bar{n}^2 = n_m^2 \frac{n^2 + 2n_m^2 + 2V(n^2 - n_m^2)}{n^2 + 2n_m^2 - V(n^2 - n_m^2)} \tag{9.24}$$

²The name comes from J. C. Maxwell Garnett (unhyphenated), the theory's originator.

This form may yield greater insight into the relative roles of the the matrix and inclusion in the optical properties, at the expense of a few more complex arithmetic operations.

Although (9.23) has the correct limit as $\varepsilon_m \rightarrow \varepsilon$, it is not symmetric under the exchange of the matrix and the inclusion. This is problematic when it is difficult to determine which component is the matrix and which is the inclusion. Nonetheless, no approximation has been more successful or widely used than (9.23).

The Maxwell Garnett approximation extends to N -component aerosol mixtures where $N > 2$ (Bohren and Huffman, 1983, p. 216). One of the N components must be identified as the matrix; the remaining $N - 1$ components are considered inclusions. Inclusions contribute to the effective permittivity $\bar{\varepsilon}$ according to their volume, permittivity, and geometry:

$$\bar{\varepsilon} = \frac{(1 - V)\varepsilon_m + \sum_{i=1}^{N-1} V_i \beta_i \varepsilon_i}{1 - V + \sum_{i=1}^{N-1} V_i \beta_i} \quad (9.25)$$

where the total volume fraction of inclusions is

$$V \equiv \sum_{i=1}^{N-1} V_i \quad (9.26)$$

The geometrical factor β_i is related to the probability distribution function of the path lengths through the inclusions. The optical average computed by (9.25) is a non-linearly weighted average (rather than a pure volume-weighted average) of the inclusions and the matrix because the matrix occupies a preferred (and asymmetric) position in the geometrical factor β_i .

The geometric factor β reduces to a simple analytic expression for idealized spherical inclusions

$$\beta_i = \frac{3\varepsilon_m}{\varepsilon_i + 2\varepsilon_m} \quad (9.27)$$

Substitution of (9.27) into (9.25) with $N = 2$ leads directly to (9.23).

9.3.5 Bruggeman Approximation

The Bruggeman approximation (Bruggeman, 1935) for the mean dielectric function of a two component mixture is (Bohren and Huffman, 1983)

$$V \frac{\varepsilon - \bar{\varepsilon}}{\varepsilon + 2\bar{\varepsilon}} + (1 - V) \frac{\varepsilon_m - \bar{\varepsilon}}{\varepsilon_m + 2\bar{\varepsilon}} = 0 \quad (9.28)$$

Certain limits of (9.28) must be carefully treated numerically First, (9.28) is indeterminate in the limit as $\varepsilon_m \rightarrow \varepsilon$. In this case, set $\bar{\varepsilon} = \varepsilon = \varepsilon_m$. Second, the limit as $V \rightarrow 0$ may cause difficulty with the quadratic equation numerical solution presented below (cf. (9.29)). In this case, direct substitution of $V = 0$ into (9.28) yields the correct result that $\bar{\varepsilon} \rightarrow \varepsilon_m$.

A prime advantage of (9.28) is its symmetry: $\bar{\varepsilon}$ is invariant under exchange of ε and ε_m . The terminology of “matrix” and “inclusion” is therefore ill-suited for the Bruggeman approximation, since conceptually, a matrix occupies more volume than an inclusion and

therefore has a preferred status. It is more consistent to simply label components by numerical subscripts (e.g., n_1, n_2) in the Bruggeman approximation. However, the very symmetry of the components allows us to continue to use our old terminology with the Bruggeman approximation without fear of applying the matrix or inclusion properties in the wrong slot (since their identities are irrelevant).

This component symmetry of the Bruggeman approximation (9.28) has conceptual advantages over other effective medium approximations (e.g., (9.23)) whenever it is difficult to assign one component the role of the matrix and the other the role of inclusion. However, (9.28) has not been quite as successful at predicting experimental results as the Maxwell Garnett approximation (Bohren and Huffman, 1983, p. 217).

Application of the Bruggeman approximation is more difficult than the Maxwell Garnett theory because of the implicit definition of $\bar{\epsilon}$ in (9.28). Fortunately, straightforward algebraic manipulation reduces the definition to a quadratic polynomial in $\bar{\epsilon}$. Multiplying (9.28) by $\epsilon + 2\bar{\epsilon}$ and then by $\epsilon_m + 2\bar{\epsilon}$ we obtain

$$\begin{aligned}
 V(\epsilon - \bar{\epsilon}) + (1 - V) \frac{(\epsilon_m - \bar{\epsilon})(\epsilon + 2\bar{\epsilon})}{\epsilon_m + 2\bar{\epsilon}} &= 0 \\
 V(\epsilon - \bar{\epsilon})(\epsilon_m + 2\bar{\epsilon}) + (1 - V)(\epsilon_m - \bar{\epsilon})(\epsilon + 2\bar{\epsilon}) &= 0 \\
 V[\epsilon\epsilon_m + (2\epsilon - \epsilon_m)\bar{\epsilon} - 2\bar{\epsilon}^2] + (1 - V)[\epsilon_m\epsilon + (2\epsilon_m - \epsilon)\bar{\epsilon} - 2\bar{\epsilon}^2] &= 0 \\
 (-2V + 2V - 2)\bar{\epsilon}^2 + [V(2\epsilon - \epsilon_m) + (1 - V)(2\epsilon_m - \epsilon)]\bar{\epsilon} + V\epsilon\epsilon_m - V\epsilon\epsilon_m + \epsilon\epsilon_m &= 0 \\
 -2\bar{\epsilon}^2 + [2V\epsilon - V\epsilon_m + 2\epsilon_m - \epsilon - 2V\epsilon_m + V\epsilon]\bar{\epsilon} + \epsilon\epsilon_m &= 0 \\
 -2\bar{\epsilon}^2 + [(3V - 1)\epsilon + (2 - 3V)\epsilon_m]\bar{\epsilon} + \epsilon\epsilon_m &= 0 \\
 2\bar{\epsilon}^2 + [(1 - 3V)\epsilon + (3V - 2)\epsilon_m]\bar{\epsilon} - \epsilon\epsilon_m &= 0 \quad (9.29)
 \end{aligned}$$

This quadratic equation is analytically solvable for $\bar{\epsilon}$. In deciding which of the roots is physical, one must discard roots which make (9.28) indeterminate, i.e., $\bar{\epsilon} \neq -\epsilon/2$ and $\bar{\epsilon} \neq -\epsilon_m/2$. Finally, the square root of $\bar{\epsilon}$ with the positive imaginary component, if any, must be taken to conform with the sign conventions (9.1) and (9.4). In practice, root finding methods (e.g., bracketing) may be preferable when a large number of smoothly varying spectral properties must be solved for.

In terms of refractive indices, the Bruggeman approximation (9.28) is equivalent to

$$V \frac{n^2 - \bar{n}^2}{n^2 + 2\bar{n}^2} + (1 - V) \frac{n_m^2 - \bar{n}^2}{n_m^2 + 2\bar{n}^2} = 0 \quad (9.30)$$

where V is the volume fraction of the inclusion, and n and n_m are the inclusion and matrix refractive indices, respectively. Recall that the Bruggeman approximation is symmetric under interchange of the components, so either component may be labeled the matrix and the other the inclusion. The solution to (9.30) is obtained by substituting (9.9) into (9.29):

$$2\bar{n}^4 + [(1 - 3V)n^2 + (3V - 2)n_m^2]\bar{n}^2 - n^2n_m^2 = 0 \quad (9.31)$$

which is a quadratic equation in \bar{n}^2 . The preceding discussions on physically realistic solutions to (9.29) apply equally to (9.31).

The Bruggeman approximation extends to N -component aerosol mixtures where $N > 2$.

9.3.6 Extended Effective Medium Approximation

The extended effective medium approximation (EEMA) (Videen and Chýlek, 1998) relaxes the assumption (implicit in other effective medium approximations) that the grain sizes are small compared to the wavelength of light. The resulting extended effective refractive index \bar{n} is obtained by iterative solution to

$$\bar{n}_{k+1}^2 = n^2 \frac{A_k(1 - V) + VB_k}{A_k(1 - V) - 2VB_k} \quad (9.32)$$

where \bar{n} is the effective refractive index, n_m is the matrix (medium) refractive index, n is the inclusion refractive index, k denotes the iteration, V is the volume fraction of the inclusion, A_k and B_k are given by

$$A_k = -\frac{12i\pi^2\bar{n}^3}{\lambda^3} \quad (9.33a)$$

$$B_k = \frac{3}{4\pi r^3} \sum_n (2n + 1)[a_n(r, n_m/\bar{n}_k) + b_n(r, n_m/\bar{n}_k)] \quad (9.33b)$$

where r is the inclusion radius, λ is the incident wavelength, and $a_n(r, n)$ and $b_n(r, n)$ are the traditional Mie scattering coefficients.

The most general definition of the size parameter χ is the ratio of particle circumference times real refractive index of the surrounding medium to wavelength

$$\chi = 2\pi r n_r / \lambda \quad (9.34)$$

For particles in air, $n_r \approx 1$ so $\chi \approx 2\pi r / \lambda$. The size parameter χ_p of inclusions in cloud droplets is approximately $n_r \approx 1.33$ times the size parameter χ of the same inclusion in air or in vacuum. Videen and Chýlek (1998) show that the extended effective medium approximation is more accurate than Maxwell Garnett and Bruggeman approximations for inclusion size parameters $\chi_p > 0.5$.

9.4 Refractive Indices of Dust

Laboratory and field measurements of dust refractive properties are reported in Patterson et al. (1977); Volz (1973); Patterson (1981); Bohren and Huffman (1983); Tanré et al. (1988); Sokolik et al. (1993); Hess et al. (1998). Refractive properties of salts (e.g., NaCl, $(\text{NH}_4)_2\text{SO}_4$, NH_4NO_3) are in Volz (1973); Tang and Munkelwitz (1994); Tang (1997). Refractive properties of pure water are reported in Ray (1972); Segelstein (1981); Wieliczka et al. (1989); Pope and Fry (1997) (liquid phase) and Ray (1972); Warren (1984); Perovich and Govoni (1991) (ice phase). Sophisticated models may be used in conjunction with field measurements to constrain optical properties. Multiple studies have used this technique to estimate n_i for dust (Dubovik and King, 2000; Dubovik, 2001; Dubovik et al., 2002a,b; Colarco et al., 2002; Sinyuk et al., 2003; Torres, 2003). Uncertainty in dust optical properties straddles the boundary between dust causing net cooling and net heating of the climate system. This boundary occurs at a single scattering albedo $\varpi \sim 0.91$ (Liao and Seinfeld, 1998b).

The Aerosol Robotic Network, AERONET, for example, retrieves size distributions from multi-spectral solar almucantar radiances (Dubovik and King, 2000). The almucantar radiances are radiance measurements in a circle of equal scattering angle centered in a plane about the Sun, i.e., radiance measurements at known forward scattering phase function angles. Dubovik et al. (2000) quantify the accuracy of the retrievals. Dubovik et al. (2002b) show that spherical particle assumptions bias retrieved dust properties. In particular, Mie theory over-estimates the concentration of small ($D < 0.2 \mu\text{m}$) particles and under-estimates the real refractive index at shorter wavelengths.

At $0.64 \mu\text{m}$, Kaufman et al. (2001) found $\varpi = 0.97 \pm 0.02$ from a combination of satellite measurements and in situ remote sensing from AERONET. This is in contrast to $\varpi = 0.87 \pm 0.04$ typical of earlier studies (Sokolik and Toon, 1996). Colarco et al. (2002) determined the UV imaginary index of refraction n_i of Saharan dust particles from TOMS data using a three-dimensional model of dust transport. At Sal and Tenerife, $n_i = 0.0048(0.0024\text{--}0.0060)$ and $n_i = 0.004(0.002\text{--}0.005)$ at $\lambda = 331$ and 360 nm, respectively. At Dakar, $n_i = 0.006(0.0024\text{--}0.0207)$ and $n_i = 0.005(0.0020\text{--}0.0175)$ at $\lambda = 331$ and 360 nm, respectively. After integrating over the measured size distributions, they obtained single scattering albedos at $\lambda = 331$ nm of $\varpi = 0.81(0.65\text{--}0.90)$, $0.84(0.82\text{--}0.91)$, and $0.86(0.83\text{--}0.89)$ at Dakar, Sal, and Tenerife, respectively.

9.5 Liquid or solid mantle coatings

The problem of determining the optical properties of a coated sphere (or cylinder) has been solved analytically. Naturally, the solutions bear a strong resemblance to Mie theory. Additional features are caused by interference patterns between the reflections of the core and the mantle.

9.6 Homogeneously Mixed Liquids

9.6.1 Partial Molar Refraction

The partial molar refraction approximation assumes that all components are homogeneously mixed in the aerosol. Thus the approach is best-suited to liquid aerosols. The parameterization technique, described and evaluated by Stelson (1990), depends on the observed additivity of a quantity known as the molar refraction R [$\text{m}^3 \text{mol}^{-1}$] of condensed phase species. The molar refraction may be simply defined in terms of the molar volume and the refractive index n as

$$R = \left(\frac{n^2 - 1}{n^2 + 2} \right) \tilde{V} \quad (9.35)$$

where the molar volume \tilde{V} [$\text{m}^3 \text{mol}^{-1}$] is the physical volume occupied by the solution per mole of solution.

$$\tilde{V} = \bar{M}/\rho \quad (9.36)$$

If the ratio of the two quadratic functions of n in (9.35) appears non-intuitive, it is worthwhile to trace its origins because it appears in many optical approximations. The factor $(n^2 - 1)/(n^2 + 2)$ appears in the a_1 coefficient of Mie theory. The a coefficients are defined in terms of spherical Bessel functions, and when the Bessel functions are expanded into power series (e.g., [Bohren and Huffman, 1983](#), p. 131), the dominant term in the a_1 coefficient contains the quadratic factor.

The mean molecular weight of a solution $\bar{\mathcal{M}}$ [kg mol⁻¹] is the sum of the dimensionless volume mixing ratio (i.e., molar fraction) χ_i of each species times its mean molecular weight \mathcal{M}_i .

$$\bar{\mathcal{M}} = \sum_{i=1}^N \chi_i \mathcal{M}_i \quad (9.37)$$

Dividing $\bar{\mathcal{M}}$ by the density of the bulk solution ρ we obtain the bulk molar volume \tilde{V} in m³ mol⁻¹

$$\tilde{V} = \bar{\mathcal{M}}/\rho = \sum_{i=1}^N \chi_i \mathcal{M}_i / \rho \quad (9.38)$$

The molar refraction R (9.35) of a solution is the sum of the partial molar refractions of all the constituent species R_i , weighted by the respective volume mixing ratios χ_i

$$R = \sum_{i=1}^N \chi_i R_i \quad (9.39)$$

To illustrate the usefulness of the partial molar refraction approximation we consider a two component solution. For concreteness, imagine that the first component is liquid water and the second component is NaCl, so that the solution is similar to deliquescent sea salt aerosol (which would also include MgSO₄). The physical properties of the components and of the bulk solution are labeled with and without subscripts, respectively, (e.g., \tilde{V}_1 , \tilde{V}_2 , and \tilde{V}). Using (9.39) and then (9.35) we see that

$$R = \chi_1 R_1 + \chi_2 R_2$$

If we consider the properties of the first component (e.g., pure water) as known, and the properties of the solution are measured, then the molar refraction of the second component (e.g., NaCl) may be inferred as

$$\begin{aligned} R_2 &= \frac{R}{\chi_2} - \frac{\chi_1 R_1}{\chi_2} \\ &= \frac{\tilde{V}}{\chi_2} \left(\frac{n^2 - 1}{n^2 + 2} \right) - \frac{\chi_1 \tilde{V}_1}{\chi_2} \left(\frac{n_1^2 - 1}{n_1^2 + 2} \right) \end{aligned} \quad (9.40)$$

Since all the quantities on the RHS are known, R_2 is determined. [Stelson \(1990\)](#) show that the R_2 determined from (9.40) is generally independent of ionic strength.

In modeling studies, often the mass fractions of the various species are known (or predicted) and it is the mean refractive index of the bulk solution that is of interest. Inverting (9.35) to obtain n in terms of R and \tilde{V} we obtain

$$n = \left(\frac{1 + 2R/\tilde{V}}{1 - R/\tilde{V}} \right)^{1/2} \quad (9.41)$$

Thus the quantity R/\tilde{V} is seen to determine the optical properties of the bulk solution. We may rewrite R/\tilde{V} in terms of the physical volume V [kg m^{-3}] of the bulk solution, and the mass fraction M_i and density ρ_i of each component. Combining (9.38) and (9.39) we obtain

$$\begin{aligned} \frac{R}{\tilde{V}} &= \frac{\sum_{i=1}^N \chi_i R_i}{\sum_{i=1}^N \chi_i \mathcal{M}_i / \rho} \\ &= \end{aligned} \quad (9.42)$$

9.7 Sulfate Aerosols

According to (Kiehl et al., 2000)

$$\frac{\tilde{\psi}_e}{\psi_e} = \exp \left(c_1 + \frac{c_2}{c_3 + \text{RH}} + \frac{c_4}{c_5 + \text{RH}} \right) \quad (9.43)$$

For H_2SO_4 with $\tilde{D}_n = 0.1 \mu\text{m}$ and $\ln \sigma_g = 0.7$, Kiehl et al. (2000) showed $[c_1, \dots, c_5] = [11.24, -0.304, -1.088, -177.6, 15.37]$.

9.8 Radiative Heating of Particles

Due to human influence the fraction of Earth's aerosol composed of absorbing substances, especially carbon, is constantly increasing. It is therefore of interest to quantify the aerosol-induced heating. In highly absorptive atmospheric conditions, it may be possible to use sophisticated instruments to determine aerosol properties such as the single scattering albedo from the measured temperature change resulting from radiant heating.

Net particle heating q_p is the result of latent, sensible, and radiant heating, each a complex microphysical process. Condensation and deposition of vapor to the surface of a particle cause latent heating. Evaporation and sublimation of vapor from the surface of a particle cause latent cooling. Thus latent heating, denoted q_l , requires mass transfer to or from the particle surface. Thermal conductance, that is, the transfer of heat to or from the surface of the particle by molecular diffusion, is called sensible heating and denoted by q_h . Absorption and emission of radiant energy by a particle is called radiant heating, denoted q_r .

$$q_p = q_l + q_h + q_r \quad (9.44)$$

We now briefly digress to discuss the physical units employed in this section. To understand aerosol heating it is convenient to work in terms of power, or energy per unit time.

Thus we shall express q_p , q_l , q_h , and q_r in Js^{-1} or Watts. It is technically correct to say that these q_x measure a heating rate, i.e., the rate at which heat, in any of its forms, is transferred. However, in the literature the terminology “heating rate” is generally used for quantities measured in temperature change per unit time, e.g., Ks^{-1} or Kday^{-1} .

Meteorological models often predict heating rates related, but not identical to q_x . Most often it is the heatings per unit volume, q_x^v , $\text{J m}^{-3} \text{s}^{-1} = \text{W m}^{-3}$, that are available. q^v is the integral of the particle heating weighted by the particle distribution in a unit volume,

$$q^v = \int n_n(D)q(D) dD \quad (9.45)$$

Heatings per unit mass are also used. These are denoted by q_x^m in units of $\text{J kg}^{-1} \text{s}^{-1}$ or W kg^{-1} . The conversion between volumetric and specific heating is $q^v = \rho q^m$ where ρ is the density.

9.8.1 Latent Heating

The heat budget (9.44) of wetted particles is driven by the latent heating which occurs as particles constantly adjust to changing humidity in their environment by seeking a thermodynamically stable size. During the continual processes of condensation and evaporation any net change of mass changes the latent heat stored by the particle so that

$$q_l = l \frac{dM}{dt} \quad (9.46)$$

The rate of diffusional growth of a particle depends on $\Delta\rho_v$, the difference between the vapor density at the surface of the particle, $\rho_{v,r}$ and the vapor density far from the surface, in the surrounding medium, $\rho_{v,\infty}$.

$$\Delta\rho_v = \rho_{v,\infty} - \rho_{v,r} \quad (9.47)$$

The solution to the vapor diffusion equation (see §11.4.2) for a spherical particle yields

$$\frac{dM}{dt} = 4\pi r f_m D_v (\rho_{v,\infty} - \rho_{v,r}) \quad (9.48)$$

where f_m is the mass ventilation coefficient. The mass ventilation coefficient f_m is of order unity and accounts for the alteration of vapor convection and diffusion to the particle due to particle motion. It can be shown that the limiting behavior of f_m is characterized by the dimensionless product $\text{Sc}_v^{1/3} \text{Re}^{1/2}$, where Re is the particle Reynolds number (3.13) and Sc_v is the Schmidt number of vapor in air. Empirical parameterizations (see Pruppacher and Klett, 1998, p. 541) show

$$f_m = \begin{cases} 1 & : \text{Re} \rightarrow 0 \\ 1.0 + 0.108(\text{Sc}_v^{1/3} \text{Re}^{1/2})^2 & : \text{Sc}_v^{1/3} \text{Re}^{1/2} < 1.4 \\ 0.78 + 0.38 \text{Sc}_v^{1/3} \text{Re}^{1/2} & : 1.4 \leq \text{Sc}_v^{1/3} \text{Re}^{1/2} \leq 51.4 \end{cases} \quad (9.49)$$

Thus whether the dependence on $\text{Sc}_v^{1/3} \text{Re}^{1/2}$ is quadratic or linear depends on $\text{Sc}_v^{1/3} \text{Re}^{1/2}$ itself.

By analogy to (5.40) we have

$$\text{Sc}_v = \nu / D_{\text{H}_2\text{O}} \quad (9.50)$$

where ν is the kinematic viscosity of air and $D_{\text{H}_2\text{O}}$, the diffusivity of vapor in air, is given by (11.17).

Combining (9.48) with (9.46) yields

$$q_l = 4\pi r f_m D_v l \Delta \rho_v \quad (9.51)$$

When curvature effects are negligible and the particle is (at least coated with) liquid water, the surface vapor pressure is the saturated vapor pressure over planar surfaces, $\rho_{v,r} = \rho_{v,s}(T_p)$.

The Ideal Gas Law (8.12) states that $\rho_{v,s}(T_p) = \tilde{e}/(R_v T_p)$ so that q_l depends on T_p directly, and implicitly through \tilde{e}_s (14.6). The temperature dependence can be factored out of (9.51) by expressing the vapor density gradient in terms of ΔT

$$\begin{aligned} \rho_{v,\infty} - \rho_{v,r} &= \rho_{v,\infty} - \rho_{v,s}(T_p) \\ &= \rho_{v,s}(T_\infty) - \rho_{v,s}(T_p) + \rho_{v,\infty} - \rho_{v,s}(T_\infty) \\ &= \frac{\rho_{v,s}(T_\infty) - \rho_{v,s}(T_p)}{T_\infty - T_p} \times (T_\infty - T_p) + \rho_{v,\infty} - \rho_{v,s}(T_\infty) \\ &\approx \left(\frac{d\rho_v}{dT} \right)_{\text{sat}} \Delta T + \rho_{v,s}(T_\infty) \left(\frac{\rho_{v,\infty}}{\rho_{v,s}(T_\infty)} - 1 \right) \\ &\approx \left(\frac{d\rho_v}{dT} \right)_{\text{sat}} \Delta T - (1 - \text{RH}_\infty) \rho_{v,s}(T_\infty) \end{aligned} \quad (9.52)$$

where RH_∞ is the relative humidity far from the particle. In the penultimate step we follow Pruppacher and Klett (1998) and assume the vapor density gradient may be approximated by the mean slope of the saturation vapor density curve evaluated somewhere in $T \in [T_p, T_\infty]$. This approximation is valid for the small ΔT typically found in atmospheric particles and it is exact in the limit $\Delta T \rightarrow 0$. The approximation (9.52) allows us to rewrite (9.51) as

$$q_l = 4\pi r f_m D_v \left[\left(\frac{d\rho_v}{dT} \right)_{\text{sat}} l \Delta T - (1 - \text{RH}_\infty) \rho_{v,s}(T_\infty) \right] \quad (9.53)$$

Casting q_l into a form with a linear dependence on ΔT (9.53) plus a constant will prove helpful in solving for ΔT in §9.8.4.

It is important to bear in mind that diffusional growth (9.48) is only one of several limiting growth processes, others being surface- and volume-dependent chemical reactions (Seinfeld and Pandis, 1997, p. 685). However, we shall neglect the effects of chemistry on particle mass and on particle temperature, T_p .

Thermal Conductivity of Snow

The thermal conductivity of snow controls the efficiency of snowpack sensible heat flux. Jordan (1991) uses

$$k_s = k_a + (7.75 \times 10^{-5} \rho_s + 1.105 \times 10^{-6} \rho_s^2)(k_i - k_a) \quad (9.54)$$

where k_s , k_i , and k_a are the thermal conductivity of snow, ice, and air, respectively. The heat capacity of snow is the sum of the heat capacities of its liquid and ice components.

9.8.2 Sensible Heating

Heat diffusion and mass diffusion (§9.8.1) from a particle are exact mathematical analogues of each other. Thus Fick's First Law (11.35) suggests that the rate of sensible heat transfer is proportional to the difference between the surface temperature of the particle, T_p , and the temperature of the surrounding medium, T_∞ .

$$\Delta T = T_\infty - T_p \quad (9.55)$$

The sign convention for ΔT is arbitrary and we chose (9.55) to follow Pruppacher and Klett (1998). Heat flows to the particle when $\Delta T > 0$, from the particle when $\Delta T < 0$. In complete analogy to (9.48), the solution to the heat diffusion equation for a spherical particle is

$$q_h = 4\pi r f_t k_a \Delta T \quad (9.56)$$

where k_a ($\text{W m}^{-1} \text{K}^{-1}$) is the thermal conductivity of dry air (Pruppacher and Klett, 1998, p. 508)

$$k_a = 0.0043794 + 7.12 \times 10^{-5} T \quad (9.57)$$

Related to k_a is the thermal diffusivity of air κ_a ($\text{m}^2 \text{s}^{-1}$) (Pruppacher and Klett, 1998, p. 507)

$$\kappa_a = k_a / (\rho c_p) \quad (9.58)$$

The sign convention in (9.56) ensures that particles get warmer ($q_h > 0$) when $T_\infty > T_p$ and heat is conducted to the particle. Thus q_h (9.56) and q_l (9.53) both depend linearly on ΔT .

The thermal ventilation coefficient f_t is a factor of order unity which accounts for the effects of particle motion on heat conduction. Since heat diffusion and mass diffusion are mathematically analogous, f_t is usually expressed in terms of f_m . To obtain f_t from (9.49), we simply replace the mechanical diffusivity $D_{\text{H}_2\text{O}}$ by the thermal diffusivity of air κ_a (9.58) in (9.50) to obtain a Schmidt number for thermal diffusion Sc_t

$$\text{Sc}_t = \nu / \kappa_a \quad (9.59)$$

Using Sc_t in place of Sc_v (9.49), we obtain

$$f_t = \begin{cases} 1 & : \text{Re} \rightarrow 0 \\ 1.0 + 0.108(\text{Sc}_t^{1/3} \text{Re}^{1/2})^2 & : \text{Sc}_t^{1/3} \text{Re}^{1/2} < 1.4 \\ 0.78 + 0.38 \text{Sc}_t^{1/3} \text{Re}^{1/2} & : 1.4 \leq \text{Sc}_t^{1/3} \text{Re}^{1/2} \leq 51.4 \end{cases} \quad (9.60)$$

Radiant heating q_r is generally of secondary importance for T_a , because $q_r \ll q_l$. When this is the case, the net particle heating is a balance of latent and sensible heat transfer. A growing cloud droplet, for example, condenses more water vapor than it evaporates. The excess latent heat of condensation is ultimately conducted to the atmosphere by thermal diffusion, i.e., sensible heat transfer. The balance of latent and sensible heating is described in many texts (Pruppacher and Klett, 1978, p. 447), (Pruppacher and Klett, 1998, p. 542), (Rogers and Yau, 1994, p. 103).

9.8.3 Radiant Heating

Radiant heating q_r may be very important in the heat balance of dry particles since $q_l \approx 0$, and, as shown below, for particles not in thermal equilibrium. An experimental apparatus may employ powerful radiant heating techniques such as lasers to probe aerosols.

There are many approaches to the problem of determining q_r . Under the assumptions of the Mie approximation, q_r depends on the mean intensity \bar{I}_ν or actinic flux intercepted by the particle and on the surface temperature of the particle T_p but not on the orientation of the particle in space. A particle with equivalent-sphere radius r_s will radiate isotropically and absorb incident radiation as a perfect blackbody modulated by its absorption efficiency Q_a

$$q_r(r_s) = 4\pi \int_0^\infty \pi r_s^2 Q_a(r_s, \lambda) [\bar{I}_\lambda(\lambda) - B_\lambda(T_p, \lambda)] d\lambda \quad (9.61)$$

where B_λ is the Planck function. Thus q_r depends explicitly on T_p through B_λ . If we decompose $\bar{I}_\lambda(\lambda)$ into the sum of a collimated light source of strength $F(\lambda)$ (e.g., the sun) and a mean intensity from the diffuse field (which does not include the collimated source) of strength \bar{I}_λ^D . Then we have

$$\bar{I}_\lambda(\lambda) = F(\lambda) + \bar{I}_\lambda^D(\lambda) \quad (9.62)$$

$$q_r(r_s) = \int_0^\infty \pi r_s^2 Q_a(r_s, \lambda) [F(\lambda) + 4\pi \bar{I}_\lambda^D(\lambda) - 4\pi B_\lambda(T_p, \lambda)] d\lambda \quad (9.63)$$

Thus q_r is itself the net result of radiant heating, caused by F and \bar{I}_λ^D , compensated by radiant cooling, caused by B_λ . Neglecting F for the time being, (9.63) makes clear that the largest radiative contributions to q_r occur where the radiation field is out of thermal equilibrium, i.e., where $\bar{I}_\lambda^D \neq B_\lambda$. At cloud top, for instance, $\bar{I}_\lambda^D \approx \frac{1}{2}B_\lambda$ (Barkstrom, 1978).

We may further simplify (9.63) by considering the case of a spectrally uniform, collimated source, e.g., a laser. In this case $F(\lambda) = F(\lambda_0) \equiv F_0$. We shall assume that the diffuse radiation field is in thermal equilibrium at all wavelengths. Finally we shall drop r_s in favor of r for simplicity, with the understanding r_s should be used in practice, where appropriate. With $\bar{I}_\lambda = B_\lambda$, (9.63) reduces to

$$q_r(r) = \pi r^2 F_0 Q_a(r, \lambda_0) \quad (9.64)$$

The validity of the assumption of thermal equilibrium depends on the application, but we note that radiant cooling must become significant when $T_p \gg T_\infty$.

9.8.4 Particle Temperature Evolution

Substituting (9.51), (9.56), and (9.61) into (9.44) we obtain

$$q_p = 4\pi r f_m D_v l \Delta\rho_v + 4\pi r f_t k_a \Delta T + q_r \quad (9.65)$$

The heat gained or lost by the particle when $q_p \neq 0$ (9.44) causes T_p to change. The heating will thus cause ΔT to change at a rate proportional the particle mass M and the

specific heat at constant pressure c_p of the particle

$$\begin{aligned} q_p &= M c_p \frac{dT_p}{dt} \\ &= -M c_p \frac{d\Delta T}{dt} \end{aligned} \quad (9.66)$$

where $d\Delta T = -dT_p$ has been substituted from (9.55) under the assumption that T_∞ is fixed.

Setting (9.65) equal to (9.66) we obtain

$$\begin{aligned} -M c_p \frac{d\Delta T}{dt} &= 4\pi r f_m D_v l \Delta \rho_v + 4\pi r f_t k_a \Delta T + q_r \\ \frac{d\Delta T}{dt} &= -\frac{4\pi r f_m D_v l}{M c_p} \Delta \rho_v - \frac{4\pi r f_t k_a}{M c_p} \Delta T - \frac{q_r}{M c_p} \\ &= -\frac{4\pi r (f_m D_v l \Delta \rho_v + f_t k_a \Delta T)}{M c_p} - \frac{q_r}{M c_p} \\ &= -\frac{3(f_m D_v l \Delta \rho_v + f_t k_a \Delta T)}{r^2 \rho_p c_p} - \frac{q_r}{M c_p} \end{aligned} \quad (9.67)$$

The RHS of (9.67) implicitly depends on ΔT both through $\Delta \rho_v$ (9.52) and through q_r (9.61). To solve (9.67) analytically, we introduce the approximation for $\Delta \rho_v$ (9.52) into (9.67)

$$\frac{d\Delta T}{dt} = -\frac{3[f_m D_v l \left(\frac{d\rho_v}{dT}\right)_{\text{sat}} + f_t k_a]}{r^2 \rho_p c_p} \Delta T + \frac{3f_m D_v l (1 - \text{RH}_\infty) \rho_{v,s}(T_\infty)}{r^2 \rho_p c_p} - \frac{q_r}{M c_p} \quad (9.68)$$

For dry particles, which cannot participate in latent heating, all factors containing l are zero and we obtain the much simpler relation

$$\frac{d\Delta T}{dt} = -\frac{3f_m D_v l f_t k_a}{r^2 \rho_p c_p} \Delta T - \frac{q_r}{M c_p} \quad (9.69)$$

The two terms on the RHS represent sensible and radiative heat transfer, respectively.

For the time being we shall neglect the dependence of q_r on ΔT and treat (9.68) as a linear, first order differential equation for ΔT

$$\begin{aligned} \frac{d\Delta T}{dt} + A \Delta T &= B \quad \text{where} \\ A &= \frac{3[f_m D_v l \left(\frac{d\rho_v}{dT}\right)_{\text{sat}} + f_t k_a]}{r^2 \rho_p c_p} \\ &= \frac{4\pi r [f_m D_v l \left(\frac{d\rho_v}{dT}\right)_{\text{sat}} + f_t k_a]}{M c_p} \\ B &= \frac{3f_m D_v l (1 - \text{RH}_\infty) \rho_{v,s}(T_\infty)}{r^2 \rho_p c_p} - \frac{q_r}{M c_p} \end{aligned} \quad (9.70)$$

The A term and the B term are independent, but $B - A$ is positive when the particle is losing mass, and negative when the particle is gaining mass.

The solution to (9.71) may be obtained by multiplying each side by the integrating factor e^{At} . Then the LHS side becomes is the perfect differential of $e^{At}\Delta T$ and the RHS may be integrated by standard techniques. The constant of integration is identified by imposing the temperature gradient initial condition $\Delta T(t=0) = T_\infty - T_p(t=0) \equiv \Delta_0 T$. The result is

$$\begin{aligned}\Delta T(t) &= \frac{B}{A} + \left(\Delta_0 T - \frac{B}{A} \right) e^{-At} \\ &= \Delta_0 T e^{-At} + \frac{B}{A} (1 - e^{-At})\end{aligned}\quad (9.71)$$

It is instructive to examine the limiting cases of (9.71). As $t \rightarrow \infty$, $\Delta T \rightarrow B/A$. Thus the particle asymptotes to a steady state temperature difference with the environment given by B/A .

Inserting (9.71) into (9.71) yields

$$\frac{B}{A} = \frac{f_m D_v l (1 - RH_\infty) \rho_{v,s}(T_\infty)}{f_m D_v l \left(\frac{d\rho_v}{dT} \right)_{\text{sat}} + f_t k_a} - \frac{q_r}{4\pi r [f_m D_v l \left(\frac{d\rho_v}{dT} \right)_{\text{sat}} + f_t k_a]} \quad (9.72)$$

The relaxation (e-folding) time for the particle-environment heating gradient to reach steady state in this (simplified) scenario is $\tau_h = A^{-1}$.

$$\begin{aligned}\Delta T(t) &= \frac{B}{A} + \left(\Delta_0 T - \frac{B}{A} \right) e^{-t/\tau_h} \\ \tau_h &= \frac{r^2 \rho_p c_p}{3[f_m D_v l \left(\frac{d\rho_v}{dT} \right)_{\text{sat}} + f_t k_a]} \\ &= \frac{M c_p}{4\pi r [f_m D_v l \left(\frac{d\rho_v}{dT} \right)_{\text{sat}} + f_t k_a]}\end{aligned}\quad (9.73)$$

τ_h is also called the adaptation timescale. In the absence of latent heating processes, ΔT and τ_h depend only on conduction and radiant heating. Thus the heating balance for dry particles (9.73) reduces to

$$\begin{aligned}\Delta T(t) &= \frac{B}{A} + \left(\Delta_0 T - \frac{B}{A} \right) e^{-t/\tau_h} \\ \tau_h &= \frac{r^2 \rho_p c_p}{3f_t k_a} \\ &= \frac{M c_p}{4\pi r f_t k_a}\end{aligned}\quad (9.74)$$

$$Q_s = Q_a / (1 - \varpi) \quad (9.75)$$

9.8.5 Temperature Adjustment

Chapter 10

Gas Phase Chemistry

Mineral dust aerosol affects atmospheric chemistry through both heterogeneous and photochemical processes. Heterogeneous chemistry includes reactions occurring on the surface of mineral aerosol. Mineral dust affects atmospheric photochemistry by scattering and absorbing sunlight and thus altering the actinic flux field. Through these mechanisms, mineral dust may significantly alter tropospheric concentrations of S(IV), NO_y, O₃, and OH.

10.1 Literature Review

[Brimblecombe \(1996\)](#) is a good introductory treatment of air composition and chemistry. [Calvert et al. \(1985\)](#) examined mechanisms of HNO₃ and H₂O₂ formation in the troposphere. [Chameides and Davis \(1982\)](#) examined the effect of free radicals on the composition of cloud water and rain. [Chameides and Stelson \(1992\)](#) showed that the atmospheric cycles of sulfur and sea salt aerosol are coupled. [Graedel et al. \(1986\)](#) showed that transition metals can alter cloud droplet chemical compositions. [Graedel and Goldberg \(1983\)](#) present a detailed model of raindrop chemistry. [Hedin and Likens \(1996\)](#) discussed the role of atmospheric dust in the acid rain problem. The absorption cross sections and quantum yields of the most important photochemical paths in atmospheric chemistry are summarized every few years in [DeMore et al. \(1997\)](#). [Klippel and Warneck \(1980\)](#) discuss the formaldehyde content of atmospheric aerosol. [Leighton et al. \(1996\)](#) develop and validate a three dimensional cloud chemistry model. Chemistry in a rainband has been simulated by [Barth et al. \(1992\)](#); [Barth \(1994\)](#); [Leighton et al. \(1990\)](#) [Pandis et al. \(1995\)](#) present a thorough overview of the dynamics of tropospheric aerosols. [Pilinis and Li \(1998\)](#) discuss the effects of particle shape and internal inhomogeneity on radiative forcing. [Solomon et al. \(1996\)](#) examined the role of natural aerosol variations in anthropogenic ozone depletion. [Müller and Brasseur \(1995\)](#) describe the development and validation of the global chemical transport model IMAGES. [Brasseur et al. \(1998\)](#) describe the development and validation of the global chemical transport model MOZART. Column, in situ, and episodic aerosol radiative forcing has been studied by many authors (e.g., [Jayaraman et al., 1998](#); [Liao and Seinfeld, 1998b](#); [Pan et al., 1998](#); [Stenchikov et al., 1998](#)). Aerosol forcing of climate has been studied by many authors (e.g., [Kiehl and Briegleb, 1993](#); [Koloutsou-Vakakis and Rood, 1998](#); [Tegen et al., 1996](#); [Miller and Tegen, 1998a,b](#); [Shay-El et al., 1998](#); [Alpert et al., 1998](#); [Boucher, 1995](#); [Charlson and Wigley, 1994](#);

d’Almeida et al., 1991; Haywood and Ramaswamy, 1998; Liao and Seinfeld, 1998a; Schult et al., 1997; Tegen et al., 1997; Wong et al., 1998). Global sulfur aerosol distributions have been studied by many authors (e.g., Rasch et al., 2000; Barth et al., 2000; d’Almeida et al., 1991; Tegen et al., 1997).

10.2 Oxidation States

The oxidation state of an atom measures its valence, and thus its reactivity, in a substance. The oxidation state of an atom in a pure element is zero (e.g., Ar). An ion is a compound whose net charge is not zero. In a monatomic ion the charge and the oxidation state are the same. For example, both the oxidation state and charge of H^+ are +1. For homonuclear compounds formed by covalent bonds (e.g., N_2 , O_2), the electrons are split evenly between the atoms. For heteronuclear compounds formed by covalent bonds, the electrons are captured by the elements with the stronger attraction. For example, oxygen has a greater attraction for electrons than hydrogen, and strips the electrons from the hydrogen. In H_2O therefore, the oxidation state of hydrogen is +1 and that of the oxygen is -2 (each hydrogen lost its electron to the oxygen). In non-metallic covalent compounds, hydrogen always loses its electrons to other atoms and is assigned an oxidation state of +1.

Oxygen is nearly always assigned an oxidation state of -2 in covalent compounds, e.g., SO_2 , NO_2 , CO_2 . One exception is for peroxides, e.g., H_2O_2 , where oxygen has an oxidation state of -1 . The total number of electrons is conserved so that, for an electrically neutral structure, the sum of the oxidation states equals zero. For example, HNO_3 has oxidation states of hydrogen, nitrogen, and oxygen of +1, +5, and -2 , respectively. The sum of the oxidation states is $1 \times (1) + 1 \times (5) + 3 \times (-2) = 0$. For an ion, the sum of the oxidation states equals the total charge of the ion. For example, the sulfate ion SO_4^{2-} has oxidation states of sulfur and oxygen of +6 and -2 , respectively. The sum of the oxidation states is $1 \times (+6) + 4 \times (-2) = -2$.

In the atmospheric literature, oxidation states are usually expressed as Roman numerals. Thus the oxidation states of sulfur and oxygen in SO_4^{2-} are written as +VI and $-II$, respectively. Often, the oxidation state of a compound determines its reactivity, and thus is a good predictor of its atmospheric residence time. For example, most anthropogenic sulfur is emitted to the atmosphere as SO_2 , which is an S(IV) compound. Through various oxidation reactions, S(IV) is usually transformed to S(VI), which is highly stable. For sulfur, the solubility of the compound increases with oxidation, so that S(VI) compounds are highly soluble. As a result, much of the S(VI) in the atmosphere is in the form of particles or droplets and its residence time is determined by dry and wet deposition processes.

Table 10.1 lists the members of important families of atmospheric chemicals.

Table 10.2 lists the oxidation states of important atmospheric sulfur compounds.

Table 10.3 lists the oxidation states of important atmospheric nitrogen compounds.

Table 10.1: Constituents of Important Families of Atmospheric Compounds^a

Family	Name	Members
CCl _y	Organic chlorine	CFCl ₃ (CFC-11) + CF ₂ Cl ₂ (CFC-12) + CFCl ₂ CF ₂ Cl + (CFC-113) + CCl ₄ + CF ₂ HCl + CH ₃ Cl
CFCs	Chlorofluorocarbons	CFC-11, CFC-12, CFC-113, CFC-114, CFC-115
ClO _x	Oxides of chlorine	ClO
Cl _y	Inorganic chlorine	Cl + 2Cl ₂ + ClO + OClO + 2Cl ₂ O ₂ + HOCl + HCl + BrCl + ClONO ₂
HCFCs	Hydrochlorofluorocarbons	HCFC-22, HCFC-123, HCFC-124
HFCs	Hydrofluorocarbons	
HO _x	Hydrogen radicals	H, OH, HO ₂
NO _x	Oxides of nitrogen	NO, NO ₂
NO _x	Odd nitrogen family	N + NO + NO ₂ + NO ₃ + 2 × N ₂ O ₅ + HO ₂ NO ₂
NO _y	Reactive odd nitrogen	NO _x + N ₂ O ₅ , HNO ₃ , NO ₃ , HNO ₄ , HNO ₂ , PAN
O _x	Odd oxygen	O(³ P), O(¹ D), O ₃
SO _x	Oxides of sulfur	SO ₂ , SO ₄

^aSources:Table 10.2: Oxidation States of Atmospheric Sulfur Species^a

Formula	Name	Oxidation state
H ₂ S	Hydrogen sulfide	−2
CH ₃ SCH ₃	Dimethyl sulfide (DMS)	
CS ₂	Carbon disulfide	
OCS	Carbonyl sulfide	
SO ₂	Sulfur dioxide	4
HSO ₃ [−]	Bisulfite ion	
SO ₃ ^{2−}	Sulfite ion	
H ₂ SO ₄	Sulfuric acid	6
HSO ₄ [−]	Bisulfate ion	
SO ₄ ^{2−}	Sulfate ion	
CH ₃ SO ₃ H	Methane sulfonic acid (MSA)	

^aSources:

Table 10.3: Oxidation States of Atmospheric Nitrogen Species^a

Formula	Name	Oxidation state
NH ₃	Ammonia	-3
N ₂	Nitrogen	0
N ₂ O	Nitrous oxide	1
NO	Nitric oxide	2
HNO ₂	Nitrous acid	3
NO ₂	Nitrogen dioxide	4
HNO ₃	Nitric acid	5
NO ₃ ⁻	Nitrate radical	
N ₂ O ₅	Dinitrogen pentoxide	
NO ₃	Nitrate	6

^aSources:

10.3 Stratospheric Chemistry

Ozone is a very important molecule.



Reactions (R1)-(R4) were first proposed as the mechanism for ozone production in the stratosphere by Sidney Chapman in 1930; they are now called the Chapman mechanism. M is a third body which mediates reaction (R2). Usually M is an O₂ or N₂ which gives some of its thermal energy to facilitate the reaction.

The Chapman mechanism is a useful too for demonstrating many of the concepts of atmospheric chemical cycles, including photochemistry, second-order reactions, rate limiting steps, diurnal cycles, and chemical families.

By the 1960s it became clear that the Chapman mechanism alone overpredicts the abundance of ozone in the stratosphere. Additional ozone destruction mechanisms are necessary to bring observations into agreement with the predictions of (R1)-(R4). In the 1970s a number of catalytic mechanisms for ozone destruction were proposed



10.4 Sulfur Chemistry

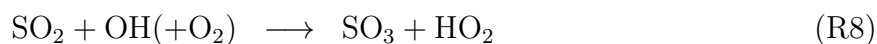
The anthropogenic contribution to the total sulfur burden of the atmosphere is greater than XXX%. Sulfur is important because ...

10.4.1 Sulfur Emissions

[Benkovitz et al. \(1996\)](#) provides a global data of sulfur emissions.

10.4.2 Gas Phase Sulfur Chemistry

Gas phase oxidation of SO₂ occurs in the presence of the OH radical and water vapor



10.5 Nitrogen Chemistry

Approximately 80% of Earth's atmosphere by weight is nitrogen in the form of N₂. Nitrogen is crucial source of energy to the biosphere, but most organisms cannot utilize N₂ directly. Instead, these biochemical processes require nitrogen that has been fixed, or converted to a chemically useful state. The next most abundant compounds of nitrogen in the atmosphere are nitrous oxide (NO₂) and ammonia (NH₃).

10.5.1 Nitrogen Emissions

[Benkovitz et al. \(1996\)](#) provides a global data of nitrogen emissions.

10.5.2 Gas Phase Nitrogen Chemistry

In the troposphere, the photochemistry of nitrogen oxides provides the main source of atomic oxygen. Since atomic oxygen is the rate limiting constituent in ozone formation, nitrogen photochemistry is crucial to determining ozone levels in the troposphere.

Chapter 11

Heterogeneous Chemistry

Chemistry which occurs at the interface between thermodynamic phases is called heterogeneous chemistry. Atmospheric aerosols provide surfaces which demarcate the vapor and solid or liquid phases. Usually the chemistry occurring at the surface of liquid aerosols is insignificant compared to the chemistry occurring inside the liquid. This is because the vapor phase constituents may diffuse through the surface boundary into the liquid where there is a much larger volume of reactants. Atmospheric chemistry in the liquid phase is called aqueous chemistry because water is by far the dominant solvent in the (lower) atmosphere. We discuss aqueous chemistry more fully in §12. In this chapter, we shall concentrate on the chemistry occurring at the interface between solid and liquid phases. We henceforth restrict the term heterogeneous chemistry to refer to chemistry solid and vapor phases. For this reason, heterogeneous chemistry is also called surface chemistry.

Reactions on aerosol surfaces were recognized as fundamental to the Earth system only in the recent past. The annual springtime catalytic destruction of Antarctic stratospheric ozone, i.e., the “ozone hole”, was attributed to surface heterogeneous chemistry only in 1986 (Solomon et al., 1986; McElroy et al., 1986). Since then, a multitude of studies have examined the role of surface heterogeneous chemistry on volcanic aerosols, polar stratospheric clouds (PSCs), and cirrus clouds.

Heterogeneous chemistry requires additional parameters not necessary in pure gas phase chemistry. The most significant single parameter required, of course, is knowledge of the abundances of species on the surface. For concreteness, we shall assume that the solid surface facilitating reactions is an aerosol, such as mineral dust. Such surfaces are often composed of reactive compounds. For example, mineral dust particles are approximately five percent calcium carbonate (CaCO_3) by weight (Pye, 1987). Thus neutralizing reactions between the surface and acids adsorbed from the gas phase are possible.

11.1 Mass Transfer Rates

The loss rate of an atmospheric species to an aerosol surface may be expressed as a pseudo first order reaction rate, K , which is a function of aerosol radius and ambient conditions.

The gas-phase diffusion limited surface uptake rate k is

$$k(r) = 4\pi r D_A f \times \left(\frac{\frac{3}{4}\alpha(1 + \text{Kn})}{\text{Kn}^2 + \text{Kn} + 0.283\text{Kn}\alpha + \frac{3}{4}\alpha} \right)^{-1} \quad (11.1)$$

The total pseudo-first-order rate coefficient K is

$$K = \int_0^\infty k(r)n(r) dr \quad (11.2)$$

where K is in s^{-1} and k is in $\text{m}^3 \text{s}^{-1}$.



Thus the rate of depletion of $\text{A}_{(\text{g})}$ is $k\text{A}_{(\text{g})}$ molecule s^{-1} .

11.1.1 Mean Free Path

$$\lambda_{\text{BB}} = \frac{1}{(\pi\sqrt{2}N_{\text{B}}\sigma_{\text{B}}^2)} \quad (11.3)$$

$$\lambda_{\text{BB}} = \frac{2\mu}{p(8M/\pi R^*T)^{1/2}} \quad (11.4)$$

$$\text{Kn}_{\text{AB}} = \frac{2\lambda_{\text{AB}}}{D} = \frac{\lambda_{\text{AB}}}{r} \quad (11.5)$$

$$\lambda_{\text{AB}} = (\pi\sqrt{2}N_{\text{A}}\sigma_{\text{A}}^2 + \pi\sqrt{1 + m_{\text{AB}}}N_{\text{air}}\bar{\sigma}_{\text{AB}}^2)^{-1} \quad (11.6)$$

$$\lambda_{\text{AB}} = (\pi\sqrt{1 + m_{\text{AB}}}N_{\text{air}}\bar{\sigma}_{\text{AB}}^2)^{-1} \quad (11.7)$$

Chapman-Enskog theory Hirschfelder et al (1954)

$$\lambda_{\text{AB}} = \frac{3}{8\pi} \frac{[\pi k^3 T^3 (1 + m_{\text{AB}})/(2\mathcal{M}_{\text{A}})]^{1/2}}{\rho \bar{\sigma}_{\text{AB}} \Omega_{\text{AB}}^{(1,1)}} \quad (11.8)$$

This expression is very unwieldy. However, it contains useful insights into limiting cases for λ_{AB} . If the molecules are considered as hard spheres then the collision integral $\Omega_{\text{AB}}^{(1,1)} = 1$ and (11.8) reduces to

$$\lambda_{\text{AB}} = \frac{32D_{\text{AB}}}{3\pi(1 + m_{\text{AB}})\bar{v}_{\text{A}}} \quad (11.9)$$

Taking the limits of (11.9) we find

$$\lim_{m_{AB} \rightarrow x} \lambda_{AB} = \begin{cases} \frac{32D_{AB}}{3\pi v_A} = 3.395 \frac{D_{AB}}{v_A} & : m_{AB} \ll 1 \\ \frac{16D_{AB}}{3\pi v_A} = 1.700 \frac{D_{AB}}{v_A} & : m_{AB} = 1 \\ \frac{32D_{AB}}{3\pi m_{AB} v_A} = 3.395 \frac{D_{AB}}{m_{AB} v_A} & : m_{AB} \gg 1 \end{cases} \quad (11.10)$$

Thus for all cases of interest in the atmosphere, we may say that λ_{AB} is of order D_{AB}/\bar{v}_A . A number of simple expressions for λ_{AB} in terms of D_{AB} have been derived from the kinetic theory of gases. These include the expression of Fuchs and Sutugin (1971, MFC)

$$\lambda_{AB} = \frac{3D_{AB}}{v_A} \quad (11.11)$$

The expression used by Loyalka (1973)

$$\lambda_{AB} = \frac{4D_{AB}}{\sqrt{\pi}v_A} = 2.257 \frac{D_{AB}}{v_A} \quad (11.12)$$

and an expression derived from applying the kinetic gas theory to Fick's First Law (11.35)

$$\lambda = \frac{2D}{v_m} \quad (11.13)$$

The four alternative definitions of λ_{AB} , (11.9), (11.11), (11.12), and (11.13), differ from one another by constants of order unity. These definitions are employed to determine mass transfer coefficients in §11.4.4. Which expression to use may be determined by which theory of mass transfer is employed. The ambiguity in λ_{AB} reflects a corresponding ambiguity in D_{AB} . Thus the validity of the expression chosen for λ_{AB} or D_{AB} may depend on the application.

11.1.2 Binary Gaseous Diffusion Coefficient

Consider the binary diffusivity of a trace gas A in an atmosphere of gas B. For concreteness, imagine B is dry air. The diffusivities of the various species are computed as in Seinfeld and Pandis (1997).

$$m_{AB} = \mathcal{M}_A/\mathcal{M}_B \quad (11.14)$$

$$\bar{\sigma}_{AB} = \frac{\sigma_A + \sigma_B}{2} \quad (11.15)$$

$$D_{AB} = \frac{3\pi v_A(1 + m_{AB})\lambda_{AB}}{32} \quad (11.16)$$

Thus values for B in this procedure should be weighted averages of the properties of N_2 and O_2 . When the diffusivity appears with only a single subscript, e.g., D_A , it implies the

Table 11.1: Molecular Collision Diameters σ_A (m) for Important Atmospheric Gases^a

Formula	Name	σ_A m	
CO ₂	Carbon Dioxide	3.34×10^{-10}	CRC95
O ₂	Oxygen	2.98×10^{-10}	CRC95
N ₂	Nitrogen	3.15×10^{-10}	CRC95
Air	Dry air	3.46×10^{-10}	SeP97
HNO ₃	Nitric Acid	$??? \times 10^{-10}$	
	Everything else	$??? \times 10^{-10}$	

^aSources: CRC95 = [Lide and Frederikse \(1995\)](#), p. 6-244; SeP97 = [Seinfeld and Pandis \(1997\)](#).

diffusivity of A in air. The least well-known of the parameters required in (11.15)–(11.16) is σ_A . Table 11.1 gives σ for some important atmospheric gases. The collision diameter of dry air, $\sigma_{\text{air}} = 3.46 \times 10^{-10}$, is apparently a weighted average of σ_{N_2} and σ_{O_2} . Since σ_A is poorly known for many important reactants, it is difficult to compute D_A for every species of interest. It is often preferable to use measurements of D_A if they are available. Table 11.2 lists the modeled and measured diffusion coefficients of many important atmospheric gases in air. The modeled values are computed using (11.15)–(11.16) and the values of σ_A given in Table 11.1. Some studies assume $D_A = 1.0 \times 10^{-5} \text{ m}^2 \text{ s}^{-1}$ for all atmospheric species. This is not a good idea for chemical reactions which are gas-phase diffusion limited. For such reactions, the error in $d[A]/dt$ scales linearly with the error in D_A . Table 11.2 shows D_A varies by a factor of about two for important atmospheric reactants.

The diffusivity of water vapor is better measured than other atmospheric gases. [Pruppacher and Klett \(1978\)](#) recommend

$$D_{\text{H}_2\text{O}} = 2.11 \times 10^{-5} \times \frac{p_0}{p} \left(\frac{T}{T_0} \right)^{1.94} \quad (11.17)$$

where $p_0 = 101325 \text{ Pa}$, and $T_0 = 273.15 \text{ K}$, and $D_{\text{H}_2\text{O}}$ is in $\text{m}^2 \text{ s}^{-1}$.

11.2 Surface Reaction Rates

Heterogeneous chemical reactions on aerosol surfaces may proceed no faster than the reactants can diffuse to the surface of the aerosol. We now focus on determining the rate of diffusion of a molecular species to an aerosol surface.

Consider an aerosol distributed such that $n(D) dD$ is the number concentration of aerosol particles with size between D and $D + \Delta D$. We wish to calculate the rate of adsorption of the gaseous species A from the atmosphere onto the surface of the aerosol distribution. As shown in §11.4.2, this rate will not vary linearly with the surface area of the aerosol except in extremely rarified conditions.

Table 11.2: Modeled And Measured Binary Gaseous Diffusion Coefficients^{ab}

Species	Diffusivity		Reference
	$p_0 D_{X\text{air}}$	$\text{atm m}^2 \text{s}^{-1}$	
	Model	Measurement	
CH ₄		2.28×10^{-5}	Sch86
CO ₂		$1.59\text{--}1.70 \times 10^{-5}$	Sch86
CS ₂		1.05×10^{-5}	Sch86
H ₂ O		2.64×10^{-5}	Sch86
		2.11×10^{-5}	PrK98
^c HNO ₃		1.27×10^{-5}	PrK98
NH ₃		2.34×10^{-5}	Sch86
		2.18×10^{-5}	PrK98
N ₂ O ₅		1.22×10^{-5}	PrK98
O ₂		2.07×10^{-5}	Sch86
O ₃		1.57×10^{-5}	PrK98
SO ₂		1.26×10^{-5}	Sch86
		1.30×10^{-5}	PrK98

^aSources: Schwartz (1986), p. 435, Pruppacher and Klett (1998), p. 746.

^bSources: Measured and modeled D_A of many important atmospheric species in air at STP. Shown is the product $p_0 D_{X\text{air}}$ in $\text{atm m}^2 \text{s}^{-1}$ where $p_0 = 1$ atm. Dividing this number by the ambient pressure p atm yield the binary diffusivity in $\text{m}^2 \text{s}^{-1}$ at the ambient pressure. The model results are produced using (11.15)–(11.16).

^cSee (11.17) for temperature and pressure dependence

11.3 Uptake coefficients

Two parameters are used to describe the uptake of gas phase species by a surface. The first is the mass accommodation coefficient α . The mass accommodation coefficient is the probability that a molecule which makes contact with a condensed surface, e.g., through a collision, adheres to the surface. For a liquid surface, the molecule must enter the liquid phase, i.e., become hydrolyzed. For a solid surface, the molecule adheres to the surface, a process called adsorption. By definition, α only counts reversible uptake, i.e., molecules which are free to desorb and rejoin the atmosphere. The term sticking coefficient may be used for α when the surface is solid. Table 11.3 lists the accommodation coefficients measured for many important atmospheric gases and aerosols. Frank Müller maintains an online database of mass accommodation coefficients at http://www.mi.uni-hamburg.de/technische_meteorologie/Meso/homepages/fmueller/mass_acc.html.

For solid surfaces, mass accommodation is dominated by physisorption or chemisorption rather than mass transport across the interface. Physisorption, or physical absorption, is due to attractive physical forces, such the attraction due to permanent dipoles. Chemisorption, or chemical absorption, is due to exchange of electrons between the surface and the molecules.

If a molecule attaches to a surface and then undergoes a reaction and chemical transfor-

Table 11.3: Measured Mass Accommodation Coefficients^a

Gas	Surface Type	Surface Composition	T K	α	Uncertainty	Reference
H ₂ O	Water ice	H ₂ O(s)	200	0.5	2	JPL97
	Water ice	H ₂ O(s)	173–273	0.01–1.0		PrK98
	Liquid water	H ₂ O(l)		0.01–1.0		PrK98
	Nitric acid liquid	HNO ₃ ·nH ₂ O(l)	278	> 0.3		JPL97
	Nitric acid ice	HNO ₃ ·3H ₂ O(s)	197			JPL97
	Sulfuric acid	H ₂ SO ₄ ·nH ₂ O(l)	298	> 0.002		JPL97
	Sodium Chloride	NaCl(s)	299	> 0.5		JPL97
	Sodium Chloride	NaCl(l)	298	> 0.0004		JPL97
	Carbon/Soot	C (l)	298	> 0.0004		JPL97
	Carbon/Soot	C (l)	298	> 0.0004		JPL97
HO ₂	Liquid water	H ₂ O(l)	275	> 0.02		JPL97
	Liquid water	H ₂ O(l)		> 0.01–0.2		DCZ96
	Aqueous salts	NH ₄ HSO ₄ (aq) and LiNO ₃ (aq)	293	> 0.2		JPL97
	Sodium chloride	NaCl(s)	295	0.02	5	JPL97
	Potassium chloride	KCl(s)	295	0.02	5	JPL97
	Sulfuric acid	H ₂ SO ₄ (l)	295	> 0.05	5	DCZ96
O ₃	Water ice	H ₂ O(s)	195–262	> 0.04		JPL97
	Liquid water	H ₂ O(l)	292	> 0.002		JPL97
	Liquid water	H ₂ O(l)		0.0005		SeP97
	Nitric acid ice	HNO ₃ ·nH ₂ O(s)	195	> 0.002		JPL97
	Sulfuric acid	H ₂ SO ₄ ·nH ₂ O(l)	≈ 195	> 0.00025		JPL97

^aSources: DCZ96 = Dentener et al. (1996); JPL97 = DeMore et al. (1997), pp. 224–227; Sep97 = Seinfeld and Pandis (1997), p. 634.; PrK98 = Pruppacher and Klett (1998), p. 164 Table 5.4., http://www.mi.uni-hamburg.de/technische_meteorologie/Meso/homepages/fmueller/mass_acc.html

mation, it is no longer able to desorb to the atmosphere with its original identity. In this case the molecule is permanently lost to the atmosphere. The uptake coefficient γ measures the total probability that a vapor species molecule enters the surface phase and is irreversibly consumed by a chemical reaction or adsorption.

$$\gamma = \frac{\text{Number of molecules taken up on the surface per second}}{\text{Total number of gas-surface collisions per second}} \quad (11.18)$$

Underwood et al. (2001a) present a detailed, layer-by-layer model of heterogeneous uptake.

Grassian (2002) reviews measurements and models of uptake of nitrogen oxides on tropospheric aerosols.

Underwood et al. (2001b) explain why the measured initial true uptake coefficient γ_0 may not be suitable for use in models. Most diffusion and kinetic-limited uptake models (e.g., §11.4) assume that reactant molecules collide with a smooth spherical surface once per approach. This is true for smooth, spherical particles. Underwood et al. note that non-smooth, aspherical particles such as mineral dust present opportunities for more than one collision per approach. For such particles, the uptake coefficient should be adjusted by the number of collisions per approach, R_G , so that

$$\gamma^* = R_G \gamma_0 \quad (11.19)$$

They found that $1.0 \leq R_G \leq 10$ for a variety of laboratory powders. Nature produces more complex aspherical shapes than laboratory powders. Authentic samples of China Loess had $R_G \approx 22$. Applying this factor using (11.19), nitric acid uptake on dust increases from $\gamma_{0,\text{HNO}_3} = 5.2 \times 10^{-5}$ to $\gamma_{\text{HNO}_3}^* = 1.1 \times 10^{-3}$ (Underwood et al., 2001b). Thus the *sfcrcaspsph* correction leads to an enormous change in the simulated gaseous uptake of natural dust particles.

Underwood et al. (2001b) define R_G as the ratio of the Brunauer-Emmett-Teller (BET) surface area to the surface area of a smooth particle of the same diameter. If the particles are ellipsoidal with major and minor axes of length of D_A and D_B , respectively, then R_G may be defined analytically. Using the properties of ellipsoids described in §18.11.2, we find that

$$R_G = \frac{S_e}{\pi D^2} \quad (11.20)$$

Hanisch and Crowley (2001a) define the BET-corrected uptake coefficient γ^{BET} as the product of the initial uptake coefficient γ_0 and the ratio of the aperture-to-BET areas:

$$\gamma^{\text{BET}} = \frac{A}{S^{\text{BET}}} \gamma_0 \quad (11.21)$$

where $A [\text{m}^2]$ is the cross-sectional area of the Knudsen cell aperture and $S^{\text{BET}} [\text{m}^2]$ is the BET area. This BET correction reduces values of γ_0 by 2–3 order of magnitude, but may not be applicable to mineral dust. Hanisch and Crowley (2001a) give two strong reasons. First, S^{BET} is proportional to sample mass while A remains constant with sample mass. Thus, if applicable, (11.21) predicts that γ^{BET} measurements will exhibit a sensitivity to total sample mass for particles of a given size. This sensitivity was not observed in measurements of HNO_3 uptake on sand-sized Al_2O_3 when sample mass was varied between 30–100 mg. Second, (11.21) predicts that γ^{BET} measurements will exhibit a sensitivity to sample particle size for a given total sample mass. A series of measurements of HNO_3 uptake on Al_2O_3 particles ranging from $D < 10 \mu\text{m}$ to $74 < D < 149 \mu\text{m}$ showed no such size-sensitivity.

The two corrections to γ_0 presented thus far, (11.19) and (11.21), are independent. The shape correction (11.19) increases the effective uptake of atmospheric particles by accounting for the multiple gas-particle collisions per approach that occur on realistic particles. The BET correction (11.21) decreases the measured initial uptake rate γ_0 by accounting for the BET

area of uptake (which is much larger than the Knudsen cell aperture) during the experiment. A third correction, the pore diffusion correction is discussed in [Underwood et al. \(2001b\)](#) and [Hanisch and Crowley \(2001a\)](#).

Our description of heterogeneous uptake follows the nomenclature of the review paper by [Kolb et al. \(1995\)](#). Gaseous uptake by a liquid surface is the most complicated form of removal, so we shall treat this first. We shall then consider uptake to solid surfaces as a limiting case of the liquid phase uptake.

The resistance-in-series method considers gaseous uptake to condensed surfaces as an analog of an electrical circuit. The flux of molecules (current) across a physical barrier (resistance) causes a drop in gas phase density (voltage) of the molecule. Implicit in this model is the assumption that the various resistances may be decoupled and treated as independent steps in a rate limited problem. This is almost always a valid assumption in the atmosphere. The total reactive uptake of the gas phase species is denoted by γ_{ttl} , which is analogous to a conductance. The corresponding resistance to uptake, γ_{ttl}^{-1} , is obtained as the series sum of the resistance due to gas phase diffusion, Γ_{dff}^{-1} , the resistance due to surface accomodation, α , and the resistance due to solubility and reaction $(\Gamma_{\text{sol}} + \Gamma_{\text{rxn}})^{-1}$

$$\frac{1}{\gamma_{\text{ttl}}} = \frac{1}{\Gamma_{\text{dff}}} + \frac{1}{\alpha} + \frac{1}{\Gamma_{\text{sol}} + \Gamma_{\text{rxn}}} \quad (11.22)$$

The nomenclature capitalizes the individual uptake rates Γ_{dff} , Γ_{sol} , and Γ_{rxn} , to indicate that they represent normalized, process-limited rates rather than absolute probabilities. In other words Γ_{dff} , Γ_{sol} , and Γ_{rxn} , unlike α , may exceed unity. When Γ_{dff} , Γ_{sol} , and Γ_{rxn} are all large, i.e., offer little resistance, then $\gamma_{\text{ttl}} \rightarrow \alpha$. Note that allowance for time dependence in (11.22) may be made in any of the uptake coefficients.

With the definition of γ_{ttl} in (11.22), the total net flux of molecules from the gaseous species A to the condensed phase is

$$\tilde{J}_A = \frac{N_A \gamma_{\text{ttl}} \bar{v}_A}{4} \quad (11.23)$$

This expression provides the basic link between the chemical reactivity of an aerosol, γ_{ttl} , which is usually obtained from measurements, and the quantity of most interest to chemical models, \tilde{J}_A . In modeling applications, \tilde{J}_A (11.23) is multiplied by the total surface area of the aerosol to yield the rate of change of gas phase A. Note that (11.23) is in the form of a kinetic collision rate (11.55) times an adjustment factor, γ_{ttl} . Thus γ_{ttl} accounts for all rate limiting processes except kinetic transport to the surface. In other words, γ_{ttl} is the mass transport rate normalized by the Boltzmann gas kinetic flux ([Kolb et al., 1995](#)).

11.3.1 Laboratory Measurements of γ_{ttl}

In practice, γ may be measured under controlled conditions for a particular vapor species A and type of aerosol. Table 11.4 lists the uptake coefficients measured for common reactions between many important atmospheric gases and aerosol surfaces.

Table 11.4: Measured Uptake Coefficients¹²³⁴

Gas	Surface Type	Surface Composition	T K	γ	Δ	Ref.	Notes
$\text{HNO}_3 + \text{Surface} \longrightarrow \text{Products}$							
HNO_3	Liquid water	$\text{H}_2\text{O}(\text{l})$	268	0.07		SeP97	
	Liquid water	$\text{H}_2\text{O}(\text{l})$	293	0.19		SeP97	
$\text{HNO}_3 + \text{C}(\text{s}) \longrightarrow \text{Products}$							
HNO_3	Carbon/Soot	$\text{C}(\text{s})$	190–440	0.04	5	JPL97	
	Hexane Soot			1×10^{-5}		Gra02	??
	Hexane Soot			7×10^{-5}		Gra02	
$\text{HNO}_3 + \text{Dust} \longrightarrow \text{Products}$							
	Al_2O_3			$(13 \pm 3.3) \times 10^{-2}$		HaC01a	??
	Al_2O_3			$(1.6 \pm 1.4) \times 10^{-3}$		HaC01a	??
	Al_2O_3			$(6.7 \pm 1.9) \times 10^{-4}$		HaC01a	??
HNO_3	Alumina	$\alpha\text{-Al}_2\text{O}_3$		$(9.7 \pm 0.5) \times 10^{-5}$		ULA01, Gra02	
HNO_3	Alumina	$\alpha\text{-Al}_2\text{O}_3$		2.0×10^{-3}		USP01	
	Arizona Dust			$(5.7 \pm 1.5) \times 10^{-2}$		HaC01a	
	Calcium Carbonate	CaCO_3		7.1×10^{-2}		Fenter	
	Calcium Carbonate	CaCO_3		2.4×10^{-4}		Gra02	
	Calcium Carbonate	CaCO_3		$(9.7 \pm 2.4) \times 10^{-2}$		HaC01a	??
	Calcium Carbonate	CaCO_3		$(1.75 \pm 0.39) \times 10^{-3}$		HaC01a	??
	Calcium Carbonate	CaCO_3		$(9.6 \pm 1.2) \times 10^{-4}$		HaC01a	??
	Ca-montmorillonite	$\text{CaCam}(\text{Mg}[\text{Si}_4\text{O}_{10}](\text{OH}_2) \times \text{p}(\text{Al}, \text{Fe})_2[\text{Si}_4\text{O}_{10}]; \text{m} : \text{p} = 0.8\text{--}0.9 \cdot \text{nH}_2\text{O})$		11.4×10^{-2}		HaC01b	
	Calcium Oxide	CaO		$(6.1 \pm 0.3) \times 10^{-3}$		ULA01, Gra02	
	Calcium Oxide	CaO		1.6×10^{-2}		USP01	??
	Chinese Dust (Taklamakan)			17.1×10^{-2}		HaC01b	
	Dolomite	$\text{CaMg}[\text{CO}_3]_2$		14.0×10^{-2}		HaC01b	
	Gobi Dust			$(5.2 \pm 0.3) \times 10^{-5}$		ULA01, Gra02	??

Table 11.4: (continued)

Gas	Surface Type	Surface Composition	T K	γ	Δ	Ref.	Notes
	Gobi Dust			1.1×10^{-3}		USP01	
	Illite	$\text{KAl}_2[\text{AlSi}_3\text{O}_{10}](\text{OH})_2$		10.8×10^{-2}		HaC01b	
	Illite/smectite (70:30)	$\text{KAl}_2[\text{AlSi}_3\text{O}_{10}](\text{OH})_2/\text{Mg}_3[\text{Si}_4\text{O}_{10}](\text{OH})_2$		8.9×10^{-2}		HaC01b	
	Iron Oxide	$\alpha\text{-Fe}_2\text{O}_3$		$(5.3 \pm 0.3) \times 10^{-5}$		ULA01, Gra02	
	Kaolinite	$\text{Al}_2\text{Si}_2\text{O}_5(\text{OH})_4$		11.4×10^{-2}		HaC01b	
	Magnesium Oxide	MgO		$(3.7 \pm 0.2) \times 10^{-4}$		ULA01	
	Magnesium Oxide	MgO		1.4×10^{-3}		USP01	??
	Magnesium Oxide	MgO		4.0×10^{-4}		Gra02	
	Na-montmorillonite	$\text{NaCam}(\text{Mg}[\text{Si}_4\text{O}_{10}](\text{OH}_2) \times \text{p}(\text{Al}, \text{Fe})_2[\text{Si}_4\text{O}_{10}]; \text{m} : \text{p} = 0.8\text{--}0.9 \cdot \text{nH}_2\text{O}$		8.1×10^{-2}		HaC01b	
	Orthoclase	$\text{K}[\text{AlSi}_3\text{O}_8]$		8.4×10^{-2}		HaC01b	
	Palygorskite	$(\text{Mg}, \text{Al})_2[\text{OH}[\text{Si}_4\text{O}_{10}]] \cdot 2\text{H}_2\text{O} + 2\text{H}_2\text{O}$		19.6×10^{-2}		HaC01b	
	Quartz	SiO_2		$(2.9 \pm 0.2) \times 10^{-5}$		ULA01, Gra02	
	Ripidolite (chlorite)	$(\text{Fe}, \text{Mg})_{\text{n-p}}(\text{Fe}, \text{Al})_{2\text{p}}\text{Si}_{4-\text{p}} \cdot \text{xH}_2\text{O}, \text{n} \approx 5, \text{p} \approx 0.5\text{--}2$		10.2×10^{-2}		HaC01b	
	Saharan Dust (Cape Verde)			$(11 \pm 3) \times 10^{-2}$		HaC01a	??
	Saharan Dust (Cape Verde)			13.6×10^{-2}		HaC01b	
	Saharan Dust (Cape Verde)	296		0.1		HaC03a	
	Saharan Sand			$(2.0 \pm 0.1) \times 10^{-5}$		ULA01	
	Saharan Sand			$R_G \times 2.0 \times 10^{-5}$		USP01	??

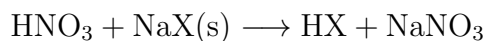


Table 11.4: (continued)

Gas	Surface Type	Surface Composition	T K	γ	Δ	Ref.	Note
HNO ₃	Sodium Chloride	NaCl(s)	295–298	0.02	3	JPL97	
	Sodium Bromide	NaBr(s)	≈ 290	0.02	10	JPL97	
	Potassium Bromide	KBr(s)	≈ 290	0.02	10	JPL97	
	Potassium Chloride	KCl(s)	≈ 290	0.02	10	JPL97	
$\text{N}_2\text{O}_5 + \text{H}_2\text{O} \longrightarrow 2\text{HNO}_3$							
N ₂ O ₅	Water ice	H ₂ O(s)	195–200	0.01	3	JPL97	
	Liquid water	H ₂ O(l)	260–295	0.05	2	JPL97	
	Liquid water	H ₂ O(l)	283	0.04		SeP97	
	Nitric acid ice	HNO ₃ ·3H ₂ O(s)	200	0.0003	3	JPL97	
	Sulfuric acid	H ₂ SO ₄ ·nH ₂ O(aq)	195–300	≈ 0.1		JPL97	
	Sulfuric acid monohydrate	H ₂ SO ₄ ·H ₂ O(s)	200–300		3	JPL97	
	Sulfuric acid tetrahydrate	H ₂ SO ₄ ·4H ₂ O(s)	195–207	0.006	2	JPL97	
	Ternary acid	H ₂ SO ₄ ·nHNO ₃ ·nH ₂ O(aq)	195–218			JPL97	
$\text{N}_2\text{O}_5 + \text{Surface} \longrightarrow \text{Products}$							
N ₂ O ₅	Ammonium sulfate	(NH ₄) ₂ SO ₄ (aq)		0.06–0.12		DCZ96	
	Sulfuric acid	H ₂ SO ₄ ·nH ₂ O(aq)		0.06–0.12		DCZ96	
$\text{N}_2\text{O}_5 + \text{NaCl(s)} \longrightarrow \text{ClNO}_2 + \text{NaNO}_3\text{(s)}$							
N ₂ O ₅	Sodium chloride	NaCl(s)	300	0.0005	20	JPL97	
	Sodium chloride	NaCl(aq)	300	> 0.02	20	JPL97	
$\text{N}_2\text{O}_5 + \text{MBr(s)} \longrightarrow \text{Products}$							
N ₂ O ₅	Sodium bromide	NaBr(s)	≈ 300			JPL97	
	Potassium bromide	KBr(s)	≈ 300	0.004	10	JPL97	
$\text{NH}_3 + \text{H}_2\text{SO}_4 \longrightarrow \text{NH}_4\text{HSO}_4$							
NH ₃	Sulfuric acid	H ₂ SO ₄ ·nH ₂ O(l)	288–300	0.4	2.5	JPL97	
$\text{NO}_3 + \text{H}_2\text{O} \longrightarrow \text{HNO}_3 + \text{OH}$							
NO ₃	Dust			0.1		ZhC99	
NO ₃	Liquid water	H ₂ O(l)	273	0.0002	20	JPL97	

Table 11.4: (continued)

Gas	Surface Type	Surface Composition	T K	γ	Δ	Ref.	Notes
O ₃	Liquid water	H ₂ O(l)		0.0002		SeP97	
	Alumina	Al ₂ O ₃ (s)	210–300	O ₃ + Surface → Products		JPL97	
	Alumina	α -Al ₂ O ₃		$(8 \pm 5) \times 10^{-5}$		MUG02	
	Alumina ($D \sim 25 \mu\text{m}$)	α -Al ₂ O ₃		$(1.4 \pm 0.3) \times 10^{-4}$		MUG03	
	Alumina ($D \sim 25 \mu\text{m}$)	α -Al ₂ O ₃		7.6×10^{-6}		MUG03 (steady-state at 4.5 h)	
	Alumina ($D \sim 1 \mu\text{m}$)	α -Al ₂ O ₃		$(9 \pm 3) \times 10^{-5}$		MUG03	
	Carbon/Soot	C(s)	≈ 300	0.003	20	JPL97	
	Carbon	C(s)		0.0004		DCZ96	
	Iron	Fe(s)		0.0004		DCZ96	
	Iron Oxide	α -Fe ₂ O ₃		$(1.8 \pm 0.7) \times 10^{-4}$		MUG02	
	Quartz	SiO ₂		$(5 \pm 3) \times 10^{-5}$		MUG02	
	China Loess			$(2.7 \pm 0.9) \times 10^{-5}$		MUG02	
	Saharan Dust (Cape Verde)	296		3.0×10^{-5}		HaC03b	??
	Saharan Sand			$(6 \pm 3) \times 10^{-5}$		MUG02	
	Ground			$(6 \pm 3) \times 10^{-5}$		MUG02	
	Sieved ($D < 50 \mu\text{m}$)			$(4 \pm 2) \times 10^{-6}$		MUG02	
	Sodium chloride	NaCl(s)	≈ 300	$> 2 \times 10^{-10}$	20	JPL97	

The total uptake coefficient γ depends on which reactions are involved. In the laboratory, the allowed reactions are controlled by using pure gases and aerosol surfaces. This allows the γ for each reaction to be isolated and measure separately. The relationship developed in ...may be used to infer α from γ for the surface types presented in Table 11.4.

The total areal molecular flux γ_{ttl} into the condensed phase is often represented in terms of the gas phase concentration and a total deposition resistance r_d or its inverse the deposition velocity v_d

$$v_d = r_d^{-1} \quad (11.24)$$

$$\begin{aligned} \tilde{J}_A &= N_A/r_d \\ &= N_A v_d \end{aligned} \quad (11.25)$$

The units of r_d and v_d are s m^{-1} and m s^{-1} , respectively. The definitions of r_d and v_d for gaseous deposition to aerosol surfaces are completely analogous to the definitions of aerosol deposition to land surfaces in §5.4. Combining (11.25) with (11.23) we obtain

$$v_d = \frac{\gamma_{\text{ttl}} \bar{v}_A}{4} \quad (11.26)$$

$$\gamma_{\text{ttl}} = \frac{4v_d}{\bar{v}_A} \quad (11.27)$$

Since no reference (11.27) does not depend on the geometry of the surface, it applies equally well to flat surfaces and curved particles. Table 11.5 below takes advantage of this to convert field deposition resistance measurements to uptake coefficients. We now examine the individual resistances Γ_{diff} , Γ_{sol} , and Γ_{rxn} which comprise γ_{ttl} (11.22).

11.3.2 Gas Transport Limitation

$$\Gamma_{\text{sol}} = \frac{4HR^*T}{\sqrt{\pi}\bar{v}_m} \left(\frac{D_{(l)}}{t} \right)^{1/2} \quad (11.28)$$

$$\Gamma_{\text{rxn}} = \frac{4HR^*T}{\bar{v}_m} \sqrt{D_{(l)}k} \quad (11.29)$$

$$\gamma_{\text{ttl}} = \frac{1}{\alpha} + \frac{1}{\Gamma_{\text{sol}} + \Gamma_{\text{rxn}}} \quad (11.30)$$

where $D_{(l)}$ is the liquid phase diffusion coefficient. In the limit of low solubility or long exposure time, $\Gamma_{\text{sol}} \rightarrow 0$ so that

$$\gamma_{\text{ttl}} = \frac{1}{\alpha} + \frac{1}{\Gamma_{\text{rxn}}} \quad (11.31)$$

However, when no gas phase diffusion limitation exists, Kolb et al. (1995) show

11.3.3 Uptake on Solids

Uptake by solid surfaces is limited by the ability of the species to diffuse to the interior of the aerosol. Kolb et al. (1995) cite typical condensed phase diffusion coefficients of 10^{-5} and $10^{-12} \text{ cm}^2 \text{ s}^{-1}$ for diffusion on liquid and solid surfaces, respectively. Thus, the condensed phase diffusion coefficient for solids is virtually zero. As a result, net resistance to solid phase uptake may be interpreted as the limit of (11.22) as $\Gamma_{\text{sol}}, \Gamma_{\text{rxn}} \rightarrow 0$. Under these conditions, the chemistry is restricted to occur only at the solid surface itself. Thus the solid uptake rate is linearly proportional to both the reaction rate and the species concentration.

Due to heterogeneous chemistry, the number of surface sites hospitable to a given species is not constant with time. On a solid surface, these sites may become occupied by the products of chemical reactions as the aerosol ages. The surface of a liquid aerosol may also become saturated with a given reactant. Site coverage or surface saturation cause $\alpha \rightarrow 0$.

Table 11.5: Deposition Velocity of O₃ Over Various Surfaces^{ab}

Gas	Texture	Condition	v_d m s ⁻¹	r_d s m ⁻¹	γ	Ref.
O ₃	Sand	Moist	0.0025	400	2.7×10^{-5}	Ald69
O ₃	Sand	Dry	0.005	200	5.5×10^{-5}	Ald69
O ₃	Bare soil	Loamy	0.025–0.05	20–40	$2.7\text{--}5.4 \times 10^{-4}$	TRW73
O ₃	Bare soil	High ^c θ	0.0077–0.014	70–130	$8.5\text{--}17 \times 10^{-5}$	TRW73
O ₃	Bare soil	Cold	0.10	10	1.1×10^{-3}	WCW81
O ₃	Sand	Day	0.025	40	2.7×10^{-4}	GaR80
O ₃	Sand	Night	0.017	60	1.9×10^{-4}	GaR80
O ₃	Sand	Loamy, dry	0.033	30	3.6×10^{-4}	GaR80
O ₃	Sand		0.0014	714	1.5×10^{-5}	Gar76
O ₃	CaCO ₃		0.0022	455	2.4×10^{-5}	Gar76
O ₃	Soil	^c $\theta = 27\%$	0.0084	119	9.2×10^{-5}	Gar76
O ₃	Soil	$\theta = 4\%$	0.0176	57	1.9×10^{-4}	Gar76
O ₃	Sand, rock	Day	0.0011	909	1.2×10^{-5}	SBP87
O ₃	Sand, rock	Night	0.0003	3333	3.3×10^{-6}	SBP87
O ₃	Sahara	Day	0.0015	667	1.6×10^{-5}	GHM95
O ₃	Sahara	Night	0.00065	1538	7.1×10^{-6}	GHM95

^aSources: Dentener et al. (1996)

^b γ is inferred from v_d using $\gamma = 4v_d/\bar{v}_m$ (11.27) for a temperature $T = 300$ K.

^c θ is volumetric water content.

11.3.4 Field Measurements of γ_{ttl}

Uptake coefficients may also be inferred from field measurements. For example, bare soil surfaces are comprised of the parent materials of atmospheric dust. Many field observations of trace gas uptake by bare surfaces exist. In most such measurements, the overall dry deposition resistance is inferred by measuring the vertical gradient of the trace gas concentration (5.17). Using these measurements as proxies for trace gas uptake by atmospheric dust requires the assumption that the trace gas uptake is not significantly affected by sub-soil microbes, plant matter, or bulk properties of the soil that are not duplicated by the airborne dust. Table 11.5 lists the deposition velocities of O₃ measured over various surfaces. An important advantage of field measurements of reactive uptake is that the measured uptake coefficient includes all realistic paths of uptake. Unfortunately, the exact reactions defining these all the paths is unknown. Nevertheless, inferences of γ from field measurements are important since they place independent bounds on heterogeneous transfer rates.

11.4 Vapor Diffusion to Spherical Particles

In order to relate α or γ to k , we must develop a more exact theory of gas phase diffusion to aerosol surfaces. Molecules come into contact with aerosol surfaces through gas phase diffusion modified by the motion of the aerosol. The characteristics of gaseous transfer to

solid surfaces depend on the density of the gaseous medium. The two extremes of media are called the continuum regime and the kinetic regime. The continuum regime describes gaseous diffusion of vapors to an aerosol when the mean free path between molecular collisions is much smaller than the size of the aerosol. Gaseous diffusion in the troposphere is described by the continuum regime.

The kinetic regime describes the diffusion of vapors to an aerosol in atmospheres where the mean free path between molecular collisions is comparable to or larger than the size of the aerosol. In this case, vapor deposition to surface is described by “billiard ball physics”, where the gaseous molecules do not interfere with one another, nor do they possess the properties of a continuum. Gaseous diffusion processes above the tropopause may need to account for kinetic effects.

11.4.1 Knudsen Number

In order to quantify the deposition of gases to aerosol surfaces it is important to distinguish between two important limits, or regimes, of molecule-aerosol interactions. Particles which are much smaller than the mean free path between molecular collisions do not experience the molecular vapor as a continuous fluid. Vapor molecules do not “see” the particle surface as a significant obstacle, and collide with it relatively infrequently. From the point of view of the particle, the gas molecules collide with it in discrete intervals, rather than in a continuous barrage. This limit of molecule-aerosol interaction is called the non-continuum regime or the kinetic regime.

At the other extreme, molecules may be so numerous, or the particles so large, that the molecules can not travel very far without striking the particle or colliding with another molecule. In this case the particle is subject to a continuous barrage of molecular collisions. From the point of view of the particle, the molecules form a continuous fluid which unceasingly exert pressure on the particle. This limit of molecule-aerosol interaction is called the continuum regime.

The Knudsen number Kn is the dimensionless parameter used to locate molecule-aerosol interactions along the spectrum from the kinetic to the continuum regime. Thus Kn depends upon both the size of the particle and the mean free path λ of the medium

$$Kn = \frac{2\lambda}{D} = \frac{\lambda}{r} \quad (11.32)$$

11.4.2 Continuum Regime

In this section we examine the diffusion of a gaseous species A to the surface of a spherical particle in the continuum regime, i.e., $Kn_{AB} \ll 1$. We shall assume that the particle is motionless and the atmosphere is stagnant, subject only to Brownian diffusion. The effects of particle motion on these results will be discussed in §11.4.5. Since the particle geometry is assumed spherical, we shall cast our equations in spherical coordinates where r is the distance from the center of the particle.

The physical scenario to consider is that of a spherical aerosol of radius R_p in contact with gas phase species A whose ambient concentration (many particle diameters away) is N_∞ and whose concentration at any radial position r is $N(r)$. There is no angular dependence

in this system, only radial. Imagine a sphere concentric to this particle. Mass conservation requires that the rate of change of $[A]$ inside the hypothetical spherical shell must be due to the flux of A through the surface of the shell. We denote this radial flux at distance r by $\tilde{J}_A(r)$ molecule $m^{-2} s^{-1}$. Since $\tilde{J}_A(r)$ has dimensions of per unit area, it may also be called the areal flux. The governing differential equation of the system may be obtained by considering the mass balance of an infinitesimally thin spherical shell passing through r . The rate of change of the number of molecules of A within the shell is simply the difference between the number flux of molecules entering at r and the flux leaving at $r + \Delta r$. The total number flux of molecules is the area times the radial number flux, i.e., $4\pi r^2 \tilde{J}_A(r)$. The volume of the shell is $4\pi r^2 \Delta r$. The rate of change of concentration is the quotient of these two quantities

$$\begin{aligned}
 \frac{\partial N}{\partial t} &= \lim_{\Delta r \rightarrow 0} \frac{4\pi r^2 \tilde{J}_A(r) - 4\pi(r + \Delta r)^2 \tilde{J}_A(r + \Delta r)}{4\pi r^2 \Delta r} \\
 &= \lim_{\Delta r \rightarrow 0} \frac{r^2 \tilde{J}_A(r) - r^2 \tilde{J}_A(r + \Delta r) - 2r\Delta r \tilde{J}_A(r + \Delta r) - (\Delta r)^2 \tilde{J}_A(r + \Delta r)}{r^2 \Delta r} \\
 &= \lim_{\Delta r \rightarrow 0} - \left(\frac{\tilde{J}_A(r + \Delta r) - \tilde{J}_A(r)}{\Delta r} + \frac{2}{r} \tilde{J}_A(r + \Delta r) + \frac{\Delta r}{r^2} \tilde{J}_A(r + \Delta r) \right) \\
 &= - \left(\frac{\partial \tilde{J}_A}{\partial r} + \frac{2\tilde{J}_A}{r} \right)
 \end{aligned} \tag{11.33}$$

The negative sign on the RHS indicates that N decreases for positive \tilde{J}_A , i.e., when the net flux of A is outwards. Equation (11.33) is mathematically equivalent to

$$\frac{\partial N}{\partial t} = -\frac{1}{r^2} \frac{\partial}{\partial r} r^2 \tilde{J}_A(r) \tag{11.34}$$

To proceed further, we turn to the results of physical experiments. Fick's First Law states that the flux of a vapor is proportional to its concentration gradient, and that the constant of proportionality is, by definition, the bulk diffusivity of the vapor

$$\tilde{J}_A = -D_A \frac{\partial N_A}{\partial r} \tag{11.35}$$

where D_A is the binary diffusion coefficient of A in air. In stating Fick's law (11.35), we have maintained the usual convention that the origin of coordinates ($r = 0$) is at the center of the particles, so that \tilde{J}_A is positive for a net flux of molecules from the particle to the atmosphere. A mnemonic for this convention is to remember that \tilde{J}_A is positive when net molecular flow is toward larger r . However, we are usually more interested in particle absorption than desorption so the convention expressed in (11.35) may prove confusing. One must bear in mind that negative radial fluxes indicate net uptake by the particle.

The evaluation of D_A is discussed in §11.1.2. Applying Fick's Law (11.35) to (11.33) results in

$$\frac{\partial N_A}{\partial t} = D_A \left(\frac{\partial^2 N_A}{\partial r^2} + \frac{2}{r} \frac{\partial N_A}{\partial r} \right) \tag{11.36}$$

Also known as Fick's Second Law, this is the standard, second order, time dependent diffusion equation in radial coordinates. The second term on the RHS of (11.36) arises from the spherical geometry of the problem. This term becomes significant as $r \rightarrow 0$ and vanishes $r \rightarrow \infty$. In the latter case, (11.36) reduces to the one dimensional diffusion equation in Cartesian coordinates.

The solution to (11.36) requires two conditions in space and one condition in time. Let us examine the evolution of the system in which a particle is placed in a uniform atmosphere of concentration N_∞ at $t = 0$. Let N_S denote the equilibrium gas phase concentration at the surface of the particle. Then the boundary and initial conditions of the system are

$$N_A(r, 0) = N_\infty, \quad r > R_p \quad (11.37)$$

$$N_A(R_p, t) = N_S \quad (11.38)$$

$$N_A(\infty, t) = N_\infty \quad (11.39)$$

The solution to (11.36) subject to (11.38) may be obtained by the method of Laplace transforms or similarity functions, see Seinfeld and Pandis (1997) or Pruppacher and Klett (1998) for details.

The full, time-dependent solution of (11.36) is

$$\begin{aligned} N(r, t) &= N_\infty - \frac{R_p}{r}(N_\infty - N_S) + \frac{2R_p}{r\sqrt{\pi}}(N_\infty - N_S) \int_0^{(r-R_p)/(2\sqrt{D_A t})} e^{-x^2} dx \quad (11.40) \\ &= N_\infty - \frac{R_p}{r}(N_\infty - N_S) \left[1 - \operatorname{erf} \left(\frac{r - R_p}{2\sqrt{D_A t}} \right) \right] \\ &= N_\infty - \frac{R_p}{r}(N_\infty - N_S) \operatorname{cerf} \left(\frac{r - R_p}{2\sqrt{D_A t}} \right) \quad (11.41) \end{aligned}$$

where the last two steps simply re-express the third term on the RHS of (11.40) in terms of the error function and of the complementary error function (Section 18.5). This time-dependent term vanishes as $t \rightarrow \infty$ and the upper limit of integration approaches zero. The first two terms on the RHS of (11.40) are time-independent, and define the steady state concentration at any distance r

$$N(r) = N_\infty - \frac{R_p}{r}(N_\infty - N_S) \quad (11.42)$$

If we apply Fick's Law (11.35) to (11.40) and (11.42), we obtain time-varying and steady

state radial fluxes at any distance from the particle

$$\begin{aligned}
\tilde{J}(r, t) &= -D_A \frac{\partial N(r, t)}{\partial r} \\
&= -D_A (N_\infty - N_S) \frac{R_p}{r} \left\{ \frac{1}{r} + \frac{2}{r\sqrt{\pi}} \int_0^{(r-R_p)/(2\sqrt{D_A t})} e^{-x^2} dx \right. \\
&\quad \left. + \frac{2}{\sqrt{\pi}} \exp \left[-\left(\frac{r-R_p}{2\sqrt{D_A t}} \right)^2 \right] \left(\frac{1}{2\sqrt{D_A t}} \right) \right\} \\
&= -D_A (N_\infty - N_S) \frac{R_p}{r} \left\{ \frac{1}{r} + \frac{2}{r\sqrt{\pi}} \int_0^{(r-R_p)/(2\sqrt{D_A t})} e^{-x^2} dx \right. \\
&\quad \left. + \frac{1}{\sqrt{\pi D_A t}} \exp \left[-\left(\frac{r-R_p}{2\sqrt{D_A t}} \right)^2 \right] \right\} \\
&= -D_A (N_\infty - N_S) \frac{R_p}{r} \left\{ \frac{1}{r} \operatorname{erf} \left(\frac{r-R_p}{2\sqrt{D_A t}} \right) + \frac{\partial}{\partial r} \left[\operatorname{erf} \left(\frac{r-R_p}{2\sqrt{D_A t}} \right) \right] \right\} \quad (11.43)
\end{aligned}$$

Note that we have used the chain rule in differentiating the upper limit of integration. We shall examine three aspects of (11.43) in closer detail: the steady state behavior ($t \rightarrow \infty$), the time varying behavior at the particle surface ($r = R_p$), and the steady state behavior at the particle surface.

Substituting $t \rightarrow \infty$ into (11.43) we find that the steady state radial flux at any distance $r > R_p$ is

$$\tilde{J}(r) = -\frac{D_A (N_\infty - N_S) R_p}{r^2} \quad (11.44)$$

The dependence on R_p stems from the boundary condition (11.38) that the particle is a perfect source or sink of radius R_p . The fact that \tilde{J} depends linearly rather than quadratically on R_p is a characteristic of diffusive, as opposed to kinetic, transport. The inverse dependence of \tilde{J} on r^2 arises from mass continuity.

Substituting $r = R_p$ into (11.43) we obtain we obtain the time-varying radial flux to the surface of the particle

$$\tilde{J}(R_p, t) = -\frac{D_A (N_\infty - N_S)}{R_p} \left(1 + \frac{R_p}{\sqrt{\pi D_A t}} \right) \quad (11.45)$$

The flux at the droplet surface will reach steady state conditions when the time-dependent term vanishes, i.e., when $t \gg \tau_c$ where

$$\tau_c = \frac{R_p^2}{\pi D_A} \quad (11.46)$$

τ_c is the timescale for continuum diffusion to the surface of a particle. At STP, $\tau_c < 1.7 \times 10^{-6}$ s for $R_p < 100 \mu\text{m}$.

Setting $r = R_p$ in (11.44) or $t \rightarrow \infty$ in (11.45) we obtain

$$\tilde{J}(R_p) = -\frac{D_A(N_\infty - N_S)}{R_p} \quad (11.47)$$

Thus continuum diffusion theory shows the steady state radial flux of A at the particle's surface decreases linearly with R_p . The total steady state flux of A from the atmosphere to the particle's surface J_c is the radial flux at $r = R_p$ (11.47) times the particle area. J_c is the spherical flux. The subscript c denotes that J_c was obtained from continuum diffusion theory, i.e., for $\text{Kn}_{AB} \rightarrow 0$.

$$\begin{aligned} J_c &\equiv -4\pi R_p^2 \tilde{J}(R_p) \\ &= 4\pi R_p D_A (N_\infty - N_S) \end{aligned} \quad (11.48)$$

Note that the spherical flux J_c and the radial flux \tilde{J} have the opposite sign convention. The factor of negative one was imposed so that J_c is positive during radial inflow (net uptake by the particle), and negative during radial outflow. This result (11.48) is due to Maxwell and so is called the Maxwellian flux.

Experiments and intuition, however, suggest that continuum diffusion does not apply to gas molecules within about one mean free path of the particle surface. The spherical flux J_c varies linearly with particle size R_p rather than with the particle area R_p^2 . This result is somewhat surprising. As we show in §11.4.3, the spherical flux predicted by kinetic theory (valid when $\text{Kn}_{AB} \gg 1$) does vary with R_p^2 . The problem of accounting for both continuum and kinetic diffusion is non-trivial, and will be discussed in §11.4.4. We shall show that useful results for $\text{Kn}_{AB} \approx 0$ and for $\text{Kn}_{AB} \gg 1$ may be expressed in terms of J_c (11.48).

Corrections to the spherical flux J_c (11.48) for the effects of kinetic transfer to the aerosol surface, mass accommodation, reactive uptake, and Henry's Law equilibrium, may all need to be evaluated before determining the expected molecular flux to a particle. Let us denote the actual molecular uptake by the particle as J and define generic properties J which are independent of exactly how J is defined.

We may easily manipulate J_c to obtain the rate of growth/shrinkage of droplet mass M , and the rate of change of concentration of A

$$\begin{aligned} \left(\frac{dM}{dt} \right)_0 &= J_c \mathcal{M}_A \\ &= 4\pi R_p D_A \mathcal{M}_A (N_\infty - N_S) \end{aligned} \quad (11.49)$$

where the zero subscript indicates the result applies only to stationary particles. For A = H₂O, (11.49) is the classical solution to diffusion equation for condensational growth of cloud drops.

The maximum diffusive flux of A to the particle (11.48) occurs when $N_S = 0$

$$J_c^{\max} = 4\pi R_p D_A N_\infty \quad (11.50)$$

If the rate of change of ambient [A] is due solely to mass uptake following gaseous diffusion, then (11.50) implies

$$\frac{d[A]}{dt} = -4\pi R_p D_A [A] \quad (11.51)$$

$$= -J_c^{\max} \quad (11.52)$$

One subtlety to note is that we have not modified the flux due bulk diffusion J_c (11.48) by the accommodation coefficient α . The reason for this is that we wish to avoid double counting α . The continuum fluxes predicted in this section should not be applied in isolation. These fluxes describe the first resistance a molecule must overcome in order to meet a surface. Bulk phase diffusion merely describes the rate at which molecules flow by a stationary particle. When molecules are close enough to the particle, they may collide with the particle, but only by making a kinetic jump (Brownian diffusion) from the near surface to the surface of the particle. The mass accommodation coefficient is defined to modify the efficiency of this final step, the kinetic collision described in the next section.

11.4.3 Kinetic Regime

In this section we examine the diffusion of a gaseous species A to the surface of a spherical particle in the kinetic regime, i.e., $\text{Kn}_{AB} \gg 1$. Note that the kinetic regime describes the actions of any molecule in isolation, including the final jump of a molecule in a continuum to the particle interface. This is called Interfacial transport. Thus we shall apply the kinetic regime results to describe the final step of diffusive transfer of bulk gas molecules to a particle.

The equipartition theorem states that the thermal energy available is equally divided among translational and rotational degrees of freedom. The thermal energy of a molecule varies linearly with the temperature, i.e., $E \sim kT$. When the thermal energy is expressed as kinetic energy,

$$\begin{aligned} kT &\propto Mv^2 \\ v &\propto \sqrt{\frac{T}{M}} \end{aligned} \quad (11.53)$$

Thus, the square-root dependence of v_m on temperature and mass stems from equipartition theorem.

The mean speed of molecules in random thermal motion may be computed from Maxwell-Boltzmann statistics. The mean molecular speed \bar{v}_m is obtained by averaging the Maxwell-Boltzmann distribution of speeds. For the gaseous species A with molecular mass \mathcal{M}_A ,

$$\bar{v}_A = \sqrt{\frac{8R^*T}{\pi\mathcal{M}_A}} \quad (11.54)$$

where R^* is the universal gas constant and T is the ambient temperature. \bar{v}_A is call the thermal speed of the molecule. For oxygen molecules at STP, $\bar{v}_{O_2} = 425 \text{ m s}^{-1}$. For ozone molecules at 300 K $\bar{v}_{O_3} = 364 \text{ m s}^{-1}$.

The kinetic theory of gases can be used to compute the number flux of A, i.e., the number of molecules of A crossing a unit surface in a unit time. Denoting the number concentration of species A by $N_A = [A]$,

$$\tilde{J}_A = \frac{1}{4} N_A \bar{v}_A \quad (11.55)$$

where the subscript k denotes that the flux applies only in the kinetic regime. As expected, \tilde{J}_A varies linearly with N_A . Since Brownian diffusion is isotropic, the orientation of the

surface does not appear in (11.55). Thus the flux to a concave surface is simply \tilde{J}_A times the surface area. A sphere of radius R_p has a surface area of $4\pi R_p^2$ so that the number J_k^* of kinetic collisions of A with the surface is

$$J_k^* = \pi R_p^2 N_A \bar{v}_A \quad (11.56)$$

where the superscript * denotes that the flux does not account for uptake or reaction probabilities.

For heterogeneous chemistry, we are interested in the net uptake of A by the surface. As mentioned earlier, molecules of A may be desorbed from the surface as well as adsorbed by the surface. Thus the net flux of A to the surface is determined by the gradient in the ambient vapor and the surface concentrations, N_∞ and N_S , respectively. Also we may impose the condition that only a fraction α of the surface collisions result in surface capture of the molecule. With these two conditions, (11.56) becomes

$$J_k = \pi R_p^2 \bar{v}_A \alpha (N_\infty - N_S) \quad (11.57)$$

Laboratory measurements of α are possible, though difficult. Table 11.3 lists measurements of α relevant to mineral dust chemistry.

A useful metric of the sensitivity of J to the difference between the kinetic regime and the continuum regimes is obtained by taking the ratio of (11.57) to (11.48).

$$\frac{J_k}{J_c} = \frac{\alpha \bar{v}_A R_p}{4D_{AB}} \quad (11.58)$$

If we assume that $D_{AB} = \lambda_{AB} \bar{v}_A / 3$ (11.11), then (11.58) becomes

$$\frac{J_k}{J_c} = \frac{3\alpha R_p}{4Kn_{AB}} \quad (11.59)$$

The maximum flux of A to the particle through kinetic collisions occurs when $N_S = 0$

$$J_k^{\max} = \pi R_p^2 \bar{v}_A \alpha N_\infty \quad (11.60)$$

If the rate of change of ambient [A] is due solely to mass uptake of kinetic collisions, then (11.60) implies

$$\frac{d[A]}{dt} = -\pi R_p^2 \bar{v}_A \alpha [A] \quad (11.61)$$

$$= -J_k^{\max} \quad (11.62)$$

11.4.4 Transition Regime

As shown in the previous two sections, the rate of uptake of gas phase molecules by a surface depends on the “regime” which characterizes the mean free path of the molecules relative to the size of the particle. When the Knudsen number $Kn \gg 1$, only the kinetic regime is important. Bulk phase diffusion is too slow to compete with kinetic impacts from the far field, and (11.57) describes the loss of A to the surface. When Kn is of order unity or

less, both kinetic impacts and continuum, bulk phase diffusion effects are important. Bulk phase diffusion serves to transport $[A]$ within order one mean free path of the particle, and the final step to the particle surface is a reversible kinetic jump. In practice there is no clear distinction between the two regimes, but the rate of uptake should smoothly transition between the two.

In the troposphere, continuum diffusion is significant to atmospheric aerosols of interest. We shall first estimate the total surface uptake by assuming that continuum that kinetic transport acts in series to bulk gas phase diffusion. This assumption neglects matching the boundary conditions between the continuum and kinetic regimes, but serves to illustrate the overall physics of the problem. A solution which accounts for the boundary conditions will be shown below. First we define the characteristic time scales for diffusive and interfacial transport, using (11.52) and (11.62), respectively

$$\tau_{\text{dg}} = 4\pi R_p D_A \quad (11.63)$$

$$\tau_i = \pi R_p^2 \bar{v}_A \alpha \quad (11.64)$$

Adding (11.52) in series to (11.62) to obtain the total uptake

$$\begin{aligned} \frac{1}{\tau_t} &= \frac{1}{\tau_{\text{dg}}} + \frac{1}{\tau_{\text{kn}}} \\ &= \frac{1}{4\pi R_p D_A} + \frac{1}{\pi R_p^2 \bar{v}_A \alpha} \\ &= \frac{1}{4\pi R_p D_A} \times \frac{\alpha \bar{v}_A R_p}{\alpha \bar{v}_A R_p} + \frac{1}{\pi R_p^2 \bar{v}_A \alpha} \times \frac{4D_A}{4D_A} \\ &= \frac{4D_A + \alpha \bar{v}_A R_p}{4\pi \alpha \bar{v}_A R_p^2 D_A} \\ \tau_t &= \frac{4\pi \alpha \bar{v}_A R_p^2 D_A}{4D_A + \alpha \bar{v}_A R_p} \end{aligned} \quad (11.65)$$

The most common assumption which rigorously meshes the kinetic theory with the continuum theory of gaseous deposition is due to Fuchs (1964). His technique is to match the flux prediction by continuum transport theory to the flux predicted by kinetic transport theory at a distance Δ from the surface of the particle. Thus flux matching assumes that continuum processes control the transport of the gas from the ambient background to a radial distance Δ from the surface of the particle. For $R_p < r < R_p + \Delta$, the gas transfer is assumed to obey kinetic theory. This is a reasonable hypothesis, since, at the microscopic level, the last jump of a vapor phase molecule before colliding with the surface must appear to the molecule as a kinetic jump. Thus the flux matching technique recognizes that the fluid continuum description does not apply to individual molecules on the microscopic level. Implicit in the flux matching assumption is that $\Delta \sim \lambda$. The exact value of Δ depends on the form of the assumptions employed. We now present the original formulation of Fuchs (1964), which makes no assumption on the relative masses of the trace gas A and the medium B. We shall assume that the medium B is air.

The solution of this problem leads to an expression for J in terms of D_{AB} . As noted previously, there are many possible expressions for D_{AB} in terms of λ_{AB} . Substituting $D_{AB} =$

$\lambda_{AB}\bar{v}_A/3$ and expressing the result in terms of J_c (11.48) leads to

$$\frac{J}{J_c} = \frac{3}{4} \times \frac{1 + \text{Kn}\Delta/\lambda}{\frac{3}{4} + \text{Kn} + (\Delta/\lambda)\text{Kn}^2} \quad (11.66)$$

where the subscript $_{AB}$ is implied for all quantities. Using the assumptions of (11.59), (11.66) implies

$$\frac{J}{J_k} = \frac{1 + \text{Kn}\Delta/\lambda}{1 + (\text{Kn}\Delta/\lambda) + \frac{3}{4}\text{Kn}^{-1}} \quad (11.67)$$

Fuchs and Sutugin (1971, MFC) proposed, for $\alpha = 1$, (Seinfeld and Pandis, 1997)

$$\frac{J}{J_c} = \frac{1 + \text{Kn}}{1 + 1.71\text{Kn} + \frac{4}{3}\text{Kn}^2} \quad (11.68)$$

which, for $\alpha \neq 1$, becomes

$$\frac{J}{J_c} = \frac{\frac{3}{4}\alpha(1 + \text{Kn})}{\text{Kn}^2 + \text{Kn} + 0.283\text{Kn}\alpha + \frac{3}{4}\alpha} \quad (11.69)$$

Many variations of (11.66) have been proposed. Fuchs and Sutugin (1970, MFC) proposed (Brasseur et al., 1999)

$$-\frac{d[A]}{dt} = \pi\alpha\bar{v}_A R_p^2[A] \left(1 + \frac{3\alpha(1 + 0.47\text{Kn})}{4\text{Kn}(1 + \text{Kn})}\right)^{-1} \quad (11.70)$$

It is unclear whether (11.70) is or should be identical to (11.69)

11.4.5 Aerosol Motion

11.5 Diffusion Limited Rates

Chapter 12

Aqueous Chemistry

Many different physical quantities are used to measure the abundance of a dissolved species in liquid or particulate matter. When the phase of the species and particle is liquid, we refer to the trace species as the solute and the bulk substance (usually water) as the solvent. The mixture of the solute and the solvent is called the solution. Most often in atmospheric chemistry the solvent is considered to be pure liquid water. However, a significant fraction of some aerosols may be solute. For example, a typical stratospheric sulfuric acid aerosol may be composed of 75% H_2SO_4 and 25% H_2O by weight.

Aqueous phase chemical reactions are usually expressed in terms of the solute molarity or molar concentration c . Molarity expresses the solute concentration in mol L^{-1} . However, since the volume of a solution depends on its temperature, molar concentration changes with temperature. Concentration may also be expressed in terms of molality, or mol kg^{-1} . Molality has the advantage of being analogous to a mass mixing ratio, i.e., it does not change due to temperature or volume fluctuations. Because 1 kg of liquid water is approximately 1 L at STP, dilute aqueous solutions in water have the property that the molarity is approximately numerically equal to the molality.

The molality of a solution is proportional to the mass fraction of solute in the solution.

Another useful measure is the molar concentration, measured in mol m^{-3} . The molar concentration c and molality X may be expressed in terms of each other using

$$X = \frac{c}{\rho - \mathcal{M}c} \quad (12.1)$$

$$c = \frac{X\rho_s}{\mathcal{M}X + 1} \quad (12.2)$$

where ρ_s is the density of the solution (solute + solvent) and \mathcal{M} is the molecular weight of the solute.

12.1 Henry's Law

The English chemist William Henry first quantified the linear dependence of the molar fraction of ideal dilute solutions. He related the partial pressure p_A of a gaseous species A to the molality X_A of A in an aqueous dilute solution. Molality is another term for volume

mixing ratio, i.e., the number of molecules of A per molecule of liquid. According to Henry's Law

$$[X_A] = H_A p_A \quad (12.3)$$

where H_A is the Henry's law coefficient of species A. The traditional units of H_A are $\text{mol L}^{-1} \text{atm}^{-1}$, and these are the dimensions used by Seinfeld and Pandis (1997). In these units, p_A should be specified in atmospheres (atm), and $[X_A]$ will be in mol L^{-1} . The dimensions of mol L^{-1} are often abbreviated simply as M. Thus the dimensions of H_A are often written Matm^{-1} . However, many other units for H are used in the literature. The review article Sander (1999a) presents an excellent summary of the various definitions, dimensions, and conversion factors for Henry's law constants.

Further complicating matters, some chemists define H_A by placing it on the LHS of (12.3) (e.g., Atkins, 1990). Whichever system of units and definition of H are employed, it is imperative to be sure that the dimensions of $[X_A]$, H_A , and p_A are commensurate. Using $\text{mol L}^{-1} \text{atm}^{-1}$ in (12.3), H_A increases with solubility and very soluble gases have large Henry's Law coefficients (e.g., $H_{\text{HNO}_3} = 2.1 \times 10^5 \text{ mol L}^{-1} \text{atm}^{-1}$).

Table 12.1 shows H at 298 K for many important atmospheric compounds. Sander (1999b) maintains an online database of Henry's Law coefficients and useful ancillary material at <http://www.mpch-mainz.mpg.de/~sander/res/henry.html>. The solubility of these compounds spans eight orders of magnitude. Liquid water is relatively impermeable to gases such as NO and O₃. Most of the mass of these insoluble species is present in the gas phase in the interstitial air between aerosols and clouds. Since fewer molecules of insoluble species must diffuse into the liquid phase, these species quickly adjust to a Henry's Law equilibrium in typical clouds. Highly soluble species, on the other hand, may be diffusion limited and take a long time to reach Henry's Law equilibrium. Thus more care must be taken before assuming gases such as HNO₃ and H₂O₂ are in Henry's Law equilibrium.

We emphasize that Henry's Law (12.3) is valid only for dilute solutions of A. Solutions comprised mostly of A obey another law, Raoult's Law (e.g., Atkins, 1990; Seinfeld and Pandis, 1997).

The temperature dependence of H_A is given by

$$H_A(T) = H_A(T_0) \exp \left[\frac{\Delta H_A}{R^*} \left(\frac{1}{T_0} - \frac{1}{T} \right) \right] \quad (12.4)$$

where R^* is the universal gas constant and ΔH_A is the change in enthalpy of A due to its dissolution into the aqueous phase, i.e., the heat released by the phase change of A from the vapor to the aqueous state. ΔH_A is sometimes called the heat of dissolution.

12.2 Aqueous Equilibria

The most important liquid in the atmosphere is water. Solutions for which liquid water is the solvent are called aqueous solutions. Many trace gases dissolved in an aqueous solution rapidly dissociate into ions. Table 12.2 lists the equilibrium constant and temperature dependence of many important atmospheric species in equilibrium with liquid water.

Table 12.1: Henry's Law coefficients of Gases Dissolving in Liquid Water^a

^b Formula	Name	^c H_{298} M atm ⁻¹
O ₂	Oxygen	1.3×10^{-3}
NO	Nitric oxide	1.9×10^{-3}
C ₂ H ₄		4.8×10^{-3}
NO ₂	Nitrogen dioxide	1.0×10^{-2}
O ₃	Ozone	1.13×10^{-2}
N ₂ O	Nitrous oxide	2.5×10^{-2}
CO ₂	Carbon dioxide	3.4×10^{-2}
H ₂ S	Hydrogen sulfide	0.12
CH ₃ SCH ₃	Dimethyl sulfide (DMS)	0.56
SO ₂	Sulfur dioxide	1.23
OH	Hydroxyl	25
HNO ₂	Nitrous acid	49
NH ₃	Ammonia	62
HCl	Hydrogen chloride	727
HO ₂	Hydroperoxyl	2.0×10^3
H ₂ O ₂	Hydrogen peroxide	7.45×10^4
HNO ₃	Nitric acid	2.1×10^5
^d NO ₃	Nitrate	2.1×10^5

^aSources: Seinfeld and Pandis (1997), p. 341; DeMore et al. (1997), p. 246, Table 65, <http://www.mpch-mainz.mpg.de/~sander/res/henry.html>

^bCompounds are listed in order of increasing solubility

^cValues of H (mol L⁻¹ atm⁻¹) are for 298 K

^dDeMore et al. (1997), p. 246, Table 65 report $H_{\text{NO}_3} = 0.6 \pm 0.3 \text{ mol L}^{-1} \text{ atm}^{-1}$. The discrepancy is unexplained.

12.2.1 Water

A small fraction of the water solvent dissociates into hydrogen ions and hydroxide ions



The equilibrium constant for (R11) $K'_{\text{H}_2\text{O}}$ is

$$K'_{\text{H}_2\text{O}} = \frac{[\text{H}^+][\text{OH}^-]}{[\text{H}_2\text{O}]} \quad (12.5)$$

where the measured value of $K'_{\text{H}_2\text{O}}$ at 298 K is 1.82×10^{-16} M. Such a small number of ions per H₂O molecule means that $[\text{H}_2\text{O}]$ is constant to a very good approximation. Studies of bulk liquid water tell us that the molar concentration of pure water, $[\text{H}_2\text{O}]$, is about 55.5 M. Since $[\text{H}_2\text{O}]$ is nearly constant, it is usual to define a new equilibrium constant for (R11) which

Table 12.2: Aqueous Equilibrium Constants of Important Atmospheric Trace Gases^a

Symbol	Equilibrium	^b K_{298} mol L ⁻¹	^b ΔH_{298} kcal mol ⁻¹	^b $\Delta H_{298}/R^*$ K	Ref.
^c K_{R11}	$\text{H}_2\text{O} \rightleftharpoons \text{H}^+ + \text{OH}^-$	1.0×10^{-14}	13.35	-6710	SeP97
K_{R13}	$\text{CO}_2 \cdot \text{H}_2\text{O} \rightleftharpoons \text{H}^+ + \text{HCO}_3^-$	4.3×10^{-7}	1.83	-1000	SeP97
K_{R14}	$\text{HCO}_3^- \rightleftharpoons \text{H}^+ + \text{CO}_3^{2-}$	4.7×10^{-11}	3.55	-1760	SeP97
K_{R16}	$\text{SO}_2 \cdot \text{H}_2\text{O} \rightleftharpoons \text{H}^+ + \text{SO}_3^{2-}$	1.3×10^{-2}	-4.16	1960	SeP97
K_{R17}	$\text{HSO}_3^- \rightleftharpoons \text{H}^+ + \text{SO}_3^{2-}$	6.6×10^{-8}	-2.23	1500	SeP97
K_{R19}	$\text{NH}_3 \cdot \text{H}_2\text{O} \rightleftharpoons \text{OH}^- + \text{NH}_4^+$	1.7×10^{-5}	8.65	-450	SeP97
K_{R21}	$\text{HNO}_3 \cdot \text{H}_2\text{O} \rightleftharpoons \text{H}^+ + \text{NO}_3^-$	15.4	???	8700	SeP97
K_{R23}	$\text{H}_2\text{O}_2 \cdot \text{H}_2\text{O} \rightleftharpoons \text{H}^+ + \text{HO}_2^-$	2.2×10^{-12}	???	-3730	SeP97

^aSources: Adapted from Seinfeld and Pandis (1997)

^bValues for equilibrium constant K , and reaction enthalpies ΔH and $\Delta H/R^*$ are specified at 298 K

^cAs shown in (12.6), the units of K_{R11} are M².

subsumes $[\text{H}_2\text{O}]$ into its definition

$$\begin{aligned}
 K_{\text{H}_2\text{O}} &= K'_{\text{H}_2\text{O}}[\text{H}_2\text{O}] \\
 &= [\text{H}^+][\text{OH}^-] \\
 &= 1.0 \times 10^{-14} \text{ M}^2 \text{ at } 298 \text{ K}
 \end{aligned} \tag{12.6}$$

An explicit expression for $[\text{OH}^-]$ in terms of $[\text{H}^+]$ is useful in expressing the charge balance for the solution (discussed below)

$$[\text{OH}^-] = \frac{K_{\text{H}_2\text{O}}}{[\text{H}^+]} \tag{12.7}$$

In pure liquid water there can be only one hydrogen ion per hydroxide ion so that $[\text{H}^+] = [\text{OH}^-] = 1.0 \times 10^{-7} \text{ M}$ (R11). By convention, the concentration of hydrogen ions in a solution defines the pH of the solution

$$\text{pH} = -\log_{10}[\text{H}^+] \tag{12.8}$$

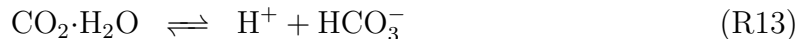
Thus as $[\text{H}^+]$ increases, pH decreases. According to (12.6) the pH of pure water at 298 K is 7.0. Note that $[\text{H}^+]$ in (12.8) must be in units of $\text{M} \equiv \text{mol L}^{-1}$ to produce standard pH values.

12.2.2 Carbon Dioxide CO_2

Carbon dioxide is the most abundant trace gas in the atmosphere following H_2O . Since CO_2 has a very long atmospheric residence time, it is well mixed in the troposphere and stratosphere. The anthropogenic contribution of CO_2 to the atmosphere has made the question of net CO_2 uptake or release by the oceans very important. Carbonates are also

prevalent in the atmosphere on mineral dust aerosol. These carbonates may play a role in buffering acid rain. To gain understanding of these processes we now examine the aqueous equilibria of CO_2 and its products.

A CO_2 molecule dissolved in pure water ends in one of three complexes: $\text{CO}_2\cdot\text{H}_2\text{O}$, HCO_3^- , or CO_3^{2-}



When it dissolves in water, CO_2 molecules attach to H_2O forming $\text{CO}_2\cdot\text{H}_2\text{O}$ (R12). This is called hydrolysis. Hydrolyzed CO_2 is written either $\text{CO}_2\cdot\text{H}_2\text{O}$ or $\text{CO}_2(\text{aq})$. The symbols are different but denote the same compound. The $\text{CO}_2\cdot\text{H}_2\text{O}$ may dissociate into a hydrogen ion and a bicarbonate ion (R13). The HCO_3^- may further dissociate into a hydrogen and a carbonate ion (R14).

The equilibrium constants of equilibrium reactions (R12)–(R14) are

$$K_{\text{R12}} = \frac{[\text{CO}_2\cdot\text{H}_2\text{O}]}{p_{\text{CO}_2}} \quad (12.9)$$

$$\equiv H_{\text{CO}_2}$$

$$K_{\text{R13}} = \frac{[\text{H}^+][\text{HCO}_3^-]}{[\text{CO}_2\cdot\text{H}_2\text{O}]} \quad (12.10)$$

$$K_{\text{R14}} = \frac{[\text{H}^+][\text{CO}_3^{2-}]}{[\text{HCO}_3^-]} \quad (12.11)$$

Note that (12.9) is the definition of the Henry's Law coefficient for CO_2 (12.3). The measured values of K_{R13} and K_{R14} at 298 K are given in Table 12.2.

The concentrations of $\text{CO}_2\cdot\text{H}_2\text{O}$, HCO_3^- , and CO_3^{2-} may be expressed in terms of (12.9)–(12.11). Rearranging (12.9)

$$[\text{CO}_2\cdot\text{H}_2\text{O}] = H_{\text{CO}_2} p_{\text{CO}_2} \quad (12.12)$$

Again, this is simply a statement of Henry's Law equilibrium (12.3). Note that $[\text{CO}_2\cdot\text{H}_2\text{O}]$ depends on temperature through H_{CO_2} (12.4). Making use of (12.12) in (12.10)

$$\begin{aligned} [\text{HCO}_3^-] &= \frac{K_{\text{R13}}[\text{CO}_2\cdot\text{H}_2\text{O}]}{[\text{H}^+]} \\ &= \frac{p_{\text{CO}_2} H_{\text{CO}_2} K_{\text{R13}}}{[\text{H}^+]} \end{aligned} \quad (12.13)$$

In addition to temperature, $[\text{HCO}_3^-]$ also depends on pH. Using (12.13) in (12.11)

$$\begin{aligned} [\text{CO}_3^{2-}] &= \frac{K_{\text{R14}}[\text{HCO}_3^-]}{[\text{H}^+]} \\ &= \frac{p_{\text{CO}_2} H_{\text{CO}_2} K_{\text{R13}} K_{\text{R14}}}{[\text{H}^+]^2} \end{aligned} \quad (12.14)$$

Thus $[\text{CO}_3^{2-}]$ increases rapidly with increasing pH. If this seems confusing, remember that pH increases as $[\text{H}^+]$ decreases.

HCO_3^- and CO_3^{2-} are inevitable products of CO_2 dissolution. The $\text{CO}_2 \cdot \text{H}_2\text{O}$ which dissociates into these products is replaced by additional dissolved CO_2 . This additional CO_2 is not accounted for in the definition of Henry's Law (12.3). Thus (12.12) does not account for the CO_2 which was subsequently converted to HCO_3^- and CO_3^{2-} . In order to compute the total amount of CO_2 dissolved in the droplets in any form, we define CO_2^Σ as

$$[\text{CO}_2^\Sigma] = [\text{CO}_2 \cdot \text{H}_2\text{O}] + [\text{HCO}_3^-] + [\text{CO}_3^{2-}] \quad (12.15)$$

Then, using (12.12)–(12.14) we find

$$[\text{CO}_2^\Sigma] = p_{\text{CO}_2} H_{\text{CO}_2} \left(1 + \frac{K_{\text{R13}}}{[\text{H}^+]} + \frac{K_{\text{R13}} K_{\text{R14}}}{[\text{H}^+]^2} \right) \quad (12.16)$$

$$\equiv p_{\text{CO}_2} H_{\text{CO}_2}^* \quad (12.17)$$

where (12.17) defines the effective Henry's Law coefficient $H_{\text{CO}_2}^*$.

The effective Henry's Law coefficient H^* of a compound accounts for the total dissolution of the compound in the aqueous phase including all dissociation pathways. Thus $H^* \geq H$ for all compounds.

Until now, we have not discussed the charge balance in the solution. In bulk liquids the number of positive ions must equal the number of negative ions, a condition called electroneutrality. The electroneutrality equation for a system composed of N^+ positive ions and N^- negative ions is

$$\sum_{i=1}^{N^+} q_i [A_i] = \sum_{i=1}^{N^-} q_i [A_i] \quad (12.18)$$

where q_i is the net charge and $[A_i]$ the concentration of ion A_i . In a closed system containing only CO_2 and liquid water, electroneutrality (12.18) requires that

$$1 \times [\text{H}^+] = 1 \times [\text{OH}^-] + 1 \times [\text{HCO}_3^-] + 2 \times [\text{CO}_3^{2-}] \quad (12.19)$$

where we have explicitly weighted each solute by its net charge q_i . Electroneutrality provides the closure condition which allows us to determine the concentration of all the ions in a system.

The electroneutrality condition in terms of $[\text{H}^+]$ is obtained by substituting $[\text{OH}^-]$ (12.7), $[\text{HCO}_3^-]$ (12.13), and $[\text{CO}_3^{2-}]$ (12.14) into (12.19)

$$[\text{H}^+] = \frac{K_{\text{H}_2\text{O}}}{[\text{H}^+]} + \frac{p_{\text{CO}_2} H_{\text{CO}_2} K_{\text{R13}}}{[\text{H}^+]} + \frac{2p_{\text{CO}_2} H_{\text{CO}_2} K_{\text{R13}} K_{\text{R14}}}{[\text{H}^+]^2} \quad (12.20)$$

This is a cubic equation in one unknown, $[\text{H}^+]$

$$[\text{H}^+]^3 - (K_{\text{H}_2\text{O}} + p_{\text{CO}_2} H_{\text{CO}_2} K_{\text{R13}})[\text{H}^+] - 2p_{\text{CO}_2} H_{\text{CO}_2} K_{\text{R13}} K_{\text{R14}} = 0 \quad (12.21)$$

The ambient temperature T determines the rate coefficients $K_{\text{H}_2\text{O}}$, H_{CO_2} , K_{R13} , and K_{R14} through (12.4). If T and p_{CO_2} are known, then (12.21) may be solved numerically for $[\text{H}^+]$.

Consider a system of pure liquid water at 298 K in equilibrium solution with the CO₂ concentration typical of the preindustrial era, $p_{\text{CO}_2} = 270$ ppm. For concreteness, imagine this system as a cloud droplet in a pristine area. We gather the properties describing this system from Tables 12.1 and 12.2

$$\begin{aligned} p_{\text{CO}_2} &= 270 \times 10^{-6} \text{ atm} \\ K_{\text{H}_2\text{O}} &= 1.0 \times 10^{-14} \text{ M}^2 \\ H_{\text{CO}_2} &= 3.4 \times 10^{-2} \text{ M atm}^{-1} \\ K_{\text{R13}} &= 4.3 \times 10^{-7} \text{ M} \\ K_{\text{R14}} &= 4.7 \times 10^{-11} \text{ M} \end{aligned}$$

To obtain the pH, we must solve

$$x^3 + bx + c = 0 \quad (12.22)$$

where the coefficients are defined by (12.20)

$$\begin{aligned} b &= -(K_{\text{H}_2\text{O}} + p_{\text{CO}_2} H_{\text{CO}_2} K_{\text{R13}}) \\ &= -3.96 \times 10^{-12} \\ c &= -2p_{\text{CO}_2} H_{\text{CO}_2} K_{\text{R13}} K_{\text{R14}} \\ &= -371 \times 10^{-24} \end{aligned}$$

This solution to (12.22) is obtained by numerical methods and we find that

$$\begin{aligned} \text{H}^+ &= 2.70 \times 10^{-6} \text{ M} \\ \text{OH} &= 2.70 \times 10^{-6} \text{ M} \\ \text{pH} &= x.x \\ \text{CO}_2 \cdot \text{H}_2\text{O} &= 2.70 \times 10^{-6} \text{ atm} \times \frac{3.4 \times 10^{-2} \text{ M}}{\text{atm}} = 91.8 \text{ nM} \\ \text{HCO}_3^- &= \times 10^{-6} \text{ atm} \times \frac{3.4 \times 10^{-2} \text{ M}}{\text{atm}} = 91.8 \text{ nM} \\ \text{CO}_3^{2-} &= \times 10^{-6} \text{ atm} \times \frac{3.4 \times 10^{-2} \text{ M}}{\text{atm}} = 91.8 \text{ nM} \end{aligned} \quad (12.23)$$

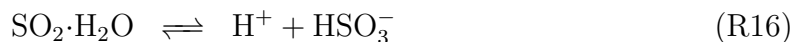
In the year 2000, the ambient concentration of CO₂ was about $p_{\text{CO}_2} = 355$ ppm, an increase of 31% relative to preindustrial levels. At these modern levels, the coefficients b and c in (12.22) become XXX and YYY, respectively. The concentrations in (12.23) become These new constants yield a pH for pure rainwater of XXX. Thus anthropogenic activities have increased the pH of rain by XXX%.

12.2.3 Sulfur Dioxide SO₂

Aqueous phase chemistry plays a very important role in the overall oxidation of S(IV) to S(VI) in the atmosphere, producing perhaps as much as 50% (Barth et al., 2000). SO₂ emissions center over industrial regions, and understanding phenomena such as acid rain

and ship-tracks depends on understanding SO_2 aqueous phase chemistry. The equilibrium Henry's Law constant of SO_2 is 1.23 M atm^{-1} at 298 K. Thus SO_2 itself is not highly soluble in water. However, as we shall show below, total SO_2 dissolution is highly sensitive to pH and this can result in very high concentrations of SO_2 in cloud water.

SO_2 equilibrates with water by the types of paths as CO_2 . A gaseous SO_2 molecule dissolved in pure water ends in one of three complexes: $\text{SO}_2 \cdot \text{H}_2\text{O}$, HSO_3^- , or SO_3^{2-}



After dissolving in liquid water (R15), the hydrolyzed sulfur dioxide may dissociate into a hydrogen ion and a bisulfite ion (R16). The HSO_3^- may further dissociate into a hydrogen and a sulfite ion (R17). The equilibrium constants of equilibrium reactions (R15)–(R17) are

$$K_{\text{R15}} = \frac{[\text{SO}_2 \cdot \text{H}_2\text{O}]}{p_{\text{SO}_2}} \quad (12.24)$$

$$\equiv H_{\text{SO}_2}$$

$$K_{\text{R16}} = \frac{[\text{H}^+][\text{HSO}_3^-]}{[\text{SO}_2 \cdot \text{H}_2\text{O}]} \quad (12.25)$$

$$K_{\text{R17}} = \frac{[\text{H}^+][\text{SO}_3^{2-}]}{[\text{HSO}_3^-]} \quad (12.26)$$

Note that (12.24) is the definition of the Henry's Law coefficient for SO_2 (12.3). The measured values of K_{R16} and K_{R17} at 298 K are given in Table 12.2.

The concentrations of $\text{SO}_2 \cdot \text{H}_2\text{O}$, HSO_3^- , and SO_3^{2-} may be expressed in terms of (12.24)–(12.26). Rearranging (12.24) leads to

$$[\text{SO}_2 \cdot \text{H}_2\text{O}] = H_{\text{SO}_2} p_{\text{SO}_2} \quad (12.27)$$

Again, this is simply a statement of Henry's Law equilibrium (12.3). Note that $[\text{SO}_2 \cdot \text{H}_2\text{O}]$ depends on temperature through H_{SO_2} (12.4). Making use of (12.27) in (12.25)

$$\begin{aligned} [\text{HSO}_3^-] &= \frac{K_{\text{R16}}[\text{SO}_2 \cdot \text{H}_2\text{O}]}{[\text{H}^+]} \\ &= \frac{p_{\text{SO}_2} H_{\text{SO}_2} K_{\text{R16}}}{[\text{H}^+]} \end{aligned} \quad (12.28)$$

In addition to temperature, $[\text{HSO}_3^-]$ also depends on pH. Using (12.28) in (12.26)

$$\begin{aligned} [\text{SO}_3^{2-}] &= \frac{K_{\text{R17}}[\text{HSO}_3^-]}{[\text{H}^+]} \\ &= \frac{p_{\text{SO}_2} H_{\text{SO}_2} K_{\text{R16}} K_{\text{R17}}}{[\text{H}^+]^2} \end{aligned} \quad (12.29)$$

Since pH increases as $[\text{H}^+]$ decreases (12.8), $[\text{SO}_3^{2-}]$ increases rapidly with increasing pH. The equilibrium concentration of HSO_3^- increases by nearly one order of magnitude per unit

pH for $1 < \text{pH} < 8$, while $[\text{SO}_3^{2-}]$ increases nearly twice as fast! The strong pH sensitivity of $[\text{HSO}_3^-]$ and $[\text{SO}_3^{2-}]$ is responsible for enabling chemical mechanisms in certain pH regimes, and disabling them in others. Many sure features of cloud droplet chemistry are illustrated below in §12.3.

We define the total dissolved SO_2 , SO_2^Σ , as the sum of the three reservoirs

$$[\text{SO}_2^\Sigma] = [\text{SO}_2 \cdot \text{H}_2\text{O}] + [\text{HSO}_3^-] + [\text{SO}_3^{2-}] \quad (12.30)$$

As shown in Table (10.2), $[\text{SO}_2^\Sigma]$ is the total dissolved sulfur in oxidation state 4. Thus, in accordance with common usage, we shall use $[\text{S(IV)}]$ instead of $[\text{SO}_2^\Sigma]$ in the following. Then, using (12.27)–(12.29) we find

$$[\text{S(IV)}] = p_{\text{SO}_2} H_{\text{SO}_2} \left(1 + \frac{K_{\text{R16}}}{[\text{H}^+]} + \frac{K_{\text{R16}} K_{\text{R17}}}{[\text{H}^+]^2} \right) \quad (12.31)$$

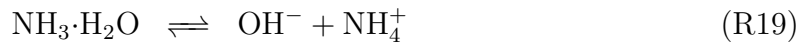
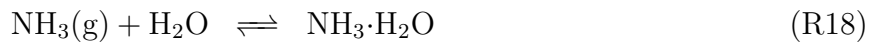
$$\equiv p_{\text{SO}_2} H_{\text{S(IV)}}^* \quad (12.32)$$

where (12.32) defines the effective Henry's Law coefficient $H_{\text{S(IV)}}^*$. The pH sensitivity of $[\text{HSO}_3^-]$ and $[\text{SO}_3^{2-}]$ discussed above causes $H_{\text{S(IV)}}^*$ to increase by an order of magnitude per unit pH for $1 < \text{pH} < 8$. For $\text{pH} < 2$, most aqueous S(IV) in the form of $\text{SO}_2 \cdot \text{H}_2\text{O}$. For $2 < \text{pH} < 7$, the typical range for urban regions, aqueous S(IV) is mostly in the form of HSO_3^- . For $\text{pH} > 7$, aqueous S(IV) is mostly SO_3^{2-} .

12.2.4 Ammonia NH_3

Ammonia is the dominant basic gas in the atmosphere. The equilibrium Henry's Law constant of NH_3 is 62 M atm^{-1} at 298 K. If clouds with $\text{pH} < 5$ are present, nearly all gas phase ammonia will dissolve into the cloud droplets. Thus NH_3 is able to contribute to neutralizing very acidic cloud droplets.

NH_3 dissolved in pure water will end in one of two forms, $\text{NH}_3 \cdot \text{H}_2\text{O}$ or NH_4^+



After dissolving in liquid water (R18), ammonia may dissociate into ammonium ions and hydroxyl ions (R19). Note that the notation NH_4OH is often used instead of $\text{NH}_3 \cdot \text{H}_2\text{O}$. The equilibrium constants of (R18) and (R19) are, respectively

$$K_{\text{R18}} = \frac{[\text{NH}_3 \cdot \text{H}_2\text{O}]}{p_{\text{NH}_3}} \quad (12.33)$$

$$\equiv H_{\text{NH}_3}$$

$$K_{\text{R19}} = \frac{[\text{OH}^-][\text{NH}_4^+]}{[\text{NH}_3 \cdot \text{H}_2\text{O}]} \quad (12.34)$$

The aqueous phase concentrations of $\text{NH}_3 \cdot \text{H}_2\text{O}$ and NH_4^+ may be expressed in terms of (12.33)–(12.34). Rearranging (12.33) leads to

$$[\text{NH}_3 \cdot \text{H}_2\text{O}] = H_{\text{NH}_3} p_{\text{NH}_3} \quad (12.35)$$

which is simply a statement of Henry's Law equilibrium (12.3). Note that $[\text{NH}_3 \cdot \text{H}_2\text{O}]$ depends on temperature through H_{NH_3} (12.4). Making use of (12.35) in (12.34)

$$\begin{aligned} [\text{NH}_4^+] &= \frac{K_{\text{R19}}[\text{NH}_3 \cdot \text{H}_2\text{O}]}{[\text{OH}^-]} \\ &= \frac{p_{\text{NH}_3} H_{\text{NH}_3} K_{\text{R19}}}{[\text{OH}^-]} \\ &= \frac{p_{\text{NH}_3} H_{\text{NH}_3} K_{\text{R19}} [\text{H}^+]}{K_{\text{H}_2\text{O}}} \end{aligned} \quad (12.36)$$

It is traditional to describe concentrations in terms of $[\text{H}^+]$, so we substituted (12.7) for $[\text{OH}^-]$ in the last line. Since $[\text{H}^+]$ decreases as pH increases (12.8), $[\text{NH}_4^+]$ also decreases with increasing pH. Thus ammonia tries to neutralize acidic solutions. This is in contrast to the acidic species we have studied until now.

The total dissolved NH_3 is the sum of the two reservoirs

$$[\text{NH}_3^\Sigma] = [\text{NH}_4^\Sigma] = [\text{NH}_3 \cdot \text{H}_2\text{O}] + [\text{NH}_4^+] \quad (12.37)$$

Thus, NH_3^Σ and NH_4^Σ are equivalent, and, following tradition, we prefer the former. Then, using (12.35)–(12.36) we find

$$[\text{NH}_3^\Sigma] = p_{\text{NH}_3} H_{\text{NH}_3} \left(1 + \frac{K_{\text{R19}}[\text{H}^+]}{K_{\text{H}_2\text{O}}} \right) \quad (12.38)$$

$$\equiv p_{\text{NH}_3} H_{\text{NH}_3}^* \quad (12.39)$$

where $H_{\text{NH}_3}^*$ is the effective Henry's Law coefficient for hydrogen peroxide. The fraction of NH_3^Σ which is NH_4^+ is (12.36) divided by (12.38)

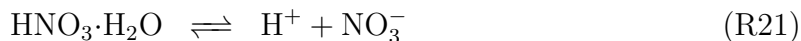
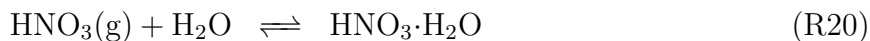
$$\begin{aligned} \frac{[\text{NH}_4^+]}{[\text{NH}_3^\Sigma]} &= \frac{p_{\text{NH}_3} H_{\text{NH}_3} K_{\text{R19}} [\text{H}^+]}{K_{\text{H}_2\text{O}}} \times \frac{1}{p_{\text{NH}_3} H_{\text{NH}_3}} \times \frac{K_{\text{H}_2\text{O}}}{K_{\text{H}_2\text{O}} + K_{\text{R19}} [\text{H}^+]} \\ &= \frac{K_{\text{R19}} [\text{H}^+]}{K_{\text{H}_2\text{O}} + K_{\text{R19}} [\text{H}^+]} \end{aligned} \quad (12.40)$$

As shown in Table 12.2, $K_{\text{R19}} = 1.7 \times 10^{-5} \text{ M}$ at 298 K. Thus $K_{\text{R19}} \times [\text{H}^+] \gg K_{\text{H}_2\text{O}}$ for $\text{pH} < 8$. Thus $[\text{NH}_3^\Sigma]$ is dominated by $[\text{NH}_4^+]$ in most clouds.

12.2.5 Nitric Acid HNO_3

Aqueous phase chemistry is an important pathway for the oxidation of odd nitrogen into nitrates. The aqueous pathway is very efficient because the large Henry's law constants for nitric acid and for nitrate exceed those of all other major atmospheric species. As shown in Table 12.1, $H_{\text{HNO}_3} = H_{\text{NO}_3} = 2.1 \times 10^5 \text{ M atm}^{-1}$ in the presence of clouds. This high solubility means that most gas phase HNO_3 and NO_3 is dissolved in clouds when clouds are present.

Dissolved HNO_3 in pure water takes one of two paths



After dissolving in liquid water (R20), nitric acid may dissociate into nitrate and hydrogen ions (R21). The equilibrium constants of (R20) and (R21) are, respectively

$$K_{\text{R20}} = \frac{[\text{HNO}_3 \cdot \text{H}_2\text{O}]}{p_{\text{HNO}_3}} \quad (12.41)$$

$$\begin{aligned} &\equiv H_{\text{HNO}_3} \\ K_{\text{R21}} &= \frac{[\text{H}^+][\text{NO}_3^-]}{[\text{HNO}_3 \cdot \text{H}_2\text{O}]} \end{aligned} \quad (12.42)$$

The aqueous phase concentrations of $\text{HNO}_3 \cdot \text{H}_2\text{O}$ and NO_3^- may be expressed in terms of (12.41)–(12.42). Rearranging (12.41) leads to

$$[\text{HNO}_3 \cdot \text{H}_2\text{O}] = H_{\text{HNO}_3} p_{\text{HNO}_3} \quad (12.43)$$

which is simply a statement of Henry's Law equilibrium (12.3). Note that $[\text{HNO}_3 \cdot \text{H}_2\text{O}]$ depends on temperature through H_{HNO_3} (12.4). Making use of (12.43) in (12.42)

$$\begin{aligned} [\text{NO}_3^-] &= \frac{K_{\text{R21}}[\text{HNO}_3 \cdot \text{H}_2\text{O}]}{[\text{H}^+]} \\ &= \frac{p_{\text{HNO}_3} H_{\text{HNO}_3} K_{\text{R21}}}{[\text{H}^+]} \end{aligned} \quad (12.44)$$

Thus $[\text{NO}_3^-]$ depends upon pH as well as temperature.

We define the total dissolved HNO_3 , HNO_3^Σ , as the sum of the two reservoirs

$$[\text{HNO}_3^\Sigma] = [\text{HNO}_3 \cdot \text{H}_2\text{O}] + [\text{NO}_3^-] \quad (12.45)$$

Then, using (12.43)–(12.44) we find

$$[\text{HNO}_3^\Sigma] = p_{\text{HNO}_3} H_{\text{HNO}_3} \left(1 + \frac{K_{\text{R21}}}{[\text{H}^+]} \right) \quad (12.46)$$

$$\equiv p_{\text{HNO}_3} H_{\text{HNO}_3}^* \quad (12.47)$$

where $H_{\text{HNO}_3}^*$ is the effective Henry's Law coefficient for nitric acid.

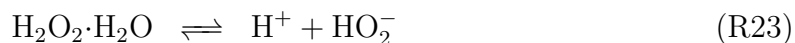
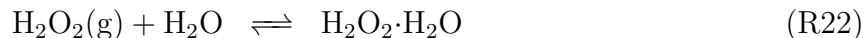
Although $\text{HNO}_3 \cdot \text{H}_2\text{O}$ and NO_3^- are both possible reservoirs for dissolved HNO_3 , the extreme solubility of HNO_3 causes virtually all HNO_3 dissolved in cloud water forms NO_3^- , not $\text{HNO}_3 \cdot \text{H}_2\text{O}$. To see what precludes $\text{HNO}_3 \cdot \text{H}_2\text{O}$ from being an important reservoir, we must examine the equilibrium coefficients in (12.46). As shown in Table 12.2, $K_{\text{R21}} = 15.4 \text{ M}$ at 298 K. Since $K_{\text{R21}} \gg 1 \gg [\text{H}^+]$, the RHS of (12.46) is always dominated by the concentration of NO_3^- , even in the most acidic cloud droplets. Thus we may approximate $H_{\text{HNO}_3}^*$ (12.47) as

$$\begin{aligned} H_{\text{HNO}_3}^* &\approx \frac{H_{\text{HNO}_3} K_{\text{R21}}}{[\text{H}^+]} \\ &= \frac{3.23 \times 10^6 \text{ M}^2 \text{ atm}^{-1}}{[\text{H}^+]} \quad \text{at 298 K} \end{aligned} \quad (12.48)$$

12.2.6 Hydrogen Peroxide H_2O_2

Hydrogen peroxide is a very soluble atmospheric gas, and an important ingredient in aqueous phase reactions involving both sulfur and nitrogen. The equilibrium Henry's Law constant of H_2O_2 is $7.45 \times 10^4 \text{ M atm}^{-1}$ at 298 K. Thus H_2O_2 can be found in relatively large concentrations in cloud water. Moreover, [Anastasio et al. \(1994\)](#) describe a photochemical production mechanism for H_2O_2 in the aqueous phase. Thus H_2O_2 is likely to participate in most sulfur and nitrogen reduction.

Once H_2O_2 dissolves in pure water, it takes one of two paths



After dissolving in liquid water ([R22](#)), hydrogen peroxide may dissociate into hydroperoxyl and hydrogen ions ([R23](#)). The equilibrium constants of ([R22](#)) and ([R23](#)) are, respectively

$$K_{\text{R22}} = \frac{[\text{H}_2\text{O}_2 \cdot \text{H}_2\text{O}]}{p_{\text{H}_2\text{O}_2}} \quad (12.49)$$

$$\equiv H_{\text{H}_2\text{O}_2}$$

$$K_{\text{R23}} = \frac{[\text{H}^+][\text{HO}_2^-]}{[\text{H}_2\text{O}_2 \cdot \text{H}_2\text{O}]} \quad (12.50)$$

The aqueous phase concentrations of $\text{H}_2\text{O}_2 \cdot \text{H}_2\text{O}$ and HO_2^- may be expressed in terms of ([12.49](#))–([12.50](#)). Rearranging ([12.49](#)) leads to

$$[\text{H}_2\text{O}_2 \cdot \text{H}_2\text{O}] = H_{\text{H}_2\text{O}_2} p_{\text{H}_2\text{O}_2} \quad (12.51)$$

which is simply a statement of Henry's Law equilibrium ([12.3](#)). Note that $[\text{H}_2\text{O}_2 \cdot \text{H}_2\text{O}]$ depends on temperature through $H_{\text{H}_2\text{O}_2}$ ([12.4](#)). Making use of ([12.51](#)) in ([12.50](#))

$$\begin{aligned} [\text{HO}_2^-] &= \frac{K_{\text{R23}}[\text{H}_2\text{O}_2 \cdot \text{H}_2\text{O}]}{[\text{H}^+]} \\ &= \frac{p_{\text{H}_2\text{O}_2} H_{\text{H}_2\text{O}_2} K_{\text{R23}}}{[\text{H}^+]} \end{aligned} \quad (12.52)$$

Thus $[\text{HO}_2^-]$ depends upon pH as well as temperature.

We define the total dissolved H_2O_2 , $\text{H}_2\text{O}_2^\Sigma$, as the sum of the two reservoirs

$$[\text{H}_2\text{O}_2^\Sigma] = [\text{H}_2\text{O}_2 \cdot \text{H}_2\text{O}] + [\text{HO}_2^-] \quad (12.53)$$

Then, using ([12.51](#))–([12.52](#)) we find

$$[\text{H}_2\text{O}_2^\Sigma] = p_{\text{H}_2\text{O}_2} H_{\text{H}_2\text{O}_2} \left(1 + \frac{K_{\text{R23}}}{[\text{H}^+]} \right) \quad (12.54)$$

$$\equiv p_{\text{H}_2\text{O}_2} H_{\text{H}_2\text{O}_2}^* \quad (12.55)$$

where $H_{\text{H}_2\text{O}_2}^*$ is the effective Henry's Law coefficient for hydrogen peroxide.

Although $\text{H}_2\text{O}_2\cdot\text{H}_2\text{O}$ and HO_2^- are both possible reservoirs for dissolved H_2O_2 , $\text{H}_2\text{O}_2\cdot\text{H}_2\text{O}$ is a very weak electrolyte (i.e., does not readily ionize in cloud water to form HO_2^-). To see what precludes HO_2^- from being an important reservoir, we must examine the equilibrium coefficients in (12.54). As shown in Table 12.2, $K_{\text{R23}} = 2.2 \times 10^{-12}$ M at 298 K. Thus $K_{\text{R23}}/[\text{H}^+] < 10^{-4}$ for $\text{pH} < 7.5$. Thus (12.54) is dominated by the concentration of $\text{H}_2\text{O}_2\cdot\text{H}_2\text{O}$, even in very basic cloud droplets.

12.3 Aqueous Sulfur Chemistry

Uptake and subsequent processing of atmospheric SO_2 by aerosol and clouds is one of the most important, and most studied aspects of atmospheric aqueous chemistry. The solubility of S(IV) is strongly pH-dependent, as the effective Henry's Law constant $H_{\text{S(IV)}}^*$ increases by approximately one order of magnitude per unit pH for $1 < \text{pH} < 8$ (§12.3). As the uptake of S(IV) to droplets depends on pH, so is the relative importance of aqueous phase oxidation of S(IV).

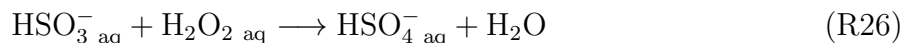
In clouds or aerosols, SO_2 may be oxidized by ozone



Such reactions are fast in the aqueous phase, but slow enough to be neglected in the gas phase (Seinfeld and Pandis, 1997, p. 363). For example,



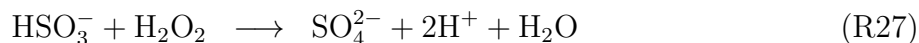
Hydrogen peroxide may form in cloud water Anastasio et al. (1994). Hydrogen peroxide oxidizes SO_2 via



Reaction (R26) requires sufficient aqueous volume to be of importance and may, to a first approximation, be neglected on mineral aerosol (Dentener et al., 1996).

12.4 Aqueous Iron Chemistry

In this section we discuss the catalysis of S(IV) oxidation by Fe(III) and Mn(II). We shall assume this chemistry takes place in the liquid phase. The basic mechanism is known to be



This reaction mechanism was modeled by Pandis and Seinfeld (1989) and Pandis et al. (1992).

12.5 Aqueous Nitrogen Chemistry

Nitrates may be formed through heterogeneous chemistry in the atmosphere and are biologically useful. Thus we shall now concentrate on determining the effects of aerosol chemistry on nitrate production.

12.6 Mass Transport and Diffusion

The uptake of gaseous species onto liquid or solid aerosols is subject to the constraints of mass transport. The equilibrium predicted by Henry's law, for example, will only be reached if there are no barriers to solute transport from the gaseous to the aqueous phase. Such barriers, or, more properly, resistances to mass transport might be due to interfacial resistance, aerodynamic resistance, the rate of diffusion, etc. For more in depth discussion of these processes see, e.g., [Schwartz \(1986\)](#); [Lelieveld and Crutzen \(1991\)](#); [Seinfeld and Pandis \(1997\)](#); [DeMore et al. \(1997\)](#).

Chapter 13

Aerosol Physics

Aerosol physics encompass the processes that nucleate, grow, maintain, and destroy atmospheric particulates. Before describing these processes quantitatively, we first define a set of standard terminology to use. Most definitions are taken verbatim from [Vali \(1985\)](#), and some are followed with supplementary descriptions. aerosol particle: Solid or liquid particle mostly consisting of some substance(s) other than water, and without the stable bulk liquid or solid phases of water on it. haze particle: Partly or wholly water-soluble aerosol particle at humidities exceeding that necessary for deliquescence and in stable equilibrium with respect to changes in humidity. cloud droplet: Bulk (thermodynamically stable) liquid-water droplet, usually formed on a cloud-condensation nucleus, and growing to a size (mass) determined by the available supply of vapor. ice crystal: Bulk (thermodynamically stable) solid water, initially formed by the freezing of a cloud droplet or by deposition nucleation, and growing to a size (mass) determined by the available supply of water vapor. Condensation nuclei (CN): Those particles that will grow to visible size when any liquid condenses on them at supersaturations just below that necessary to activate small ions. Aitken nuclei (AN): Those particles that grow to visible size when water condenses on them at supersaturations just below those that will activate small ions.

The definitions of CN and AN refer to methods of detection and counting of aerosol. Instruments make the aerosol “visible” by condensing some liquid (to count CN) or water specifically (to count AN).

Cloud condensation nuclei (CCN): Particles that can serve as nuclei of atmospheric cloud droplets, i.e., particles on which liquid water condenses at supersaturations typical of atmospheric cloud formation (fraction of a percent to a few percent, depending on cloud type). Concentrations of CCN need to be given in terms of a supersaturation spectrum covering the range of interest or at some specified supersaturation value.

Primary processes (mechanisms) of ice formation: Nucleation of ice from the liquid or vapor phases of water, either homogeneously or heterogeneously. The purpose of this terminology is to emphasize the distinction from secondary processes.

Secondary processes (mechanisms) of ice formation: Creation of ice particles by processes that require prior existence of some other macroscopic (thermodynamically stable) ice particles; examples are splintering of freezing drops, crystal fragmentation, etc.

Ice nuclei (IN): Generic name for substances, usually in the form of aerosol particles, which under suitable conditions of supersaturation or supercooling nucleate ice. This term

is to be used if no distinction is intended or is possible as to the specific nucleation mechanism involved.

Ice nucleation modes: Names or short phrases are needed to refer to particular nucleation modes. Since the details of the molecular embryo formation are difficult to ascertain, it is of great importance that references to nucleation modes be made with the utmost care for clarity of usage, relying, if needed, on more complete descriptions of the phenomenon in question. In terms of ice nucleation, the basic distinction that has to be made is whether nucleation is from the vapor or from the liquid phase. There may be some ambiguity when the metastable phase is the vapor, since the formation of liquid or liquid-like layers might actually be involved in the creation of ice embryos, but unless there is definite evidence for this, the pragmatic view is to consider the bulk vapor as the initial phase. The following definitions aid in making these distinctions.

Deposition nucleation: The formation of ice in a (supersaturated) vapor environment.

Freezing nucleation: The formation of ice in a (supercooled) liquid environment.

1. Condensation freezing: The sequence of events whereby a cloud condensation nucleus (CCN) initiates freezing of the condensate.
2. Contact freezing: Nucleation of a supercooled droplet subsequent to an aerosol particle's coming into contact with it. (This name is preferable to contact nucleation as it focuses attention on the fact that the basic process is freezing.)
3. Immersion freezing: Nucleation of supercooled water by a nucleus suspended in the body of water.

Instrumentation for aerosol measurements:

1. Aethalometer
2. Nephelometer
3. Spectroradiometer
4. Pyranometer
5. Condensation Particle Counter (CPC)
6. Cloud Condensation Nuclei Counter (CCNC)
7. Optical Particle Counter (OPC)
8. Cloud Droplet Probe (CDP)

Chapter 14

Chemistry and Mineral Dust

Mineral dust facilitates both heterogeneous (surface) chemistry and aqueous phase chemistry. One of the greatest challenges in assessing the influence of mineral dust on atmospheric chemistry is in constraining which mechanisms operate in a given meteorological environment (e.g., relative humidity), because the mineralogical composition of dust is very uncertain.

It is known that sulfate and nitrate concentrations vary with mineral. Perhaps the greatest uncertainty is whether or not the mineral dust aerosol is wetted. A wetted particle is simply one on which liquid phase solution exists. A slightly wetted particle may have liquid water in only some facial crevices or nooks. A completely wetted particle is covered in solution. Due to the great size of mineral particles, once a particle is wetted it may act as a giant CCN, immediately growing into a cloud droplet (or at least competing for the vapor to do so). In this case the hygroscopic growth may significantly enhance the cross-sectional area and the volume of the aerosol. Of course the dry volume of the dust particle does not change, but the water coating may significantly alter the particles aerodynamic properties (e.g., fall speed) and optical properties. Thus, there is a complete spectrum of plausible aqueous states that a mineral dust particle may occupy, ranging from completely dry to an activated cloud droplet. Table 14.1 lists the deliquescence relative humidities of electrolyte solutions at 298 K.

Needless to say, the reaction surface available for chemistry is crucial in determining the chemical role of the particle. Surface reactions may occur on a complete dry particle, but it is often found that the overall rate of reaction decreases as the particle ages. The older the particle, the more of its surface that has been covered with reaction products. Once every available surface site has adsorbed the reactants and facilitated a reaction, there is no more space for reactions involving the particle's minerals (e.g., iron). Aqueous reactions, on the other hand, may occur through the entire volume of the droplet. Assuming the reactions are not significantly limited by diffusion, then the volume suitable for reactions greatly exceeds the equivalent volume of surface chemistry sites.

However, surface reactions may operate in all weather, whereas aqueous reactions require specific conditions. Thus the importance of surface chemistry relative to aqueous chemistry depends not only on the reaction mechanism, but upon the synoptic scale environment. For example, surface reactions may be more important than aqueous reactions over arid regions such as deserts.

Thus a complete description of chemistry on mineral dust requires specifications of parameters for both surface and aqueous chemistry.

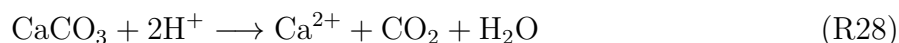
Table 14.1: Deliquescence Relative Humidity of Electrolyte Solutions at 298 K^a

Formula	Name	RHD %
KCl	Potassium chloride	84.2 ± 0.3
Na ₂ SO ₄	Sodium sulfate	84.2 ± 0.4
NH ₄ Cl	Ammonium chloride	80.0
(NH ₄) ₂ SO ₄	Ammonium sulfate	79.9 ± 0.5
NaCl	Sodium chloride	75.3 ± 0.1
NaNO ₃	Sodium nitrate	74.3 ± 0.4
(NH ₄) ₃ H(SO ₄) ₂	Letovicite	69.0
NH ₄ NO ₃	Ammonium nitrate	61.8
NaHSO ₄	Sodium bisulfate	52.0
NH ₄ HSO ₄	Ammonium bisulfate	40.0

^aSources: Source: Adapted from [Seinfeld and Pandis \(1997\)](#), p. 508.

14.1 Role of Carbonate

Wetted alkaline substances such as mineral dust tend to neutralize acidic solutions and thus increase solution pH. The calcium carbonate (CaCO₃) content of soils is important in determining the soil alkalinity. CaCO₃ may neutralize acidity through



The calcium content of arid soils is typically about 5% by weight ([Pye, 1987](#); [Dentener et al., 1996](#)).

The global distributions of CaCO₃, as well as other important crustal minerals, must be obtained from in situ soil samples. The IGBP global soil dataset ([Carter and Scholes, 1998](#); [Global Soil Data Task, 1999](#)) assembles many thousand soil profiles, or pedons, into one quality-controlled dataset. The SOILDATA program included with the dataset is designed to select statistically unbiased samples of soil parameters for any soil vertical level or horizon for a specified geographic region. The resulting global distribution of CaCO₃ peaks strongly around the Arabian Peninsula and Iran, where CaCO₃ accounts for up to 15% of topsoil (defined as soil within 5 cm of surface) mass. The global mean continental CaCO₃ topsoil content is about 2.5%. Water soluble Ca²⁺ is highly correlated ($r \approx 0.8$) with Al near source regions in China. In contrast, Si correlates very poorly with Al in Asian and African dust. Thus Ca is a potentially-useful tracer for total dust.

14.2 Hygroscopic Growth

Heterogeneous chemistry on mineral aerosol is very sensitive to the presence of liquid phase water. Uptake coefficients on wetted aerosols are often orders of magnitude higher than

on dry solids (Table 11.4). Due to its highly varying composition, dust, unfortunately, has no single deliquescence point as do pure salts (Table 14.1). However, observations of the hygroscopic growth factors on mineral dust allow us to make some generalizations.

The theory of hygroscopic growth is discussed in many texts (e.g., Hänel, 1976; Pruppacher and Klett, 1978; Ruhnke and Deepak, 1984; Seinfeld and Pandis, 1997; Wong et al., 1998). Five sophisticated thermodynamic equilibrium models of inorganic aerosol growth are inter-compared in Zhang et al. (2000). First, the increase in aerosol mass due to the accumulation of liquid phase water is called hygroscopic growth.

Wong et al. (1998) provide parameterizations for the hygroscopic growth of H_2SO_4 and $(\text{NH}_4)_2\text{SO}_4$ as a function of RH alone. Consider a size distribution $n(D)$ of dry aerosol with number median diameter \tilde{D}_n and geometric standard deviation σ_g . Our goal is to predict the corresponding size distribution of the aerosol in the wetted state, i.e., at any RH. Let \tilde{D}'_n and σ'_g denote the wet median diameter and geometric standard deviation, respectively. Wong et al. (1998) showed that expressions of the form

$$\frac{\tilde{D}'_n}{\tilde{D}_n} = 1.0 + \exp \left(a_1 + \frac{a_2}{a_3 + \text{RH}} + \frac{a_4}{a_5 + \text{RH}} \right) \quad (14.1)$$

$$\frac{\sigma'_g}{\sigma_g} = 1.0 + \exp \left(b_1 + \frac{b_2}{b_3 + \text{RH}} + \frac{b_4}{b_5 + \text{RH}} \right) \quad (14.2)$$

where a_i and b_i are fitting coefficients.

Hänel (1976) reviewed theoretical and observational approaches to determining the hygroscopic growth factor. He characterized his results in terms of the water activity of a particle's liquid coating with respect to a plane surface. This quantity, called the activity coefficient a for short, is an empirical parameter which defines the thermodynamic properties of the solution relative to the thermodynamic properties of pure water. It may be expressed directly in terms of another measurable parameter, the van't Hoff factor i of the solute as (e.g., Hänel, 1976; Pruppacher and Klett, 1978)

$$a = \frac{n_w}{n_w + i n_s} \quad (14.3)$$

where n_w is the mole number of water, and n_s is the mole number of the dry solute. Table 14.2 contains parameterizations for the activity coefficient of many important atmospheric aerosol species.

Table 14.2: Activity Coefficients^{ab}

$x, \%$	$(\text{NH}_4)_2\text{SO}_4$	NH_4HSO_4	$(\text{NH}_4)_3\text{H}(\text{SO}_4)_2$	Na_2SO_4	NaHSO_4	NaNO_3
C_1	0-78 -2.715e-3	0-97 -3.05e-3	0-78 -2.42e-3	0-40 -3.55e-3	^c 40-67 -1.99e-2	0-98 -5.52e-3
C_2	3.113e-5	-2.94e-5	-4.615e-5	9.63e-5	-1.92e-5	1.286e-4
C_3	-2.336e-6	-4.43e-7	-2.83e-7	-2.97e-6	1.47e-6	-3.496e-6
C_4	1.412e-8	^d	1.843e-8
A_1	5.92e-3	5.87e-3	5.66e-3	8.871e-3	7.56e-3	6.512e-3
A_2	-5.036e-6	-1.89e-6	2.96e-6	3.195e-5	2.36e-5	3.025e-5
A_3	1.024e-8	1.763e-7	6.68e-8	2.28e-7	2.33e-7	1.437e-7
$\sigma(a_w)$	2.76e-3	7.94e-3	5.97e-3	3.87e-3	3.39e-3	6.65e-3
$\sigma(\rho)$	8.98e-5	4.03e-4	2.13e-3	1.71e-3	7.55e-4	3.83e-4

^aSources: [Tang and Munkelwitz \(1994\)](#), p. 18805, Table 1. Coefficients C_i for use in the parameterization $a_w = 1.0 + \sum_{i=1}^{i=4} C_i x^i$ where a_w is water activity and x is the solute weight as a percent of the total solution weight. Coefficients A_i for use in the parameterization $\rho_s = 0.9971 + \sum_{i=1}^{i=3} A_i x^i$ where ρ_s is the density of the solution.

^bRead -2.715e-3 as -2.715×10^{-3}

^cFor this concentration range only, $a_w = 1.557 + \sum C_i x^i$

^dEllipsis indicates coefficient is zero (?)

Table 14.3: Saturation Vapor Pressure of Water Over Planar Surfaces^{ab}

^c Coefficient	Liquid	Ice
c_0	6.107799961	6.109177956
c_1	$4.436518521 \times 10^{-1}$	$5.034698970 \times 10^{-1}$
c_2	$1.428945805 \times 10^{-2}$	$1.886013408 \times 10^{-2}$
c_3	$2.650648471 \times 10^{-4}$	$4.176223716 \times 10^{-4}$
c_4	$3.031240396 \times 10^{-6}$	$5.824720280 \times 10^{-6}$
c_5	$2.034080948 \times 10^{-8}$	$4.838803174 \times 10^{-8}$
c_6	$6.136820929 \times 10^{-11}$	$1.838826904 \times 10^{-10}$
c_0	6.107799961	6.10690449
c_1	$4.436518521 \times 10^{-1}$	$5.02660639 \times 10^{-1}$
c_2	$1.428945805 \times 10^{-2}$	$1.87743264 \times 10^{-2}$
c_3	$2.650648471 \times 10^{-4}$	$4.13476180 \times 10^{-4}$
c_4	$3.031240396 \times 10^{-6}$	$5.72333773 \times 10^{-6}$
c_5	$2.034080948 \times 10^{-8}$	$4.71651246 \times 10^{-8}$
c_6	$6.136820929 \times 10^{-11}$	$1.78086695 \times 10^{-10}$

^aSources: Pruppacher and Klett (1978) p. 625, Pruppacher and Klett (1998) p. 854

^bRange of validity is $-50 < T_c < 50$ C

^cCoefficients for use in $\tilde{e}_\infty(T_c) = c_0 + T_c(c_1 + T_c(c_2 + T_c(c_3 + T_c(c_4 + T_c(c_5 + c_6 T_c))))))$, where T_c is the temperature in Celsius and $\tilde{e}_\infty(T)$ is the saturated vapor pressure in mb. (14.6)

The relations between the total mass of the aerosol m_t , the liquid water mass of the aerosol m_w , the dry mass of the soluble component m_s , the dry mass of insoluble component m_u , and the total dry mass of the aerosol m_d are

$$m_d = m_s + m_u \quad (14.4)$$

$$m_t = m_d + m_w \quad (14.5)$$

We shall now consider the relationship between the ambient relative humidity RH and aerosol mass. Recall that the equilibrium vapor pressure of a gas in contact with the condensed phase of the gas is the saturation vapor pressure of the gas and depends only on temperature. However, as shown in §..., the saturation vapor pressure of a gas over a curved surface, \tilde{e}_S , depends additionally on the radius of curvature of the surface. Thus let $\tilde{e}_\infty(T)$ and $\tilde{e}_S(T, R_p)$ represent the saturated water vapor pressure far from the aerosol surface, and at the aerosol surface, respectively. Parameterizations for the saturated vapor pressure of water over planar liquid and ice surfaces are described in Table 14.3. The relationship between \tilde{e}_∞ and \tilde{e}_S is called Kelvin's Law

$$\tilde{e}_S = \tilde{e}_\infty \exp\left(\frac{2\mathcal{M}_{\text{H}_2\text{O}}\sigma}{\rho_w R^* T R_p}\right) \quad (14.6)$$

The difference between RH_∞ and RH^* exceeds 1% for $R_p \lesssim 0.1 \mu\text{m}$ and exceeds 10% for $R_p \lesssim 0.01 \mu\text{m}$.

The relative humidity RH is simply the ratio of the ambient water vapor pressure, e , to the saturated vapor pressure for the same temperature

$$\text{RH} = \frac{e}{\tilde{e}_\infty(T)} \quad (14.7)$$

Note that p is used for partial pressures of most atmospheric gases, e.g., p_{CO_2} , but the letter e is reserved specifically for the partial pressure of water vapor, and thus an H_2O subscript for p would be redundant. The relative humidity at the surface of the particle is RH_S . RH_S differs from RH_∞ due to the Kelvin effect (14.6), i.e., curvature. Combining (14.6) and (14.7)

$$\text{RH}_S = \text{RH} \exp\left(\frac{2\mathcal{M}_{\text{H}_2\text{O}}\sigma}{\rho_w R^* T R_p}\right) \quad (14.8)$$

We define the mean linear mass increase coefficient $\bar{\mu}$ as

$$\bar{\mu} = \frac{m_w(1 - \text{RH}_S)}{m_d \text{RH}_S} \quad (14.9)$$

The quantities on the RHS of (14.9) are observable, so $\bar{\mu}$ may be measured in field or laboratory experiments. For practical reasons $\bar{\mu}$ is usually inferred from macroscopic aggregations of aerosol samples where curvature effects may be ignored. However, $\bar{\mu}$ itself is independent of size. Thus it is valid to apply an $\bar{\mu}$ inferred from measurements of macroscopic, bulk aerosol samples to individual aerosol particles (Hänel, 1976).

Inverting (14.9) allows us to express m_w in terms of m_d

$$\frac{m_w}{m_d} = \frac{\bar{\mu} \text{RH}_S}{1 - \text{RH}_S} \quad (14.10)$$

Table 14.4 shows water activity a_w , mean linear mass increase coefficient $\bar{\mu}$, and water uptake per unit mass of dry material m_w/m_d for both increasing and decreasing a_w . $\bar{\mu}$ reaches a maximum value of 0.133 at $\text{RH} \approx 80\%$. The aerosol contains more water on the decreasing branch of relative humidity than on the increasing branch. This is called the hysteresis effect. The water mass of the aerosol exceeds the dry mass when $\text{RH} \gtrsim 90\%$. The representativeness of these results is unknown. Examining the adsorption of water vapor on clays, sand and soot at 298 K, Winkler (1970, MFC), as cited by Pruppacher and Klett (1978), p. 119, found that $m_w \lesssim 0.5m_d$ for $\text{RH} < 95\%$.

The wet radius r may be expressed in terms of the dry radius r_d according to

$$\frac{r}{r_d} = \left(1 + \frac{\bar{\mu}\rho_{p,d}\text{RH}_S}{\rho_w(1 - \text{RH}_S)}\right)^{1/3} \quad (14.11)$$

where ρ_d and ρ_w are the densities of the dry aerosol and of liquid water, respectively. Equation (14.12) is valid for $\text{RH} < 0.90\text{--}0.95$ and for $r_d > 0.1\text{ }\mu\text{m}$. If these constraints are too restrictive, Hänel (1976) derived an expression valid for smaller particles at higher RH

$$\frac{r}{r_d} = \left(1 + \frac{\bar{\mu}\rho_d\text{RH}_S}{\rho_w(1 - \text{RH}_S)}\right)^{1/3} - \frac{2\sigma v_w}{R_w T r_d} \frac{\text{RH}_S}{1 - \text{RH}_S} \left(1 + \frac{\bar{\mu}\rho_d\text{RH}_S}{\rho_w(1 - \text{RH}_S)}\right)^{-1/3} \quad (14.12)$$

Equation (14.12) is valid for $0.70 < \text{RH} < 0.99$ and for $r_d > 0.04\text{ }\mu\text{m}$.

Table 14.4: Observed Hygroscopic Growth of Saharan Dust^a

Increasing a_w			Decreasing a_w		
a_w	$\bar{\mu}$	m_w/m_d	a_w	$\bar{\mu}$	m_w/m_d
0.204	0.032	0.008			
			0.224	0.049	0.014
			0.294	0.045	0.019
0.349	0.024	0.013			
0.457	0.021	0.018			
			0.506	0.047	0.048
0.590	0.024	0.034			
			0.623	0.072	0.119
0.648	0.033	0.060			
0.700	0.088	0.206			
			0.701	0.175	0.410
0.751	0.130	0.392			
			0.753	0.158	0.482
0.789	0.133	0.497			
0.843	0.120	0.644			
0.896	0.107	0.922			
0.900	0.105	0.945			
0.955	0.075	1.604			
0.971	0.072	2.411			
0.976	0.071	2.887			
0.986	0.067	4.719			
0.990	0.065	6.435			
0.997	0.065	20.90			
1.000	0.081	∞			

^aSource: Hänel (1976), p. 115, Table IV. Measurements taken over the Atlantic from April 16–25, 1969. The aerosol samples were identified as Saharan dust based on prevailing meteorology and sample analysis.

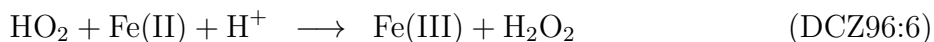
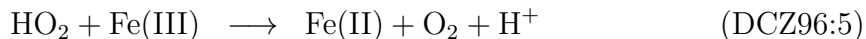
14.2.1 Zhang's Mechanism

Zhang and Carmichael (1999) studied the influence of mineral dust on tropospheric chemistry in East Asia.

14.2.2 Dentener's Mechanism

Zhang et al. (1994) studied the synoptic scale impact of mineral dust on particulate nitrate and sulfate formation. Using similar methods on a global scale, Dentener et al. (1996) performed the first global study of heterogeneous chemistry on mineral dust particles. The framework they developed for heterogeneous chemistry on mineral dust provides an excellent overview of the roles of mineral dust as an agent for sulfur and nitrogen oxidation.

Dentener et al. (1996) assumed HO_2 transfers to both dry and wetted dust particles, where it reacts with Fe to produce H_2O_2 .



Unfortunately, measurements of α are not available for HO_2 to mineral dust transfer itself. However α has been measured for liquid water and H_2SO_4 surfaces. These measurements show $\alpha(\text{HO}_2 \rightarrow \text{H}_2\text{O}) > 0.01$ – 0.2 and $\alpha(\text{HO}_2 \rightarrow \text{H}_2\text{SO}_4) > 0.05$, respectively. Saharan dust at relative humidity $\text{RH} > 50\%$ takes up significant amounts of water. Based on these measurements, Dentener et al. (1996) chose $\gamma(\text{HO}_2 \rightarrow \text{dust}) = 0.1$ for both wetted and dry mineral aerosol.

Dentener et al. (1996) ignored transfer of gas phase OH and H_2O_2 to mineral dust surfaces for two reasons. First, the loss rate of OH to mineral dust surfaces is expected to be negligible compared to its quick destruction due to gas phase processes. Second, hydrogen peroxide has a large mass accommodation coefficient for aqueous surfaces, but the small volume of water available on dust particles seems to imply a very small sink for H_2O_2 . There are two reasons why this assumption should be re-examined. First, dust particles may act as giant CCN, or become incorporated in existing cloud droplets through collisions. Sufficient aqueous volume is available in cloud droplets to process large amounts of H_2O_2 in, e.g., SO_2 reduction. The second reason is that reaction (DCZ96:6) may cause dust particles to be a source of H_2O_2 rather than a sink.

Dentener et al. (1996) paid particular attention to the role of heterogeneous chemistry on mineral dust as a sink for odd nitrogen. In particular, they simulated the processing of N_2O_5 . N_2O_5 concentration is a maximum at nighttime, when boundary layer relative humidity also peaks. Thus mineral dust particles are likely to have enough water to allow the conversion of N_2O_5 to HNO_3 via

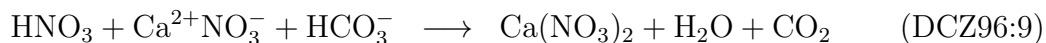
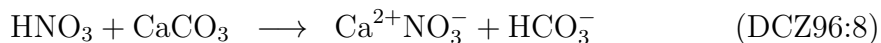


Unfortunately, the uptake of N_2O_5 on mineral particles has not been directly measured so that estimates of $\gamma(\text{N}_2\text{O}_5 \rightarrow \text{dust})$ must be based on uptake by other surfaces. Various studies, summarized by Dentener et al. (1996), show that $0.06 < \gamma(\text{N}_2\text{O}_5 \rightarrow \text{H}_2\text{SO}_4) < 0.12$, $0.05 < \gamma(\text{N}_2\text{O}_5 \rightarrow (\text{NH}_4)_2\text{SO}_4) < 0.09$, $\gamma(\text{N}_2\text{O}_5 \rightarrow \text{H}_2\text{O}) \sim 0.05$, $\gamma(\text{N}_2\text{O}_5 \rightarrow \text{H}_2\text{SO}_4) \sim 0.05$, but that $\gamma(\text{N}_2\text{O}_5 \rightarrow \text{dry salts}) \sim 10^{-4}$. Because of the relatively high probability of wetted dust particles at night, Dentener et al. (1996) chose $\gamma(\text{N}_2\text{O}_5 \rightarrow \text{dust}) = 0.1$, a value much closer to the uptake coefficients observed on liquid surfaces than on dry surfaces.

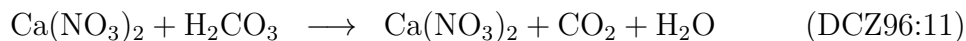
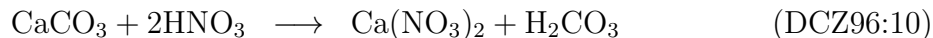
Gas phase NO_3 may also adsorb onto dust surfaces. However, Dentener et al. (1996) found NO_3 adsorption to have a small effect on overall removal of NO_x and therefore neglected it.

Dentener et al. (1996) paid very careful attention to uptake of HNO_3 and SO_2 on mineral dust. The abundance of CaCO_3 in dust allows it to neutralize these strong acids. Two of the three main conclusions of Dentener et al. (1996) were that production of SO_4^{2-} and NO_3^- in the atmosphere was strongly affected by the presence of mineral dust.

Once sequestered on mineral dust nitric acid is assumed to be neutralized by alkaline material, usually CaCO_3 (Dentener et al., 1996)

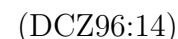
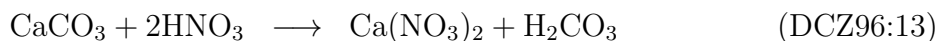


This reaction is fast, and is considered diffusion-limited. [Krueger et al. \(2003\)](#) first observed this mechanism in the laboratory. They showed that the calcium nitrate end-product deliquesces at low RH.

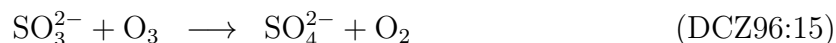


The deliquescence in [\(DCZ96:12\)](#) helps explain the high reactivity of HNO_3 and CaCO_3 .

The uptake and neutralization of sulfur dioxide on mineral surfaces may be substantially more complicated. SO_2 strongly adsorbs to the oxide surfaces characteristic of mineral dust ([Usher et al., 2002](#)). However, SO_2 adsorption onto pure quartz appears negligible. For CaCO_3 ,



Once sequestered on wetted mineral dust, SO_2 dissociates H_2O to form the sulfite ion SO_3^{2-} via [\(R16\)](#)–[\(R17\)](#). The sulfite may be oxidized into sulfate by ozone



This reaction is only expected to take place in the presence of liquid water at very high pH. For $\text{pH} > 8$, [\(DCZ96:15\)](#) proceeds very quickly, becoming limited only by gas phase diffusion processes. The range of pH which must be accounted for when considering heterogeneous chemistry on mineral dust is quite large. [Dentener et al. \(1996\)](#) assume that, on mineral dust aerosol (as opposed to in cloud droplets), there is not a sufficient volume of water to allow H_2O_2 oxidation of SO_2 [\(DCZ96:17\)](#) to compete with [\(DCZ96:15\)](#).

Unfortunately, direct measurement of the uptake of SO_2 and NO_3^- onto dust are not available. Their uptake coefficients on liquid water are known to be about 0.1. [Dentener et al. \(1996\)](#) summarize the uptake coefficients that have been measured for a variety of “dry” aerosols such as Fe_2O_3 , fly ash, and soot. These measurements indicate $10^{-3} < \gamma(\text{SO}_2 \rightarrow \text{dry aerosol}) < 10^{-6}$. The uptake coefficients tended to decrease with prolonged exposure, but their rate of decrease was much less at high relative humidity.

More recent experiments have measure the uptake of HNO_3 onto mineral dust in a laboratory flow tube (V. Grassian, personal communication, 1999, 2003). It is found that mineral dust is coated with a surface layer of H_2O at very low relative humidities, i.e., $\text{RH} > 30\%$. This liquid coating uptakes HNO_3 at rates corresponding to $10^{-4} < \gamma(\text{HNO}_3 \rightarrow \text{dust}) < 10^{-3}$ ([Underwood et al., 2001a](#); [Grassian, 2002](#); [Krueger et al., 2003](#)). These rates are much smaller than the $\gamma = 0.1$ employed by [Dentener et al. \(1996\)](#) and [Bauer et al. \(2004\)](#) and explain much of the difference in model results.

The rate of SO_2 deposition to mineral dust aerosol has also been inferred from measurements of surface resistance to SO_2 transfer over calcareous soils, Fe_2O_3 , and other proxies for mineral dust. A measured value of the resistance to surface transfer by dry deposition

Table 14.5: Uptake Coefficients of Mineral Dust in UCI CTM^a

Reaction	Uptake γ	References ^b
$\text{H}_2\text{O}_2 + \text{Dust} \longrightarrow \text{Products}$	1.0×10^{-4}	1
$\text{HNO}_3 + \text{Dust} \longrightarrow \text{Products}$	1.1×10^{-3}	1, 3, 5
$\text{HO}_2 + \text{Dust} \longrightarrow \text{Products}$	0.1	1, 4
$\text{N}_2\text{O}_5 + \text{Dust} \longrightarrow \text{Products}$	1.0×10^{-3}	1, 3
$\text{NO}_2 + \text{Dust} \longrightarrow \text{Products}$	4.4×10^{-5}	5
$\text{NO}_3 + \text{Dust} \longrightarrow \text{Products}$	0.1	2, 4
$\text{O}_3 + \text{Dust} \longrightarrow \text{Products}$	5.0×10^{-5}	1, 3, 4, 7
$\text{OH} + \text{Dust} \longrightarrow \text{Products}$	1.0×10^{-5}	4

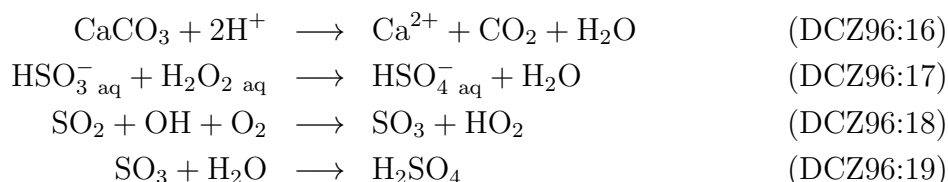
^aSources: $\text{RH}_t = 50\%$

^bReferences: 1, Dentener et al. (1996); 2, Seinfeld and Pandis (1997); 3, DeMore et al. (1997); 4, Zhang and Carmichael (1999); 5, Underwood et al. (2001b); 6, Underwood et al. (2001a); 7, Michel et al. (2002); 8, Michel et al. (2003);

r_d is converted to a deposition velocity v_d using (11.24). Then, the uptake coefficient γ is inferred using the approximation (Schwartz, 1992)

$$\gamma = \frac{v_d}{\bar{v}_m} \quad (14.13)$$

where \bar{v}_m is the ambient thermal speed of SO_2 molecules (11.54).



14.2.3 Bauer's Mechanism

Bauer et al. (2004) performed global model simulations of heterogeneous chemistry on mineral dust and compared them to observations in Italy during the MINATROC campaign.

14.2.4 My Mechanism

We have implemented a representation of heterogeneous chemistry on mineral dust based on Zhang et al. (1994) and Zhang and Carmichael (1999). This scheme accounts for uptake of H_2O_2 , HNO_3 , HO_2 , N_2O_5 , NO_2 , NO_3 , O_3 , OH , and SO_2 on mineral dust particles. Table 14.6 shows the uptake coefficients employed in the global mineral dust model (Bian and Zender, 2003a,b).

fxm: Redundant? ¹ To be consistent with the deliquescence approximation we employ

Table 14.6: Uptake coefficients in Global Mineral Dust Model^a

$\gamma(\text{HO}_2 \rightarrow \text{dust})$	=	0.1
$\gamma(\text{O}_3 \rightarrow \text{dust})$	=	0.00005
$^a\gamma(\text{N}_2\text{O}_5 \rightarrow \text{dust})$	=	$\begin{cases} 0.001 & : \text{RH} < \text{RH}_t \\ 0.1 & : \text{RH} \geq \text{RH}_t \end{cases}$
$^a\gamma(\text{HNO}_3 \rightarrow \text{dust})$	=	0.1
$^a\gamma(\text{SO}_2 \rightarrow \text{dust})$	=	$\begin{cases} 3 \times 10^{-4} & : \text{RH} < \text{RH}_t \\ 0.1 & : \text{RH} \geq \text{RH}_t \end{cases}$

^aSource: Source of best guess value. Most values adopted from [Dentener et al. \(1996\)](#), $\text{RH}_t = 50\%$

Table 14.7: Reactions Included in Global Mineral Dust Model^a

Index	Reaction	Uptake coefficient	Humidity	Reference
Zen00:1	$\text{HNO}_3 + \text{Dust} \rightarrow \text{Products}$	0.005	-1.0	DCZ96

^aSources: DCZ96 = [Dentener et al. \(1996\)](#); JPL97 = [DeMore et al. \(1997\)](#); HeC99 = [He and Carmichael \(1999\)](#); BrS86 = [Brasseur and Solomon \(1986\)](#); Gra99 = [Grassian \(1999\)](#);

separate mass uptake coefficients above and below RH_t . Furthermore, some reactions take place only when the empirical alkalinity relationship is obeyed:

$$[\text{NO}_3^-] + 2[\text{SO}_4^{2-}] < 2[\text{Ca}^{2+}] \quad (14.14)$$

The mineral dust model employs the following heterogeneous pathways.



Table [14.7](#) lists the reactions employed in the mineral dust model of [Zender \(2000\)](#).

14.3 Global Sulfur Cycle

[Barth et al. \(2000\)](#) developed a global model of the atmospheric sulfur cycle. Their model provides instructive examples of the use of the (computational) time saving approximations which are currently required in large scale atmospheric models.

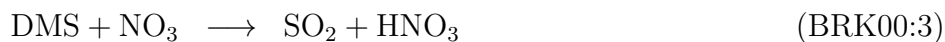
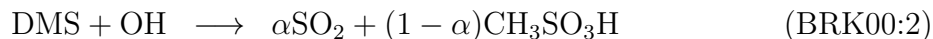
Anthropogenic emissions of sulfur are interpolated from the GEIA emissions inventory ([Benkovitz et al., 1996](#)) representative of the year 1985. The GEIA database assumes sulfur emissions (67 Tg S yr^{-1}) are 98% SO_2 and 2% SO_4^{2-} 2% by weight. Gas phase SO_2 is converted to SO_4^{2-} via a multistep reaction (e.g., [Seinfeld and Pandis, 1997](#)). [Barth et al. \(2000\)](#) assume that the rate limiting reaction in this chain is



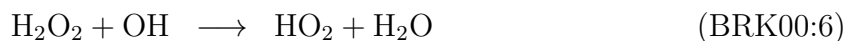
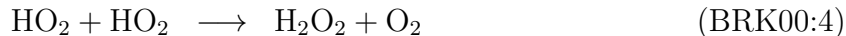
The OH radical concentration required in ([BRK00:1](#)), as well as NH_3 , HO_2 , and O_3 required in subsequent reactions, is prescribed from the monthly values generated by the IMAGES model ([Müller and Brasseur, 1995](#)).

¹Uptake only when $[\text{NO}_3^-] + 2[\text{SO}_4^{2-}] < 2[\text{Ca}^{2+}]$

Conversion of DMS to SO_2 is the main natural path for production of sulfate. Natural emissions of DMS are interpolated from the global monthly dataset of [Benkovitz et al. \(1994\)](#).

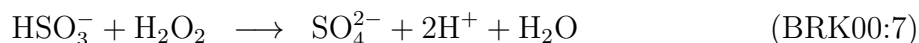


Hydrogen peroxide is entirely prognostic within the model. Gas phase H_2O_2 is produced by HO_2 , photolyzed, and destroyed by OH according to



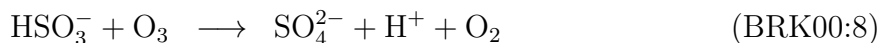
The photolysis rate coefficient $J_{\text{H}_2\text{O}_2}$ in ([BRK00:5](#)) is diagnosed from the diurnal-average zenith angle and the gridbox height.

Aqueous phase hydrogen peroxide oxidizes HSO_3^-



Trace metals in solution can catalyze production of H_2O_2 ([Anastasio et al., 1994](#); [Dentener et al., 1996](#)). However, [Barth et al. \(2000\)](#) assume H_2O_2 is in Henry's law equilibrium. Wetted mineral dust aerosol, which is rich in trace metals, is likely to provide an extreme test of this assumption ([Dentener et al., 1996](#)).

Aqueous phase ozone reacts with sulfite ions to produce sulfate and oxygen



As mentioned below, H_2O_2 and O_3 are assumed to be in Henry's law equilibrium. The rates of oxidation by O_3 are highly sensitive to droplet pH. Therefore the model evaluates the aqueous phase reactions ([BRK00:7](#))–([BRK00:9](#)), and the droplet pH, every two minutes.

The aqueous and gas phase concentrations of H_2O_2 , O_3 , and SO_2 are assumed to be in Henry's Law equilibrium at all times.



The final two gas phase components, H_2SO_3 and HSO_3^- , produce H^+ when they hydrolyze.



Table [14.8](#) lists the reaction rates employed in the global sulfur model of [Barth et al. \(2000\)](#).

Table 14.8: Reactions Included in Global Sulfur Model of Barth et al. (2000)^a

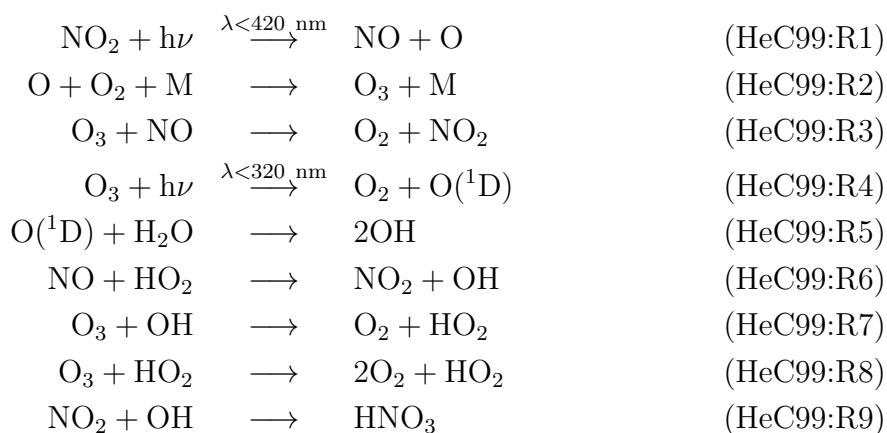
Index	Reaction	Rate	E/R	Reference
GasChemistry				
BRK00:1	$\text{SO}_2 + \text{OH} + \text{M} \longrightarrow$	$k_0 = 3.0 \times 10^{-31} (T/300)^{-3.3}$ $k_\infty = 1.5 \times 10^{-12}$		JPL97 JPL97
BRK00:2	$\text{DMS} + \text{OH} \longrightarrow$	$\alpha \text{SO}_2 + (1 - \alpha) \text{CH}_3\text{SO}_3\text{H}$		Y90
BRK00:3	$\text{DMS} + \text{NO}_3 \longrightarrow$	$\text{SO}_2 + \text{HNO}_3$		JPL97
BRK00:4	$\text{HO}_2 + \text{HO}_2 \longrightarrow$	$\text{H}_2\text{O}_2 + \text{O}_2$	-590	JPL97
BRK00:5	$\text{H}_2\text{O}_2 + \text{h}\nu \longrightarrow$	2OH		
BRK00:6	$\text{H}_2\text{O}_2 + \text{OH} \longrightarrow$	$\text{HO}_2 + \text{H}_2\text{O}$	160	JPL97
AqueousChemistry				
BRK00:7	$\text{HSO}_3^- + \text{H}_2\text{O}_2 \longrightarrow$	$\text{SO}_4^{2-} + 2\text{H}^+ + \text{H}_2\text{O}$	4750	HC85
BRK00:8	$\text{HSO}_3^- + \text{O}_3 \longrightarrow$	$\text{SO}_4^{2-} + \text{H}^+ + \text{O}_2$	5300	HC85
BRK00:9	$\text{SO}_3^{2-} + \text{O}_3 \longrightarrow$	$\text{SO}_4^{2-} + \text{O}_2$	5280	HC85
EquilibriumReactions				
BRK00:10	$\text{H}_2\text{O}_2(\text{g}) \rightleftharpoons$	$\text{H}_2\text{O}_2(\text{aq})$	-6621	LK86
BRK00:11	$\text{O}_3(\text{g}) \rightleftharpoons$	$\text{O}_3(\text{aq})$	-2560	NBS65
BRK00:12	$\text{SO}_2(\text{g}) \rightleftharpoons$	$\text{SO}_2(\text{aq})$	-3120	NBS65
BRK00:13	$\text{H}_2\text{SO}_3 \rightleftharpoons$	$\text{HSO}_3^- + \text{H}^+$	-2015	M82
BRK00:14	$\text{HSO}_3^- \rightleftharpoons$	$\text{SO}_3^{2-} + \text{H}^+$	-1505	M82

^aSources: Sources: JPL97 = DeMore et al. (1997).^bhello

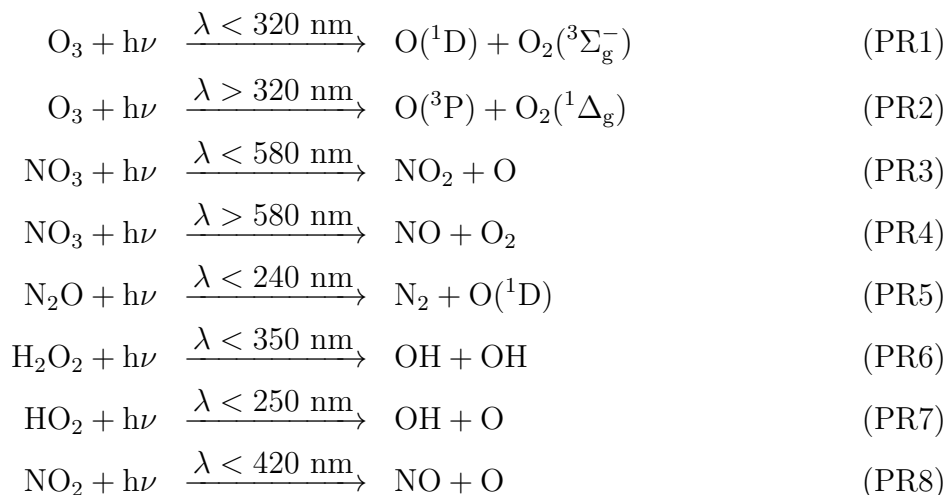
Chapter 15

Photochemistry

[He and Carmichael \(1999\)](#) studied the sensitivity of photolysis rates and and ozone production to mineral aerosol properties.



A more complete set of photodissociation reactions is



15.1 Heterogeneous Photochemistry

Absorption bands of adsorbed species are usually red-shifted relative to bands of the gas phase species. Photolysis of the adsorbed species may be significantly more efficient if the shift crosses the sharp cutoff of atmospheric UV radiation near $\lambda = 290\text{ }\mu\text{m}$.

Chapter 16

Biogeochemistry

16.1 Biogeochemistry Literature

The minerals composing dust may be of significant biogeochemical relevance to many ecosystems. The “Iron Hypothesis” suggests that dust delivers the crucial micronutrient Fe(III) to otherwise iron-limited ecosystems ([Martin and Fitzwater, 1988](#); [Martin, 1990](#)). [Dymond et al. \(1997\)](#) describe a method to use the Al/Ti ratios of ocean sediments as a proxy for ocean paleoproductivity (specifically of biogenic opal). [Moore et al. \(2000\)](#) show that increased Aeolian deposition to the Southern Ocean at the last glacial maximum contributed significantly to an increased net CO₂ flux. [Fung et al. \(2000\)](#) study the iron supply and demand in the upper ocean. [Gao et al. \(2001\)](#) estimate the deposition of iron to the global ocean from observations. [Moore et al. \(2002a\)](#) use an intermediate complexity marine ecosystem model ([Moore et al., 2002b](#)) to study the role of dust-borne iron in nutrient transport. [Measures and Vink \(2000\)](#) describe the use of dissolved Al to estimate dust deposition fluxes to the ocean. [Johnson \(2001\)](#) argues that the interplanetary dust flux to remote oceans is a significant compared to terrestrial and upwelling Fe fluxes. [Elbaz-Poulichet et al. \(2001\)](#) assess the trace metal (including Fe) budgets of the western Mediterranean Sea. [Ridame et al. \(1999\)](#) present estimates of the deposition budgets of Fe, Al, and total dust in the northwestern Mediterranean between 1985–1997. [Bishop et al. \(2002\)](#) show direct observations of enhanced particulate carbon occur in the North Pacific after passage of a Gobi dust storm. [Johnson et al. \(2002\)](#) summarize the current knowledge and uncertainties in linking oceanic iron inputs to nutrient production, fixation, and export to the deep ocean. [Gabric et al. \(2002\)](#) present evidence for a coupling between SeaWiFS AOD and upper ocean chlorophyll concentration at daily, weekly and monthly timescales. The AOD is thought to be dust from Australia. In near coastal zones, riverine mineral fluxes to the ocean margin are often more important than atmospheric inputs. [Jones et al. \(2002\)](#) describe a model of the riverine fluxes of dissolved HCO₃⁻, Si, and Ge to the ocean based on a global lithological map. [Gehlen et al. \(2003\)](#) implemented Al and Si geochemistry in an ocean ecosystem model to evaluate dust deposition fields. [Gao et al. \(2003\)](#) estimate Fe deposition from wet scavenging. [Hand et al. \(2004\)](#) estimate soluble iron from observations and a global mineral aerosol model. [Jickells et al. \(2005\)](#) review the connections between Fe, dust, ocean biogeochemistry, and climate. [Mahowald et al. \(2005\)](#) review understanding of transport, solubility, and deposi-

tion of iron to the ocean via dust aerosols. [Luo et al. \(2005\)](#) estimate global iron solubility and Al concentration from observations and a global aerosol model. [Moore et al. \(2005\)](#) describe dust-mediated impacts of paleo, pre-industrial, present day, and future climates on ocean biogeochemistry and air-sea CO₂ exchange. [Schüßler et al. \(2005\)](#) analyze the cycling of Al in the Arabian Sea based on three years of measurements of atmospheric and marine Al concentrations. [Chase et al. \(2006\)](#) use measurements of atmospheric and marine Fe concentrations in the Gulf of Aqaba to infer dust deposition and constrain Fe solubility.

16.2 Limiting Nutrients: Iron

16.3 Limiting Nutrients: Nitrogen

16.4 Limiting Nutrients: Phosphorous

[Ammerman et al. \(2003\)](#) argue that phosphorous deficiency may limit or co-limit phytoplankton growth in much of the North Atlantic. It is thought that the North Atlantic shows less nitrogen deficiency than the Pacific Ocean because mineral dust deposition is much stronger in the North Atlantic. Nitrogen fixation is often limited by the availability of iron since the enzyme nitrogenase (which converts N₂ to NH₄) has high iron requirements. Should dust provide this iron, it could explain why the Atlantic may be less nitrogen- and more phosphorous-limited than the Pacific.

Chapter 17

Implementation in NCAR models

This section describes how the above physics and chemistry have been implemented in the NCAR-Dust model.

17.1 Initialization

The model requires as input global distributions of soil texture, mass fractions of mobilized dust, leaf area index, soil moisture and wind speed.

At startup, the model computes $C_{\text{St}}(D, p_0, T_0)$ (5.26) for each size at a temperature and pressure representative of arid erosion regions on Earth (currently $p = 1000$ mb and $T = 295$ K). The model computes u_{St} (5.18) every timestep and applies the time-invariant correction factor $C_{\text{St}}(D, p_0, T_0)$ to obtain v_g . In this manner the iterative solution to (5.25) is avoided every timestep.

The model iteratively solves (3.36) until the fractional difference between successive iteration is less than 10^{-5} . Convergence is usually be obtained within five iterations.

17.2 Main Loop

17.2.1 Mobilization

A more computationally amenable form of (3.36) is employed.

$$u_{*t} = \begin{cases} \left[\frac{0.1666681\rho_p g D}{-1+1.928B^{0.0922}} \left(1 + \frac{6 \times 10^{-7}}{\rho_p g D^{2.5}} \right) \right]^{1/2} \rho^{-1/2} & : 0.03 \leq B \leq 10 \\ \left[0.0144\rho_p g D (1 - 0.0858e^{-0.0617(B-10)})^2 \left(1 + \frac{6 \times 10^{-7}}{\rho_p g D^{2.5}} \right) \right]^{1/2} \rho^{-1/2} & : B > 10 \end{cases} \quad (17.1)$$

Expression (17.1) isolates all the microphysical properties are in the first term on the RHS. This term contains the size and density of the aerosol and thus needs to be computed only once for a given aerosol size. The other term, $\rho^{-1/2}$ depends on the ambient environmental conditions which are the same for all aerosol sizes. Hence the (presumably) time-varying environmental term is all that need be recomputed each timestep.

To convert the streamwise particle flux to a total vertical dust flux, we use (3.101) with the clay mass fraction M'_{clay} defined by $M'_{\text{clay}} = \min(M_{\text{clay}}, 0.20)$.

Chapter 18

Appendix

18.1 Physical Constants

Table 18.1 list the values of common physical constants. These values should be consistent with the 1998 CODATA adjustment reported in [Mohr and Taylor \(2000\)](#).

Table 18.1: Physical Constants

Symbol	Name	Value	Units	^a Reference
h	Planck's constant	6.626196×10^{-34}	J s	
M_{\oplus}	Mass of Earth	5.98×10^{24}	kg	
R^*	Universal gas constant	8.31441	J mol ⁻¹ K ⁻¹	
G	Newtonian constant of gravitation	6.673×10^{-11}	m ³ kg ⁻¹ s ⁻² N m ² kg ⁻¹	MoT00
k	Boltzmann's constant	1.38063×10^{-23}	J K ⁻¹	
σ	Stefan-Boltzmann constant	5.67032×10^{-8}	W m ⁻² K ⁻⁴	
T_0	Freezing point of water	273.15	K	Bol80
T_T	Triple point of water	273.16	K	Bol80
σ	^b Surface tension of liquid water	7.610×10^{-3}	N m ⁻¹ , J m ⁻²	PrK78
$\mathcal{M}_{\text{H}_2\text{O}}$	^c Mean molecular weight of H ₂ O	1.8015259×10^{-2}	kg mol ⁻¹	RRG98
ρ_w	Density of liquid water	1000.0	kg m ⁻³	

^aSources: Bol80 = [Bolton \(1980\)](#), RRG98 = [Rothman et al. \(1998\)](#), MoT00 = [Mohr and Taylor \(2000\)](#)

^bSee (18.3) for temperature dependence

^cBased on isotopic composition of species in Earth's atmosphere

Table 18.2: Conversion Factors Describing Species Abundances^a

Name	Symbol(s)	Units	q	χ	p	ρ
Number concentration	$N_A, [A]$	molecule m ⁻³	$\frac{q_A \rho \mathcal{N} N_A}{\mathcal{M}_A}$			
Mass mixing ratio	q_A	kg kg ⁻¹	$\frac{N_A \mathcal{M}_A}{\rho \mathcal{N}}$			
Volume mixing ratio, Number mixing ratio, Mole fraction Volume fraction	χ_A	mol mol ⁻¹	$\frac{q_A \mathcal{M}_d}{\mathcal{M}_A}$			
Partial pressure	p_A	Pa	$\rho_A R_A T$			
Mass density	ρ_A	kg m ⁻³				

^a The formulae are written in terms of a generic species A. The formulae use conventional notation where p is the ambient pressure, T_v is virtual temperature, $\rho = p/(R_d T_v)$ is mass density, R_d is the gas constant of dry air, \mathcal{M} is a mean molecular weight, and \mathcal{N} is Avagadro's number.

18.2 Common Chemical Conversions

Implementation of chemistry in numerical models often requires conversion between various quantities related to the concentration of chemical species. Table 18.2 summarizes these conversions.

18.3 Surface Tension of Water

The boundary between two adjoining thermodynamic phases a transitional region only a few molecules thick. The distinct properties of the substance on either side of the boundary may cause discrete jumps in thermodynamic properties across the boundary, even when the phases are in equilibrium. In fact, the boundary surface itself behaves as a thermodynamically distinct phase of the substance with its own internal energy. The internal energy of this surface phase depends on the the area of the boundary surface, Ω . Because the surface phase is infinitesimally thin, the change in internal energy due to pressure-volume work which applies to other phases (i.e., liquid, solid, or vapor) of the substance does not apply to the surface phase. Instead, the conjugate pair of variables describing the isentropic change in energy as the boundary surface changes are the surface tension, σ , and Ω . These conjugate variables are defined such that the change in internal energy of the system at constant entropy is the product of the surface tension and the boundary area

$$dE_t = \sigma d\Omega \quad (18.1)$$

where σ is a force per unit length (Pa m^{-1}) or energy per unit area (J m^{-2}). Although (18.1) is valid for any surface phase species, we shall now restrict our attention to liquid water. The surface tension of liquid water σ is positive definite. Thus work must be performed to increase Ω .

The underlying cause of surface tension effects is the polar nature of the water molecule. Molecules internal to a liquid phase droplet experience a symmetric, attractive force field generated by the dipole moments of the surrounding molecules. Molecules in the surface phase, on the other hand, have no neighbors across the boundary (in the vapor phase) and so experience a net attraction towards the center of the droplet. This inward attraction maintains the surface tension of the droplet.

A system consisting of the liquid, vapor, and surface phases of water obeys the standard thermodynamic rules for equilibrium. In other words, the Gibbs free energy must be a minimum

The pressure difference between the liquid water in the droplet and the vapor phases outside the droplet is thus

$$P = \frac{2\sigma}{r} \quad (18.2)$$

Thus the pressure excess varies inversely with the size of the droplet. As the droplets become so large that $r \rightarrow \infty$, $P \rightarrow 0$. Thus the pressure excess over a bulk planar surface of water (e.g., the ocean) is zero. For a droplet of size $r = 1 \mu\text{m}$, the pressure excess is about ...

The surface tension of water has a moderate temperature dependence, which appears to be linear to within the uncertainty of the observations (Pruppacher and Klett, 1978, p. 104).

$$\sigma = 7.610 \times 10^{-3} - 1.55 \times 10^{-5}(T - 273.15) \quad 243 < T < 313 \text{ K} \quad (18.3)$$

where σ is in N m^{-1} or J m^{-2} .

18.4 Atmospheric Viscosity

Viscosity is a key quantity in all fluid mechanics because it determines the efficiency of diffusive relative to advective processes. The dynamic viscosity μ appears directly in the momentum equations (18.93). The observed linear relationship between the shear stress in a fluid and its velocity gradient is known as Newton's law of friction.

$$\tau = \mu \frac{du}{dz} \quad (18.4)$$

Thus μ is the ratio of the shear stress to the velocity gradient of the fluid (Kundu, 1990, p. 7).

For ideal gases μ is largely determined by the momentum transfer due to molecular collisions. This momentum is proportional to the molecular velocity (11.54). For cloud and aerosol processes we need to specify μ in regions where collisional processes ensure rapid equipartition of energy. In such regions the mean molecular velocity varies quadratically

with temperature $mv^2 \propto kT$. Thus μ depends only on T , being roughly proportional to \sqrt{T} . For Earth's atmosphere an approximate expression for μ is (Rogers and Yau, 1994, p. 102).

$$\mu = 1.72 \times 10^{-5} \left(\frac{T}{273} \right)^{3/2} \frac{393}{T + 120} \quad (18.5)$$

The units of μ are $\text{kg m}^{-1} \text{s}^{-1}$. The scaled equations of motion often make it more convenient to work with the kinematic viscosity ν , which is the ratio of the dynamic viscosity to the density. Thus ν depends on both T and p and is simply defined as

$$\nu \equiv \mu/\rho \quad (18.6)$$

The units of ν are $\text{m}^2 \text{s}^{-1}$. Near the surface in arid regions, typical values of μ and ν are $1.7 \times 10^{-5} \text{ kg m}^{-1} \text{s}^{-1}$ and $1.3 \times 10^{-5} \text{ m}^2 \text{s}^{-1}$, respectively.

18.5 Error Function

The error function $\text{erf}(x)$ may be defined as the partial integral of a Gaussian curve

$$\text{erf}(z) = \frac{2}{\sqrt{\pi}} \int_0^z e^{-x^2} dx \quad (18.7)$$

The error function is bounded by the limits $\text{erf}(0) = 0$ and $\text{erf}(\infty) = 1$. The complementary error function is defined eponymously as $\text{cerf}(x) = 1 - \text{erf}(x)$.

18.6 Gamma Function

The gamma function $\Gamma(x)$ is defined by

$$\Gamma(x) = \int_0^\infty t^{x-1} e^{-t} dt \quad (18.8)$$

Useful special values of the gamma function include

$$\Gamma\left(\frac{1}{2}\right) = \sqrt{\pi} \quad (18.9)$$

$$\Gamma(n+1) = n! \quad \text{where } n \in \mathcal{I} \quad (18.10)$$

where n is an integer. The recurrence properties of gamma functions are

$$\begin{aligned} \Gamma(z) &= (z-1)\Gamma(z-1) & z > 1 \\ \Gamma(z) &= \frac{\Gamma(z+1)}{z} & z < 0 \end{aligned}$$

Thus we see that

$$\begin{aligned} \Gamma\left(-\frac{1}{2}\right) &= \frac{\Gamma\left(\frac{1}{2}\right)}{-\frac{1}{2}} \\ &= -2\Gamma\left(\frac{1}{2}\right) \\ &= -2\sqrt{\pi} \end{aligned} \quad (18.11)$$

18.7 Incomplete Gamma Functions

The four members of the Incomplete Gamma Function family are $\Gamma(\alpha, x)$, $\gamma(\alpha, x)$, $P(\alpha, x)$, and $Q(\alpha, x)$ (Abramowitz and Stegun, 1964; Press et al., 1996, p. 209).

$$\begin{aligned}
 P(\alpha, x) &\equiv 1 - Q(\alpha, x) \equiv \frac{\gamma(\alpha, x)}{\Gamma(\alpha)} \equiv \frac{1}{\Gamma(\alpha)} \int_0^x t^{\alpha-1} e^{-t} dt \\
 Q(\alpha, x) &\equiv 1 - P(\alpha, x) \equiv \frac{\Gamma(\alpha, x)}{\Gamma(\alpha)} \equiv \frac{1}{\Gamma(\alpha)} \int_x^\infty t^{\alpha-1} e^{-t} dt \\
 \gamma(\alpha, x) &\equiv \Gamma(\alpha) P(\alpha, x) \equiv \Gamma(\alpha) [1 - Q(\alpha, x)] \equiv \Gamma(\alpha) - \Gamma(\alpha, x) \equiv \int_0^x t^{\alpha-1} e^{-t} dt \\
 \Gamma(\alpha, x) &\equiv \Gamma(\alpha) Q(\alpha, x) \equiv \Gamma(\alpha) [1 - P(\alpha, x)] \equiv \Gamma(\alpha) - \gamma(\alpha, x) \equiv \int_x^\infty t^{\alpha-1} e^{-t} dt
 \end{aligned} \tag{18.12}$$

The nomenclature for incomplete gamma functions is confusing. The most precise name for $\Gamma(\alpha, x)$ is the “upper incomplete gamma function”. Here “upper” refers to both “upper”-case gamma and to the bounds of integration, $x \rightarrow \infty$. One important reference, MathWorld, calls $\Gamma(\alpha, x)$ the “incomplete gamma function” but we avoid that terminology. The upper incomplete gamma function $\Gamma(\alpha, x)$ reduces to the regular (or complete) gamma function $\Gamma(\alpha)$ when $x = 0$ (e.g., Abramowitz and Stegun, 1964).

The most precise name for $\gamma(\alpha, x)$ is the “lower incomplete gamma function” for self-evident reasons. The upper and lower incomplete gamma functions satisfy

$$\Gamma(\alpha, x) + \gamma(\alpha, x) = \Gamma(\alpha) \tag{18.13}$$

Equation (18.13) demonstrates the property for which the “incomplete gamma functions” are named.

The regularized gamma functions $P(\alpha, x)$ and $Q(\alpha, x)$ satisfy

$$P(\alpha, x) + Q(\alpha, x) = 1 \tag{18.14}$$

The regularized functions $P(\alpha, x)$ and $Q(\alpha, x)$ functions are the lower and upper incomplete gamma functions $\gamma(\alpha, x)$ and $\Gamma(\alpha, x)$, respectively, normalized by the complete gamma function $\Gamma(\alpha)$. Computing $P(\alpha, x)$ and $Q(\alpha, x)$ may be more numerically tractable than computing $\gamma(\alpha, x)$ and $\Gamma(\alpha, x)$ when $\Gamma(\alpha)$ is large. Most references call $P(\alpha, x)$ the “the incomplete gamma function” (which is somewhat ambiguous) or, more precisely, “the regularized incomplete gamma function” (e.g., Abramowitz and Stegun, 1964; Press et al., 1996). Most references call $Q(\alpha, x)$ “the complemented regularized incomplete gamma function”. For these reasons, we try to avoid the generic and ambiguous terminology “the incomplete gamma function”. One must be very careful to check which form of “the incomplete gamma function” numerical libraries implement against the defining relations (18.12).

18.8 Marshall-Palmer Distribution

The Marshall-Palmer distribution function is described in terms of the mean diameter D_n mm, the total number distribution N_0 m³ mm⁻¹, and the precipitation rate R mm hr⁻¹

as follows

$$p_{\text{MP}}(D) = N_0 \exp(-\Lambda D_n) \quad (18.15)$$

where $N_0 = 8 \times 10^3 \text{ mm}^{-1}$ and $\Lambda = 4.1 R^{-0.21} \text{ mm}^{-1}$ were determined empirically.

18.9 Rayleigh Distributions

A single parameter distribution which has been used to approximate wind speed observations in nature is the Rayleigh distribution. The Rayleigh distribution function is

$$p_R(U) = \frac{U}{\sigma^2} \exp\left(-\frac{U^2}{2\sigma^2}\right) \quad (18.16)$$

where σ is the scale parameter.

The cumulative distribution function of (18.16) is

$$\int_0^U p_R(U) dU = 1 - \exp\left(-\frac{U^2}{2\sigma^2}\right) \quad (18.17)$$

Related to (18.16) is the Rayleigh tail distribution. The tail obeys (18.16) for $U > U_t$, i.e.,

$$p_{\text{Rt}}(U) = \begin{cases} 0 & : U < U_t \\ \frac{U}{\sigma^2} \exp\left(-\frac{U_t^2 - U^2}{2\sigma^2}\right) & : U \geq U_t \end{cases} \quad (18.18)$$

where U_t is the lower limit of the distribution. Thus (18.18) is a truncated Rayleigh distribution which is normalized for wind speeds U greater than a threshold U_t .

The cumulative distribution function of (18.18) is

$$\int_0^U p_{\text{Rt}}(U) dU = 1 - \exp\left(-\frac{U_t^2 - U^2}{2\sigma^2}\right) \quad (18.19)$$

18.10 Weibull Distribution

The Weibull distribution function is

$$p_W(U) = \frac{k}{c} \left(\frac{U}{c}\right)^{k-1} \exp\left[-\left(\frac{U}{c}\right)^k\right] \quad (18.20)$$

where c and k are known as the scale parameter and the shape parameter, respectively. The scale parameter determines the maximum value of p_W , while the shape parameter determines the variance of the distribution. As will be shown below, (18.20) is normalized on the interval $U \in [0, \infty)$.

For applications to wind erosion, we are interested in higher moments of the Weibull distribution. For generality, consider the n th moment of the Weibull distribution, defined by

$$p_W(U, n) \equiv U^n p_W(U) \quad (18.21)$$

$$\begin{aligned} &= U^n \left(\frac{k}{c}\right) \left(\frac{U}{c}\right)^{k-1} \exp \left[- \left(\frac{U}{c}\right)^k \right] \\ &= k U^{n+k-1} c^{k-2} \exp \left[- \left(\frac{U}{c}\right)^k \right] \end{aligned} \quad (18.22)$$

Hence $p_W(U, n)$ reduces to $p_W(U)$ for $n = 0$.

We define the cumulative PDF of the n th moment of the Weibull distribution as

$$W(U_t, n) \equiv \int_{U_t}^{\infty} p_W(U, n) dU = \int_{U_t}^{\infty} U^n p_W(U) dU \quad (18.23)$$

$$= \int_{U_t}^{\infty} U^n \left(\frac{k}{c}\right) \left(\frac{U}{c}\right)^{k-1} \exp \left[- \left(\frac{U}{c}\right)^k \right] dU \quad (18.24)$$

The limits of integration in (18.24) ensure that $p_W(U, n)$ contributes to $W(U_t, n)$ only for $U > U_t$. Hence U_t is called the threshold wind speed. For $n = 0$, (18.22) gives the probability that wind speed U exceeds the threshold windspeed U_t . For $n > 0$, $W(U_t, n)$ defines statistical moments of the wind speeds greater (faster) than U_t . For example, $n = 1$ defines the mean wind speed faster than U_t . The mean wind speed is proportional to the mean momentum transport, a useful quantity to know because it is conserved. The cumulative PDF of the second moment ($n = 2$) defines the mean square wind speed exceeding U_t . The mean square wind speed is proportional to the kinetic energy, another conserved quantity.

Defining $W(U_t, n)$ (18.22) to include $U > U_t$ rather than the complementary convention $U < U_t$ is convenient for threshold phenomena. The complementary (opposite) convention ($U < U_t$) is appropriate for other processes and is often employed. One must be careful to understand the sense (i.e., the convention) of a cumulative PDF function before employing it.

To simplify (18.24) we make the change of variables

$$\begin{aligned} x &= (U/c)^k \\ (U/c)^{(k-1)} &= x^{(k-1)/k} \\ U^n &= c^n x^{n/k} \\ dU &= c k^{-1} x^{-(k-1)/k} \\ dx &= k c^{-1} \left(\frac{U}{c}\right)^{k-1} \end{aligned} \quad (18.25)$$

This change of variables maps $U \in [U_t, \infty)$ to $x \in [x_t, \infty)$ where we have defined $x_t = (U_t/c)^k$.

Substituting this into (18.24) we obtain

$$\begin{aligned}
 W(U_t, n) &= \int_{x_t}^{\infty} c^n x^{n/k} k c^{-1} x^{(k-1)/k} e^{-x} c k^{-1} x^{-(k-1)/k} dx \\
 &= c^n \int_{x_t}^{\infty} x^{n/k} e^{-x} dx \\
 &= c^n \int_{x_t}^{\infty} x^{\alpha-1} e^{-x} dx
 \end{aligned} \tag{18.26}$$

where we defined $\alpha = 1 + n/k$ in the last step. The integral expression on the RHS of (18.26) is the upper incomplete gamma function $\Gamma(\alpha, x_t)$. Section 18.7 describes incomplete gamma function properties.

Rewriting (18.26) in terms of (18.12) we obtain

$$\begin{aligned}
 W(U_t, n) &= c^n \Gamma(\alpha, x_t) \\
 &= c^n \Gamma\left(\frac{k+n}{k}, \left(\frac{U_t}{c}\right)^k\right)
 \end{aligned} \tag{18.27}$$

Thus the moments of the Weibull distribution are given by the gamma function when $U_t = 0 \text{ m s}^{-1}$ and by the (upper) incomplete gamma function when $U_t > 0 \text{ m s}^{-1}$.

The cumulative distribution function of the full Weibull PDF (18.20) is solved by setting $U_t = 0 \text{ m s}^{-1}$ and $n = 0$ in (18.27)

$$W(U_t = 0, n = 0) = c^0 \Gamma(1, 0) = \Gamma(1) = 1 \tag{18.28}$$

Hence (18.28) verifies that the Weibull PDF (18.20) correctly normalizes to one when integrated over all wind speeds.

Equation (18.27) makes a number of useful wind speed statistics readily available. First, the probability of the wind speed exceeding the threshold wind speed is

$$\begin{aligned}
 p(U > U_t) = W(U_t, 0) &= \Gamma(1, x_t) \\
 &= \int_{x_t}^{\infty} e^{-x} dx \\
 &= e^{-x_t} \\
 &= \exp\left[-\left(\frac{U_t}{c}\right)^k\right]
 \end{aligned} \tag{18.29}$$

Of course $p(U < U_t) = 1 - p(U > U_t)$. In a Weibull distribution the frequency of occurrence of winds exceeding U_t decreases exponentially with U_t . Thus the Weibull distribution produces wind speed statistics analogous to the Boltzmann statistics of energy levels.

The windspeed U_i such that a given fraction p_i of the Weibull PDF exceeds U_i is obtained

by inverting (18.29)

$$\begin{aligned}
 \exp \left[- \left(\frac{U_i}{c} \right)^k \right] &= p_i \\
 - \left(\frac{U_i}{c} \right)^k &= \ln p_i \\
 - \left(\frac{U_i}{c} \right) &= (\ln p_i)^{1/k} \\
 U_i &= c(-\ln p_i)^{1/k}
 \end{aligned} \tag{18.30}$$

According to (18.30) the median wind speed \tilde{U} is

$$\tilde{U} \equiv U(p_i = 0.5) = c(\ln 2)^{1/k} \tag{18.31}$$

The optimal sampling and weighting of the Weibull PDF (18.20) (or any PDF) depends on the purpose. Relation (18.30) can be used to sample (and weight) the Weibull PDF itself (18.20), not higher order moments (18.22). Wind erosion integrals (3.108) depend on quadratic, cubic, and quartic, wind speed moments, e.g., (3.41), (3.42), (3.52), and (3.67). Accurate evaluation of such integrals should optimally sample the probability distributions of the higher order moments.

The mean wind speed \bar{U} is, by definition, the first moment ($n = 1$) of the entire Weibull distribution (18.27)

$$\bar{U} \equiv W(U_t = 0, n = 1) = c[\Gamma(1 + 1/k)] \tag{18.32}$$

18.10.1 Truncated Weibull Distributions

If a PDF and cumulative distribution are both expressible in closed form, then it is straightforward to determine statistical properties of the truncated PDF, i.e., arbitrarily bounded segments of the PDF. For the Weibull PDF (18.20) and cumulative PDF (18.24), it is often useful to know the statistical properties between two wind speeds defined such that $U_1 < U_2$. The linearity of integrals applied to (18.24) allows us to immediately express the probability that $U_1 < U < U_2$

$$W(U_1, U_2; 0) \equiv p(U_1 < U < U_2) = W(U_1, 0) - W(U_2, 0) \tag{18.33}$$

$$= \exp \left[- \left(\frac{U_1}{c} \right)^k \right] - \exp \left[- \left(\frac{U_2}{c} \right)^k \right] \tag{18.34}$$

where we substituted (18.29) to obtain the closed form in the final step. Similarly, the normalization property (18.28) allows us to determine the mean wind speed \bar{U} of any Weibull

PDF truncated to $[U_1, U_2]$

$$\bar{U} = W(U_1, U_2; 1) = \frac{W(U_1, 1) - W(U_2, 1)}{W(U_1, 0) - W(U_2, 0)} \quad (18.35)$$

$$= c \times \left[\Gamma\left(\frac{k+1}{k}, \left(\frac{U_1}{c}\right)^k\right) - \Gamma\left(\frac{k+1}{k}, \left(\frac{U_2}{c}\right)^k\right) \right] \\ \times \left\{ \exp\left[-\left(\frac{U_1}{c}\right)^k\right] - \exp\left[-\left(\frac{U_2}{c}\right)^k\right] \right\}^{-1} \quad (18.36)$$

where we substituted $n = 1$ into (18.27) to obtain the closed form in (18.36). The final term is the inverse of (18.34) and normalizes the mean to the probability contained in the truncated region.

18.10.2 Wind Speed Observations

In atmospheric studies \bar{U} is often a predicted or observed quantity from which we obtain the scale parameter

$$c = \bar{U}[\Gamma(1 + 1/k)]^{-1} \quad (18.37)$$

Gillette and Passi (1988) noted that $\Gamma(1 + 1/k) \approx 0.9$ over the usual range of k values. Thus typical values of the scale parameter are $c \approx 1.1\bar{U} \text{ m s}^{-1}$.

Justus et al. (1978) examined hourly surface wind speeds at a site in the continental United States. They found an empirical relationship between the shape parameter and the mean wind speed

$$k = C_k \sqrt{\bar{U}} \quad (18.38)$$

where \bar{U} is in m s^{-1} . They used the normalized standard deviation of the measured wind speed distribution, (σ/\bar{U}) to classify sites as low (10 percentile), average, or high (90 percentile) variability. For low, average, and high variability winds C_k is approximately 1.05, 0.94, and 0.83, respectively. We assume the surface winds are highly variable during dust events (i.e., when $U > U_t$) and employ $C_k = 0.83$.

The shape parameter k_{atm} may be transferred from reference height z_r (e.g., 10 m) to some other height z_{atm} using (Justus et al., 1978)

$$k_{\text{atm}} = k_r [1 - 0.088 \ln(z_r/10)] / [1 - 0.088 \ln(z_{\text{atm}}/10)] \quad (18.39)$$

18.11 Aspherical Shapes

Natural aerosols come in a variety of shapes. This morphology plays a significant role in thermodynamics, dry deposition, optics, and chemical uptake. A fundamental understanding of aerosol physics is best grounded in the spherical particle assumption. Practical applications, however, must account for aspherical effects. For now we defer a related problem, non-smooth surfaces.

18.11.1 Cylinders

Few aspherical shapes are analytically tractable. As a result, cylinders are the most studied variant.

18.11.2 Ellipsoids

The most convenient, aspherical shape without corners is the ellipsoid. An ellipsoid is a solid of revolution generated by rotating an ellipse about one its major axis D_A to form an oblate ellipsoid, or about its minor axis D_B to form a prolate ellipsoid.

Our discussion of ellipse properties is based on the following assumptions:

1. The major axis of an ellipse is denoted the A -axis. The length of the major axis is $D_A = 2r_A = 2A$. Rotation about the A -axis forms an oblate ellipsoid. Then the third axis $C = A$.
2. The minor axis of an ellipsoid is denoted the B -axis. The length of the minor axis is $D_B = 2r_B = 2B$. Rotation about the B -axis forms a prolate ellipsoid. Then the third axis $C = B$.

With these conventions, the eccentricity e surface area S_e of the ellipsoid are

$$e = \frac{\sqrt{D_A^2 - D_B^2}}{D_A} \quad (18.40)$$

$$\begin{aligned} S_e &= \frac{2\pi}{2e} \left\{ r_A^2 + r_B^2 \left[\log \left(\frac{1+e}{1-e} \right) \right] \right\} \\ &= 2\pi r_B^2 + 2\pi \frac{D_B D_A}{e} \sin^{-1} e \end{aligned} \quad (18.41)$$

18.11.3 Hexagonal Prisms

The most common aspherical shape with edges encountered in atmospheric particles are hexagonal prisms, a shape found in natural snow, ice, and mineral dust crystals (Auer and Veal, 1970; Heymsfield, 1972; Knollenberg, 1972; Heymsfield and Platt, 1984; Ginoux, 2003; Neshyba et al., 2003). Hexagonal prisms often form from Ice Nuclei under the right temperature and humidity conditions. We now develop in detail the geometric properties and the V/S technique (Section 5.4.3) for hexagonal prisms.

Hexagonal prisms are characterized by two lengths. The prism length c is the distance between the opposite hexagonal faces, also known as the c -axis. The half-width a of basal face of a hexagonal prism is also the width of its six facets. The tranverse or basal face of a prism is likewise known as the a -axis.

Together a and c completely characterize the geometry of the prism. It is convenient to define the aspect ratio Γ as the ratio of the c -axis length to the a -axis width (the full width $2a$, not the half-width a):

$$\Gamma \equiv \frac{c}{2a} \quad (18.42)$$

With this definition, prisms with $\Gamma < 1$ are called hexagonal plates and prisms with $\Gamma > 1$ are called hexagonal columns, respectively.

The surface area S_h [m²] and volume V_h [m³] of a hexagonal prism are

$$S_h = 6ac + 3\sqrt{3}a^2 = 3a(2c + \sqrt{3}a) \quad (18.43)$$

$$V_h = \frac{3\sqrt{3}a^2c}{2} \quad (18.44)$$

These definitions may be re-cast in terms of a and Γ by using $c = 2a\Gamma$ from (18.42)

$$S_h = 12a^2\Gamma + 3\sqrt{3}a^2 = 3a^2(4\Gamma + \sqrt{3}) \quad (18.45)$$

$$V_h = 3\sqrt{3}a^3\Gamma \quad (18.46)$$

It is more convenient to describe hexagons in terms of (a, Γ) than (a, c) . This is because natural hexagonal prisms may share similar aspect ratios over a large range of sizes.

The radius r_s of a sphere of equivalent surface area to hexagonal prism is obtained by setting $S_s = S_h$

$$\begin{aligned} S_s &= S_h \\ 4\pi r_s^2 &= 3a^2(4\Gamma + \sqrt{3}) \\ r_s &= \left[\frac{3a^2(4\Gamma + \sqrt{3})}{4\pi} \right]^{1/2} \\ &= \left[\frac{6ac + 3\sqrt{3}a^2}{4\pi} \right]^{1/2} \end{aligned} \quad (18.47)$$

Similarly, we set $V_s = V_h$ to find the radius r_v of spheres of equivalent volume:

$$\begin{aligned} V_s &= V_h \\ \frac{4\pi r_v^3}{3} &= 3\sqrt{3}a^3\Gamma \\ r_v &= 3\sqrt{3}a^3\Gamma \\ r_v &= \left[\frac{9\sqrt{3}a^3\Gamma}{4\pi} \right]^{1/3} \\ &= \left[\frac{9\sqrt{3}a^2c}{8\pi} \right]^{1/3} \end{aligned} \quad (18.48)$$

The geometry of equal volume-to-area (in particular, surface area) spheres is described by Grenfell and Warren (1999) and Neshyba et al. (2003). The radius $r_{v/s}$ of the sphere

with the same volume-to-total surface area ratio as a hexagonal prism is determined by

$$\begin{aligned}
 \frac{V_s}{S_s} &= \frac{V_h}{S_h} \\
 \left(\frac{4\pi r_{V/S}^3}{3} \right) / (4\pi r_{V/S}^2) &= \frac{3\sqrt{3}a^3\Gamma}{3a^2(4\Gamma + \sqrt{3})} \\
 \frac{r_{V/S}}{3} &= \frac{\sqrt{3}a\Gamma}{4\Gamma + \sqrt{3}} \\
 r_{V/S} &= \frac{3\sqrt{3}a\Gamma}{4\Gamma + \sqrt{3}} \\
 &= \frac{3\sqrt{3}ac}{4c + 2\sqrt{3}a}
 \end{aligned} \tag{18.49}$$

Grenfell and Warren (1999) point out that (18.48)–(18.50) apply equally if cross-sectional area A is used instead of surface area S . This is because the ratio $S/A = 4$ for all randomly oriented convex shapes. Since randomly oriented spheres and hexagonal crystals have the same ratio $S/A = 4$, this ratio would factor out of both sides of the above derivation yielding $r_S = r_A$ and $r_{V/S} = r_{V/A}$ where r_A and $r_{V/A}$ are the radii of spheres of equivalent cross-sectional area and volume-to-cross-sectional area, respectively.

Following the derivation of (5.36), we find the number $N_{V/S}$ of spheres with equal V/S ratios to hexagonal prisms that have the same total volume as N_h hexagonal prisms

$$\begin{aligned}
 N_{V/S} V_{V/S} &= N_h V_h \tag{18.50} \\
 N_{V/S} \frac{4\pi r_{V/S}^3}{3} &= N_h 3\sqrt{3}a^3\Gamma \\
 \frac{N_{V/S}}{N_h} &= \frac{9\sqrt{3}a^3\Gamma}{4\pi r_{V/S}^3} \\
 &= \frac{9\sqrt{3}a^3\Gamma}{4\pi} \left(\frac{4\Gamma + \sqrt{3}}{3\sqrt{3}a\Gamma} \right)^3 \\
 &= \frac{9\sqrt{3}a^3\Gamma}{4\pi} \times \frac{(4\Gamma + \sqrt{3})^3}{81\sqrt{3}a^3\Gamma^3} \\
 &= \frac{1}{4\pi} \times \frac{(4\Gamma + \sqrt{3})^3}{9\Gamma^2} \\
 &= \frac{(4\Gamma + \sqrt{3})^3}{36\pi\Gamma^2} \tag{18.51}
 \end{aligned}$$

Neshyba et al. (2003) plot the behavior of (18.51) and show that the minimum number of V/S-spheres per hexagonal crystal is $N_{V/S} = 1.65$ which occurs at aspect ratio $\Gamma = 0.866$.

It is useful to define the size parameter χ_h of hexagonal prisms when discussing their

optical properties. Following [Neshyba et al. \(2003\)](#),

$$\begin{aligned}\chi_h &= \frac{2\pi}{\lambda} \sqrt{\frac{ac}{2}} \\ \chi_h &= \frac{2\pi a}{\lambda} \sqrt{\Gamma}\end{aligned}\tag{18.52}$$

This can be compared to the size parameter for spherical particles ([9.34](#)) .

18.12 Vector Mathematics

18.12.1 Del Operator

We define the del operator in Cartesian coordinates as

$$\nabla = \hat{\mathbf{i}} \frac{\partial}{\partial x} + \hat{\mathbf{j}} \frac{\partial}{\partial y} + \hat{\mathbf{k}} \frac{\partial}{\partial z}\tag{18.53}$$

where $\hat{\mathbf{i}}$, $\hat{\mathbf{j}}$, and $\hat{\mathbf{k}}$ are the unit vectors in the x , y , and z directions, respectively. Thus ∇ is a vector differential operator. Another name for ∇ is nabla. The del operator can act on both scalar and vector fields. These operations are given distinct names to make clear the type of field ∇ is operating on, and exactly how ∇ operates on the field. In all cases, however, the operations employ the del operator.

18.12.2 Gradient

Every continuous, differentiable scalar field u defines a vector field called the gradient of u or $\text{grad } u$. The grad operator is written ∇ . In Cartesian coordinates, the gradient of u is

$$\nabla u = \frac{\partial u}{\partial x} \hat{\mathbf{i}} + \frac{\partial u}{\partial y} \hat{\mathbf{j}} + \frac{\partial u}{\partial z} \hat{\mathbf{k}}\tag{18.54}$$

Note that the unit vectors appear after the differential operators, differentiation of the unit vectors is not implied. The gradient of u points in the direction of most rapidly changing u , and the magnitude of ∇u is the rate of change of u along that direction.

18.12.3 Divergence

Associated with every continuous and differentiable vector field \mathbf{v} is a scalar field called the divergence of \mathbf{v} , or $\text{div } \mathbf{v}$. The div operator is written $\nabla \cdot$. In Cartesian coordinates, the divergence of \mathbf{v} is

$$\nabla \cdot \mathbf{v} = \frac{\partial v_x}{\partial x} + \frac{\partial v_y}{\partial y} + \frac{\partial v_z}{\partial z}\tag{18.55}$$

The “ \cdot ” operator denotes the inner product and is read “dot”. Hence the divergence operator equals “del dot”. For definiteness, let \mathbf{v} represent the fluid velocity field and consider an infinitesimal control volume dV with surface area dS centered at the point P . Then value of $\nabla \cdot \mathbf{v}$ at P is the fluid outflow through S per unit volume.

18.12.4 Curl

Associated with every continuous and differentiable vector field \mathbf{v} is another vector field called the curl of \mathbf{v} , or $\text{curl } \mathbf{v}$. The curl operator is written $\nabla \times$. In Cartesian coordinates, the curl of \mathbf{v} is

$$\nabla \times \mathbf{v} = \left(\frac{\partial v_z}{\partial y} - \frac{\partial v_y}{\partial z} \right) \hat{\mathbf{i}} + \left(\frac{\partial v_x}{\partial z} - \frac{\partial v_z}{\partial x} \right) \hat{\mathbf{j}} + \left(\frac{\partial v_y}{\partial x} - \frac{\partial v_x}{\partial y} \right) \hat{\mathbf{k}} \quad (18.56)$$

Hence the curl operator equals “del cross”. When \mathbf{v} represents the fluid velocity, then $\nabla \times \mathbf{v}$ is called the vorticity. In this case, the vorticity $\nabla \times \mathbf{v}$ at the point P is twice the angular velocity of the fluid at P .

18.12.5 Laplacian

Finally, we define an operator called the Laplacian which, like del (18.53), can act on both scalar and vector fields. The Laplacian operator is written ∇^2 , which is often read as del square. The Laplacian is not del times del, but rather del dot del. In Cartesian coordinates the Laplacian operator is

$$\begin{aligned} \nabla^2 &= \nabla \cdot \nabla = \left(\hat{\mathbf{i}} \frac{\partial}{\partial x} + \hat{\mathbf{j}} \frac{\partial}{\partial y} + \hat{\mathbf{k}} \frac{\partial}{\partial z} \right) \cdot \left(\hat{\mathbf{i}} \frac{\partial}{\partial x} + \hat{\mathbf{j}} \frac{\partial}{\partial y} + \hat{\mathbf{k}} \frac{\partial}{\partial z} \right) \\ &= \frac{\partial^2}{\partial x^2} + \frac{\partial^2}{\partial y^2} + \frac{\partial^2}{\partial z^2} \end{aligned} \quad (18.57)$$

The similarity between (18.57) and (18.53) explains why the Laplacian is often called “del square”. In Cartesian coordinates the Laplacian of u and the Laplacian of \mathbf{v} are

$$\nabla^2 u = \frac{\partial^2 u}{\partial x^2} + \frac{\partial^2 u}{\partial y^2} + \frac{\partial^2 u}{\partial z^2} \quad (18.58)$$

$$\begin{aligned} \nabla^2 \mathbf{v} &= \left(\frac{\partial^2 v_x}{\partial x^2} + \frac{\partial^2 v_x}{\partial y^2} + \frac{\partial^2 v_x}{\partial z^2} \right) \hat{\mathbf{i}} + \left(\frac{\partial^2 v_y}{\partial x^2} + \frac{\partial^2 v_y}{\partial y^2} + \frac{\partial^2 v_y}{\partial z^2} \right) \hat{\mathbf{j}} \\ &\quad + \left(\frac{\partial^2 v_z}{\partial x^2} + \frac{\partial^2 v_z}{\partial y^2} + \frac{\partial^2 v_z}{\partial z^2} \right) \hat{\mathbf{k}} \end{aligned} \quad (18.59)$$

Hence the Laplacian of a scalar field is a scalar field and the Laplacian of a vector field is a vector field. Comparing (18.59) to (18.54) and (18.55), we see that the Laplacian of a scalar function is the divergence of the gradient of the function. The Laplacian of a vector field is not the gradient of the divergence of the field.

18.13 Spherical Coordinates

The spherical coordinate system is the primary coordinate system used in large scale meteorology. Virtually all meteorological applications use latitude ϕ as the meridional coordinate and longitude λ as the azimuthal coordinate. The latitude angle ϕ projects onto the z -axis and is defined in the domain $-\pi/2 \leq \phi \leq \pi/2$ so that $\phi = 0$ is at the equator. The longitude

angle λ is defined in the domain $0 \leq \lambda < 2\pi$ so that $\lambda = 0$ is on the x -axis (at Greenwich). We shall refer to such coordinates as spherical coordinates or spherical meteorological coordinates.

There is, however, a potential source of confusion in using spherical coordinates. The confusion arises when sciences besides large scale meteorology are involved. In many (most?) sciences besides large scale meteorology, it is traditional to work with spherical polar coordinates. The additional term “polar” indicates that the angle θ which projects onto the z -axis is defined in the domain $0 \leq \theta \leq \pi$ so that $\theta = 0$ is at the North pole. Thus many physicists, astronomers, geodysists, and radiative transfer theoreticians are used to working with the co-latitude θ , rather than with the latitude, ϕ . To compound the confusion, meteorologists use ϕ for the meridional angle while astronomers and radiative transfer theorists use ϕ for the azimuthal angle.

18.13.1 Cartesian-Spherical Transformations

Spherical polar coordinates (r, θ, ϕ) transform into Cartesian coordinates (x, y, z) as

$$x = r \sin \theta \cos \phi \quad (18.60a)$$

$$y = r \sin \theta \sin \phi \quad (18.60b)$$

$$z = r \cos \theta \quad (18.60c)$$

Cartesian coordinates (x, y, z) transform into spherical polar coordinates (r, θ, ϕ) as

$$r = \sqrt{x^2 + y^2 + z^2} \quad (18.61a)$$

$$\theta = \arccos(z/r) \quad (18.61b)$$

$$\phi = \arctan(y/x) \quad (18.61c)$$

Cartesian unit vectors $(\hat{\mathbf{i}}, \hat{\mathbf{j}}, \hat{\mathbf{k}})$ transform into spherical polar unit vectors $(\hat{\mathbf{r}}, \hat{\boldsymbol{\theta}}, \hat{\boldsymbol{\phi}})$

$$\hat{\mathbf{r}} = \sin \theta \cos \phi \hat{\mathbf{i}} + \sin \theta \sin \phi \hat{\mathbf{j}} + \cos \theta \hat{\mathbf{k}} \quad (18.62a)$$

$$\hat{\boldsymbol{\theta}} = \cos \theta \cos \phi \hat{\mathbf{i}} + \cos \theta \sin \phi \hat{\mathbf{j}} - \sin \theta \hat{\mathbf{k}} \quad (18.62b)$$

$$\hat{\boldsymbol{\phi}} = -\sin \phi \hat{\mathbf{i}} + \cos \phi \hat{\mathbf{j}} \quad (18.62c)$$

It can be verified the basis vectors are orthonormal.

Spherical meteorological coordinates (r, ϕ, λ) transform into Cartesian coordinates (x, y, z) as

$$x = r \cos \phi \cos \lambda \quad (18.63a)$$

$$y = r \cos \phi \sin \lambda \quad (18.63b)$$

$$z = r \sin \phi \quad (18.63c)$$

Cartesian coordinates (x, y, z) transform into spherical meteorological coordinates (r, ϕ, λ) as

$$r = \sqrt{x^2 + y^2 + z^2} \quad (18.64a)$$

$$\phi = \arcsin(z/r) \quad (18.64b)$$

$$\lambda = \arctan(y/x) \quad (18.64c)$$

Cartesian unit vectors ($\hat{\mathbf{i}}, \hat{\mathbf{j}}, \hat{\mathbf{k}}$) transform into spherical meteorological unit vectors ($\hat{\mathbf{r}}, \hat{\phi}, \hat{\lambda}$) (20160117 fxm: verify this)

$$\hat{\mathbf{r}} = \cos \phi \cos \lambda \hat{\mathbf{i}} + \cos \phi \sin \lambda \hat{\mathbf{j}} + \sin \phi \hat{\mathbf{k}} \quad (18.65a)$$

$$\hat{\phi} = \sin \phi \cos \lambda \hat{\mathbf{i}} + \sin \phi \sin \lambda \hat{\mathbf{j}} - \cos \phi \hat{\mathbf{k}} \quad (18.65b)$$

$$\hat{\lambda} = -\sin \lambda \hat{\mathbf{i}} + \cos \lambda \hat{\mathbf{j}} \quad (18.65c)$$

18.13.2 Gradient

In spherical meteorological coordinates, the gradient of u is

$$\nabla u = \frac{\partial u}{\partial r} \hat{\mathbf{r}} + \frac{1}{r} \frac{\partial u}{\partial \phi} \hat{\phi} + \frac{1}{r \cos \phi} \frac{\partial u}{\partial \lambda} \hat{\lambda} \quad (18.66)$$

In spherical polar coordinates, the gradient of u is

$$\nabla u = \frac{\partial u}{\partial r} \hat{\mathbf{r}} + \frac{1}{r} \frac{\partial u}{\partial \theta} \hat{\theta} + \frac{1}{r \sin \theta} \frac{\partial u}{\partial \phi} \hat{\phi} \quad (18.67)$$

18.13.3 Divergence

In spherical meteorological coordinates, the divergence of \mathbf{v} is

$$\begin{aligned} \nabla \cdot \mathbf{v} &= \frac{1}{r^2} \frac{\partial}{\partial r} (r^2 v_r) + \frac{1}{r \sin \phi} \frac{\partial}{\partial \phi} (\cos \phi v_\phi) + \frac{1}{r \sin \phi} \frac{\partial v_\lambda}{\partial \lambda} \\ &= \frac{1}{r^2 \cos \phi} \left(\cos \phi \frac{\partial}{\partial r} (r v_r) + r \frac{\partial}{\partial \phi} (\cos \phi v_\phi) + r \frac{\partial v_\lambda}{\partial \lambda} \right) \end{aligned} \quad (18.68)$$

In spherical polar coordinates, the divergence of \mathbf{v} is

$$\begin{aligned} \nabla \cdot \mathbf{v} &= \frac{1}{r^2} \frac{\partial}{\partial r} (r^2 v_r) + \frac{1}{r \sin \theta} \frac{\partial}{\partial \theta} (\sin \theta v_\theta) + \frac{1}{r \sin \theta} \frac{\partial v_\phi}{\partial \phi} \\ &= \frac{1}{r^2 \sin \theta} \left(\sin \theta \frac{\partial}{\partial r} (r v_r) + r \frac{\partial}{\partial \theta} (\sin \theta v_\theta) + r \frac{\partial v_\phi}{\partial \phi} \right) \end{aligned} \quad (18.69)$$

18.13.4 Curl

In spherical meteorological coordinates, the curl of \mathbf{v} is

$$\begin{aligned} \nabla \times \mathbf{v} &= \frac{1}{r \cos \phi} \left(\frac{\partial v_\phi}{\partial \lambda} - \frac{\partial}{\partial \phi} (\cos \phi v_\lambda) \right) \hat{\mathbf{r}} + \frac{1}{r} \left(\frac{\partial}{\partial r} (r v_\lambda) - \frac{1}{\cos \phi} \frac{\partial v_r}{\partial \lambda} \right) \hat{\phi} \\ &\quad + \frac{1}{r} \left(\frac{\partial v_r}{\partial \phi} - \frac{\partial}{\partial r} (r v_\phi) \right) \hat{\lambda} \end{aligned} \quad (18.70)$$

In spherical polar coordinates, the curl of \mathbf{v} is

$$\begin{aligned} \nabla \times \mathbf{v} &= \frac{1}{r \sin \theta} \left(\frac{\partial v_\theta}{\partial \phi} - \frac{\partial}{\partial \theta} (\sin \theta v_\phi) \right) \hat{\mathbf{r}} + \frac{1}{r} \left(\frac{\partial}{\partial r} (r v_\phi) - \frac{1}{\sin \theta} \frac{\partial v_r}{\partial \phi} \right) \hat{\theta} \\ &\quad + \frac{1}{r} \left(\frac{\partial v_r}{\partial \theta} - \frac{\partial}{\partial r} (r v_\theta) \right) \hat{\phi} \end{aligned} \quad (18.71)$$

18.13.5 Laplacian

In spherical polar coordinates, the Laplacian of u is

$$\begin{aligned}\nabla^2 u &= \frac{1}{r^2} \frac{\partial}{\partial r} \left(r^2 \frac{\partial u}{\partial r} \right) + \frac{1}{r^2 \sin \theta} \frac{\partial}{\partial \theta} \left(\sin \theta \frac{\partial u}{\partial \theta} \right) + \frac{1}{r^2 \sin^2 \theta} \frac{\partial^2 u}{\partial \phi^2} \\ &= \frac{1}{r} \frac{\partial^2}{\partial r^2} (ru) + \frac{1}{r^2 \sin \theta} \frac{\partial}{\partial \theta} \left(\sin \theta \frac{\partial u}{\partial \theta} \right) + \frac{1}{r^2 \sin^2 \theta} \frac{\partial^2 u}{\partial \phi^2}\end{aligned}\quad (18.72)$$

The vector Laplacian consists of the scalar Laplacian applied to each individual component of the vector. In spherical polar coordinates, the Laplacian of \mathbf{v} is quite complex. It is most easily derived by taking the curl of (18.71) and applying (??) to the result. The radial ($\hat{\mathbf{r}}$) component of the result is

$$\begin{aligned}\nabla^2 \mathbf{v} \Big|_r &= \left(-\frac{2}{r^2} + \frac{2}{r} \frac{\partial}{\partial r} + \frac{\partial^2}{\partial r^2} + \frac{\cos \theta}{r^2 \sin \theta} \frac{\partial}{\partial \theta} + \frac{1}{r^2} \frac{\partial^2}{\partial \theta^2} + \frac{1}{r^2 \sin^2 \theta} \frac{\partial^2}{\partial \phi^2} \right) v_r \\ &\quad + \left(-\frac{2}{r^2} \frac{\partial}{\partial \theta} - \frac{2 \cos \theta}{r^2 \sin \theta} \right) v_\theta + \left(-\frac{2}{r^2 \sin \theta} \frac{\partial}{\partial \phi} \right) v_\phi\end{aligned}\quad (18.73)$$

Using (18.72) to simplify the operator on the radial component of v_r , we obtain

$$\begin{aligned}\nabla^2 \mathbf{v} &= \left(\nabla^2 v_r - \frac{2}{r^2} v_r - \frac{2}{r^2} \frac{\partial v_\theta}{\partial \theta} - \frac{2 \cos \theta}{r^2 \sin \theta} v_\theta - \frac{2}{r^2 \sin \theta} \frac{\partial v_\phi}{\partial \phi} \right) \hat{\mathbf{r}} \\ &\quad + \left(\nabla^2 v_\theta - \frac{1}{r^2 \sin^2 \theta} v_\theta + \frac{2}{r^2} \frac{\partial v_r}{\partial \theta} - \frac{2 \cos \theta}{r^2 \sin^2 \theta} \frac{\partial v_\phi}{\partial \phi} \right) \hat{\boldsymbol{\theta}} \\ &\quad + \left(\nabla^2 v_\phi - \frac{1}{r^2 \sin^2 \theta} v_\phi + \frac{2}{r^2 \sin \theta} \frac{\partial v_r}{\partial \phi} + \frac{2 \cos \theta}{r^2 \sin^2 \theta} \frac{\partial v_\theta}{\partial \phi} \right) \hat{\boldsymbol{\phi}}\end{aligned}\quad (18.74)$$

Quantities satisfying the vector wave equation on the sphere will require (18.74).

18.14 Fluid Mechanics

Let the vector field \mathbf{v} represent the fluid velocity. The velocity is a function of position \mathbf{r} and time t . In Cartesian coordinates, the components of \mathbf{v} are

$$\mathbf{v} = v_x \hat{\mathbf{i}} + v_y \hat{\mathbf{j}} + v_z \hat{\mathbf{k}} \quad (18.75)$$

where $\hat{\mathbf{i}}$, $\hat{\mathbf{j}}$, and $\hat{\mathbf{k}}$ are the unit vectors in the x , y , and z directions, respectively. The magnitude of \mathbf{v} , or wind speed, is

$$|\mathbf{v}| = U = (\mathbf{v} \cdot \mathbf{v})^{1/2} = (v_x^2 + v_y^2 + v_z^2)^{1/2} \quad (18.76)$$

The wind speed U is measured in m s^{-1} .

Consider a scalar field T that is a function of space and time, i.e., $T = T(x, y, z, t)$. For concreteness, say T_0 represents the temperature at a given point (x_0, y_0, z_0) . The partial derivative of T with respect to time, $\partial_t T$ represents the change in T due to internal sources

and sinks. Condensation or evaporation of water vapor, chemical reactions, and radiative processes are examples of internal sources and sinks of heat. Such internal processes can alter T_0 in the absence of any transport, i.e., when $\mathbf{v} = 0$. However, T_0 may also change due to advective processes. For example, wind may bring warmer air to a cool region, increasing the local temperature.

The material derivative embodies these processes. The material derivative is the sum of the rates of change of a property due to internal processes and to advection

$$\frac{D}{Dt} = \frac{\partial}{\partial t} + \mathbf{v} \cdot \nabla \quad (18.77)$$

Since internal and advective processes are the only physical processes which can alter a conserved quantity, the material derivative in (18.77) is also called the total derivative. The material derivative in (18.77) is also called the Lagrangian derivative or the

To continue our example with the temperature field T

$$\frac{DT}{Dt} = \frac{\partial T}{\partial t} + \mathbf{v} \cdot \nabla T \quad (18.78)$$

The LHS is the rate of change of T following a fluid element. The RHS has two contributions. The first, $\frac{\partial T}{\partial t}$, is any temporal change in T not due to motion. For example, a fixed amount of condensation increases T in a parcel regardless of how fast the parcel moves. However, the Lagrangian description of the parcel.

Consider a fixed parcel of fluid in motion with its environment. To develop a mental picture of this parcel let us imagine that every molecule in it is colored green, and that the parcel moves within a medium of blue molecules. Regardless of how the fluid motion deforms the shape of the green parcel, its mass is unchanged. Since the mass of the parcel is conserved, its density must change if its volume changes. Conservation of mass requires that changes in local fluid density occur only with a corresponding change in mass convergence or divergence.

$$\frac{\partial \rho}{\partial t} + \nabla \cdot (\rho \mathbf{v}) = 0 \quad (18.79)$$

This is the equation of continuity in flux form. Using the product rule, (18.79) becomes

$$\begin{aligned} \frac{\partial \rho}{\partial t} + \rho \nabla \cdot \mathbf{v} + \mathbf{v} \cdot \nabla \rho &= 0 \\ \frac{D\rho}{Dt} + \rho \nabla \cdot \mathbf{v} &= 0 \\ \frac{1}{\rho} \frac{D\rho}{Dt} + \nabla \cdot \mathbf{v} &= 0 \end{aligned} \quad (18.80)$$

The latter is the equation of continuity in velocity divergence form. The first term in (18.79) is the fractional rate of change of density. The divergence theorem tells us that the second term, $\nabla \cdot \mathbf{v}$, equals the fractional rate of change of volume. Thus the conservation of mass implies that the fractional rate of change of density must compensate the fractional rate of change of volume.

In steady state flow the density of a fluid does not change with time so that $\partial_t \rho = 0$ and

$$\rho \nabla \cdot \mathbf{v} + \mathbf{v} \cdot \nabla \rho = 0 \quad (18.81)$$

If the fluid is incompressible, (18.81) simplifies further. Incompressibility does not mean that the fluid flow is everywhere uniform. Rather, it means that when the flow in one direction changes, due to an impediment, say, that there is a corresponding change in the flow in the other directions such that the density of the fluid does not change. In this sense a balloon filled with water is incompressible. Squeezing it in one direction does not change the density of the water because the balloon expands in other directions allowing water to remain at a constant density. The mathematical expression of the property of incompressibility can be shown to be (e.g., Dutton, 1986)

$$\nabla \cdot \mathbf{v} = 0 \quad (18.82)$$

In Cartesian coordinates (18.82) becomes

$$\frac{\partial u_x}{\partial x} + \frac{\partial u_y}{\partial y} + \frac{\partial u_z}{\partial z} = 0 \quad (18.83)$$

All of classical mechanics are based on Newton's laws of motion. The first law states that Newton's Second Law of motion states that there is a conserved quantity called momentum which is the mass M of an object times its velocity \mathbf{v}

$$\mathbf{p} = M\mathbf{v} \quad (18.84)$$

Since momentum \mathbf{p} is conserved and mass M is fixed, (18.84) implies that the velocity \mathbf{v} of an object remains constant until an external force is applied. Hence, a body in motion remains in motion until an external force is applied. The second law is often quoted in a form which may be obtained by differentiating (18.84) with respect to time

$$\begin{aligned} \mathbf{F} &= M \frac{d\mathbf{v}}{dt} \\ \mathbf{F} &= M\mathbf{a} \end{aligned} \quad (18.85)$$

where \mathbf{F} denotes force and \mathbf{a} acceleration. Thus force \mathbf{F} is the time rate of change of momentum \mathbf{p} . Equation (18.85) states that an applied force \mathbf{F} alters the velocity of an object by inducing an acceleration \mathbf{a} . Although (18.84) and (18.85) may appear to be solely definitions at this point, their richness and predictive capacity quickly become apparent when physical laws are substituted for \mathbf{F} . For example, the force of gravitation \mathbf{F}_g between two objects of masses M_1 and M_2 is

$$\mathbf{F}_g = -\frac{GM_1M_2}{r^2}\hat{\mathbf{r}} \quad (18.86)$$

where the objects are separated by a displacement \mathbf{r} and $G = 6.672 \times 10^{-11} \text{ N m}^2 \text{ kg}^{-1}$ is the universal gravitational constant. All of celestial mechanics follows from substituting (18.86) into (18.85).

The fluid dynamical momentum equations are obtained by rewriting Newton's second law of motion (18.85) to take account of forces and geometries. First we express (18.85) in terms of a fluid density ρ

$$\rho \frac{d\mathbf{v}}{dt} = \mathbf{F} \quad (18.87)$$

We are now following the fluid dynamical convention of placing the acceleration terms on the LHS and the applied forces on the RHS. The material derivative (18.77) describes the time rate of change of a fluid parcel's momentum due to the net force \mathbf{F} on the parcel

$$\rho \frac{D\mathbf{v}}{dt} = \mathbf{F} \quad (18.88)$$

$$\frac{\partial \mathbf{v}}{\partial t} + \mathbf{v} \cdot \nabla \mathbf{v} = \frac{\mathbf{F}}{\rho} \quad (18.89)$$

The net force on a fluid parcel is the vector sum of the external forces and internal forces on the parcel. External forces act on all the fluid independent of its state of motion. External forces are also called body forces. The only body force of relevance to large scale fluid mechanics is gravity. Coulomb attraction is another important body force which may be important for some aerosol motion.

Internal forces, on the other hand, may depend on the state of motion of the fluid. Internal forces depend on the position and orientation of the parcel. These forces are called stresses and expressed as a force per unit area. Since the stress depends on both position and orientation, the stress must be expressed as a tensor T , called the stress tensor. The stress tensor represents all permutations of directionally-dependent forces. For example, T_{xz} is the stress acting in the direction of the x axis (i.e., along $\hat{\mathbf{i}}$) on a surface normal to the z coordinate axis (i.e., normal to $\hat{\mathbf{k}}$). The stress at any point of a parcel is the vector sum of stresses acting normal to the surface and forces acting tangential to the surface. It can be shown that the stress normal to a parcel is, in fact, the pressure p . The surface tangential stresses to a parcel are also called shear stress, frictional stress, viscous stress or simply drag. The viscous stress is also a tensor, and denoted τ . Thus \mathbf{F} (18.89) is more commonly written as

$$\begin{aligned} \mathbf{F} &= \rho \mathbf{g} + \nabla T \\ &= \rho \mathbf{g} - \nabla p + \nabla \cdot \tau \end{aligned} \quad (18.90)$$

where $\mathbf{g} = -g\hat{\mathbf{k}}$. The pressure gradient is preceded by a negative sign so that acceleration is positive towards the direction of decreasing pressure. We may proceed further if we assume the shear stress term $\nabla \cdot \tau$ obeys Newton's law of friction (18.4). This is an excellent assumption for most fluids.

$$\mathbf{F} = \rho \mathbf{g} - \nabla p + \mu \nabla^2 \mathbf{v} \quad (18.91)$$

Inserting (18.91) in (18.89), the momentum equations become

$$\frac{\partial \mathbf{v}}{\partial t} + \mathbf{v} \cdot \nabla \mathbf{v} = \mathbf{g} + \frac{1}{\rho} \nabla p + \frac{\mu}{\rho} \nabla^2 \mathbf{v} \quad (18.92)$$

In Euler's equations of motion, conservation of momentum (Newton's second law of motion) appears as

$$\begin{aligned} \frac{D\mathbf{v}}{Dt} &= -\frac{1}{\rho} \nabla p + \mathbf{g} + \frac{\mu}{\rho} \nabla^2 \mathbf{v} \\ \frac{\partial \mathbf{v}}{\partial t} + \mathbf{v} \cdot \nabla \mathbf{v} &= -\frac{1}{\rho} \nabla p + \mathbf{g} + \frac{\mu}{\rho} \nabla^2 \mathbf{v} \end{aligned} \quad (18.93)$$

where p is the atmospheric pressure, \mathbf{g} is the gravitational acceleration, and μ is the dynamic viscosity of air. The advective term $\mathbf{A} = \mathbf{v} \cdot \nabla \mathbf{v}$ on the LHS can be confusing. The unique interpretation is $\mathbf{A} = (\mathbf{v} \cdot \nabla) \mathbf{v}$, i.e., \mathbf{A} is the result of $\mathbf{v} \cdot \nabla$ (a scalar operator) operating on the vector \mathbf{v} .

$$\begin{aligned} \mathbf{A} = & \left(v_x \frac{\partial v_x}{\partial x} + v_y \frac{\partial v_x}{\partial y} + v_z \frac{\partial v_x}{\partial z} \right) \hat{\mathbf{i}} + \left(v_x \frac{\partial v_y}{\partial x} + v_y \frac{\partial v_y}{\partial y} + v_z \frac{\partial v_y}{\partial z} \right) \hat{\mathbf{j}} \\ & + \left(v_x \frac{\partial v_z}{\partial x} + v_y \frac{\partial v_z}{\partial y} + v_z \frac{\partial v_z}{\partial z} \right) \hat{\mathbf{k}} \end{aligned} \quad (18.94)$$

One common misinterpretation of A is $\mathbf{v} \cdot (\nabla \mathbf{v})$ which is meaningless since $\nabla \mathbf{v}$ is undefined. Another misinterpretation of A is $\mathbf{v} \cdot \nabla \cdot \mathbf{v}$. This is also fallacious since, no matter which inner product is computed first ($\mathbf{v} \cdot \nabla$ or $\nabla \cdot \mathbf{v}$), the final operation would have to be the inner product of a scalar and a vector.

In Cartesian coordinates, the x component of (18.93) is

$$\frac{\partial v_x}{\partial t} + \left(v_x \frac{\partial v_x}{\partial x} + v_y \frac{\partial v_x}{\partial y} + v_z \frac{\partial v_x}{\partial z} \right) = -\frac{1}{\rho} \frac{\partial p}{\partial x} + \frac{\mu}{\rho} \left(\frac{\partial^2 v_x}{\partial x^2} + \frac{\partial^2 v_x}{\partial y^2} + \frac{\partial^2 v_x}{\partial z^2} \right) \quad (18.95)$$

Bibliography

- Abraham, F. F. (1970), Functional dependence of drag coefficient of a sphere on Reynolds number, *Phys. Fluids*, 13, 2194–2195. [5.4.2](#)
- Abramowitz, M., and I. Stegun (1964), *Handbook of Mathematical Functions*, 1046 pp., Dover, New York. [18.7](#), [18.7](#), [18.7](#)
- Adams, J. M., and H. Faure (1995), Review and atlas of palaeovegetation: Preliminary land ecosystem maps of the world since the Last Glacial Maximum, “<http://stommel.tamu.edu/%7Ebaum/paleoveg.html>”. [7](#)
- Alfaro, S. C., and L. Gomes (1995), Improving the large-scale modeling of the saltation flux of soil particles in presence of nonerodible elements, *J. Geophys. Res.*, 100(D8), 16,357–16,366. [3.4](#)
- Alfaro, S. C., and L. Gomes (2001), Modeling mineral aerosol production by wind erosion: Emission intensities and aerosol size distributions in source areas, *J. Geophys. Res.*, 106(D16), 18,075–18,084. [1.2](#), [3.4](#)
- Alfaro, S. C., A. Gaudichet, L. Gomes, and M. Maillé (1997), Modeling the size distribution of a soil aerosol produced by sandblasting, *J. Geophys. Res.*, 102(D10), 11,239–11,249. [1.2](#), [3.4](#)
- Alfaro, S. C., A. Gaudichet, L. Gomes, and M. Maillé (1998), Mineral aerosol production by wind erosion: Aerosol particle sizes and binding energies, *Geophys. Res. Lett.*, 25(7), 991–994. [3.4](#)
- Alpert, P., Y. J. Kaufman, Y. Shay-El, D. Tanré, A. da Silva, S. Schubert, and J. H. Joseph (1998), Quantification of dust-forced heating of the lower troposphere, *Nature*, 395, 367–370. [10.1](#)
- Ammerman, J. W., R. R. Hood, D. A. Case, and J. B. Cotner (2003), Phosphorus deficiency in the Atlantic: An emerging paradigm in oceanography, *Eos Trans. AGU*, 84(18), 165–170. [16.4](#)
- An, Z. S., J. J. Cao, K. K. Anderson, H. Kawahata, and R. Arimoto (2005), Biogeochemical records of past global iron connections, sub judice, *Global Biogeochem. Cycles*. [7](#)

- Anastasio, C., B. C. Faust, and J. M. Allen (1994), Aqueous phase photochemical formation of hydrogen peroxide in authentic cloud waters, *J. Geophys. Res.*, 99(D4), 8231–8248. [12.2.6](#), [12.3](#), [14.3](#)
- Andersen, K. K., A. Armengaud, and C. Genthon (1998), Atmospheric dust under glacial and interglacial conditions, *Geophys. Res. Lett.*, 25(13), 2281–2284. [7](#)
- Andreas, E. L. (1998), A new sea spray generation function for wind speeds up to 32 m s^{-1} , *J. Phys. Oceanogr.*, 28, 2175–2184. [4.1](#), [4.2](#), [4.2](#), [4.2](#), [4.2](#), [4.2](#)
- Andreas, E. L., J. B. Edson, E. C. Monahan, M. P. Rouault, and S. D. Smith (1995), The spray contribution to net evaporation from the sea: A review of recent progress, *Bound.-Lay. Meteorol.*, 72, 3–52. [4.1](#)
- Aoki, T., T. Y. Tanaka, A. Uchiyama, M. Chiba, M. Mikami, S. Yabuki, and J. R. Key (2005a), Sensitivity experiments of direct radiative forcing caused by mineral dust simulated with a chemical transport model, *J. Meteorol. Soc. Japan*, 83A, 315–331. [5.4.2](#)
- Aoki, T., et al. (2005b), Spectral albedo of desert surfaces measured in western and central China, *J. Meteorol. Soc. Japan*, 83A, 279–290. [5.4.2](#)
- Archer, D., A. Winguth, D. Lea, and N. Mahowald (2000), What caused the glacial/interglacial atmospheric $p\text{CO}_2$ cycles?, *Rev. Geophys.*, 38(2), 159–189. [7](#)
- Arimoto, R. (2001), Eolian dust and climate: relationships to sources, tropospheric chemistry, transport and deposition, *Earth Sci. Revs.*, 54(1–3), 29–42. [1.2](#)
- Arimoto, R., et al. (2006), Characterization of Asian dust during ACE-Asia, In Press in *Global and Planetary Changes*. [1.2](#)
- Arya, S. P. (1988), Introduction to Micrometeorology, no. 42 in International Geophysics Series, Academic Press, New York, NY. [2.2.5](#)
- Atkins, P. W. (1990), Physical Chemistry, fourth ed., W. H. Freeman and Company. [12.1](#), [12.1](#)
- Auer, A. H., Jr., and D. L. Veal (1970), The dimension of ice crystals in natural clouds, *J. Atmos. Sci.*, 27, 919–926. [5.4.2](#), [18.11.3](#)
- Baas, A. C. W. (2005), Dust emission models and the propagation of a typographical error, unpublished manuscript. [3.3](#), [3.3.3](#)
- Bagnold, R. A. (1941), *The Physics of Blown Sand and Desert Dunes*, Methuen & Co. Ltd., London. [3.1](#), [3.2.1](#), [3.2.1](#), [3.2.1](#), [3.2.3](#), [3.2.3](#), [3.2.3](#), [3.3](#), [3.3.1](#), [3.3.1](#), [3.3.4](#)
- Balkanski, Y. J., D. J. Jacob, G. M. Gardner, W. C. Graustein, and K. K. Turekian (1993), Transport and residence times of tropospheric aerosols inferred from a global three-dimensional simulation of ^{210}Pb , *J. Geophys. Res.*, 98(D11), 20,573–20,586. [6.1](#)

- Ballantine, J.-A. C., G. S. Okin, D. E. Prentiss, and D. A. Roberts (2005), Mapping North African landforms using continental scale unmixing of MODIS imagery, *Rem. Sens. Environ.*, 97, 470–483, doi:10.1016/j.rse.2005.04.023. [3.8](#)
- Barkstrom, B. R. (1978), Some effects of 8–12 μ m radiant energy transfer on the mass and heat budgets of cloud droplets, *J. Atmos. Sci.*, 35, 665–673. [9.8.3](#)
- Barth, M. C. (1994), Numerical modeling of Sulfur and Nitrogen chemistry in a narrow cold-frontal rainband: The impact of meteorological and chemical parameters, *J. Appl. Meteorol.*, 33(7), 855–868. [10.1](#)
- Barth, M. C., D. A. Hegg, and P. V. Hobbs (1992), Numerical modeling of cloud and precipitation chemistry associated with two rainbands and some comparisons with observations, *J. Geophys. Res.*, 97(D5), 5825–5845. [10.1](#)
- Barth, M. C., P. J. Rasch, J. T. Kiehl, C. M. Benkovitz, and S. E. Schwartz (2000), Sulfur chemistry in the National Center for Atmospheric Research Community Climate Model: Description, evaluation, features and sensitivity to aqueous chemistry, *J. Geophys. Res.*, 105(D1), 1387–1416. [10.1](#), [12.2.3](#), [14.3](#), [14.3](#), [14.3](#), [14.8](#)
- Basu, S., M. I. Richardson, and R. J. Wilson (2004), Simulation of the Martian dust cycle with the GFDL Mars GCM, *J. Geophys. Res.*, 109(E11), E11,006, doi:10.1029/2004JE002,243. [1.2](#)
- Batt, R. G., and S. A. Peabody II (1999), Threshold friction velocities for large pebble gravel beds, *J. Geophys. Res.*, 104(D20), 24,273–24,279. [1.2](#)
- Bauer, S. E., Y. Balkanski, M. Schulz, D. Hauglustaine, and F. Dentener (2004), Global modelling of heterogeneous chemistry on mineral aerosol surfaces: The influence on tropospheric ozone chemistry and comparison to observations, *J. Geophys. Res.* [14.2.2](#), [14.2.3](#)
- Belly, P. Y. (1964), Sand movement by wind, Technical Memorandum 1, US Army Coastal Engineering Research Center. [3.7.4](#), [3.7.4](#), [3.7.6](#)
- Benkovitz, C. M., C. M. Berkowitz, R. C. Easter, S. Nemesure, R. Wagener, and S. E. Schwartz (1994), Sulfate over the North Atlantic and adjacent continental regions: Evaluation for October and November 1986 using a three-dimensional model driven by observation-derived meteorology, *J. Geophys. Res.*, 99(D10), 20,725–20,756. [14.3](#)
- Benkovitz, C. M., M. T. Scholtz, J. Pacyna, L. Tarrasón, J. Dignon, E. C. Voldner, P. A. Spiro, J. A. Logan, and T. E. Graedel (1996), Global gridded inventories of anthropogenic emissions of Sulfur and Nitrogen, *J. Geophys. Res.*, 101(D22), 29,239–29,253. [10.4.1](#), [10.5.1](#), [14.3](#)
- Betzer, P. R., et al. (1988), Long-range transport of giant mineral aerosol particles, *Nature*, 336(6199), doi:10.1038/336,568a0, 568–571. [5.4.4](#)

- Bian, H., and C. S. Zender (2003a), Mineral dust and global tropospheric chemistry: Relative roles of photolysis and heterogeneous uptake, *J. Geophys. Res.*, 108(D21), 4672, doi:10.1029/2002JD003,143. [14.2.4](#)
- Bian, H., and C. S. Zender (2003b), Heterogeneous impact of dust on tropospheric ozone: Sensitivity to season, species, and uptake rates, *sub judice*, *J. Geophys. Res.* [14.2.4](#)
- Bigler, M., R. Röthlisberger, F. Lambert, T. F. Stocker, and D. Wagenbach (2006), Aerosol deposited in East Antarctica over the last glacial cycle: Detailed apportionment of continental and sea-salt contributions, *J. Geophys. Res.*, 111(D08205), doi:10.1029/2005JD006,469. [7](#)
- Bishop, J. K. B., R. E. Davis, and J. T. Sherman (2002), Robotic observations of dust storm enhancement of carbon biomass in the North Pacific, *Science*, 298(5594), 817–821. [16.1](#)
- Bohren, C. F., and D. R. Huffman (1983), *Absorption and Scattering of Light by Small Particles*, 530 pp., John Wiley & Sons, New York, NY. [9.2](#), [9.2](#), [9.3](#), [9.3.2](#), [9.3.4](#), [9.3.5](#), [9.3.5](#), [9.4](#), [9.6.1](#)
- Bolton, D. (1980), The computation of equivalent potential temperature, *Mon. Weather Rev.*, 108, 1046–1053. [a](#)
- Bonan, G. B. (1996), *A land surface model (LSM version 1.0) for ecological, hydrological, and atmospheric studies: Technical description and user's guide*, Tech. Rep. NCAR/TN-417+STR, National Center for Atmospheric Research, Boulder, Colo. [a](#), [3.7.4](#)
- Boothroyd, R. G. (1971), *Flow Gas-solids suspensions*, 289 pp., Chapman & Hall, London. [5.4.2](#)
- Bopp, L., K. E. Kohfeld, C. L. Quéré, and O. Aumont (2003), Dust impact on marine biota and atmospheric CO₂ during glacial periods, *Paleoceanography*, 18(2), 1046, doi:10.1029/2002PA000,810. [7](#)
- Boucher, O. (1995), GCM estimate of the indirect aerosol forcing using satellite-retrieved cloud droplet effective radii, *J. Climate*, 8(5), 1403–1409. [10.1](#)
- Brasseur, G., and S. Solomon (1986), *Aeronomy of the Middle Atmosphere*, 452 pp., D. Reidel Pub. Com., Boston. [a](#)
- Brasseur, G. P., D. A. Hauglustaine, S. Walters, P. J. Rasch, J.-F. Müller, C. Granier, and X. X. Tie (1998), MOZART, a global chemical transport model for ozone and related chemical tracers 1. Model description, *J. Geophys. Res.*, 103(D21), 28,265–28,289. [10.1](#)
- Brasseur, G. P., J. J. Orlando, and G. S. Tyndall (Eds.) (1999), *Atmospheric Chemistry and Global Change*, Oxford University Press. [11.4.4](#)
- Brimblecombe, P. (1996), Air composition & chemistry, no. 6 in *Cambridge Environmental Chemistry Series*, second ed., Cambridge Univ. Press, New York. [10.1](#)

- Brooks, N., I. Chiapello, S. di Lernia, N. Drake, M. Legrand, C. Moulin, and J. Prospero (2005), The Climate-Environment-Society nexus in the Sahara from prehistoric times to the present day, *J. North African Studies*, 10(3–4), 253–292, doi:10.1080/13629380500336,680. [1.2](#)
- Bruggeman, D. A. G. (1935), Berechnung verschiedener physikalischer konstanten von heterogenen substanzen, *Annalen der Physik*, 24, 636–679. [9.3](#), [9.3.5](#)
- Brutsaert, W. (1982), *Evaporation into the Atmosphere*, Environmental Fluid Mechanics, D. Reidel Publ. Co., London. [2.2.5](#)
- Bryan, F. O., B. G. Kauffman, W. G. Large, and P. R. Gent (1997), The NCAR CSM flux coupler, Tech. Rep. NCAR/TN-424+STR, National Center for Atmospheric Research, Boulder, CO. [a](#), [2.2.2](#)
- Cabanes, A., L. Legagneux, and F. Dominé (2003), Rate of evolution of the specific surface area of surface snow layers, *Env. Sci. & Tech.*, 37(4), 661–666, doi:10.1021/es025,880r. [5.4.3](#)
- Cakmur, R. V., R. L. Miller, and O. Torres (2004), Incorporating the effect of small-scale circulations upon dust emission in an atmospheric general circulation model, *J. Geophys. Res.*, 109(D18), D07,201, doi:10.1029/2003JD004,067. [1.2](#), [3.5.1](#)
- Calvert, J. G., A. Lazrus, G. L. Kok, B. G. Heikes, J. G. Walega, J. Lind, and C. A. Cantrell (1985), Chemical mechanisms of acid generation in the troposphere, *Nature*, 317, 27–35. [10.1](#)
- Carter, R., and R. Scholes (1998), Generating a global database of soil properties. [14.1](#)
- Chamberlain, A. C. (1983), Roughness length of sea, sand, and snow, *Bound.-Lay. Meteorol.*, 6(2), 405–409. [2.2.2](#), [2.2.2](#)
- Chameides, W. L., and D. D. Davis (1982), The free radical chemistry of cloud droplets and its impact upon the composition of rain, *J. Geophys. Res.*, 87(C7), 4863–4877. [10.1](#)
- Chameides, W. L., and A. W. Stelson (1992), Aqueous-phase chemical processes in deliquescent sea-salt aerosols: A mechanism that couples the atmospheric cycles of S and sea salt, *J. Geophys. Res.*, 97(D18), 20,565–20,580. [10.1](#)
- Charlson, R. J., and T. M. L. Wigley (1994), Sulfate aerosol and climatic change, *Sci. Amer.*, 270(2), 28–35. [10.1](#)
- Chase, Z., A. Paytan, K. S. Johnson, J. Street, and Y. Chen (2006), Input and cycling of iron in the Gulf of Aqaba, Red Sea, sub judice, *Global Biogeochem. Cycles*. [16.1](#)
- Chatenet, B., M. Marticorena, L. Gomes, and G. Bergametti (1996), Assessing the microped size distributions of desert soils erodible by wind, *Sedimentology*, 43(5), 901–911. [a](#), [3.4.2](#)
- Chester, W., and D. R. Breach (1969), On the flow past a sphere at low Reynolds number, *J. Fluid. Mech.*, 37, 751–760. [5.4.1](#)

- Chiapello, I., J. M. Prospero, J. R. Herman, and N. C. Hsu (1999), Detection of mineral dust over the North Atlantic Ocean and Africa with the Nimbus 7 TOMS, *J. Geophys. Res.*, 104(D8), 9277–9291. [1.2](#)
- Christopher, S. A., J. Wang, Q. Ji, and S.-C. Tsay (2003), Estimation of diurnal short-wave dust aerosol radiative forcing during PRIDE, *J. Geophys. Res.*, 108(D19), 8596, doi:10.1029/2002JD002,787. [9.1](#)
- Clapp, R. B., and G. M. Hornberger (1978), Empirical equations for some soil hydraulic properties, *Water Resources Research*, 14, 601–604. [3.7.2](#), [3.7.2](#), [3.7.4](#), [3.7.6](#)
- Claquin, T., M. Schulz, and Y. J. Balkanski (1999), Modeling the mineralogy of atmospheric dust sources, *J. Geophys. Res.*, 104(D18), 22,243–22,256. [1.2](#), [b](#), [5](#)
- Claquin, T., et al. (2003), Radiative forcing of climate by ice-age atmospheric dust, *Climate Dynamics*, 20, 193–202, doi:10.1007/s00,382–002–0269–1. [7](#)
- Clarke, A. D., et al. (2004), Size distributions and mixtures of dust and black carbon aerosol in Asian outflow: Physiochemistry and optical properties, *J. Geophys. Res.*, 109(D15S09), doi:10.1029/2003JD004,378. [9.1](#)
- Colarco, P., O. Toon, and B. Holben (2003), Saharan dust transport to the caribbean during PRIDE: Part 1. Influence of dust sources and removal mechanisms on the timing and magnitude of downwind AOD events from simulations of and remote sensing observations, *J. Geophys. Res.*, 108(D19), 8589, doi:10.1029/2002JD002,658. [3.9.1](#)
- Colarco, P. R., O. B. Toon, O. Torres, and P. J. Rasch (2002), Determining the UV imaginary index of refraction of Saharan dust particles from Total Ozone Mapping Spectrometer data using a three-dimensional model of dust transport, *J. Geophys. Res.*, 107(D16), doi:10.1029/2001JD000,903. [9.4](#)
- Cosby, B. J., G. M. Hornberger, R. B. Clapp, and T. R. Ginn (1984), A statistical exploration of the relationships of soil moisture characteristics to the physical properties of soils, *Water Resources Research*, 20(6), 682–690. [3.7.2](#), [3.7.2](#), [3.7.4](#), [3.7.6](#)
- Crowley, T. J. (1995), Ice age terrestrial carbon changes revisited, *Global Biogeochem. Cycles*, 9(3), 377–389. [7](#)
- Crowley, T. J., and S. K. Baum (1997), Effect of vegetation on an ice-age climate model simulation, *J. Geophys. Res.*, 102(D14), 16,463–16,480. [7](#)
- Dai, Y., et al. (2003), The Common Land Model (CLM), *Bull. Am. Meteorol. Soc.*, 84(8), 1013–1023, doi:10.1175/BAMS–84–8–1013. [2.2.6](#)
- d’Almeida, G. A., P. Koepke, and E. P. Shettle (1991), *Atmospheric Aerosols: Global Climatology and Radiative Characteristics*, A. Deepak Pub., Hampton VA. [10.1](#)
- Dana, M. T., and J. M. Hales (1976), Statistical aspects of the washout of polydisperse aerosols, *Atmos. Environ.*, 10, 44–50. [6.1](#), [6.3](#)

- DeMore, W. B., S. P. Sander, D. M. Golden, R. F. Hampson, M. J. Kurylo, C. J. Howard, A. R. Ravishankara, C. E. Kolb, and M. J. Molina (1997), Chemical kinetics and photochemical data for use in stratospheric modeling, Evaluation Number 12 97-4, Jet Propulsion Laboratory, Pasadena Calif. [10.1](#), [a](#), [a](#), [d](#), [12.6](#), [3](#), [a](#), [a](#)
- DeMott, P. J., K. Sassen, M. R. Poellot, D. Baumgardner, D. C. Rogers, S. D. Brooks, A. J. Prenni, and S. M. Kreidenweis (2003), African dust aerosols as atmospheric ice nuclei, *Geophys. Res. Lett.*, 30(14), 1732, doi:10.1029/2003GL017410. [6.6](#)
- Dentener, F. J., G. R. Carmichael, Y. Zhang, J. Lelieveld, and P. J. Crutzen (1996), Role of mineral aerosol as a reactive surface in the global troposphere, *J. Geophys. Res.*, 101(D17), 22,869–22,889. [3](#), [a](#), [a](#), [12.3](#), [14.1](#), [14.2.2](#), [14.2.2](#), [14.2.2](#), [14.2.2](#), [1](#), [a](#), [a](#), [14.3](#)
- D’Odorico, P., J.-C. Yoo, and T. M. Over (2001), An assessment of ENSO-induced patterns of rainfall erosivity in the southwestern United States, *J. Climate*, 14(21), 4230–4242. [2.2.2](#)
- Dubovik, O. (2001), personal communication. [9.4](#)
- Dubovik, O., and M. D. King (2000), A flexible inversion algorithm for retrieval of aerosol optical properties from Sun and sky radiance measurements, *J. Geophys. Res.*, 105(D16), 20,673–20,696. [9.4](#)
- Dubovik, O., A. Smirnov, B. N. Holben, M. D. King, Y. J. Kaufman, T. F. Eck, and I. Slutsker (2000), Accuracy assessments of aerosol optical properties retrieved from aironet sun and sky-radiance measurements, *J. Geophys. Res.*, 105(D8), 9791–9806. [9.4](#)
- Dubovik, O., B. Holben, T. F. Eck, A. Smirnov, Y. J. Kaufman, M. D. King, D. Tanré, and I. Slutsker (2002a), Variability of absorption and optical properties of key aerosol types observed in worldwide locations, *J. Atmos. Sci.*, 59(3), 590–608. [9.4](#)
- Dubovik, O., B. N. Holben, T. Lapyonok, A. Sinyuk, M. I. Mishchenko, P. Yang, and I. Slutsker (2002b), Non-spherical aerosol retrieval method employing light scattering by spheroids, *Geophys. Res. Lett.*, 29(10), doi:10.1029/2001GL014506. [9.4](#)
- Dunion, J. P., and C. S. Velden (2004), The impact of the Saharan Air Layer on Atlantic tropical cyclone activity, *Bull. Am. Meteorol. Soc.*, 85(3), 353–365. [6.6](#)
- Dutton, J. A. (1986), *The Ceaseless Wind*, second ed., Dover Pub., Mineola, New York. [18.14](#)
- Dymond, J., R. Collier, J. McManus, S. Honjo, and S. Manganini (1997), Can the aluminum and titanium contents of ocean sediments be used to determine the paleoproductivity of the oceans?, *Paleoceanography*, 12(4), 586–593. [16.1](#)
- Egan, W. G., and T. W. Hilgeman (1979), *Optical Properties of Inhomogeneous Materials: Applications to Geology, Astronomy, Chemistry, and Engineering*, 235 pp., Academic Press, San Diego, CA. [9.1](#)

- Elbaz-Poulichet, F., C. Guieu, and N. H. Morley (2001), A reassessment of trace metal budgets in the western Mediterranean Sea, *Marine Pollution Bulletin*, 42(8), 623–627. [16.1](#)
- Evans, R. D., I. F. Jefferson, R. Kumar, K. O’Hara-Dhand, and I. J. Smalley (2004), The nature and early history of airborne dust from North Africa; in particular the Lake Chad basin, *J. African Earth Sciences*, 39, 81–87. [3.8](#)
- Fécan, F., B. Marticorena, and G. Bergametti (1999), Parametrization of the increase of the aeolian erosion threshold wind friction velocity due to soil moisture for arid and semi-arid areas, *Annales Geophysicae*, 17, 149–157. [3.7.4](#), [3.7.4](#), [7](#), [3.7.5](#), [3.7.6](#), [3.7.6](#)
- Fung, I. Y., S. K. Meyn, I. Tegen, S. C. Doney, J. G. John, and J. K. B. Bishop (2000), Iron supply and demand in the upper ocean, *Global Biogeochem. Cycles*, 14, 281–296. [16.1](#)
- Gabric, A. J., R. Cropp, G. P. Ayers, G. McTainsh, and R. Braddock (2002), Coupling between cycles of phytoplankton biomass and aerosol optical depth as derived from SeaWiFS time series in the Subantarctic Southern Ocean, *Geophys. Res. Lett.*, 29(7), doi:10.1029/2001GL013,545. [16.1](#)
- Gabrielli, P., et al. (2004), Meteoric smoke fallout over the holocene epoch revealed by iridium and platinum in Greenland ice, *Nature*, 432(23), 1011–1014, doi:10.1038/nature03,137. [1.2.1](#)
- Gao, Y., Y. J. Kaufman, D. Tanré, D. Kolber, and P. G. Falkowski (2001), Seasonal distributions of aeolian iron fluxes to the global ocean, *Geophys. Res. Lett.*, 28(1), 29–32. [16.1](#)
- Gao, Y., S.-M. Fan, and J. L. Sarmiento (2003), Aeolian iron input to the ocean through precipitation scavenging: A modeling perspective and its implication for natural iron fertilization in the ocean, *J. Geophys. Res.*, 108, 4221, doi:10.1029/2002JD002,420. [16.1](#)
- Garnett, J. C. M. (1904), Colours in metal glasses and in metallic films, *Phil. Trans. Roy. Soc. A*, 203, 385–420. [9.3](#), [9.3.4](#)
- Garratt, J. R. (1977), Review of drag coefficients over oceans and continents, *Mon. Weather Rev.*, 105(7), 915–929. [2.2.1](#)
- Gehlen, M., C. Heinze, E. Maier-Reimer, and C. I. Measures (2003), Coupled Al-Si geochemistry in an ocean general circulation model: A tool for the validation of oceanic dust deposition fields?, *Global Biogeochem. Cycles*, 17(1), 1028, doi:10.1029/2001GB001,549. [16.1](#)
- George, J. P. (2001), Shortwave radiative forcing by mineral dust aerosols over Arabian Sea: A model study, *Current Science*, 80, 97–99. [9.1](#)
- Giles, J. (2005), The dustiest place on earth, *Nature*, 434, 816–819. [3.9.1](#)

- Gill, T. E. (1996), Eolian sediments generated by anthropogenic disturbance of playas: human impacts on the geomorphic system and geomorphic impacts on the human system, *Geomorphology*, 17(1–3), 207–228. [3.8](#)
- Gillette, D. A. (1979), Environmental factors affecting dust emission by wind erosion, in *Saharan Dust*, edited by C. Morales, SCOPE 14, pp. 71–91, ICSU, John Wiley & Sons, New York, NY, April 25–28, 1979, Gothenburg, Sweden. [3.4.2](#), [a](#), [3.4.2](#), [3.4.2](#)
- Gillette, D. A. (1981), Production of dust that may be carried great distances, in *Desert Dust: Origin, Characteristics, and Effect on Man*, edited by T. L. Péwé, Special Paper 186, pp. 11–26, Geological Society of America, GSA, Boulder, CO. [3.4.2](#), [a](#), [3.4.2](#), [3.4.2](#)
- Gillette, D. A. (1988), Threshold friction velocities for dust production for agricultural soils, *J. Geophys. Res.*, 93(D10), 12,645–12,662. [3.7.4](#), [3.7.4](#)
- Gillette, D. A. (1999), A qualitative geophysical explanation for “hot spot” dust emitting source regions, *Contr. Atmos. Phys.*, 72(1), 67–77. [1.2](#), [5](#)
- Gillette, D. A., and R. Passi (1988), Modeling dust emission caused by wind erosion, *J. Geophys. Res.*, 93(D11), 14,233–14,242. [3.4.1](#), [3.5.1](#), [18.10.2](#)
- Gillette, D. A., and P. C. Sinclair (1990), Estimation of suspension of alkaline material by dust devils in the United States, *Atmospheric Environment*, 24A(5), 1135–1142. [3.5.2](#)
- Gillette, D. A., D. W. Fryrear, T. E. Gill, T. Ley, T. A. Cahill, and E. A. Gearhart (1997), Relation of vertical flux of particles smaller than 10 μm to total aeolian horizontal mass flux at Owens Lake, *J. Geophys. Res.*, 102(D22), 26,009–26,015. [3.4](#)
- Gillette, D. A., B. Marticorena, and G. Bergametti (1998), Change in the aerodynamic roughness height by saltating grains: Experimental assessment, test of theory, and operational parameterization, *J. Geophys. Res.*, 103(D6), 6203–6209. [2.2.2](#), [3.6](#), [3.6](#), [5](#)
- Gillette, D. A., T. C. Niemeyer, and P. J. Helm (2001), Supply-limited horizontal sand drift at an ephemerally crusted, unvegetated saline playa, *J. Geophys. Res.*, 106(D16), 10.1029/2000JD900,324, 18,085–18,098. [3.8](#)
- Ginoux, P. (2003), Effects of non-sphericity on mineral dust modeling, *J. Geophys. Res.*, 108(D2), 4052, doi:10.1029/2002JD002,516. [5.4.2](#), [5.4.4](#), [18.11.3](#)
- Giorgi, F., and W. L. Chameides (1986), Rainout lifetimes of highly soluble aerosols and gases as inferred from simulation with a general circulation model, *J. Geophys. Res.*, 91, 14,367–14,376. [6.1](#)
- Global Soil Data Task (1999), Spatial Database of Soil Properties, International Geosphere-Biosphere Programme - Data and Information System, Toulouse, France. [14.1](#)
- Goldshleger, N., E. Ben-Dor, Y. Benyamini, and M. Agassi (2004), Soil reflectance as a tool for assessing physical crust arrangement of four typical soils in Israel, *Soil Science*, 169(10), 677–687, doi:10.1097/01.ss.0000146,024.61,559.e2. [3.9](#)

- Golitsyn, G. S., I. G. Granberg, A. V. Andronova, V. M. Ponomarev, S. S. Zilitinkevich, V. V. Smirnov, and M. Y. Yablokov (2003), Investigation of boundary layer fine structure in arid regions: Injection of fine dust into the atmosphere, *Water, Air and Soil Pollution: Focus*, 3(2), 245–257. [3.5.2](#)
- Gomes, L., G. Bergametti, G. Coudé-Gaussen, and P. Rognon (1990), Submicron desert dusts: A sandblasting process, *J. Geophys. Res.*, 95(D9), 13,927–13,935. [1.2](#), [3.4](#)
- Gong, S. L., L. A. Barrie, and J.-P. Blanchet (1997a), Modeling sea-salt aerosols in the atmosphere. Part 1: Model development, *J. Geophys. Res.*, 102(D3), 3805–3818. [4.1](#)
- Gong, S. L., L. A. Barrie, J. M. Prospero, D. L. Savoie, G. P. Ayers, J.-P. Blanchet, and L. Spacek (1997b), Modeling sea-salt aerosols in the atmosphere. Part 2: Atmospheric concentrations and fluxes, *J. Geophys. Res.*, 102(D3), 3819–3830. [4.1](#)
- Gong, S. L., X. Y. Zhang, T. L. Zhao, I. G. McKendry, D. A. Jaffe, and N. M. Lu (2003), Characterization of soil dust aerosol in China and its transport and distribution during 2001 ACE-Asia: 2. Model simulation and validation, *J. Geophys. Res.*, 108(D9), 4262 doi:10.1029/2002JD002,633. [3.4](#)
- Graedel, T. E., and K. I. Goldberg (1983), Kinetic studies of raindrop chemistry 1. Inorganic and organic processes, *J. Geophys. Res.*, 88(C15), 10,865–10,882. [10.1](#)
- Graedel, T. E., M. L. Mandich, and C. J. Weschler (1986), Kinetic model studies of atmospheric droplet chemistry 2. Homogeneous transition metal chemistry in raindrops, *J. Geophys. Res.*, 91(D4), 5205–5221. [10.1](#)
- Grassian, V. (1999), personal communication. [a](#)
- Grassian, V. H. (2002), Chemical reactions of nitrogen oxides on the surface of oxide, carbonate, soot, and mineral dust particles: Implications for the chemical balance of the troposphere, *J. Phys. Chem. A*, 106(6), doi:10.1021/jp012,139h, 860–877. [11.3](#), [14.2.2](#)
- Greeley, R., and J. D. Iversen (1985), Wind as a geological process, no. 4 in *Cambridge Planetary Science Series*, Cambridge Univ. Press, New York, NY. [3.2.3](#), [3.2.3](#), [3.2.3](#), [3.3](#), [3.3.4](#), [3.7](#)
- Greeley, R., D. G. Blumberg, and S. H. Williams (1996), Field measurements of the flux and speed of wind-blown sand, *Sedimentology*, 43(1), 41–52, doi:10.1111/j.1365–3091.1996.tb01,458.x. [1.2](#)
- Grenfell, T. C., and S. G. Warren (1999), Representation of a nonspherical ice particle by a collection of independent spheres for scattering and absorption of radiation, *J. Geophys. Res.*, 104(D24), 31,697–31,709. [5.4.3](#), [18.11.3](#), [18.11.3](#)
- Grini, A., and C. S. Zender (2004), Roles of saltation, sandblasting, and wind speed variability on mineral dust aerosol size distribution during the Puerto Rican Dust Experiment (PRIDE), *J. Geophys. Res.*, 109(D7), D07,202, doi:10.1029/2003JD004,233. [1.2](#), [3.4](#)

- Grini, A., G. Myhre, J. K. Sundet, and I. S. A. Isaksen (2002a), Modeling the annual cycle of sea salt in the global 3-d model OSLO CTM-2, Concentrations, fluxes and radiative impact, *J. Climate*, 15(7), 1717–1730. [4.2](#), [4.2](#)
- Grini, A., C. S. Zender, and P. Colarco (2002b), Saltation sandblasting behavior during mineral dust aerosol production, *Geophys. Res. Lett.*, 29(18), 1868, doi:10.1029/2002GL015,248. [1.2](#)
- Grini, A., G. Myhre, C. S. Zender, and I. S. A. Isaksen (2005), Model simulations of dust sources and transport in the global troposphere, *J. Geophys. Res.*, 110(D02205), doi:10.1029/2004JD005,037. [3.4](#)
- Guelle, W., Y. J. Balkanski, M. Schulz, F. Dulac, and P. Monfray (1998), Wet deposition in a global size-dependent aerosol transport model 1. Comparison of a 1 year ^{210}Pb simulation with ground measurements, *J. Geophys. Res.*, 103(D10), 11,429–11,445. [6](#), [6.1](#)
- Hamonou, E., P. Chazette, D. Balis, F. Dulac, X. Schneider, E. Galani, G. Ancellet, and A. Papayannis (1999), Characterization of the vertical structure of Saharan dust export to the Mediterranean basin, *J. Geophys. Res.*, 104(D18), 22,257–22,270. [1.2](#)
- Hand, J. L., N. Mahowald, Y. Chen, R. Siefert, C. Luo, and I. Fung (2004), Estimates of soluble iron from observations and a global mineral aerosol model: Biogeochemical implications, *sub judice*, *J. Geophys. Res.* [16.1](#)
- Hänel, G. (1976), The properties of atmospheric aerosol particles as functions of the relative humidity at thermodynamic equilibrium with the surrounding moist air, *Adv. Geophys.*, 19, 73–188. [14.2](#), [14.2](#), [14.2](#), [14.2](#), [a](#)
- Hanisch, F., and J. N. Crowley (2001a), Heterogeneous reactivity of gaseous nitric acid on Al_2O_3 , CaCO_3 , and atmospheric dust samples: A Knudsen cell study, *J. Phys. Chem. A*, 105, doi:10.1021/jp001,254+, 3096–3106. [11.3](#), [11.3](#)
- Hanisch, F., and J. N. Crowley (2001b), The heterogeneous reactivity of gaseous nitric acid on authentic mineral dust samples, and on individual mineral and clay mineral components, *Phys. Chem. Chem. Phys.*, 3, doi:10.1039/b101,254+, 2474–2482.
- Hanisch, F., and J. N. Crowley (2003a), Heterogeneous reactivity of NO and HNO_3 on mineral dust in the presence of ozone, *Phys. Chem. Chem. Phys.*, 5, doi:10.1039/b211,503d, 883–887.
- Hanisch, F., and J. N. Crowley (2003b), Ozone decomposition on Saharan dust: an experimental investigation, *Atmos. Chem. Phys.*, 3, 119–130.
- Harrison, S. P., K. E. Kohfeld, C. Roelandt, and T. Claquin (2001), The role of dust in climate changes today, at the last glacial maximum and in the future, *Earth Sci. Revs.*, 54(1–3), 43–80. [7](#)

- Haywood, J., et al. (2003), Radiative properties and direct radiative effect of saharan dust measured by the C-130 aircraft during Saharan Dust Experiment (SHADE): 1. Solar spectrum, *J. Geophys. Res.*, 108(D18), 8577, doi:10.1029/2002JD002,687. [9.1](#)
- Haywood, J. M., and V. Ramaswamy (1998), Global sensitivity studies of the direct radiative forcing due to anthropogenic sulfate and black carbon aerosols, *J. Geophys. Res.*, 103(D6), 6043–6058. [10.1](#)
- He, S., and G. R. Carmichael (1999), Sensitivity of photolysis rates and ozone production in the troposphere to aerosol properties, *J. Geophys. Res.*, 104(7), 26,307–26,324. [a](#), [15](#)
- Hedin, L. O., and G. E. Likens (1996), Atmospheric dust and acid rain, *Sci. Amer.*, pp. 88–92. [10.1](#)
- Heintzenberg, J. (1989), Fine particles in the global troposphere: A review, *Tellus*, 41B, 149–160. [1.2](#)
- Herman, J. R., P. K. Bhartia, O. Torres, C. Hsu, C. Seftor, and E. Celarier (1997), Global distribution of UV-absorbing aerosols from Nimbus 7/TOMS data, *J. Geophys. Res.*, 102(D14), 16,911–16,922. [3.9.1](#), [3.9.2](#)
- Hess, M., P. Koepke, and I. Schult (1998), Optical properties of aerosols and clouds: The software package OPAC, *Bull. Am. Meteorol. Soc.*, 79(5), 831–844. [9.4](#)
- Heymsfield, A. (1972), Ice crystal terminal velocities, *J. Atmos. Sci.*, 29, 1348–1357. [18.11.3](#)
- Heymsfield, A. J., and C. M. R. Platt (1984), A parameterization of the particle size spectrum of ice clouds in terms of the ambient temperature and the ice water content, *J. Atmos. Sci.*, 41(5), 846–855. [18.11.3](#)
- Highwood, E. J., J. M. Haywood, M. D. Silverstone, S. M. Newman, and J. P. Taylor (2003), Radiative properties and direct effect of saharan dust measured by the C-130 aircraft during Saharan Dust Experiment (SHADE): 2. Terrestrial spectrum, *J. Geophys. Res.*, 108(D18), 8578, doi:10.1029/2002JD002,552. [9.1](#)
- Hillel, D. (1982), *Introduction to Soil Physics*, Academic Press, San Diego CA. [3.7.1](#), [3.7.5](#), [3.7.6](#)
- Husar, R. B., J. M. Prospero, and L. L. Stowe (1997), Characterization of tropospheric aerosols over the oceans with the NOAA advanced very high resolution radiometer optical thickness operational product, *J. Geophys. Res.*, 102(D14), 16,889–16,909. [3.9.1](#), [3.9.2](#)
- Ichoku, C., et al. (1999), Interrelationships between aerosol characteristics and light scattering during late winter in an Eastern Mediterranean arid environment, *J. Geophys. Res.*, 104(D20), 24,371–24,393. [1.2](#)
- in *Semiarid Soils Using Airborne Hyperspectral Technology*, M. I. R. (2004), E. ben-dor and n. goldshalager and o. braun and b. kindel and a. f. h. goetz and d. bonfil and m. agassi and n. margalait and y. binayminy and a. karnieli, *Int. J. Remote Sensing*, 25(13), 2607–2624, doi:10.1080/01431160310001642,322. [3.9](#)

- Ivanova, D., D. L. Mitchell, W. P. Arnott, and M. Poellot (2001), A GCM parameterization for bimodal size spectra and ice mass removal rates in mid-latitude cirrus clouds, *Atmospheric Research*, 59–60, 89–113. [5.4.2](#)
- Iversen, J. D., and B. R. White (1982), Saltation threshold on Earth, Mars, and Venus, *Sedimentology*, 29, 111–119. [3.2](#), [3.2.1](#), [3.2.3](#), [3.2.3](#), [3.2.3](#), [3.2.3](#), [3.2.3](#), [3.2.3](#), [3.2.3](#), [3.2.3](#), [3.3](#), [3.7](#)
- Jayaraman, A., D. Lubin, S. Ramachandran, V. Ramanathan, E. Woodbridge, W. D. Collins, and K. S. Zalpuri (1998), Direct observations of aerosol radiative forcing over the tropical Indian Ocean during the January–February 1996 pre-INDOEX cruise, *J. Geophys. Res.*, 103(D12), 13,827–13,836. [10.1](#)
- Jickells, T. D., et al. (2005), Global iron connections between desert dust, ocean biogeochemistry, and climate, *Science*, 308(5718), 67–71, doi:10.1126/science.1105,959. [16.1](#)
- Johnson, K. S. (2001), Iron supply and demand in the upper ocean: Is extraterrestrial dust a significant source of bioavailable iron?, *Global Biogeochem. Cycles*, 15(1), 61–63, doi:10.1029/2000GB001,295. [16.1](#)
- Johnson, K. S., J. K. Moore, and W. O. Smith (2002), Workshop highlights iron dynamics in ocean carbon cycle, *Eos Trans. AGU*, 83(43), 482–484. [16.1](#)
- Jones, I. W., G. Munhoven, M. Tranter, P. Huybrechts, and M. J. Sharp (2002), Modelled glacial and non-glacial HCO_3^- , Si and Ge fluxes since the LGM: little potential for impact on atmospheric CO_2 concentrations and a potential proxy of continental chemical erosion, the marine Ge/Si ratio, *Global and Planetary Change*, 33, 139–153. [16.1](#)
- Jordan, R. (1991), A one-dimensional temperature model for a snow cover: Technical documentation for SNTHERM 89, Tech. Rep. Special Report 91-16, U.S. Army Cold Regions Research and Engineering Laboratory. [9.8.1](#)
- Justus, C. G., W. R. Hargraves, A. Mikhail, and D. Graber (1978), Methods for estimating wind speed frequency distributions, *J. Appl. Meteorol.*, 17(3), 350–353. [3.5](#), [3.5.1](#), [18.10.2](#), [18.10.2](#)
- Kalashnikova, O. V., and I. N. Sokolik (2004), Modeling the radiative properties of nonspherical soil-derived mineral aerosols, *J. Quant. Spectrosc. Radiat. Transfer*, 87(2), 137–166. [5.4.2](#)
- Kalashnikova, O. V., D. J. Diner, R. Kahn, and B. Gaitley (2005a), Dust aerosol retrieval results from MISR, *SPIE*. [5.4.2](#)
- Kalashnikova, O. V., R. Kahn, and W.-H. Li (2005b), The ability of multi-angle remote sensing observations to identify and distinguish mineral dust types: Part 2. Sensitivity data analysis, sub judice, *J. Geophys. Res.* [5.4.2](#)

- Kalashnikova, O. V., R. Kahn, I. N. Sokolik, and W.-H. Li (2005c), The ability of multi-angle remote sensing observations to identify and distinguish mineral dust types: Part 1. Optical models and retrievals of optically thick plumes, *sub judice*, *J. Geophys. Res.* [5.4.2](#)
- Kaufman, Y. J., D. Tanré, O. Dubovik, A. Karnieli, and L. A. Remer (2001), Absorption of sunlight by dust as inferred from satellite and ground-based remote sensing, *Geophys. Res. Lett.*, 28, 1479–1482. [9.4](#)
- Kiehl, J. T., and B. P. Briegleb (1993), The relative roles of sulfate aerosols and greenhouse gases in climate forcing, *Science*, 260, 311–314. [10.1](#)
- Kiehl, J. T., T. L. Schneider, P. J. Rasch, M. C. Barth, and J. Wong (2000), Radiative forcing due to sulfate aerosols from simulations with the National Center for Atmospheric Research Community Climate Model, Version 3, *J. Geophys. Res.*, 105(D1), 1441–1458. [9.7](#), [9.7](#)
- King, M. D., Y. J. Kaufman, D. Tanré, and T. Nakajima (1999), Remote sensing of tropospheric aerosols from space: Past, present, and future, *Bull. Am. Meteorol. Soc.*, 80(11), 2229–2259. [1.2](#)
- Klippel, W., and P. Warneck (1980), The formaldehyde content of the atmospheric aerosol, *Atmos. Environ.*, 14, 809–818. [10.1](#)
- Knollenberg, R. G. (1972), Measurements of the growth of the ice budget in a persisting contrail, *J. Atmos. Sci.*, 29, 1367–1374. [18.11.3](#)
- Koch, J., and N. O. Renno (2005), The role of convective plumes and vortices on the global aerosol budget, *Geophys. Res. Lett.*, 32, L18,806, doi:10.1029/2005GL023,420. [3.5.2](#)
- Kohfeld, K. E., and S. P. Harrison (2001), DIRTMAP: The geologic record of dust, *Earth Sci. Revs.*, 54(1–3), 81–114. [7](#)
- Kokhanovsky, A. A., T. Aoki, A. Hachikubo, M. Hori, and E. P. Zege (2005), Reflective properties of natural snow: Approximate asymptotic theory versus In Situ measurements, *IEEE Trans. Geosci. Rem. Sens.*, 43(7), 1529–1535. [5.4.2](#)
- Kolb, C. E., et al. (1995), Laboratory studies of atmospheric heterogeneous chemistry, in *Progress and Problems in Atmospheric Chemistry, Advanced Series in Physical Chemistry*, vol. 3, edited by J. R. Barker, chap. 18, pp. 771–875, World Scientific Publishing, London. [11.3](#), [11.3](#), [11.3.2](#), [11.3.3](#)
- Koloutsou-Vakakis, S., and M. J. Rood (1998), Modeling of aerosol properties related to direct climate forcing, *J. Geophys. Res.*, 103(D14), 17,009–17,032. [10.1](#)
- Koren, I., and Y. J. Kaufman (2004), Direct wind measurements of Saharan dust events from Terra and Aqua satellites, *Geophys. Res. Lett.*, 31, L06,122, doi:10.1029/2003GL019,338. [3.9](#)

- Koster, R. D., and M. J. Suarez (2001), Soil moisture memory in climate models, *J. Hydrometeor.*, 2(6), 558–570. [3.7](#)
- Koven, C. D., and I. Fung (2008), Identifying global dust source areas using high resolution land surface form, sub judice, *J. Geophys. Res.* [3.8](#)
- Krinner, G., O. Boucher, and Y. Balkanski (2006), Ice-free glacial northern Asia due to dust deposition on snow, *Clim. Dyn.*, 27, 613–625, doi:10.1007/s00382-006-0159-z. [5.4.2](#)
- Krueger, B. J., V. H. Grassian, A. Laskin, and J. P. Cowin (2003), The transformation of solid atmospheric particles into liquid droplets through heterogeneous chemistry: Laboratory insights into the processing of calcium containing mineral dust aerosol in the troposphere, *Geophys. Res. Lett.*, 30(3), 1148, doi:10.1029/2002GL016,563. [14.2.2](#), [14.2.2](#)
- Kundu, P. K. (1990), *Fluid Mechanics*, Academic Press, Inc., San Diego, CA. [18.4](#)
- Kurosaki, Y., and M. Mikami (2003), Recent frequent dust events and their relation to surface wind in East Asia, *Geophys. Res. Lett.*, 30(14), 1736, doi:10.1029/2003GL017,261. [1.2](#)
- Kurosaki, Y., and M. Mikami (2004), Effect of snow cover on threshold wind velocity of dust outbreaks, *Geophys. Res. Lett.*, 31, L03,106, doi:10.1029/2003GL018,632. [1.2](#)
- Lacaze, R., J.-L. Roujean, and J.-P. Goutorbe (1999), Spatial distribution of Sahelian land surface properties from airborne POLDER multiangular observations, *J. Geophys. Res.*, 104(D10), 12,131–12,146. [1.2](#), [2.2.2](#)
- Landing, W. M., J. J. Perry, Jr., J. L. Guentzel, G. A. Gill, and C. D. Pollman (1995), Relationships between the atmospheric deposition of trace elements, major ions, and mercury in Florida: the FAMS project (1992–1994), *Water Air Soil Pollut.*, 80, 343–352. [5.1](#)
- Large, W. G., and S. Pond (1981), Open ocean momentum flux measurements in moderate to strong winds, *J. Phys. Oceanogr.*, 11, 324–336. [a](#), [c](#), [2.2.2](#), [4.2](#)
- Large, W. G., and S. Pond (1982), Sensible and latent heat flux measurements over the oceans, *J. Phys. Oceanogr.*, 12, 464–482. [a](#), [2.2.2](#)
- Lawrence, M. G., and P. J. Crutzen (1998), The impact of cloud particle gravitational settling on soluble trace gas distributions, *Tellus*, 50B, 263–289. [6.1](#)
- Legagneux, L., A.-S. Taillandier, and F. Dominé (2004), Grain growth theories and the isothermal evolution of the specific surface area of snow, *J. Appl. Phys.*, 95(11), 6175–6184, doi:10.1063/1.1710,718. [5.4.3](#)
- Leighton, H. G., M. K. Yau, A. M. Macdonald, J. S. Pitre, and A. Giles (1990), A numerical simulation of the chemistry of a rainband, *Atmos. Environ.*, 24A(5), 1211–1217. [10.1](#)
- Leighton, H. G., L. Lauzon, and W. R. Leitch (1996), Evaluation of a three-dimensional cloud chemistry model, *Atmos. Environ.*, 30(21), 3651–3665. [10.1](#)

- Lelieveld, J., and P. J. Crutzen (1991), The role of clouds in tropospheric photochemistry, *J. Atmos. Chem.*, 12, 229–267. [12.6](#)
- Léon, J.-F., and M. Legrand (2003), Mineral dust sources in the surroundings of the north Indian Ocean, *Geophys. Res. Lett.*, 30(6), 1309, doi:10.1029/2002GL016,690. [1.2](#)
- Levin, Z., C. Price, and E. Ganor (1990), The contribution of sulfate and desert aerosols to the acidification of clouds and rain in Israel, *Atmospheric Environment*, 24A(5), 1143–1151. [6.1](#)
- Leys, J. F., and M. R. Raupach (1991), Soil flux measurements using a portable wind erosion tunnel, *Aust. J. Soil Res.*, 29, 533–552. [2.2.2](#), [3.3](#)
- Li, Z.-L., F. Becker, M. P. Stoll, Z. Wan, and Y. Zhang (1999), Channel selection for soil spectrum reconstruction in 8–13 μm region, *J. Geophys. Res.*, 104(D18), 22,271–22,285. [1.2](#)
- Liao, H., and J. H. Seinfeld (1998a), Effect of clouds on direct aerosol radiative forcing of climate, *J. Geophys. Res.*, 103(D4), 3781–3788. [10.1](#)
- Liao, H., and J. H. Seinfeld (1998b), Radiative forcing by mineral dust aerosols: sensitivity to key variables, *J. Geophys. Res.*, 103(D24), 31,637–31,645. [9.4](#), [10.1](#)
- Lide, D. R., and H. P. R. Frederikse (Eds.) (1995), *CRC Handbook of Chemistry and Physics*, 76th ed., CRC Press, New York. [3.4.2](#), [a](#)
- Lohmann, U., J. Feichter, C. C. Chuang, and J. E. Penner (1999), Prediction of the number of cloud droplets in the ECHAM GCM, *J. Geophys. Res.*, 104(D8), 9169–9198. [1.2](#)
- Long, L. L., M. R. Querry, R. J. Bell, and R. W. Alexander (1993), Optical properties of calcite and gypsum in crystalline and powdered form in the infrared and far-infrared, *Infrared Physics*, 34(2), 191–201. [9.1](#), [9.2.1](#), [9.2.1](#), [9.2.1](#)
- Lu, H., and Y. Shao (1999), A new model for dust emission by saltation bombardment, *J. Geophys. Res.*, 104(D14), 16,827–16,842. [3.3.4](#)
- Lunt, D. J., and P. J. Valdes (2002), The modern dust cycle: Comparison of model results with observation and study of sensitivities, *J. Geophys. Res.*, 107(D23), 4669, doi:10.1029/2002JD002,316. [1.2](#), [3.3](#)
- Luo, C., N. M. Mahowald, N. Meskhidze, Y. Chen, R. L. Siefert, A. R. Baker, and A. M. Johansen (2005), Estimation of iron solubility from observations and a global aerosol model, *J. Geophys. Res.*, 110, D23,307, doi:10.1029/2005JD0060,059. [16.1](#)
- MacKinnon, D. J., G. D. Clow, R. K. Tigges, R. L. Reynolds, and P. S. Chavez, Jr. (2004), Comparison of aerodynamically and model-derived roughness lengths (z_0) over diverse surfaces, central Mojave Desert, California, USA, *Geomorphology*, 63(1/2), 103–113. [3.6](#)

- Mahowald, N. M., A. R. Baker, G. Bergametti, N. Brooks, R. A. Duce, T. D. Jickells, N. Ku-bilay, J. M. Prospero, and I. Tegen (2005), Atmospheric global dust cycle and iron inputs to the ocean, *Global Biogeochem. Cycles*, 19(GB4025), doi:10.1029/2004GB002402. [16.1](#)
- Marticorena, B., and G. Bergametti (1995), Modeling the atmospheric dust cycle: 1. Design of a soil-derived dust emission scheme, *J. Geophys. Res.*, 100(D8), doi:10.1029/95JD00690, 16,415–16,430. [2.2.2](#), [2.2.2](#), [3.2.3](#), [3.3](#), [3](#), [3.4.2](#), [3.4.2](#), [3.4.2](#), [3.4.2](#), [3.4.2](#)
- Marticorena, B., G. Bergametti, B. Aumont, Y. Callot, C. N'Doumé, and M. Legrand (1997), Modeling the atmospheric dust cycle: 2. Simulation of Saharan dust sources, *J. Geophys. Res.*, 102(D4), doi:10.1029/96JD02964, 4387–4404. [3.2.3](#), [a](#), [3.4.2](#), [3.4.2](#), [a](#), [3.4.2](#)
- Martin, J. H. (1990), Glacial-interglacial CO₂ change: The iron hypothesis, *Paleoceanography*, 5, 1–13. [16.1](#)
- Martin, J. H., and S. E. Fitzwater (1988), Iron-deficiency limits phytoplankton growth in the northeast Pacific subarctic, *Nature*, 331(6154), 341–343. [16.1](#)
- Mason, B. J. (1971), *The Physics of Clouds*, second ed., Clarendon Press, Oxford. [6.5](#)
- McConnell, J. R., A. J. Aristarain, J. R. Banta, P. R. Edwards, and J. C. S. oes (2006), 20th century doubling in dust archived in an Antarctic Peninsula ice core parallels climate change and desertification in South America, *Proc. Natl. Acad. Sci.*, 104(14), 5743–5748, doi:10.1073/pnas.0607657104. [7](#)
- McElroy, M. B., R. J. Salawitch, S. C. Wofsy, and J. A. Logan (1986), Reductions of Antarctic ozone due to synergistic interactions of chlorine and bromine, *Nature*, 321, 759–762. [11](#)
- McKenna-Neuman, C., and W. G. Nickling (1989), A theoretical and wind tunnel investigation of the effect of capillary water on the entrainment of sediment by wind, *Canadian Journal of Soil Science*, 69, 79–96. [3.7.5](#), [3.7.5](#), [3.7.5](#), [3.7.6](#), [3.7.6](#)
- Measures, C. I., and S. Vink (2000), On the use of dissolved aluminum in surface waters to estimate dust deposition to the ocean, *J. Geophys. Res.*, 14(1), 317–327. [16.1](#)
- Menu, L., C. Schmechtig, and B. Marticorena (2005), Sensitivity of the sandblasting fluxes calculations to the soil size distribution accuracy: An operational numerical method, *J. Atmos. Ocean. Tech.*, 22(12), 1875–1884. [1.2](#)
- Michel, A. E., C. R. Usher, and V. H. Grassian (2002), Heterogeneous and catalytic uptake of ozone on mineral oxides and dust: A Knudsen cell investigation, *Geophys. Res. Lett.*, 29(14), doi:10.1029/2002GL014896. [7](#)
- Michel, A. E., C. R. Usher, and V. H. Grassian (2003), Reactive uptake of ozone on mineral oxides and mineral dusts, *Atmos. Env.*, 37, doi:10.1016/S1352-2310(03)00319-4, 3201–3211. [8](#)

- Miller, R. L., and I. Tegen (1998a), Climate response to soil dust aerosols, *J. Climate*, 11(12), 3247–3267. [10.1](#)
- Miller, R. L., and I. Tegen (1998b), Radiative forcing of a tropical direct circulation by soil dust aerosols, *sub judice*, *J. Atmos. Sci.* [10.1](#)
- Miller, R. L., I. Tegen, and J. Perlwitz (2004), Surface radiative forcing by soil dust aerosols and the hydrologic cycle, *J. Geophys. Res.*, 109(D04203), doi:10.1029/2003JD004,085. [9.1](#)
- Mitchell, D. L. (1996), Use of mass- and area-dimensional power laws for determining precipitation particle terminal velocities, *J. Atmos. Sci.*, 53(12), 1710–1723. [5.4.2](#)
- Mohr, P. J., and B. N. Taylor (2000), The fundamental physical constants, *Physics Today*, 53(8), BG6–BG13. [18.1](#), [a](#)
- Monahan, E. C. (1971), Oceanic whitecaps, *J. Phys. Oceanogr.*, 1, 139–144. [4.1](#)
- Monahan, E. C., K. L. Davidson, and D. E. Spiel (1982), Whitecap aerosol productivity deduced from simulation tank measurements, *J. Geophys. Res.*, 87, 8898–8904. [4.1](#), [4.2](#)
- Monahan, E. C., D. E. Spiel, and K. L. Davidson (1986), A model of marine aerosol generation via whitecaps and wave disruption, pp. 167–174, D. Reidel Pub. Co., Dordrecht, Holland. [4.1](#), [4.2](#), [4.2](#), [4.2](#), [4.2](#)
- Moore, J. K., M. R. Abbott, J. G. Richman, and D. M. Nelson (2000), The Southern Ocean at the last glacial maximum: A strong sink for atmospheric carbon dioxide, *Global Biogeochem. Cycles*, 14(1), 455–475. [16.1](#)
- Moore, J. K., S. C. Doney, D. M. Glover, and I. Y. Fung (2002a), Iron cycling and nutrient-limitation patterns in surface waters of the World Ocean, *Deep-Sea Res. II*, 49, 463–507. [16.1](#)
- Moore, J. K., S. C. Doney, J. A. Kleypas, D. M. Glover, and I. Y. Fung (2002b), An intermediate complexity marine ecosystem model for the global domain, *Deep-Sea Res. II*, 49, 403–462. [16.1](#)
- Moore, J. K., S. C. Doney, K. Lindsay, and N. Mahowald (2005), Mineral dust deposition, ocean biogeochemistry, and air-sea CO₂ exchange: Quantifying climate feedbacks at decadal timescales, *sub judice*, *Science*. [16.1](#)
- Motoyoshi, H., T. Aoki, M. Hori, O. Abe, and S. Mochizuki (2005), Possible effect of anthropogenic aerosol deposition on snow albedo reduction at Shinjo, Japan, *J. Meteorol. Soc. Japan*, 83A, 137–148. [5.4.2](#)
- Muhs, D. R. (1983), Airborne dust fall on the California Channel Islands, U.S.A., *J. Arid Environ.*, 6, 233–238. [3.4.2](#)
- Müller, J.-F., and G. Brasseur (1995), IMAGES: A three-dimensional chemical transport model of the global troposphere, *J. Geophys. Res.*, 100(D8), 16,445–16,490. [10.1](#), [14.3](#)

- Myhre, G., and F. Stordal (2001), Global sensitivity experiments of the radiative forcing due to mineral aerosols, *J. Geophys. Res.*, 106(D16), 18,193–18,204. [1.2](#)
- Myhre, G., A. Grini, J. M. Haywood, F. Stordal, B. Chatenet, D. Tanré, J. K. Sundet, and I. S. A. Isaksen (2003), Modeling the radiative impact of mineral dust during the Saharan Dust Experiment (SHADE) campaign, *J. Geophys. Res.*, 108(D18), 8579, doi:10.1029/2002JD002,566. [9.1](#)
- Namikas, S. L. (2003), Field measurement and numerical modelling of aeolian mass flux distributions on a sandy beach, *Sedimentology*, 50(2), 303–326, doi:10.1046/j.1365–3091.2003.00,556.x. [1.2](#)
- Namikas, S. L., and D. J. Sherman (1997), Predicting aeolian sand transport: revisiting the White model, *Earth Surf. Process. Landf.*, 22(6), 601–604. [3.3](#), [3.3.3](#)
- NCAR Oceanography Section (1997), The NCAR CSM ocean model, Tech. Rep. NCAR/TN–423+STR, National Center for Atmospheric Research, Boulder, Colo. [2.2.2](#)
- Neshyba, S. P., T. C. Grenfell, and S. G. Warren (2003), Representation of a nonspherical ice particle by a collection of independent spheres for scattering and absorption of radiation: 2. Hexagonal columns and plates, *J. Geophys. Res.*, 108(D15), 4448, doi:10.1029/2002JD003,302. [5.4.3](#), [5.4.3](#), [18.11.3](#), [18.11.3](#), [18.11.3](#)
- Newman, C. E., S. R. Lewis, P. L. Read, and F. Forget (2002), Modeling the Martian dust cycle. 1. Representations of dust transport processes, *J. Geophys. Res.*, 107(E12), 5123, doi:10.1029/2002JE001,910. [1.2](#)
- Nieto, P. J. G., B. A. García, J. M. F. Díaz, and M. A. R. B. na (1994), Parametric study of selective removal of atmospheric aerosol by below-cloud scavenging, *Atmos. Environ.*, 28(14), 2335–2342. [6.1](#), [6.2.2](#), [6.5](#)
- Okin, G. S. (2008), A new model of wind erosion in the presence of vegetation, *J. Geophys. Res.*, 113(F02S10), doi:10.1029/2007JF000,758. [3.6](#)
- Overpeck, J., D. Rind, A. Lacis, and R. Healy (1996), Possible role of dust-induced regional warming in abrupt climate change during the last glacial period, *Nature*, 384, 447–449, doi:10.1038/384,447a0. [7](#)
- Owen, P. R. (1964), Saltation of uniform grains in air, *J. Fluid. Mech.*, 20(2), 225–242. [3.3](#), [3.3](#), [3.3.1](#), [3.3.2](#), [3.3.4](#), [3.3.5](#), [3.4.1](#), [3.6](#), [3.6](#)
- Painter, T. H., B. Duval, W. H. Thomas, M. Mendez, S. Heintzelman, and J. Dozier (2001), Detection and quantification of snow algae with an airborne imaging spectrometer, *Appl. Environ. Microbiol.*, 67(11), 5267–5272, doi:10.1128/AEM.67.11.5267. [5.4.2](#)
- Pan, W., M. A. Tatang, G. J. McRae, and R. G. Prinn (1998), Uncertainty analysis of indirect radiative forcing by anthropogenic sulfate aerosols, *J. Geophys. Res.*, 103(D4), 3815–3823. [10.1](#)

- Pandis, S. N., and J. H. Seinfeld (1989), Sensitivity analysis of a chemical mechanism for aqueous-phase atmospheric chemistry, *J. Geophys. Res.*, 94, 1105–1126. [12.4](#)
- Pandis, S. N., J. H. Seinfeld, and C. Pilinis (1992), Heterogeneous sulphate production in an urban fog, *Atmos. Environ.*, 26, 2509–2522. [12.4](#)
- Pandis, S. N., A. S. Wexler, and J. H. Seinfeld (1995), Dynamics of tropospheric aerosols, *J. Phys. Chem.*, 99(24), 9646–9659. [10.1](#)
- Pankine, A. A., and A. P. Ingersoll (2002), Interannual variability of Martian global dust storms: Simulations with a low-order model of the general circulation, *Icarus*, 155(2), 299–323. [1.2](#), [3.3](#), [3.3.3](#)
- Patterson, E. M. (1981), Optical properties of the crustal aerosol: Relation to chemical and physical characteristics, *J. Geophys. Res.*, 86(C4), 3236–3246. [9.4](#)
- Patterson, E. M., D. A. Gillette, and B. H. Stockton (1977), Complex index of refraction between 300 and 700 nm for Saharan aerosols, *J. Geophys. Res.*, 82(21), 3153–3160. [9.4](#)
- Peltier, W. R., and S. Marshall (1995), Coupled energy-balance/ice-sheet model simulations of the glacial cycle: A possible connection between terminations and terrigenous dust, *J. Geophys. Res.*, 100(D7), 14,269–14,289. [7](#)
- Perovich, D. K., and J. W. Govoni (1991), Absorption coefficients of ice from 250 to 400 nm, *Geophys. Res. Lett.*, 18(7), 1233–1235. [9.4](#)
- Peters, K., and R. Eiden (1992), Modelling the dry deposition velocity of aerosol particles to a spruce forest, *Atmos. Environ.*, 26A(14), 2555–2564. [5.1](#)
- Peucker-Ehrenbrink, B., G. Ravizza, and A. W. Hofmann (1994), Cosmic dust: Terrestrial accretion rate and solubility in seawater, *Mineralogical Magazine*, 58A, 718–719. [1.2.1](#)
- Pilinis, C., and X. Li (1998), Particle shape and internal inhomogeneity effects on the optical properties of tropospheric aerosols of relevance to climate forcing, *J. Geophys. Res.*, 103(D4), 3789–3800. [10.1](#)
- Pitter, R. L., H. R. Pruppacher, and A. E. Hamielec (1973), A numerical study of viscous flow past thin oblate spheroid at low and intermediate Reynolds numbers, *J. Atmos. Sci.*, 30, 125–134. [5.4.2](#)
- Pope, R. M., and E. S. Fry (1997), Absorption spectrum (380–700 nm) of pure water. 2. Integrating cavity measurements, *Appl. Opt.*, 36(33), 8710–8723. [9.4](#)
- Press, W. H., S. A. Teukolsky, W. T. Vetterling, and B. P. Flannery (1996), *Numerical Recipes in Fortran 77*, second ed., 933 pp., Cambridge Univ. Press, New York, NY. [18.7](#), [18.7](#)
- Prigent, C., W. B. Rossow, E. Matthews, and B. Marticorena (1999), Microwave radiometric signatures of different surface types in deserts, *J. Geophys. Res.*, 104(D10), 12,147–12,158. [1.2](#), [2.2.2](#)

- Prospero, J. M., P. Ginoux, O. Torres, S. E. Nicholson, and T. E. Gill (2002), Environmental characterization of global sources of atmospheric soil dust derived from the NIMBUS7 TOMS absorbing aerosol product, *Rev. Geophys.*, 40(1), 1002, doi:10.1029/2000RG000095. [3.9](#), [3.9.1](#), [3.9.2](#), [b](#)
- Prospero, J. M., E. Blades, G. Mathison, and R. Naidu (2005), Interhemispheric transport of viable fungi and bacteria from Africa to the Caribbean with soil dust, *Aerobiologia*, 21, 1–19, doi:10.1007/s10453-004-5872-7. [1.2](#)
- Proudman, I., and J. R. A. Pearson (1957), Expansions at small Reynolds numbers for the flow past a sphere and a circular cylinder, *J. Fluid. Mech.*, 2, 237–262. [5.4.1](#)
- Pruppacher, H. R., and J. D. Klett (1978), *Microphysics of Clouds and Precipitation*, 714 pp., D. Reidel Publ. Co. [1](#), [5.4.1](#), [9.8.2](#), [11.1.2](#), [14.2](#), [14.2](#), [a](#), [14.2](#), [18.3](#)
- Pruppacher, H. R., and J. D. Klett (1998), *Microphysics of Clouds and Precipitation*, second ed., 954 pp., Kluwer Acad. Publ., Dordrecht, Holland. [5.4.1](#), [5.4.1](#), [6.2.2](#), [9.8.1](#), [9.8.1](#), [9.8.2](#), [9.8.2](#), [9.8.2](#), [a](#), [a](#), [11.4.2](#), [a](#)
- Pye, K. (1987), *Aeolian Dust and Dust Deposits*, Academic Press, New York, NY. [3.2.3](#), [2](#), [3.7](#), [3.7.4](#), [11](#), [14.1](#)
- Querry, M. R., G. C. Osbourn, K. Lies, R. Jordon, and R. M. Coveney, Jr. (1978), Complex refractive index of limestone in the visible and infrared, *Appl. Opt.*, 17(3), 353–356. [9.1](#), [9.2.1](#), [9.2.1](#), [9.2.1](#), [9.2.1](#)
- Ram, M., M. Stolz, and G. Koenig (1997), Eleven year cycle of dust concentration variability observed in the dust profile of the GISP2 ice core from Central Greenland: Possible solar cycle connection, *Geophys. Res. Lett.*, 24(19), 2359–2362. [7](#)
- Rasch, P. J., M. C. Barth, J. T. Kiehl, S. E. Schwartz, and C. M. Benkovitz (2000), A description of the global sulfur cycle and its controlling processes in the National Center for Atmospheric Research Community Climate Model, version 3, *J. Geophys. Res.*, 105(D1), 1367–1386. [10.1](#)
- Raupach, M. R. (1991), Saltation layers, vegetation canopies and roughness lengths, *Acta Mechanica*, 1, 83–96. [3.6](#), [3.6](#), [3.6](#)
- Raupach, M. R. (1992), Drag and drag partition on rough surfaces, *Bound.-Lay. Meteorol.*, 60, 375–395. [3.6](#), [3.6](#)
- Raupach, M. R. (1994), Simplified expressions for vegetation roughness length and zero-plane displacement as functions of canopy height and area index, *Bound.-Lay. Meteorol.*, 71, 211–216. [2.2.2](#), [3.6](#)
- Raupach, M. R., and H. Lu (2004), Representation of land-surface processes in aeolian transport models, *Environmental Modelling and Software*, 19(2), 93–112. [3.1](#), [3.3.4](#)

- Raupach, M. R., D. A. Gillette, and J. F. Leys (1993), The effect of roughness elements on wind erosion threshold, *J. Geophys. Res.*, 98(D2), 3023–3029. [3.6](#), [3.6](#)
- Raupach, M. R., P. R. Briggs, N. Ahmad, and V. E. Edge (2001a), Endosulfan transport II. Modeling airborne dispersal and deposition by spray and vapor, *J. Environ. Qual.*, 30(3), 729–740. [5.1](#)
- Raupach, M. R., P. R. Briggs, P. W. Ford, J. F. Leys, M. Muschal, B. Cooper, and V. Edge (2001b), Endosulfan transport I. Integrative assessment of airborne and waterborne pathways, *J. Environ. Qual.*, 30(3), 714–728. [5.1](#)
- Ray, P. (1972), Broadband complex refractive indices of ice and water, *Appl. Opt.*, 11, 1836–1834. [9.4](#)
- Reader, M. C., I. Fung, and N. McFarlane (1999a), The mineral dust aerosol cycle during the Last Glacial Maximum, *J. Geophys. Res.*, 104(D8), 9381–9398. [1.2](#)
- Reader, M. C., I. Fung, and N. McFarlane (1999b), Correction to “the mineral dust aerosol cycle during the Last Glacial Maximum”, *J. Geophys. Res.*, 104(D18), 22,319–22,320. [1.2](#)
- Ridame, C., C. Guieu, and M.-D. Loÿe-Pilot (1999), Trend in total atmospheric deposition fluxes of aluminium, iron, and trace metals in the northwestern Mediterranean over the past decade (1985–1997), *J. Geophys. Res.*, 104(D23), 30,127–30,138. [16.1](#)
- Rillig, M. C., S. F. Wright, M. F. Allen, and C. B. Field (1999), Rise in carbon dioxide changes soil structure, *Nature*, 400, 628. [1.2](#)
- Robertson, A., et al. (2001), Hypothesized climate forcing time series for the last 500 years, *J. Geophys. Res.*, 106(D14), 14,783–14,803. [7](#)
- Rogers, R. R., and M. K. Yau (1994), A Short Course in Cloud Physics, no. 113 in International Series in Natural Philosophy, third ed., Pergamon Press, Oxford, UK. [9.8.2](#), [18.4](#)
- Rojas, C. M., and R. E. V. Grieken (1993), Comparison of three dry deposition models applied to field measurements in the Southern Bight of the North Sea, *Atmos. Environ.*, 27A(3), 363–370. [5.1](#)
- Rothman, L. S., et al. (1998), The HITRAN molecular spectroscopic database and HAWKS (HITRAN atmospheric workstations): 1996 edition, *J. Quant. Spectrosc. Radiat. Transfer*, 60(5), 665–710. [a](#)
- Roush, T., J. Pollack, and J. Orenberg (1991), Derivation of midinfrared (5–25 μm) optical constants of some silicates and palagonite, *Icarus*, 94, 191–208. [9.1](#)
- Roush, T. L. (2005), Near-infrared (0.67–4.7 μm) optical constants estimated for montmorillonite, *Icarus*, 179, 259–264, doi:10.1016/j.icarus.2005.06.004. [9.1](#)
- Ruhnke, L. H., and A. Deepak (Eds.) (1984), Hygroscopic Aerosols, Workshop on Hygroscopic Aerosols in the Boundary Layer, A. Deepak Publishing, Hampton, VA. [14.2](#)

- S., L., I. N. Sokolik, J. L. Rajot, S. Caquineau, and A. Gaudichet (2006), Characterization of iron oxides: implications to light absorption by mineral dust aerosols, In Press in *J. Geophys. Res.* 1.2
- Sander, R. (1999a), Modeling atmospheric chemistry: Interactions between gas-phase species and liquid cloud/aerosol particles, *Surv. Geophys.*, 20, 1–31. 12.1
- Sander, R. (1999b), Compilation of henry's law constants for inorganic and organic species of potential importance in environmental chemistry (version 3), <http://www.mpch-mainz.mpg.de/~sander/res/henry.html>. 12.1
- Sassen, K., P. J. DeMott, J. M. Prospero, and M. R. Poellot (2003), Saharan dust storms and indirect aerosol effects on clouds: CRYSTAL-FACE results, *Geophys. Res. Lett.*, 30(12), 1633, doi:10.1029/2003GL017,371. 6.6
- Schaaf, C. B., et al. (2002), First operational BRDF, albedo nadir reflectance products from MODIS, *Rem. Sens. Environ.*, 83, 135–148. 3.8
- Schult, I., J. Feichter, and W. F. Cooke (1997), Effect of black carbon and sulfate aerosols on the global radiation budget, *J. Geophys. Res.*, 102(D25), 30,107–30,117. 10.1
- Schüßler, U., W. Balzer, and A. Deecken (2005), Dissolved Al distribution, particulate Al fluxes and coupling to atmospheric Al and dust deposition in the Arabian Sea, *Deep-Sea Res. II*, 52(14–15), 1862–1878, doi:10.1016/j.dsr2.2005.06.005. 16.1
- Schwartz, S. E. (1986), Mass-transport considerations pertinent to aqueous phase reactions of gases in liquid-water clouds, in *Chemistry of Multiphase Atmospheric Systems*, NATO ASI Series G: Ecological Sciences, vol. 6, edited by W. Jaeschke, pp. 415–471, Springer-Verlag, Berlin. a, 12.6
- Schwartz, S. E. (1992), Factors governing dry deposition of gases to surface water, in *Precipitation Scavenging and Atmosphere-Surface Exchange*, vol. 2, edited by S. E. Schwartz and W. G. N. Slinn, pp. 789–801, Hemisphere Publishing, Washington. 14.2.2
- Segelstein, D. J. (1981), *The complex refractive index of water*, M. S., University of Missouri, Kansas City. 9.4
- Sehmel, G. A. (1980), Particle and gas dry deposition: A review, *Atmos. Environ.*, 14(9), 983–1011. 5.1, 5.4
- Sehmel, G. A. (1984), Deposition and resuspension, in *Atmospheric Science and Power Production*, edited by D. Randerson, no. DOE/TIC-27601 (DE84005177) in series, chap. 12, pp. 533–583, Office of Health and Environmental Research, U.S. Department of Energy, Washington, DC. 5.1
- Sehmel, G. A., and W. J. Hodgson (1978a), A model for predicting dry deposition of particles and gases to environmental surfaces, *Tech. Rep. PNL-SA-6721*, Battelle, Pacific Northwest Laboratory, Richland, WA. 3.5, 5.3.1, 5.3.1, 5.4, 5.4

- Sehmel, G. A., and W. J. Hodgson (1978b), Improved predictive dry deposition velocity correlation, in Pacific Northwest Laboratory Annual Report for 1977: Atmospheric Sciences, edited by C. L. Simpson, no. PNL-2500-3 in Atmospheric Sciences, pp. 2.11–2.12, US DOE, Richland, WA. [5.3.1](#)
- Seinfeld, J. H., and S. N. Pandis (1997), *Atmospheric Chemistry and Physics*, 1326 pp., John Wiley & Sons, New York, NY. [5.4.1](#), [5.4.1](#), [5.4.1](#), [5.5.2](#), [6.5](#), [9.8.1](#), [11.1.2](#), [a](#), [a](#), [11.4.2](#), [11.4.4](#), [12.1](#), [12.1](#), [a](#), [a](#), [12.3](#), [12.6](#), [a](#), [14.2](#), [2](#), [14.3](#)
- Selah, A., and D. W. Fryrear (1995), Threshold wind velocities of wet soils as affected by wind blown sand, *Soil Science*, 160(4), 304–309. [3.7.4](#), [3.7.4](#), [7](#)
- Shannon, S., and D. J. Lunt (2011), A new dust cycle model with dynamic vegetation: LPJ-dust version 1.0, *Geosci. Model Dev.*, 4(2), 85–105, doi:10.5194/gmd-4-85-2011. [3.3](#)
- Shao, Y. (2000), *Physics and Modelling of Wind Erosion*, Atmospheric and Oceanographic Sciences Library, vol. 22, 393 pp., Kluwer AcadPublishers, Dordrecht. [3.1](#)
- Shao, Y. (2001), A model for mineral dust emission, *J. Geophys. Res.*, 106(D17), 20,239–20,254. [3.3.4](#)
- Shao, Y., and L. M. Leslie (1997), Wind erosion prediction over the Australian continent, *J. Geophys. Res.*, 102(D25), 30,091–30,105. [3.4](#)
- Shao, Y., and A. Li (1999), Numerical modelling of saltation in the atmospheric surface layer, *Bound.-Lay. Meteorol.*, 91(2), 199–225, doi:10.1023/A:1001816013,475. [3.4.1](#)
- Shao, Y., and H. Lu (2000), A simple expression for wind erosion threshold friction velocity, *J. Geophys. Res.*, 105(D17), 22,437–22,443. [3.2.3](#)
- Shao, Y., M. R. Raupach, and P. A. Findlater (1993), Effect of saltation bombardment on the entrainment of dust by wind, *J. Geophys. Res.*, 98(D7), 12,719–12,726. [3.3](#), [3.3.3](#), [3.3.4](#), [3.3.4](#), [3.3.4](#), [3.4](#), [3.4.1](#), [3.4.1](#), [3.4.1](#), [3.4.1](#), [3.4.2](#), [3.4.3](#)
- Shao, Y., M. R. Raupach, and J. F. Leys (1996), A model for predicting aeolian sand drift and dust entrainment on scales from paddock to region, *Aust. J. Soil Res.*, 34(D25), 309–342. [3.2](#), [3.2.3](#), [3.4](#), [3.4.1](#), [3.4.1](#), [3.4.2](#), [3.4.2](#), [3.5.1](#), [4](#), [3.7.4](#), [3.7.4](#)
- Shay-El, Y., P. Alpert, Y. J. Kaufman, D. Tanré, A. da Silva, S. Schubert, and J. H. Joseph (1998), Lower-tropospheric response to dust as inferred from correlations between dust frequencies and analysis increments from GEOS-1 multiyear assimilation, *sub judice*, *Tellus*. [10.1](#)
- Shinn, E. A., G. W. Smith, J. M. Prospero, P. Betzer, M. L. Hayes, V. Garrison, and R. T. Barber (2000), African dust and the demise of Caribbean coral reefs, *Geophys. Res. Lett.*, 27(19), 3029–3032. [1.2](#)
- Sinyuk, A., O. Torres, and O. Dubovik (2003), Combined use of satellite and surface observations to infer the imaginary part of refractive index of Saharan dust, *Geophys. Res. Lett.*, 30(2), 1081, doi:10.1029/2002GL016,189. [9.4](#)

- Slinn, S. A., and W. G. N. Slinn (1980), Predictions for particle deposition on natural waters, *Atmos. Environ.*, 14, 1013–1016. [5.1](#), [5.4](#), [5.5.2](#)
- Slinn, W. G. N. (1982), Air-to-sea transfer of particles, in *Air-Sea Exchange of Gases and Particles*, NATO ASI Series, vol. C 108, edited by P. S. Liss and W. G. N. Slinn, pp. 299–405, D. Reidel, Boston. [5.5.2](#), [6.1](#), [6.2.2](#), [6.2.3](#), [6.2.3](#), [6.3](#), [6.4](#)
- Slinn, W. G. N. (1984), Precipitation scavenging, in *Atmospheric Science and Power Production*, edited by D. Randerson, DOE/TIC-27601 (DE84005177), chap. 11, pp. 466–532, Office of Health and Environmental Research, U.S. Department of Energy, Washington, DC. [6.1](#), [6.2.1](#), [6.2.2](#), [6.5](#)
- Slinn, W. G. N., L. Hasse, B. B. Hicks, A. W. Hogan, D. Lal, P. S. Liss, K. O. Munnich, G. A. Sehmel, and O. Vittori (1978), Some aspects of the transfer of atmospheric trace constituents past the air-sea interface, *Atmos. Environ.*, 12, 2055–2087. [5.1](#), [5.5.2](#)
- Smith, M. H., P. M. Park, and I. E. Consterdine (1993), Marine aerosol concentration and estimated fluxes over sea, *Q. J. R. Meteorol. Soc.*, 119, 809–824. [4.1](#), [4.2](#), [4.2](#), [4.2](#), [4.2](#)
- Sokolik, I. N., and O. B. Toon (1996), Direct radiative forcing by anthropogenic airborne mineral aerosols, *Nature*, 381, 681–683. [9.4](#)
- Sokolik, I. N., and O. B. Toon (1999), Incorporation of mineralogical composition into models of the radiative properties of mineral aerosol from UV to IR wavelengths, *J. Geophys. Res.*, 104(D8), 9423–9444. [1.2](#)
- Sokolik, I. N., A. V. Andronova, and T. C. Johnson (1993), Complex refractive index of atmospheric dust aerosols, *Atmos. Environ.*, 27A, 2495–2502. [9.4](#)
- Sokolik, I. N., O. B. Toon, and R. W. Bergstrom (1998), Modeling the radiative characteristics of airborne mineral aerosols at infrared wavelengths, *J. Geophys. Res.*, 103(D8), 8813–8826. [1.2](#)
- Solomon, S., R. R. Garcia, F. S. Rowland, and D. J. Wuebbles (1986), On the depletion of Antarctic ozone, *Nature*, 321, 755–758. [11](#)
- Solomon, S., R. W. Portmann, R. R. Garcia, L. W. Thomason, L. R. Poole, and M. P. McCormick (1996), The role of aerosol variations in anthropogenic ozone depletion at northern midlatitudes, *J. Geophys. Res.*, 101(D3), 6713–6727. [10.1](#)
- Stelson (1990), Urban aerosol refractive index prediction by partial molar refraction approach, *Environ. Sci. Technol.*, 24(11), 1676–1679. [9.6.1](#), [9.6.1](#)
- Stenchikov, G. L., I. Kirchner, A. Robock, H.-F. Graf, J. C. Antuña, R. G. Grainger, A. Lambert, and L. Thomason (1998), Radiative forcing from the 1991 Mount Pinatubo volcanic eruption, *J. Geophys. Res.*, 103(D12), 13,837–13,857. [10.1](#)
- Stroeve, J., J. E. Box, F. Gao, S. Liang, A. Nolin, and C. Schaaf (2005), Accuracy assessment of the MODIS 16-day albedo product for snow: comparisons with Greenland in situ measurements, *Rem. Sens. Environ.*, 94, 46–60. [3.4.2](#)

- Sullivan, R. (2002), Threshold-of-motion wind friction speeds at the Mars Pathfinder landing site, Proc. XXXIII Lunar and Planetary Science Conference. [3.6](#)
- Sun, J., M. Zhang, and T. Liu (2001), Spatial and temporal characteristics of dust storms in China and its surrounding regions, 1960–1999: Relations to source area and climate, *J. Geophys. Res.*, 106(D10), 10,325–10,333. [3.9](#)
- Sweeney, M. R., D. R. Gaylord, and A. J. Busacca (2005), Evolution of Eureka Flat: A dust-producing engine of the Palouse loess, U.S.A., in *In Press in The Soil Record of Quaternary Climate Change*, edited by C. Olson and B. Harrison, Geological Society of America Special Paper, Boulder, CO. [3.4.2](#)
- Tang, I. N. (1997), Thermodynamic and optical properties of mixed-salt aerosols of atmospheric importance, *J. Geophys. Res.*, 102(D2), 1883–1893. [9.4](#)
- Tang, I. N., and H. R. Munkelwitz (1994), Water activities, densities, and refractive indices of aqueous sulfates and sodium nitrate droplets of atmospheric importance, *J. Geophys. Res.*, 99(D9), 18,801–18,808. [9.4](#), [a](#)
- Tanré, D., C. Devaux, M. Herman, R. Santer, and J. Y. Gac (1988), Radiative properties of desert aerosols by optical ground-based measurements at solar wavelengths, *J. Geophys. Res.*, 93(D11), 14,223–14,231. [9.4](#)
- Tanré, D., et al. (2003), Measurement and modeling of the Saharan dust radiative impact: Overview of the Saharan Dust Experiment (SHADE), *J. Geophys. Res.*, 108(D18), 8574, doi:10.1029/2002JD003,273. [9.1](#)
- Tegen, I., A. A. Lacis, and I. Fung (1996), The influence on climate forcing of mineral aerosols from disturbed soils, *Nature*, 380, 419–422. [10.1](#)
- Tegen, I., P. Hollrig, M. Chin, I. Fung, D. Jacob, and J. Penner (1997), Contribution of different aerosol species to the global aerosol extinction optical thickness: Estimates from model results, *J. Geophys. Res.*, 101(D20), 23,895–23,915. [10.1](#)
- Tegen, I., S. P. Harrison, and K. E. Kohfeld (2002a), Modeling the role of mineral aerosols in global climate cycles, *Eos Trans. AGU*, 83(36), 395–400. [3.8](#)
- Tegen, I., S. P. Harrison, K. E. Kohfeld, I. C. Prentice, M. T. Coe, and M. Heimann (2002b), The impact of vegetation and preferential source areas on global dust aerosol: Results from a model study, *J. Geophys. Res.*, 107(D21), 4576. [3.3](#)
- Torres, O. (2003), personal communication. [9.4](#)
- Torres, O., P. K. Bhartia, J. R. Herman, A. Sinyuk, P. Ginoux, and B. Holben (2002), A long-term record of aerosol optical depth from TOMS observations and comparison to AERONET measurements, *J. Atmos. Sci.*, 59(3), 398–413. [b](#)
- Tsonis, A. A. (2002), *An Introduction to Atmospheric Thermodynamics*, Cambridge Univ. Press, Cambridge UK. [8.1](#)

- Tsvetsinskaya, E. A., C. B. Schaaf, F. Gao, A. H. Strahler, R. E. Dickinson, X. Zeng, and W. Lucht (2002), Relating MODIS-derived surface albedo to soils and rock types over Northern Africa and the Arabian peninsula, *Geophys. Res. Lett.*, 29(9), doi:10.1029/2001GL014,096. [3.8](#)
- Underwood, G. M., P. Li, H. Al-Abadleh, and V. H. Grassian (2001a), A Knudsen cell study of the heterogeneous reactivity of nitric acid on oxide and mineral dust particles, *J. Phys. Chem. A*, 105(27), doi:10.1021/jp002,223h, 6609–6620. [11.3](#), [14.2.2](#), [6](#)
- Underwood, G. M., C. H. Song, M. Phadnis, G. R. Carmichael, and V. H. Grassian (2001b), Heterogeneous reactions of NO₂ and HNO₃ on oxides and mineral dust: A combined laboratory and modeling study, *J. Geophys. Res.*, 106(D16), 18,055–18,066. [11.3](#), [11.3](#), [11.3](#), [5](#)
- Usher, C. R., H. Al-Hosney, S. Carlos-Cuellar, and V. H. Grassian (2002), A laboratory study of the heterogeneous uptake and oxidation of sulfur dioxide on mineral dust particles, *J. Geophys. Res.*, 107(D23), 4713, doi:10.1029/2002JD002,051. [14.2.2](#)
- Vali, G. (1985), Nucleation terminology, *Bull. Am. Meteorol. Soc.*, 66(11), 1426–1427. [13](#)
- van Donk, S. J., X. Huang, E. L. Skidmore, A. B. Anderson, D. L. Gebhart, V. E. Prehoda, and E. M. Kellogg (2003), Wind erosion from military training lands in the Mojave Desert, California, U.S.A., *J. Arid Environ.*, 54, 687–703. [1.2](#)
- VanCuren, R. A. (2003), Asian aerosols in North America: Extracting the chemical composition and mass concentration of the Asian continental aerosol plume from long-term aerosol records in the western United States, *J. Geophys. Res.*, 108(D20), 4623, doi:10.1029/2003JD003,459. [1.2](#)
- VanCuren, R. A., and T. A. Cahill (2002), Asian aerosols in North America: Frequency and concentration of fine dust, *J. Geophys. Res.*, 107(D24), 4804, doi:10.1029/2002JD002,204. [5.4.2](#)
- Videen, G., and P. Chýlek (1998), Scattering by a composite sphere with an absorbing inclusion and effective medium approximations, *Opt. Comm.*, 158, 1–6. [9.3](#), [9.3.4](#), [9.3.6](#), [9.3.6](#)
- Vignati, E., G. de Leeuw, and R. Berkowicz (2001), Modeling coastal aerosol transport and effects of surf-produced aerosols on processes in the marine atmospheric boundary layer, *J. Geophys. Res.*, 106(D17), 20,225–20,238. [4.1](#), [4.2](#), [a](#)
- Volz, F. E. (1973), Infrared optical constants of ammonium sulfate, Sahara dust, volcanic pumice, and flyash, *Appl. Opt.*, 12(3), 564–568. [9.4](#)
- Wang, P. K. (2002), *Ice Microdynamics*, Academic Press, San Diego. [5.4.1](#), [5.4.2](#), [5.4.2](#)
- Wang, Z., H. Ueda, and M. Huang (2000), A deflation module for use in modeling long-range transport of yellow sand over East Asia, *J. Geophys. Res.*, 105(D22), 26,947–26,959. [1.2](#)

- Warren, S. G. (1984), Optical constants of ice from the ultraviolet to the microwave, *Appl. Opt.*, 23(8), 1206–1225. [9.4](#)
- Washington, R., M. Todd, N. J. Middleton, and A. S. Goudie (2003), Dust-storm source areas determined by the Total Ozone Monitoring Spectrometer and surface observations, *Annals Association American Geographers*, 93(2), 297–313. [3.9](#)
- Washington, R., et al. (2006), Links between topography, wind, deflation, lakes and dust: The case of the Bodélé Depression, Chad, *Geophys. Res. Lett.*, 33(L09401), doi:10.1029/2006GL025,827. [3.9.1](#)
- Wesely, M. L. (1989), Parameterization of surface resistances to gaseous dry deposition in region-scale numerical models, *Atmos. Environ.*, 23(6), 1293–1304. [5.1](#)
- White, B. R. (1979), Soil transport by winds on Mars, *J. Geophys. Res.*, 84(B9), 4643–4651. [3.3](#), [3.3.3](#), [3.3.3](#), [3.3.3](#), [3.3.3](#), [3.4.2](#), [3.4.2](#), [3.7](#)
- White, B. R., R. Greeley, J. D. Iversen, and J. B. Pollack (1976), Estimated grain saltation in a Martian atmosphere, *J. Geophys. Res.*, 81, 5643–5650. [3.3.3](#)
- Wieliczka, D. M., S. Weng, and M. R. Querry (1989), Wedge shaped cell for highly absorbent liquids: infrared optical constants of water, *Appl. Opt.*, 28(9), 1714–1719. [9.4](#)
- Williams, R. M. (1982), A model for the dry deposition of particles to natural water surfaces, *Atmos. Environ.*, 16(8), 1933–1938. [5.1](#), [5.4](#)
- Wolff, E. W., et al. (2006), Southern Ocean sea-ice extent, productivity and iron flux over the past eight glacial cycles, *Nature*, 440, 491–496, doi:10.1038/nature04,614. [7](#)
- Wong, J. G. D., J. T. Kiehl, B. P. Briegleb, and P. Chýlek (1998), Effect of relative humidity on the optical properties and radiative forcing of sulfate aerosols, *J. Geophys. Res.*, submitted. [10.1](#), [14.2](#)
- Yablokov, M. Y., and A. V. Andronova (2004), A model of take-off processes of desert sand aerosols in windless conditions, unpublished manuscript. [3.5.2](#)
- Yamagata, S., et al. (2004), Mineral particles in cloud droplets produced in an Artificial Cloud Experimental System (ACES), *Aerosol Sci. Technol.*, 38(4), 293–299, doi:10.1080/02786820490422,871. [6.6](#)
- Yang, H., Y. Gao, and L. Horowitz (2006), Effects of particle-size distributions of entrained dust on its emission, loading, and oceanic deposition, *sub judice*, *Geophys. Res. Lett.* [1.2](#)
- Zender, C. S. (2000), Implications of the size-resolved distribution of african mineral dust over the tropical north atlantic, *Eos Trans. AGU*, 81(48), F57. [14.2.4](#)
- Zender, C. S., and E. Y. Kwon (2005), Regional contrasts in dust emission responses to climate, *J. Geophys. Res.*, 110, D13,201, doi:10.1029/2004JD005,501. [3.9](#)

- Zender, C. S., and J. Talamantes (2006), Environmental factors controlling valley fever incidence in Kern County, California, *Int. J. Biometeorol.*, 50(3), 174–182, doi:10.1007/s00484-005-0007-6. [1.2](#)
- Zender, C. S., H. Bian, and D. Newman (2003a), Mineral Dust Entrainment And Deposition (DEAD) model: Description and 1990s dust climatology, *J. Geophys. Res.*, 108(D14), 4416, doi:10.1029/2002JD002775. [3.3](#), [3.3.3](#)
- Zender, C. S., D. J. Newman, and O. Torres (2003b), Spatial heterogeneity in aeolian erodibility: Uniform, topographic, geomorphic, and hydrologic hypotheses, *J. Geophys. Res.*, 108(D17), 4543, doi:10.1029/2002JD003039. [3.8](#)
- Zeng, X., M. Zhao, and R. E. Dickinson (1998), Intercomparison of bulk aerodynamic algorithms for the computation of sea surface fluxes using TOGA COARE and TAO data, *J. Climate*, 11(10), 2628–2644. [2.2.5](#), [2.2.5](#), [2.2.6](#), [2.2.6](#)
- Zhang, L., S. Gong, J. Padro, and L. Barrie (2001), A size-segregated particle dry deposition scheme for an atmospheric aerosol module, *Atmos. Environ.*, 35, 549–560. [5.1](#)
- Zhang, Y., and G. R. Carmichael (1999), The role of mineral aerosol in tropospheric chemistry in East Asia—a model study, *J. Appl. Meteorol.*, 38(3), 353–366. [14.2.1](#), [4](#), [14.2.4](#)
- Zhang, Y., Y. Sunwoo, V. Kotamarthi, and G. R. Carmichael (1994), Photochemical oxidant processes in the presence of dust: An evaluation of the impact of dust on particulate nitrate and ozone formation, *J. Appl. Meteorol.*, 33, 813–824. [14.2.2](#), [14.2.4](#)
- Zhang, Y., C. Seigneur, J. H. Seinfeld, M. Jacobson, S. L. Clegg, and F. S. Binkowski (2000), A comparative review of inorganic aerosol thermodynamic equilibrium modules: Similarities, differences, and their likely causes, *Atmos. Environ.*, 34, 117–137. [14.2](#)
- Zribi, M., and M. Dechambre (2003), A new empirical model to retrieve soil moisture and roughness from C-band radar data, *Rem. Sens. Environ.*, 84(1), 42–52. [2.2.2](#)

Index

- a*-axis, [201](#)
- c*-axis, [201](#)
- Takla Makan Desert, [66](#)
- Tarim Basin, [66](#)
- [, [69](#), [100](#)
- \Bodele Depression, [66](#)

- absorption coefficient, [108](#)
- absorption efficiency, [122](#)
- acceleration, [210](#)
- ACE Asia, [3](#)
- activity coefficient, [173](#)
- adaptation timescale, [124](#)
- adsorption, [135](#)
- adsorptive force, [61](#)
- ADT, [83](#)
- advective, [209](#)
- aerodynamic threshold friction velocity, [21](#)
- AERONET, [116](#), [116](#)
- aerosol particle, [169](#)
- Aethalometer, [170](#)
- air dry, [56](#)
- Aitken nuclei, [169](#)
- almucantar, [116](#)
- amorphous calcite, [107](#)
- angle of repose, [25](#)
- angular frequency, [108](#)
- AOD, [187](#)
- aqueous chemistry, [131](#)
- aqueous solutions, [156](#)
- areal flux, [146](#)
- aspect ratio, [201](#)
- AVIRIS, [83](#)

- ballistic, [12](#)
- BET, [137](#)

- BET correction, [137](#)
- Bodélé Depression, [65](#)
- body forces, [211](#)
- Boltzmann’s constant, [105](#)
- bombardment efficiency, [30](#)
- bombardment parameter, [42](#)
- Brownian diffusivity, [85](#)
- Bruggeman approximation, [110](#), [113](#)
- Brunauer-Emmett-Teller, [137](#)
- bulk aerodynamic approximation, [8](#), [9](#)
- bulk density, [60](#)
- bulk volume, [56](#)
- burst and sweep cycles, [52](#)

- C. nivalis*, [83](#)
- calcite, [107](#)
- canopy resistance, [79](#)
- CAPE, [16](#)
- capillary force, [61](#)
- Cartesian coordinates, [206](#)
- CCN, [100](#), [170](#)
- CCNC, [170](#)
- CDP, [170](#)
- Channel Islands, [47](#)
- Chapman mechanism, [128](#)
- chemisorption, [135](#)
- China, [66](#)
- Chlamydomonas nivalis*, [83](#)
- CLM, [16](#)
- close packed system, [63](#)
- Cloud condensation nuclei, [169](#)
- Cloud Condensation Nuclei Counter, [170](#)
- cloud droplet, [169](#)
- Cloud Droplet Probe, [170](#)
- coarse, [19](#)
- cohesionless threshold coefficient, [27](#)

- collection efficiency, 92
- collection volume, 94
- collision efficiency, 88, 94
- complementary error function, 147, 194
- Composition-Shape-Size, 83
- Condensation freezing, 170
- Condensation nuclei, 169
- Condensation Particle Counter, 170
- conductance, 8
- conservative bombardment, 41
- Contact freezing, 170
- contact nucleation, 170
- continuum regime, 145, 145
- convective velocity scale, 16
- CPC, 170
- CRYSTAL-FACE, 100
- CSS, 83
- curl, 205, 207

- Darcy's law, 58
- DDA, 83
- del operator, 204
- del square, 205
- density, 106
- Deposition nucleation, 170
- deposition resistance, 142
- deposition velocity, 76, 142
- diatomite, 66
- dielectric constant, 109
- dielectric function, 109
- diffusion limited, 156
- diffusiophoresis, 86
- diffusivity of vapor in air, 120
- dimensionless threshold friction speed, 21
- direct mechanism, 70
- DIRTMAP, 103
- Discrete Dipole Approximation, 83
- dispersive analysis, 109
- divergence, 204, 207
- drag, 211
- drag coefficient, 80
- drag partition, 5, 11, 53
- drag velocity, 6
- dry density, 57
- dry deposition, 75
- dry soil, 56
- dust, 19, 30
- dust devils, 53
- Dust Storm Frequency, 2
- dynamic viscosity, 89, 193
- dynamic viscosity of air, 212

- eddy fluxes, 8
- EEMA, 115
- effective Henry's Law coefficient, 160, 163
- effective medium approximations, 110
- electroneutrality, 160
- electrophoresis, 53, 86, 91
- ellipsoid, 201
- EMA, 110
- equation of continuity in flux form, 209
- equation of continuity in velocity divergence form, 209
- equipartition theorem, 150
- equivalent threshold moisture, 62
- erodibility, 11
- erosivity, 11
- error function, 147, 194
- Euler's constant, 81
- Euler's equations of motion, 211
- Eureka Flat, 47
- exchange coefficient for momentum, 5
- exchange coefficients, 10
- extended effective medium approximation, 110, 115
- external forces, 211
- extra-terrestrial, 3

- FDTD, 83
- fetch, 52
- Fick's First Law, 121, 146
- Fick's first law, 77
- Fick's Second Law, 147
- film drops, 70
- fixed, 129
- fluid threshold friction velocity, 21
- flux ratio, 41
- flux Richardson number, 14
- flux wind speed, 16
- foam, 70

- force, 210
- Freezing nucleation, 170
- Fresnel's equation, 110
- friction Reynolds number, 24
- friction speed, 6
- friction velocity, 6, 23
- frictional stress, 211
- gamma function, 194
- GCCN, 100
- giant cloud condensation nuclei, 100
- Gobi Desert, 66
- Goethite, 47
- gradient, 204, 207
- gradient Richardson number, 16
- gravimetric water content, 56
- gravitational settling, 23
- gypsum, 107
- haze particle, 169
- heat of dissolution, 156
- heating rate, 119
- Heaviside step function, 91
- Henry's Law, 156
- heterogeneous, 125
- heterogeneous chemistry, 131
- hexagonal columns, 202
- hexagonal plates, 202
- hexagonal prisms, 201
- Hollow Sphere Equivalent, 110
- Hollow Sphere Equivalent approximation, 111
- horizon, 172
- hydrolysis, 159
- hygroscopic growth, 173
- hysteresis effect, 176
- ice crystal, 169
- Ice nucleation modes, 170
- Ice Nuclei, 201
- Ice nuclei (IN), 169
- Ideal Gas Law, 105, 106, 120
- illite, 107
- Immersion freezing, 170
- impact coefficient, 33
- impact threshold friction velocity, 21
- impact-rupture-ejection, 40
- IN, 100
- in situ, 116
- inclusion, 111, 113
- incompressible, 210
- index of refraction, 107, 108
- indirect mechanism, 70
- inertial impaction, 85, 89
- integrating factor, 124
- Interfacial transport, 150
- internal forces, 211
- interparticle cohesive forces, 25
- ion, 126
- jet drops, 70
- kaolinite, 107
- Kelvin effect, 176
- Kelvin's Law, 175
- kinematic viscosity, 194
- kinematic viscosity of air, 120
- kinetic regime, 145, 145
- Knudsen number, 145
- Kramers-Kronig, 109
- Lagrangian derivative, 209
- LAI, 1
- Laplace transforms, 147
- Laplacian, 205, 208
- Large Eddy Simulation, 7
- latent cooling, 118
- latent heating, 118
- LGM, 103
- limestone, 107
- Limiting regime, 80
- loess, 47
- logarithmic wind profile, 7
- Lorentz lines, 109
- major axis, 201
- mantle, 47
- Mars, 55
- mass, 106
- mass accommodation coefficient, 135
- mass fraction, 111
- mass mean scavenging coefficient, 96
- mass mean scavenging efficiency, 98

- mass transport, 168
- mass ventilation coefficient, 119
- mass-weighted scavenging coefficient, 97
- material derivative, 209
- matric potential, 61
- matric suction, 61
- matrix, 111, 113
- Maxwell Garnett approximation, 110, 112
- Maxwell's equations, 108
- Maxwell-Boltzmann statistics, 150
- Maxwellian flux, 149
- MCA, 111
- mean linear mass increase coefficient, 176
- mean molecular weight, 105
- Meteoric dust, 3
- Mie theory, 116, 117
- MISR, 83
- modulus of rupture, 62
- modulus of surface rupture, 40
- molality, 155
- molar concentration, 155
- molar refraction, 116
- molar volume, 116
- molarity, 155
- mole number, 105
- moment, 20
- moment arm, 25
- moment of rotational inertia, 25
- momentum, 210
- momentum flux, 5
- Monin-Obukhov length, 15
- Monin-Obukhov similarity theory, 7
- montmorillonite, 107
- multi-component aerosol, 111
- nabla, 204
- Nephelometer, 170
- neutral drag coefficient, 7
- neutral exchange coefficient for momentum, 7, 71
- Newton's law of friction, 193
- Newton's laws of motion, 210
- Newton's Second Law, 210
- Newtonian fluid, 22
- nitrogen deficiency, 188
- nitrogenase, 188
- non-continuum regime, 145
- non-dimensionalizing, 22
- non-saltating roughness length, 53, 54
- North Atlantic, 188
- number mean scavenging coefficient, 97
- number mean scavenging efficiency, 98
- oblate ellipsoid, 201
- OPC, 170
- open packed system, 63
- Optical Particle Counter, 170
- oven dry, 56
- Owen effect, 53
- oxidation, 126
- oxidation state, 126
- Pacific Ocean, 188
- packing angle, 20
- Paleolake Megachad, 66
- partial molar refraction, 116
- particle temperature, 120
- Peclet number, 88
- pedons, 172
- permittivity of free space, 109
- phosphorous deficiency, 188
- photochemical, 125
- physisorption, 135
- phytoplankton, 188
- Planck function, 122
- polar stratospheric clouds, 131
- pore diffusion correction, 138
- potential flow, 89
- power, 118
- precipitation intensity, 93
- precipitation mass flux, 93
- precipitation volume flux, 93
- pressure, 105
- pressure excess, 193
- pressure potential, 59
- Primary processes (mechanisms) of ice formation, 169
- probability distribution function, 52
- prolate ellipsoid, 201
- Pyranometer, 170

- quasi-laminar layer, 52
- radial flux, 146
- radiant heating, 118
- radius fraction, 111
- Raoult's Law, 156
- Rayleigh distribution, 196
- Rayleigh tail distribution, 196
- reference height, 10
- Refractive indices, 108
- regularized gamma functions, 195
- relative humidity, 176
- relative permittivity, 109
- resistance, 8, 75
- resistance-in-series, 138
- resuspension flux, 76
- retention efficiency, 91
- Reynolds fluxes, 8
- Reynolds number, 23, 80, 89, 119
- roughness length, 10, 53
- Sahara, 66
- Saharan Air Layer, 100
- SAL, 100
- saltating friction velocity, 54
- saltating roughness length, 54
- saltation, 19, 30, 53
- sand, 19
- sandblasting, 39
- Santa Anas, 47
- saturated soil, 56
- saturated vapor pressure, 120
- scale parameter, 52, 196, 200
- scavenging coefficient, 95
- scavenging efficiency, 97
- Schmidt number, 86, 89, 119
- sea salt, 69
- SeaWiFS, 187
- secondary particles, 30
- Secondary processes (mechanisms) of ice formation, 169
- sensible heating, 118
- SHADE, 107
- shape parameter, 52, 196
- shear stress, 211
- similarity function, 14
- single scattering albedo, 115, 118
- size parameter, 203
- slip correction factor, 80
- soil moisture memory, 55
- soil texture, 55
- solute, 155
- solution, 155
- solvent, 155
- SOM, 60
- specific gas constant, 105
- specific heat at constant pressure, 123
- specific volume, 106
- spectral deposition mass flux, 76
- spectral deposition number flux, 76
- spectral precipitation intensity, 93
- spectral precipitation mass flux, 93
- Spectroradiometer, 170
- spherical coordinates, 206
- spherical flux, 149
- spherical meteorological coordinates, 206
- spherical polar coordinates, 206
- spume, 70
- stability correction factor, 13
- stability parameter, 13
- Stefan flow, 86
- sticking coefficient, 135
- sticking efficiency, 76, 91
- Stokes correction factor, 82
- Stokes number, 85
- Stokes' settling velocity, 79
- Stokes-Einstein relation, 86
- streamwise mass flux, 30
- stress partition, 5
- stress tensor, 211
- stresses, 211
- surface area, 137
- surface chemistry, 131
- surface creep, 30
- surface phase, 192
- surface stress, 8
- surface tension, 192
- surface tension of water, 61
- suspension, 30
- swelling function, 56

- Takla Makan Desert, 66
- temperature, 105
- terminal velocity, 23, 79, 81
- texture, 19
- thermal conductivity of snow, 120
- thermal conductivity of dry air, 121
- thermal diffusivity of air, 121
- thermal equilibrium, 122
- thermal speed, 150
- thermal ventilation coefficient, 121
- thermophoresis, 86, 91
- threshold friction Reynolds number, 24
- threshold gravimetric water content, 62, 65
- threshold parameter, 21
- TKE, 14
- TOMS, 65, 116
- total derivative, 209
- total potential energy, 58
- transition regime, 80
- truncated PDF, 199
- turbulence transition, 81
- Turbulent regime, 80
- turbulent surface fluxes, 8

- universal gas constant, 105
- universal gravitational constant, 210
- upper incomplete gamma function, 198
- uptake coefficient, 136

- V/A , 83
- V/S , 83
- vacuum permittivity, 109
- van't Hoff factor, 173
- vector wave equation, 208
- very fine, 19
- virtual potential temperature, 15
- viscosity ratio, 89
- viscous stress, 211
- volume, 105
- volume fraction, 111
- volumetric water content, 56
- Von Karman constant, 7, 15
- vorticity, 205

- wavenumber, 109
- wavenumber vector, 108

- Weibull distribution, 52
- wet deposition, 87
- wetted, 171
- wind friction efficiency, 11
- wind friction speed, 53
- wind speed, 53, 208
- wind stress, 8
- wind tunnel, 62

- zero plane displacement, 16